



**University of
Nottingham**
UK | CHINA | MALAYSIA

Nottingham Geospatial Institute

The Utilization of Sentinel-1 and Intermittent SBAS DInSAR for Enhanced Deformation Monitoring of Geohazards

By

David C. Gee MSc

Thesis submitted to the University of Nottingham for the degree of Doctor of Philosophy

March 2021

Declaration

The candidate confirms that the work submitted is his own, except where work which has formed jointly authored publications has been included. The contribution of the candidate and other authors to this work has been explicitly indicated below and appropriate credit given to the work of others.

The InSAR processing performed throughout the duration of this thesis was facilitated by access to the ISBAS processing chain and PUNNET software, provided by Terra Motion Limited. The results achieved would not have been possible without the ongoing developments at Terra Motion which has been led by Andrew Sowter, with significant contributions from Yuri Bykov, Ahmed Athab, Alessandro Novellino and I. Such development has been funded by Terra Motion Limited.

I jointly conceived and designed the work of chapter three, along with Andrew Sowter, Stuart Marsh, Stephen Grebby, Luke Bateson, Alessandro Novellino and Christopher Satterley. I performed the InSAR processing and led the analysis and writing of the paper, for which all of the authors contributed. The work appears in the publication: Gee, D., Bateson, L., Sowter, A., Grebby, S., Novellino, A., Cigna, F., Marsh, S., Banton, C. and Wyatt, L., 2017. Ground motion in areas of abandoned mining: application of the Intermittent SBAS (ISBAS) to the Northumberland and Durham Coalfield, UK. *Geosciences*, 7(3), p.85.
<https://doi.org/10.3390/geosciences7030085>

I developed the groundwater model produced in chapter four with assistance from Luke Bateson and Alessandro Novellino. I conducted the InSAR processing with Andrew Sowter, performed the analysis and wrote the paper, where all the authors contributed to the development and revision of the study and paper. The work has appeared in publication as follows: Gee, D., Bateson, L., Grebby, S., Novellino, A., Sowter A., Wyatt, L., Marsh, S., Morgenstern, R., Athab, A. Modelling groundwater rebound in recently abandoned coalfields using DInSAR. *Remote Sensing of Environment*. 249, 112021.
<https://doi.org/10.1016/j.rse.2020.112021>

The work of chapter five was conceived by Andrew Sowter, Ahmed Athab and I. I conducted the InSAR processing along with Andrew Sowter, Ahmed Athab and Stephen Grebby. I lead the analysis, interpretation and writing of the paper, with contributions from all the authors. The work has appears in publication: Gee, D., Sowter, A., Grebby, S., de Lange, G., Athab, A. and Marsh, S., 2019. National geohazards mapping in Europe: Interferometric analysis of the Netherlands. *Engineering Geology*. 256, pp.1-22.
<https://doi.org/10.1016/j.enggeo.2019.02.020>

This copy has been supplied on the understanding that it is copyright material and that no quotation from the thesis may be published without proper acknowledgement.

David Gee, The University of Nottingham © 2021

Acknowledgements

This PhD project was undertaken at the Nottingham Geospatial Institute (NGI), University of Nottingham in conjunction with Terra Motion Limited, the British Geological Survey, the Coal Authority and Freiberg University of Mining and Technology. This research was funded by the GeoEnergy Research Centre.

I would firstly like to thank Andrew Sowter for providing me with this opportunity and his continued support and mentoring since first working with me in 2014. I am grateful for the guidance and encouragement throughout my time at the University of Nottingham from my principal supervisors Stephen Grebby and Stuart Marsh.

I would like to thank the staff at the British Geological Survey for their time and effort in helping to develop this work, namely Luke Bateson and Alessandro Novellino.

I would also like to thank Terra Motion Limited (formerly Geomatic Ventures Limited) who have allowed me the time and facilities to conduct this research, the outcomes of which would not have been the same without such access. This includes both present and former members of staff including Andrew Sowter, Paul Bhatia, Ahmed Athab, Renoy Girindran, Yuri Bykov and Alessandro Novellino.

Further thanks go to the Christopher Satterley at the Coal Authority for his role in the coordination of the project and being a principle point of contact. Thanks also go to Lee Wyatt, Carl Banton and Philip Broughton for reviewing parts of this work and/or providing data critical to this project.

Additionally, I would like to thank the Geotechnical Institute, Freiberg University of Mining and Technology for their patience, access, and knowledge, in particular Roy Morgenstern, Heinz Konietzky and Martin Herbst.

Finally, I would like to broadly thank everyone involved for their friendship, good will and assistance since first joining the NGI in 2014.

Abstract

The monitoring of land motion can provide critical information on potential geological hazards. Geohazards are phenomena that can pose significant socio-economic and environmental risks. There have been an increasing number of geohazard mapping programmes across the world that utilise space-related technologies, such as the Global Navigation Satellite System (GNSS) and Earth Observation (EO). Differential interferometric synthetic aperture radar (DInSAR) is an EO technique that utilizes spaceborne synthetic aperture radar (SAR) data to measure millimetric rates of ground deformation from the differences in phase between image acquisitions. However, two significant limitations of DInSAR analysis are that incoherence restricts measurements to urbanised or rocky areas and free, readily available data with sufficient temporal coverage has not historically been available. In this regard, the Intermittent Small Baseline Subset (ISBAS) is a processing algorithm which is capable of computing velocities over land cover types that have typically been unfavourable for DInSAR analysis. In addition, as part of the Copernicus EO program, the Sentinel-1 satellite provides readily available conflict-free data every 6 days in Europe.

The purpose of this research is to demonstrate the potential of the ISBAS processing method and Sentinel-1 SAR data for enhanced capability to monitor ground movements related to geological hazards. Previously, the initial results utilizing the ISBAS method on archive data have identified notable deformations over former coalfields in the UK. Here, previous research was revisited over the Northumberland and Durham coalfield, whereby the ISBAS method was applied to archive and Sentinel-1 data providing deformation data spanning 3 decades. The results show that unexpected and changing amounts of ground motion can be present over former coalfields. The near complete coverage of measurements aided the interpretation and most notably temporal correlations between the rise of mine water and surface heave were made. The results showed that ISBAS measurements had the potential to be utilized to map changes in groundwater levels.

Subsequently, an analytical model based upon the principle of effective stress and concept of mine water ponds was developed to relate changes in groundwater levels to changes in the thickness of the strata and, hence, determine surface movement. The forward models estimate surface heave utilising measurements from monitoring boreholes. The models were calibrated and validated using ISBAS measurements, where good agreement was found between the model and the DInSAR, over the demonstration site of the Nottinghamshire coalfields. The ISBAS measurements were then inverted to estimate the change in groundwater levels across the whole coalfield, providing greater spatial coverage than could be inferred from the spatially sparse monitoring boreholes or the forward model. The inverse map was then utilized to predict the time it will take for groundwater to discharge out of the Coal Measures rock.

Additionally, the seamless coverage and regular revisit of Sentinel-1 affords the potential for wide-area monitoring of mining deformations and other geohazards. This was demonstrated over the Netherlands where multiple stacks of data were processed and mosaicked together to produce a wide-area-map. The motions, attributed to compressible soils, infrastructure settlement, peat oxidation, gas production, salt mining and underground and opencast mining, were validated with all available independent ancillary information such as previous persistent scatterer interferometry (PSI) deformation maps, models of subsidence and settlement susceptibility and GPS measurements. A statistical analysis showed that measurements in rural areas can provide reliable information with a high degree of confidence (5σ). Finally, the processing requirements for a full Europe-wide deformation map were calculated to determine the opportunity and challenges Sentinel-1 presents for future operational services.

Contents

1.	Introduction.....	1
1.1.	Geohazard Monitoring.....	1
1.2.	Differential Interferometric Synthetic Aperture Radar.....	1
1.3.	Research Gap.....	2
1.4.	Aims and Objectives	3
1.5.	Thesis Overview.....	3
1.6.	Summary.....	4
1.7.	References.....	4
2.	Literature Review.....	9
2.1.	Synthetic Aperture Radar (SAR).....	9
2.1.1.	SAR Origins.....	9
2.1.1.1.	Radio Detection and Ranging (Radar).....	9
2.1.1.2.	Side Looking Airborne Radar (SLAR).....	9
2.1.2.	Synthetic Aperture.....	10
2.1.3.	Coherent Imaging.....	10
2.1.4.	Polarization.....	10
2.1.5.	SAR Geometry.....	11
2.1.6.	SAR Transmission	12
2.1.7.	Range Resolution	12
2.1.8.	Azimuth Resolution.....	13
2.1.9.	Geometric Distortion.....	13
2.1.9.1.	Foreshortening.....	13
2.1.9.2.	Layover.....	14
2.1.9.3.	Shadow.....	14
2.1.10.	Image Composition.....	14
2.1.11.	European Space Agency SAR Satellites.....	15
2.1.11.1.	ERS 1/2.....	15

2.1.11.2.	ENVISAT.....	15
2.1.11.3.	Sentinel-1.....	15
2.2.	Interferometric Synthetic Aperture Radar (InSAR).....	17
2.2.1.	InSAR Geometry.....	18
2.2.2.	Interferometric Phase Contributions.....	20
2.2.2.1.	Geometric.....	20
2.2.2.2.	Topographic.....	21
2.2.2.3.	Differences in Atmospheric Propagation Delay.....	23
2.2.2.4.	Noise.....	24
2.2.2.4.1.	Incoherence.....	24
2.2.2.4.2.	Unwrapping Errors.....	25
2.2.2.4.3.	Thermal Noise.....	27
2.2.2.5.	Ground Deformation	27
2.3.	Multi-temporal Differential InSAR.....	28
2.3.1.	Conventional DInSAR Limitations.....	28
2.3.2.	Stacking.....	28
2.3.3.	Time-Series Approaches.....	29
2.3.3.1.	Persistent Scatters Interferometry.....	29
2.3.3.2.	Small Baseline Methods.....	30
2.4.	Intermittent Small Baseline Subset.....	30
2.4.1.	SBAS.....	30
2.4.2.	ISBAS.....	31
2.5.	Coal Mining.....	34
2.5.1.	Mining Subsidence.....	34
2.5.2.	Groundwater Rebound.....	36
2.5.3.	Groundwater Modelling.....	37
2.6.	Summary.....	38
2.7.	References.....	38

3.	Ground Motion in Areas of Abandoned Mining: Application of the Intermittent SBAS (ISBAS) to the Northumberland and Durham Coalfield, UK.....	48
4.	Modelling Groundwater Rebound in Recently Abandoned Coalfields using DInSAR.....	49
5.	National Geohazards Mapping in Europe: Interferometric Analysis of the Netherlands.....	50
6.	Recommendations and Conclusions.....	51
6.1.	Review of Aims and Objectives.....	51
6.1.1.	Long Term Coalfield Deformation Monitoring.....	51
6.1.2.	Sentinel-1 and ISBAS to Infer Changes in Groundwater Levels	52
6.1.3.	Wide-Area Operational Geohazard Monitoring.....	54
6.2.	Summary of Recommendations of Further Work	56
6.3.	Summary.....	56
6.4.	References.....	56

List of Figures

2.1.	SAR imaging geometry.....	11
2.2.	Geometric distortion.....	13
2.3.	Argand diagram of a Single Look Complex pixel.....	14
2.4.	Sentinel-1 operation modes.....	15
2.5.	Formation of an interferogram.....	18
2.6.	Interferometric SAR geometry.....	19
2.7.	Simulated phase in the absence of topography.....	20
2.8.	Geometric decorrelation.....	21
2.9.	Topographic interference.....	22
2.10.	Difference in path delay due to a changing atmosphere.....	24
2.11.	Decorrelation due to changes in scatter.....	25
2.12.	Relationship between ambiguity height and wavelength.....	26
2.13.	Relationship between wrapped and unwrapped phase.....	26
2.14.	Persistent and distributed scatterers.....	30
2.15.	Sentinel-1 interferograms over north Nottinghamshire.....	32
2.16.	Deformations produced by coal extraction.....	35
6.1.	Change in heave over time in North Nottinghamshire.....	52
6.2.	Deformation over all mine water ponds in the UK.....	53

List of Tables

2.1.	Radar band designations.....	9
2.2.	Characteristics of Sentinel-1 nominal measurements modes.....	17
2.3.	Published literature on the ISBAS method.....	34

Nomenclature

Acronyms and Abbreviations

AMD	Acid Mine Drainage
AOD	Above Ordnance Datum
AOI	Area of Interest
APS	Atmospheric Phase Screens
BGS	British Geological Survey
BRW	Browse
CMG	Coal Measures Group
DInSAR	Differential Interferometric Synthetic Aperture Radar
DEM	Digital Elevation Model
EO	Earth Observation
ENVISAT	Environmental Satellite
ERS	European Remote Sensing
ESA	European Space Agency
EU	European Union
EW	Extra Wide
FM	Frequency Modulated
GERC	GeoEnergy Research Centre
GIS	Geographic Information System
GPS	Global Positioning System
GNSS	Global Navigation Satellite System
GRAM	Groundwater Rebound in Abandoned Mineworkings
GRD	Ground Range Detected

InSAR	Interferometric SAR
IW	Interferometric Wide
ISBAS	Intermittent Small Baseline Subset
LAI	Leaf Area Index
LiDAR	Light Detection and Ranging
LOS	Line-of-Sight
NAP	Normaal Amsterdams Peil
NERC	Natural Environment Research Council
POD	Precise Orbit Determination
PS	Persistent Scatterer
PSI	Persistent Scatterer Interferometry
Radar	Radio Detection And Ranging
RMSE	Root Mean Square Error
ROI	Region of Interest
SAR	Synthetic Aperture Radar
SB	Small Baseline
SBAS	Small Baseline Subset
SLAR	Side Looking Airborne Radar
SLC	Single Look Complex
SM	Strip Map
SNR	Signal to Noise Ratio
SRTM	Shuttle Radar Topography Mission
TOPSAR	Terrain Observation with Progressive Scans SAR
WAM	Wide-Area-Map
WV	Wave Mode

Symbols

\emptyset	Azimuth track angle
A	Position of sensor
B_{\perp}	Perpendicular baseline
b	Bed thickness
c	Speed of light
H	Height of sensor
i	Imaginary number
n	Minimum number of interferograms
N	Total number of interferograms
P	Position on Earth
q	Real number
R	Pseudo-range
s	Complex number
s^*	Complex conjugate
T	Time
t	Transmitted signal
v	Velocity
α	Amplitude
γ	Coherence
ε	Standard error
θ	Incidence angle
λ	Wavelength
ρ	Slant range
Φ	Interferometric phase
φ	Phase

1. Introduction

1.1. Geohazard Monitoring

Geohazards are phenomena that can pose significant risk to lives, property and the surrounding environment and are therefore of significant national and international importance. They result from an undesired combination of geological processes and ground conditions, and in some instances are precipitated by anthropic activities. The United Kingdom, for example, is subject to landslides and slope failures, sinkholes, gas hazards, seismic events (e.g. earthquakes), geotechnical hazards (e.g. clay shrinkage), coastal erosion and subsidence. A number of environmental hazards have arisen from the exploitation of mineral deposits, such as coal. This has resulted in a legacy of mining subsidence, abandoned shafts, gas emissions, polluted water flows and changes in groundwater levels (Giles, 2020).

The monitoring of land motion can provide critical information on geohazards which is crucial for the sustainable development environment and management of Earth's resources as populations continue to rise and expand into areas that are at greater risk to natural and anthropogenic hazards. For example, subsidence is frequently observed at the Earth's surface when groundwater is abstracted. Conventional monitoring methods for mapping surface deformation include precise levelling, close range photogrammetry and Global Positioning Systems (GPS). However, such methods can be laborious, expensive and offer limited spatial coverage.

1.2. Differential Interferometric Synthetic Aperture Radar

An increasing number of geohazard mapping programmes across the world utilise space-related technologies, such as the Global Navigation Satellite System (GNSS) and Earth Observation (EO). EO technologies provide a systematic architecture to map and model the complex physical phenomena that result in geohazards, often at multiple scales. They can overcome the limitations of conventional surveying techniques and can make observations in regions that may not otherwise be possible due to political and/or physical constraints. Differential interferometric synthetic aperture radar (DInSAR) is an EO technique that can measure sub-centimetre changes in Earth surface height. The geodetic method utilizes synthetic aperture radar (SAR) data acquired from instruments mounted aboard sun-synchronous Earth orbiting satellites. Ground deformation can be extracted from engineered differences of phase between image pairs acquired at a different period in time (Massonet & Feigl, 1998). Accordingly, DInSAR is able to make a significant contribution to the measurement and monitoring of a wide range of geohazards including landslides (Cigna *et al.*, 2013), tectonics (Wright *et al.*, 2004), volcanology (Sigmundsson *et al.*, 2010), in addition to ground motion associated with anthropogenic activity such as oil and gas production

(Fielding *et al.*, 1998), carbon capture and storage (Rohmer *et al.*, 2015), civil engineering works (Chang *et al.*, 2017), groundwater abstraction (Sowter *et al.*, 2016) and mining (Bateson *et al.*, 2015).

A variety of persistent scatterer and small baseline (SB) interferometric techniques have been utilised to delineate and quantify coal mining related surface phenomena (e.g. Colesanti *et al.*, 2005; Leighton *et al.*, 2013; Cuenca *et al.*, 2013; Przylucka *et al.*, 2015; Du *et al.*, 2016). However, a significant limitation of DInSAR is phase decorrelation, or incoherence, which restricts the analysis to urbanised or rocky areas where temporal phase dispersion is minimized. Over vegetated areas, such as agricultural fields, forests, semi-natural areas and wetlands incoherence prevails, which restricts the spatial density and distribution of ground motion measurements that can be computed from both persistent scatterer interferometry (PSI) and small baseline (SB) techniques to just hard targets (Osmanoğlu *et al.*, 2016). In the United Kingdom, for example, urbanised areas comprise only 7% of the total land cover (EEA, 2012). Moreover, data availability has been a further limitation of time-series DInSAR, as sufficient data acquisitions are required to span a deformation event for a reliable result.

Two notable advancements are the launch of the Sentinel-1 satellite and development of the Intermittent Small Baseline Subset (ISBAS) (Sowter *et al.*, 2013) processing method. Launched in 2014, Sentinel-1 is a two-satellite constellation carrying a C-Band (5.5 cm wavelength – 5.4 GHz) SAR payload which provides conflict-free data every 6 days in Europe and at least 12 days for the majority of the global landmasses (Torres *et al.*, 2012). The ISBAS method has improved the capability to characterise deformation over land cover types that have typically been unfavourable for DInSAR analysis.

1.3 Research Gap

The initial results utilizing ISBAS on archive data over sites in the UK have identified deformation in urban and rural environments alike over former coalfields (e.g. Sowter *et al.*, 2013; Bateson *et al.*, 2015). Coalfields are thought to be highly dynamic over time in terms of surface deformation. Heave, which is often bound by existing fault structures, has been previously observed in coal measures rocks and is assumed to occur because of rising groundwater following coalfield abandonment. Many studies have recognised the impact of changing groundwater levels on the compaction of strata and deformation at the surface (e.g. Hoffmann *et al.*, 2001; Galloway and Hoffmann, 2007; Bell *et al.*, 2008; Chaussard *et al.*, 2017; Motagh *et al.*, 2017). DInSAR data facilitate the identification of areas of groundwater depletion or recharge, and so provide the means to calibrate groundwater models, delineate lithological boundaries and map aquifer storage variations and assist characterisation (e.g. Chaussard *et al.*, 2014; Castellazzi *et al.*, 2016; Béjar-Pizarro *et al.*, 2017; Castellazzi *et al.*, 2018). Additionally, DInSAR measurements have previously been utilized to calibrate and/or validate models of surface deformation associated with anthropogenic fluid injection or extraction (e.g. Rutqvist *et al.*, 2010; Pearse *et al.*, 2014; Gee *et al.*, 2016). Initial applications over mining areas also confirmed the capability of DInSAR to measure mining induced subsidence (e.g. Carnec *et al.*, 1996; Wright and Stow, 1999). More recently, spatial

distributions of heave in coal measures rocks (e.g. Sowter *et al.*, 2013; Bateson *et al.*, 2015; Sowter *et al.*, 2018; Gee *et al.*, 2019) and temporal correlations between the rise of mine water and deformation time-series (e.g. Cuenca *et al.*, 2013; Gee *et al.*, 2017) have been observed over abandoned coalfields.

The ISBAS method offers an excellent source of data to infer information about subsurface conditions and groundwater levels. Furthermore, the acquisition of Sentinel-1 data will afford a characterization of the deformation regime over three decades to determine how dynamic coalfields are during production and, subsequently, following abandonment. Sentinel-1 provides a frequent, reliable, open and seamless source of SAR data. This is a notable advancement on previous European Space Agency (ESA) missions, such as ERS and ENVISAT, and hence, regular operational monitoring at a national scale is now viable.

1.4 Aim and Objectives

With the above in mind, the overall aim of this thesis is to demonstrate the potential of the Intermittent SBAS processing method and Sentinel-1 SAR data for enhanced capability to monitor ground movements related to geological hazards, with a focus on coal mining. This is divided into three objectives:

- 1) Examine the extent to which the deformation regime changes over the lifespan of the coalfield using results derived from archive and, newly available, Sentinel-1 data.
- 2) Assess the capability of ISBAS measurements to be utilized to infer information on changes in groundwater levels over abandoned coalfields.
- 3) Evaluate the potential and determine challenges of utilizing Sentinel-1 for wide-area operational geohazard monitoring.

1.5 Thesis Overview

The thesis is organised into six chapters. Following the opening chapter, Chapter 2 describes in detail the fundamental concepts that are pertinent to this thesis, namely the technology utilized to monitor ground movements and coal mining theory. This begins with the foundational developments of radar which chronologically leads onto an overview of SAR, which includes background on the new Sentinel-1 satellite. An overview of Interferometric SAR (InSAR) and DInSAR is provided, which leads into multi-temporal DInSAR and the philosophies by which time-series methods are applied, via Persistent Scatter Interferometry (PSI) and SB methods. Following, the Small Baseline Subset (SBAS) method is introduced before outlining the most recent development of the ISBAS method. Finally, the mechanisms of mining subsidence and groundwater rebound are detailed before outlining the approaches by which groundwater rebound is modelled.

Papers form Chapters 3-5. In Chapter 3, ground motion over the Northumberland and Durham coalfield is characterised over a 20-year period with ubiquitous coverage to enable a more comprehensive geological interpretation. Correlations between the observed motion and mining, geological and hydrogeological data are examined.

The work of Chapter 3 is then progressed in Chapter 4, in which the effect of rising groundwater on the surface is investigated by developing an analytical model that relates changes in groundwater levels to surface deformation, and vice-versa.

In Chapter 5, the potential of Sentinel-1 for wide-area geohazard mapping is evaluated by generating a deformation map of the Netherlands and validating the observed measurements with independent sources of data.

Finally, Chapter 6 provides a reflective discussion and synthesis of all aspects of the thesis. The aim and objectives are restated, and a summary of each objective specifies to what extent they have been achieved. The results are scrutinized and recommendations for future research are identified.

1.6 Summary

The opening chapter has provided a contextual background into the significance of monitoring ground movements. Recent technological developments in survey methods and sources of data are subsequently outlined which afford the potential for enhanced characterisation of ground motions, and, consequently, potential for improved management of abandoned coalfields and geohazards more broadly. The gap in research has been identified and aim and objectives of the thesis are stated. The chapter finishes with an overview of the thesis and a description of each chapter in turn.

1.7 References

Bateson, L., Cigna, F., Boon, D. and Sowter, A., 2015. The application of the Intermittent SBAS (ISBAS) InSAR method to the South Wales Coalfield, UK. *International Journal of Applied Earth Observation and Geoinformation*, 34, pp.249-57.

<https://doi.org/10.1016/j.jag.2014.08.018>

Béjar-Pizarro, M., Ezquerro, P., Herrera, G., Tomás, R., Guardiola-Albert, C., Hernández, J.M.R., Merodo, J.A.F., Marchamalo, M. and Martínez, R., 2017. Mapping groundwater level and aquifer storage variations from InSAR measurements in the Madrid aquifer, Central Spain. *Journal of Hydrology*, 547, pp.678-689. <https://doi.org/10.1016/j.jhydrol.2017.02.011>

Bell, J.W., Amelung, F., Ferretti, A., Bianchi, M. and Novali, F., 2008. Permanent scatterer InSAR reveals seasonal and long-term aquifer-system response to groundwater pumping and artificial recharge. *Water Resources Research*, 44(2). <https://doi.org/10.1029/2007WR006152>

- Carnec, C., Massonnet, D. and King, C., 1996. Two examples of the use of SAR interferometry on displacement fields of small spatial extent. *Geophysical research letters*, 23(24), pp.3579-3582. <https://doi.org/10.1029/96GL03042>
- Castellazzi, P., Longuevergne, L., Martel, R., Rivera, A., Brouard, C. and Chaussard, E., 2018. Quantitative mapping of groundwater depletion at the water management scale using a combined GRACE/InSAR approach. *Remote Sensing of Environment*, 205, pp.408-418. <https://doi.org/10.1016/j.rse.2017.11.025>
- Castellazzi, P., Martel, R., Rivera, A., Huang, J., Pavlic, G., Calderhead, A.I., Chaussard, E., Garfias, J. and Salas, J., 2016. Groundwater depletion in Central Mexico: Use of GRACE and InSAR to support water resources management. *Water Resources Research*, 52(8), pp.5985-6003. <https://doi.org/10.1002/2015WR018211>
- Chang, L., Dollevoet, R.P. and Hanssen, R.F., 2017. Nationwide Railway Monitoring Using Satellite SAR Interferometry. *IEEE Journal of Selected Topics in Applied Earth Observations and Remote Sensing*, 10(2), pp.596-604. <https://doi.org/10.1109/JSTARS.2016.2584783>
- Chaussard, E., Bürgmann, R., Shirzaei, M., Fielding, E.J. and Baker, B., 2014. Predictability of hydraulic head changes and characterization of aquifer-system and fault properties from InSAR-derived ground deformation. *Journal of Geophysical Research: Solid Earth*, 119(8), pp.6572-6590. <https://doi.org/10.1002/2014JB011266>
- Chaussard, E., Milillo, P., Bürgmann, R., Perissin, D., Fielding, E.J. and Baker, B., 2017. Remote sensing of ground deformation for monitoring groundwater management practices: Application to the Santa Clara Valley during the 2012–2015 California drought. *Journal of Geophysical Research: Solid Earth*, 122(10), pp.8566-8582. <https://doi.org/10.1002/2017JB014676>
- Cigna, F., Bianchini, S. and Casagli, N., 2013. How to assess landslide activity and intensity with Persistent Scatterer Interferometry (PSI): the PSI-based matrix approach. *Landslides*, 10(3), pp.267-283. <https://doi.org/10.1007/s10346-012-0335-7>
- Colesanti, C., Mouelic, S.L., Bennani, M., Raucoules, D., Carnec, C. and Ferretti, A., 2005. Detection of mining related ground instabilities using the Permanent Scatterers technique— a case study in the east of France. *International Journal of Remote Sensing*, 26(1), pp.201-207. <https://doi.org/10.1080/0143116042000274069>
- Cuenca, M.C., Hooper, A.J. and Hanssen, R.F., 2013. Surface deformation induced by water influx in the abandoned coal mines in Limburg, The Netherlands observed by satellite radar interferometry. *Journal of Applied Geophysics*, 88, pp.1-11. <https://doi.org/10.1016/j.jappgeo.2012.10.003>
- Donnelly, L. 2006. Investigation of Geological Hazards & Mining Risks, Gallowgate, Newcastle-upon-Tyne. *Proceedings of the 10th IAEG International Congress, IAEG2006, Nottingham, UK.*

- Du, Z., Ge, L., Li, X. and Ng, A.H.M., 2016. Subsidence monitoring over the Southern Coalfield, Australia using both L-Band and C-Band SAR time series analysis. *Remote Sensing*, 8(7), p.543. <https://doi.org/10.3390/rs8070543>
- European Environment Agency, 2012. *CORINE Land Cover 2012*. Available at: <<https://land.copernicus.eu/pan-european/corine-land-cover/clc-2012/view>> [Accessed 28th April 2019].
- Fielding, E.J., Blom, R.G. and Goldstein, R.M., 1998. Rapid subsidence over oil fields measured by SAR interferometry. *Geophysical Research Letters*, 25(17), pp.3215-3218. <https://doi.org/10.1029/98GL52260>
- Galloway, D.L. and Hoffmann, J., 2007. The application of satellite differential SAR interferometry-derived ground displacements in hydrogeology. *Hydrogeology Journal*, 15(1), pp.133-154. <https://doi.org/10.1007/s10040-006-0121-5>
- Gee, D., Bateson, L., Sowter, A., Grebby, S., Novellino, A., Cigna, F., Marsh, S., Banton, C. and Wyatt, L., 2017. Ground motion in areas of abandoned mining: application of the Intermittent SBAS (ISBAS) to the Northumberland and Durham Coalfield, UK. *Geosciences*, 7(3), p.85. <https://doi.org/10.3390/geosciences7030085>
- Gee, D., Sowter, A., Grebby, S., de Lange, G., Athab, A. and Marsh, S., 2019. National geohazards mapping in Europe: Interferometric analysis of the Netherlands. *Engineering Geology*, 256, pp.1-22. <https://doi.org/10.1016/j.enggeo.2019.02.020>
- Gee, D., Sowter, A., Novellino, A., Marsh, S. and Gluyas, J., 2016. Monitoring land motion due to natural gas extraction: Validation of the Intermittent SBAS (ISBAS) DInSAR algorithm over gas fields of North Holland, the Netherlands. *Marine and Petroleum Geology*, 77, pp.1338-1354. <https://doi.org/10.1016/j.marpetgeo.2016.08.014>
- Giles, D.P., 2020. Introduction to Geological Hazards in the UK: Their Occurrence, Monitoring and Mitigation. *Geological Society, London, Engineering Geology Special Publications*, 29(1), pp.1-41. <https://doi.org/10.1144/EGSP29.1>
- Hoffmann, J., Zebker, H.A., Galloway, D.L. and Amelung, F., 2001. Seasonal subsidence and rebound in Las Vegas Valley, Nevada, observed by synthetic aperture radar interferometry. *Water Resources Research*, 37(6), pp.1551-1566. <https://doi.org/10.1029/2000WR900404>
- Leighton, J.M., Sowter, A., Tragheim, D., Bingley, R.M. and Teferle, F.N., 2013. Land motion in the urban area of Nottingham observed by ENVISAT-1. *International journal of remote sensing*, 34(3), pp.982-1003. <https://doi.org/10.1080/01431161.2012.714507>
- Massonnet, D. and Feigl, K.L., 1998. Radar interferometry and its application to changes in the Earth's surface. *Reviews of geophysics*, 36(4), pp.441-500. <https://doi.org/10.1029/97RG03139>
- Motagh, M., Shamshiri, R., Haghghi, M.H., Wetzels, H.U., Akbari, B., Nahavandchi, H., Roessner, S. and Arabi, S., 2017. Quantifying groundwater exploitation induced subsidence

- in the Rafsanjan plain, southeastern Iran, using InSAR time-series and in situ measurements. *Engineering geology*, 218, pp.134-151. <https://doi.org/10.1016/j.enggeo.2017.01.011>
- Osmanoğlu, B., Sunar, F., Wdowinski, S. and Cabral-Cano, E., 2016. Time series analysis of InSAR data: Methods and trends. *ISPRS Journal of Photogrammetry and Remote Sensing*, 115, pp.90-102. <https://doi.org/10.1016/j.isprsjprs.2015.10.003>
- Pearse, J., Singhroy, V., Samsonov, S. and Li, J., 2014. Anomalous surface heave induced by enhanced oil recovery in northern Alberta: InSAR observations and numerical modelling. *Journal of Geophysical Research: Solid Earth*, 119(8), pp.6630-6649. <https://doi.org/10.1002/2013JB010885>
- Przyłucka, M., Herrera, G., Graniczny, M., Colombo, D. and Béjar-Pizarro, M., 2015. Combination of conventional and advanced DInSAR to monitor very fast mining subsidence with TerraSAR-X Data: Bytom City (Poland). *Remote Sensing*, 7(5), pp.5300-5328. <https://doi.org/10.3390/rs70505300>
- Rohmer, J., Loschetter, A., Raucoules, D., De Michele, M., Raffard, D. and Le Gallo, Y., 2015. Revealing the surface deformation induced by deep CO₂ injection in vegetated/agricultural areas: The combination of corner-reflectors, reservoir simulations and spatio-temporal statistics. *Engineering Geology*, 197, pp.188-197. <https://doi.org/10.1016/j.enggeo.2015.08.005>
- Rutqvist, J., Vasco, D.W. and Myer, L., 2010. Coupled reservoir-geomechanical analysis of CO₂ injection and ground deformations at In Salah, Algeria. *International Journal of Greenhouse Gas Control*, 4(2), pp.225-230. <https://doi.org/10.1016/j.ijggc.2009.10.017>
- Sigmundsson, F., Hreinsdóttir, S., Hooper, A., Árnadóttir, T., Pedersen, R., Roberts, M.J., Óskarsson, N., Auriac, A., Decriem, J., Einarsson, P. and Geirsson, H., 2010. Intrusion triggering of the 2010 Eyjafjallajökull explosive eruption. *Nature*, 468(7322), pp.426-430. <https://doi.org/10.1038/nature09558>
- Sowter, A., Amat, M.B.C., Cigna, F., Marsh, S., Athab, A. and Alshammari, L., 2016. Mexico City land subsidence in 2014–2015 with Sentinel-1 IW TOPS: Results using the Intermittent SBAS (ISBAS) technique. *International Journal of Applied Earth Observation and Geoinformation*, 52, pp.230-242. <https://doi.org/10.1016/j.jag.2016.06.015>
- Sowter, A., Athab, A., Novellino, A., Grebby, S. and Gee, D., 2018. Supporting energy regulation by monitoring land motion on a regional and national scale: A case study of Scotland. *Proceedings of the Institution of Mechanical Engineers, Part A: Journal of Power and Energy*, 232(1), pp.85-99. <https://doi.org/10.1177/0957650917737225>
- Sowter, A., Bateson, L., Strange, P., Ambrose, K. and Syafiudin, M.F., 2013. DInSAR estimation of land motion using intermittent coherence with application to the South Derbyshire and Leicestershire coalfields. *Remote Sensing Letters*, 4(10), pp.979-987. <https://doi.org/10.1080/2150704X.2013.823673>
- Torres, R., Snoeij, P., Geudtner, D., Bibby, D., Davidson, M., Attema, E., Potin, P., Rommen, B., Floury, N., Brown, M. and Traver, I.N., 2012. GMES Sentinel-1 mission. *Remote Sensing of Environment*, 120, pp.9-24. <https://doi.org/10.1016/j.rse.2011.05.028>

Wright, P. and Stow, R., 1999. Detecting mining subsidence from space. *International Journal of Remote Sensing*, 20(6), pp.1183-1188. <https://doi.org/10.1080/014311699212939>

Wright, T.J., Parsons, B., England, P.C. and Fielding, E.J., 2004. InSAR observations of low slip rates on the major faults of western Tibet. *Science*, 305(5681), pp.236-239. <https://doi.org/10.1126/science.1096388>

2. Literature Review

2.1. Synthetic Aperture Radar (SAR)

2.1.1. SAR Origins

2.1.1.1. Radio Detection and Ranging (Radar)

Radio Detection And Ranging (Radar) systems are remote sensing devices that are capable of determining the presence or range of stationary or moving objects. Imaging radars transmit a microwave pulse, which is subsequently reflected back to the target and received by the transmitter. The time taken for this to occur is directly proportional to the distance between the transmitter and the reflecting target (Ulaby *et al.*, 1982). Such systems operate in the microwave (1mm – 1m) portion of the electromagnetic spectrum, within which wavelength bands have been arbitrarily designated letter codes. Codes were designated during early radar development to guarantee military security and have remained in place since (Table 2.1). Radar transmission through the atmosphere can occur without sizeable signal degradation from phenomena such as clouds, smoke, fog and aerosols. Consequently, radar systems advantageously have all weather, night-time capabilities (Massonnet & Feigl, 1998).

Initial radar systems were predominantly radial in nature, utilizing fixed antennae, and used by militaries to detect aircraft, surfaced submarines and enemy vessels. The development of the Plan Position Indicator enabled the antenna to be rotated around an axis which produced images similar to ground maps (Ulaby *et al.*, 1982). Imaging radars were subsequently installed on planes and satellites. Radar remote sensing from space began in 1978 when the Seasat satellite was launched and many scientific applications of radar have since emerged.

Table 2.1. Radar band designations

Band Designation	Wavelength λ (cm)	Frequency $\nu=c\lambda^{-1}$ [MHz (106 cycles sec ⁻¹)]
K _a	0.75 – 1.1	40 000 – 26 500
K	1.1 – 1.67	26 500 – 18 000
K _u	1.67 – 2.4	18 000 – 12 500
X	2.4 – 3.75	12 500 – 8000
C	3.75 – 7.5	8000 – 4000
S	7.5 – 15	4000 – 2000
L	15 – 30	2000 – 1000
P	30 - 100	1000 – 300

2.1.1.2. Side Looking Airborne Radar (SLAR)

Initial Side Looking Airborne Radar (SLAR) systems were similar in principle to ground-based radars, where a non-rotating antenna was mounted on an aircraft at 90° to the course of forward momentum. A substantial drawback of this technique was the resolution

achievable. Range resolution (perpendicular to the flight direction) is dependant on the bandwidth pulsed waveform, whilst the SLAR azimuth resolution (parallel to the flight direction) is dependent on the beam width and ground range (Madisetti & Williams, 1998). The beam width in turn is dependent on the antenna length and wavelength. An increase in spatial resolution is achieved by recording closer to the target or using a smaller beam width which requires a larger antenna. Hence, the resolution achievable is proportional to the length of the antenna which represents a significant hindrance for spaceborne sensors as, for example, achieving a spatial resolution of 30m from an orbital height of 700km would require an antenna width of several kilometres (Mather, 2004).

2.1.2. Synthetic Aperture

The physical limitations of SLAR antenna were inevitably reached. This was overcome by synthesising a larger antenna utilizing the forward azimuth momentum of the sensor. The amplitudes (the maximum extent of an oscillation) and phases (the proportion of a completed oscillation) are recorded whilst the satellite moves between two points at a velocity v , for a time epoch T . Utilizing the Doppler principle, the location of the targets relative to the antenna can be calculated and reconstructed as if the signal were obtained by an antenna with length $v.T$, hence, a higher spatial resolution can be achieved particularly in the azimuthal direction (Ulaby *et al.*, 1982).

2.1.3. Coherent Imaging

SAR is an active coherent imaging system. In coherent systems, two or more waves have the same frequency which means they oscillate in unison, regardless of whether the initial amplitude and phase are different (Skolnik, 1990). Coherent systems record both the amplitude and phase of the returned signal and it is the phase preserving nature of coherent systems that offer a unique opportunity over optical systems which are not phase preserving. The amplitude (or intensity) of a returned SAR signal is principally determined by the terrain slope, surface roughness and dielectric constants, whereas phase is determined by the distance spanning the target and antenna (Lu *et al.*, 2007).

2.1.4. Polarization

Radar signals are transmitted and received in different geometric planes in which its electrical field is oscillating (polarization). Radar systems permit the filtering of the signal to limit oscillations along a single plane that is perpendicular to the direction of propagation. Without such filtering unpolarized energy oscillates in all directions. Typically, radar signals are transmitted or received in a plane that is either horizontal (H) and vertical (V) to antenna's axis. Signals that are transmitted and received in the same polarization are referred to as like-polarized (i.e. HH or VV), whereas cross-polarized refers to those that

are transmitted and received in different polarizations (i.e. HV or VH) (Lillesand, Kiefer & Chipman, 2015).

2.1.5. SAR Geometry

Figure 2.1 displays the typical geometry of a SAR imaging system. The side-looking configuration is employed so that echoes from near range will always return before the echoes of those in far range. Returned signals are converted into range and sorted into range bins. If a nadir configuration was to be implemented ambiguities would result in the returned signal because any two echoes from the same transmitted signal that are reflected back at the same time will have an equivalent range and would therefore be superimposed.

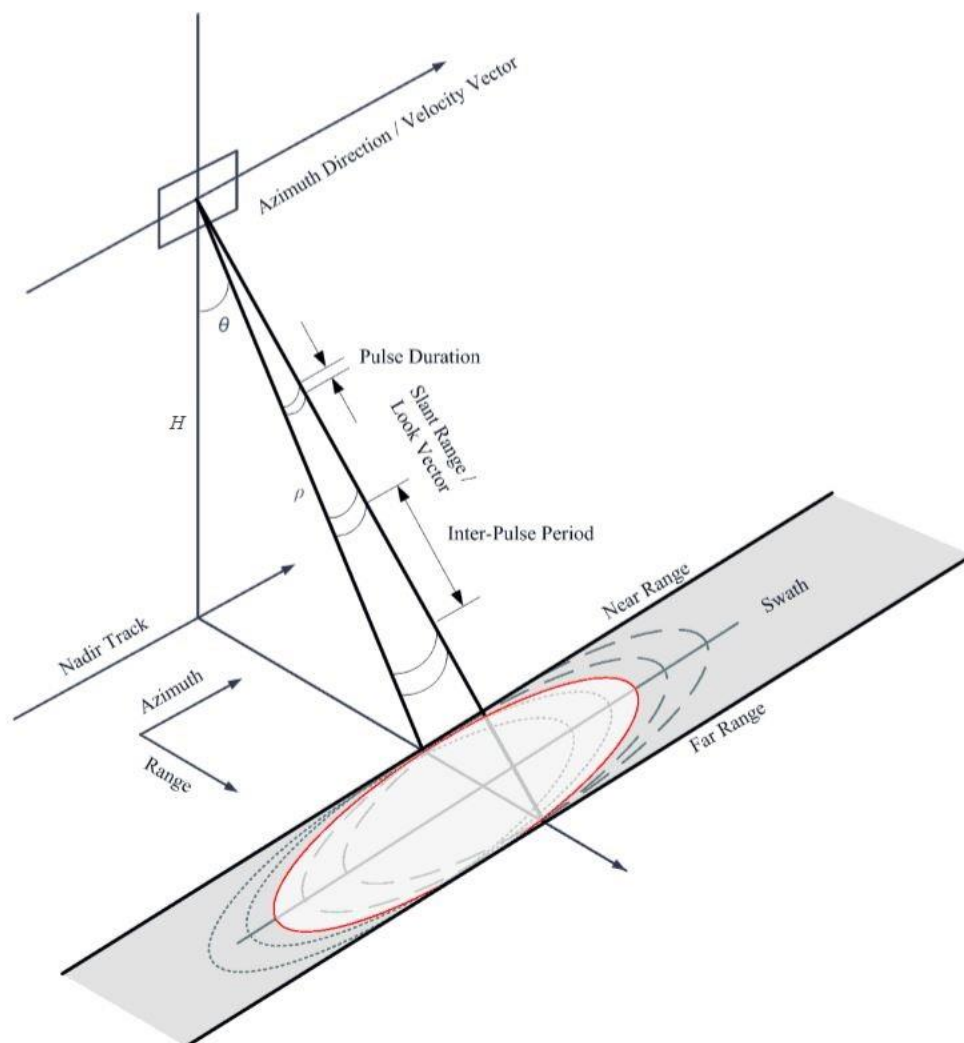


Figure 2.1. SAR imaging geometry (Skolnik, 1990).

The sensor travels along the velocity vector in the azimuth direction and the radar beam illuminates the swath on the ground. The elevation beamwidth determines the width of this swath, which is proportional to the length of the antenna and the wavelength. Near range and far range corresponds to the portions of the swath closest and furthest to nadir respectively. The incidence angle (θ) is the angle between nadir and the transmitted pulse, and slant range (ρ) is the range from sensor to the target on the ground, which is a function of the incidence angle and other factors such as topography. The antenna is targeted at 90° to the velocity vector, however, in practise the look direction veers away from the zero-Doppler direction by some squint angle (Woodhouse, 2005).

2.1.6. SAR Transmission

The sensor transmits a signal (t_i) that reaches the ground target. The backscatter is the proportion of the radar signal that is reflected off the ground target and transmitted back to the sensor (t_r). Other portions of the incident radar signal may be absorbed by the ground or reflected and scattered away from the radar. The signal is unlikely to travel along the true range (ρ), the shortest path between the antenna and the target, because it will be refracted by the atmosphere. Hence, the signal travels along the pseudo-range (R) which is calculated by converting the time delay between the transmission and the receive time and converting into distance:

$$R = \frac{1}{2}c(t_t - t_r) \quad (2.1)$$

where c is the speed of light. The pseudo-range is related to true range by:

$$\rho = R - ct_{atmosphere} \quad (2.2)$$

where $t_{atmosphere}$ is the two-way delay due to atmospheric refraction (Sowter *et al.*, 2003).

2.1.7. Range Resolution

Spatial resolution refers to the minimum distance at which neighbouring points on the ground can still be resolved as separate objects in the image. To distinguish between two features in close proximity in range, the antenna must receive all parts of the return echoes separately. In slant range, this distance must be greater than half the physical length of the pulse (Curlander & McDonough, 1991). Preceding transmission the pulse is Frequency Modulated (FM), known as chirping. The pulse is sent, backscattered and returned; the return echoes are received at different times that is directly proportional to their ranges. Chirping applies a matched filter (also known as range compression) to delay different frequency constituents of the signal so they are received by the sensor at the same time. This is notable because the shorter the pulse, the closer neighbouring targets can lie before their echoes overlap, and therefore the higher the range resolution (Woodhouse, 2005).

2.1.8. Azimuth Resolution

Azimuth resolution depends on the synthetic aperture of the antenna - to separate neighbouring features in azimuth, the spatial separation must be greater than the focused beam width on the ground. As the satellite travels along the velocity vector, the motion of the platform induces a frequency shift in the returned signal (i.e. the Doppler effect). From the period when a target first enters and subsequently leaves the beam, multiple backscattered responses are recorded from the pulses. The footprint of the beam on the ground is several kilometres, the real aperture. The synthesis, known as azimuth compression, reduces the azimuth resolution from a few kilometres to a few metres, via natural Doppler chirp, by resolving multiple returns from a target into a single response (Ulaby *et al.*, 1982).

2.1.9. Geometric Distortion

Geometric distortions are generated by topographic relief features on the ground and are a consequence of the side looking geometry and the SAR operational parameters, such as the pulse response frequency, incidence angle and antenna design. These are manifest as three image artefacts (Woodhouse, 2005): foreshortening, layover and shadow.

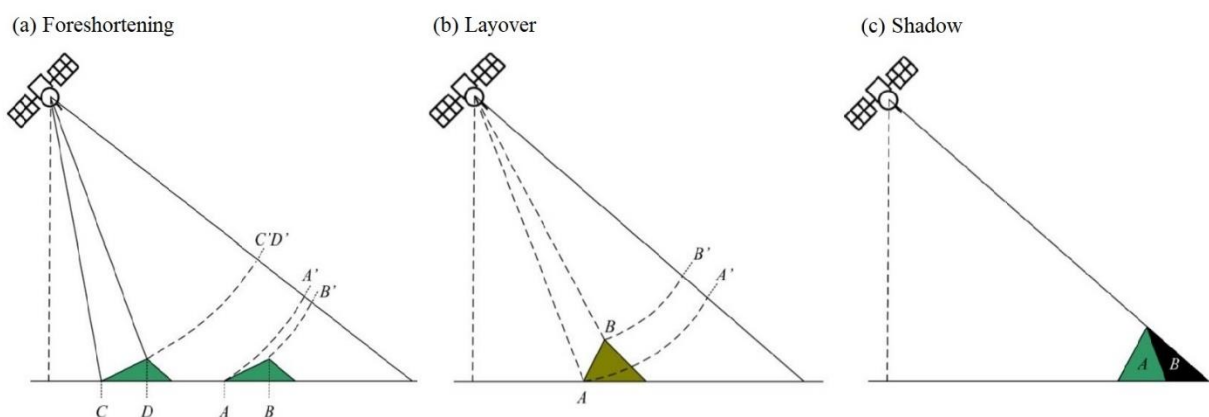


Figure 2.2. Geometric distortion (Leighton, 2010).

2.1.9.1. Foreshortening

Foreshortening occurs when topographic features, such as hillsides, face the look direction of the SAR sensor (Figure 2.2a). For example, the responses in slant range between A, at the base of the hill, and B, at the top of the hill, are close as they arrive back to the sensor at similar times, however, this is due to the topography and they do not exist so closely in ground range. In this example, C and D have an equivalent slant range - the responses are backscattered to the sensor at the same time because the path lengths are equivalent. Consequently, in the radar image C and D are indistinguishable.

2.1.9.2. Layover

Layover is an amplified version of foreshortening (Figure 2.2b). Due to the steep topography, the response from B in slant range is received before the response from A, when in ground range B is closer to the sensor than A. Consequently, B is overlaid on A in the SAR image as it is placed in the wrong range bin.

2.1.9.3. Shadow

Shadow occurs when the SAR sensor is unable to illuminate the slope facing the opposite direction from the look angle (Figure 2.2c). The topographic feature A casts a shadow, B, and no data can be acquired within this shadowed zone – this effect becomes more prominent with steep slopes and lower incidence angles.

2.1.10. Image Composition

Single Look Complex (SLC) SAR images are arrays of complex pixels which have been focused into slant range. The raw signal data for each target is dispersed in azimuth and range, focusing accumulates such energy into individual pixels. The most widely utilized methods are the wavenumber domain and range-Doppler techniques (Bamler, 1992). Each pixel represents an area on the Earth's surface whose reflection coefficient is the sum of the reflections of hundreds of individual targets (Massonnet & Feigl, 1998). In an x, y coordinate system every pixel has a real, in-phase value (q) and an imaginary, quadrature value (i) which are stored in complex form (s) (Figure 2.3). The amplitude (α) and phase (φ) values are derived via a cartesian to polar coordinate conversion:

$$\alpha = \sqrt{x^2 + y^2} \quad (2.3)$$

$$\varphi = \tan^{-1}\left(\frac{y}{x}\right) \quad (2.4)$$

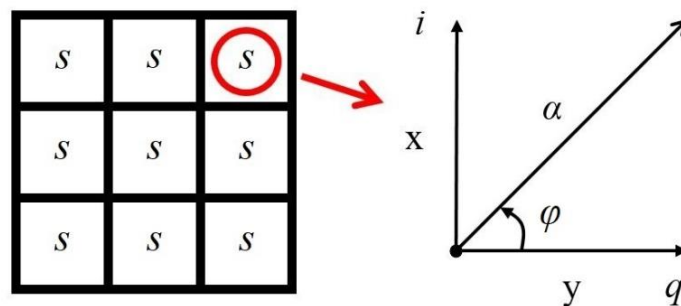


Figure 2.3. An argand diagram of a Single Look Complex (SLC) pixel with coordinates x, y .

2.1.11. European Space Agency SAR Satellites

2.1.11.1. ERS 1/2

ERS-1 was launched by the European Space Agency (ESA) on July 17th 1991, with its successor ERS-2 launched four years later on April 21st 1995. The two satellites were concordant and operated in a sun-synchronous orbit at a nominal altitude of 785 km at an inclination of 98.5°, with a 35-day revisit time. The satellites carried three primary sensors; a Ku-band radar altimeter, an along-track scanning radiometer and a C-band (5.6 cm — 5.3 GHz) active microwave instrumentation (AMI) module. Within the AMI contained a SAR system, operational in either Wave or Image Mode, and a microwave scatterometer that functioned in Wind Mode. In Image Mode, SAR data was produced over a 100km right-looking swath with a VV polarisation, four-look resolution in the vicinity of 30m and a 23° look angle at beam centre (Lillesand, Keifer & Chipman, 2015). ERS-1 was withdrawn from operation on March 10th 2000 and ERS-2 withdrawn on September 5th 2011.

2.1.11.2. ENVISAT

ENVISAT was launched by ESA on March 1st 2002 and maneuvered into an orbit that emulated ERS-2's, so to cover a near identical ground track. The Advanced Synthetic Aperture Radar (ASAR) system functioned in the C-band, at a similar wavelength to the SAR system on board ERS-1 and ERS-2. The sensor could be operated in a variety of modes including Wide Swath Mode, Global Monitoring Mode and Alternating Polarization Mode. Crucially for uniformity between ERS-1 and ERS-2 it retained the Image and Wave modes operational on previous satellites. Connection with the satellite was lost on April 8th 2012, just after the tenth anniversary of its launch (Lillesand, Keifer & Chipman, 2015).

2.1.11.3. Sentinel-1

Copernicus is an EU programme, managed and coordinated by the European Commission, founded to develop European information services based on *in situ* and satellite Earth Observation (EO) data. It aims to achieve continuous, autonomous and global EO capacity through data acquired from satellites and ground, air and sea-based sensors. The European Space Agency (ESA) coordinates the delivery of data from a constellation of six satellite missions, called Sentinel's, which provide information for the monitoring of the atmosphere, marine environment, land, climate change as well as for security and emergency management.

The first mission, Sentinel-1, is a two-satellite constellation operating in a sun-synchronous orbit at an altitude of 693km, 180° apart. Each satellite carries a 12m C-Band (5.555 cm wavelength — 5.405GHz) SAR payload, the first of which, Sentinel-1a, was launched on 3rd April 2014, with Sentinel-1b launched on 25th April 2016. The Sentinel-1 mission is designed to build upon the successes of previous ERS 1/2 and ENVISAT missions, whilst upgrading key mission parameters to meet end user requirements such as improved reliability, revisit

time, geographic coverage and rapid hassle-free data distribution. The mission maintains a conflict free repeat-pass of six-days over Europe and 12 days for the majority of other global landmasses. Its expected life cycle is on the order of 15-20 years, which will ensure a reliable service and a consistent data library, making it particularly suited for applications focused on long time-series, such as Interferometric SAR (InSAR) (Torres *et al.*, 2012).

Sentinel-1 operates in four imaging capacities: interferometric wide-swath mode (IW); wave mode (WV); strip-map mode (SM); and extra wide-swath mode (EW) (Figure 2.4; Table 2.2). Interferometric wide data are acquired using the Terrain Observation with Progressive Scans SAR (TOPSAR) technique, a form of ScanSAR imaging whereby imagery is acquired in individual bursts by cyclically alternating the antenna beam between multiple adjacent sub-swaths (De Zan & Guarnieri, 2006). Such a configuration is employed to harmonise along track performance to reduce scalloping and meet the requirements for a wide swath (250 km). The IW products are formed of three sub-swaths, in turn made up of 7-10 bursts considered individual zero-doppler SLC images (Torres *et al.*, 2012).

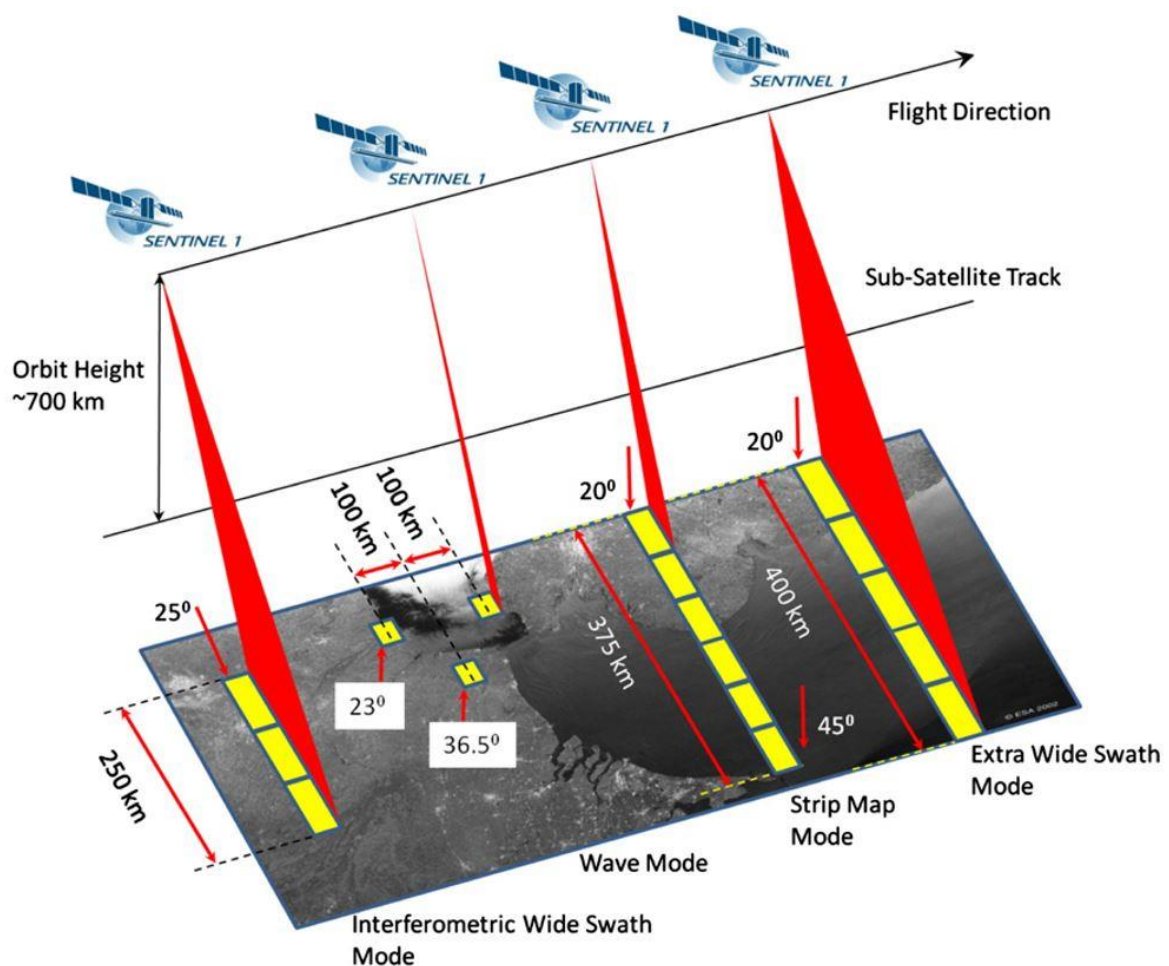


Figure 2.4. Sentinel-1 operation modes (Torres *et al.*, 2012).

Table 2.2. The characteristics of Sentinel-1 nominal measurement modes (Torres *et al.*, 2012).

Parameter	Interferometric Wide-swath mode (IW)	Wave mode (WV)	Strip Map mode (SM)	Extra Wide-swath mode (EW)
Polarization	Dual (HH+HV, VV+VH)	Single (HH, VV)	Dual (HH+HV, VV+VH)	Dual (HH+HV, VV+VH)
Incidence angles	29°–46°	23°–37° (mid incidence angle)	20°–47°	20°–47°
Azimuth resolution	<20 m	<5 m	<5 m	<40 m
Ground range resolution	<5 m	<5 m	<5 m	<20 m
Azimuth and range looks	Single	Single	Single	Single
Swath	>250 km	Vignette 20×20 km	>80 km	>410 km

2.2. Interferometric Synthetic Aperture Radar (InSAR)

Interferometric Synthetic Aperture Radar (InSAR) is geodetic method of measuring changes in Earth surface height. InSAR is based upon interferometry, where the interference of electromagnetic waves from two SAR images is utilized to derive precise changes in elevation. The phase of a SAR image is essentially random and difficult to predict; however, the phase contribution is the sum of phase from scattering, noise and range. Scattering is a deterministic quantity; should two images be acquired under equal conditions (i.e. under the same atmospheric conditions and from the same position in space), then the scattering components would also be equal. In practise, the scattering components are often similar, and the level of phase correlation between the signals (i.e. coherence) depends on the determination of Doppler centroid frequency, baseline geometry and temporal decorrelation. Noise is Gaussian and can be filtered relatively effectively. The remaining component is related to the range, so if the phase of the two acquisitions are relatively similar then differencing this information enables the retrieval of the corresponding small changes in sensor-ground distance, or surface height (Hanssen, 2001). The change in phase between two images, referred to as an interferogram, is more useful than the phase of a single image, which is the basic premise of InSAR. In an array with coordinates (x,y) , once the second image, referred to as the slave, is co-registered to the slant-range coordinate system of the first image, referred to as the master, the interferometric phase at pixel d is derived by multiplying the complex pixel (s_1) of the master by the complex conjugate (s_2^*) of the slave:

$$d(x,y) = s_1(x,y)s_2^*(x,y) \quad (2.5)$$

where the resultant array is complex, comprised of the amplitude values which have been multiplied, and the interferometric phase (Φ) (Figure 2.5).

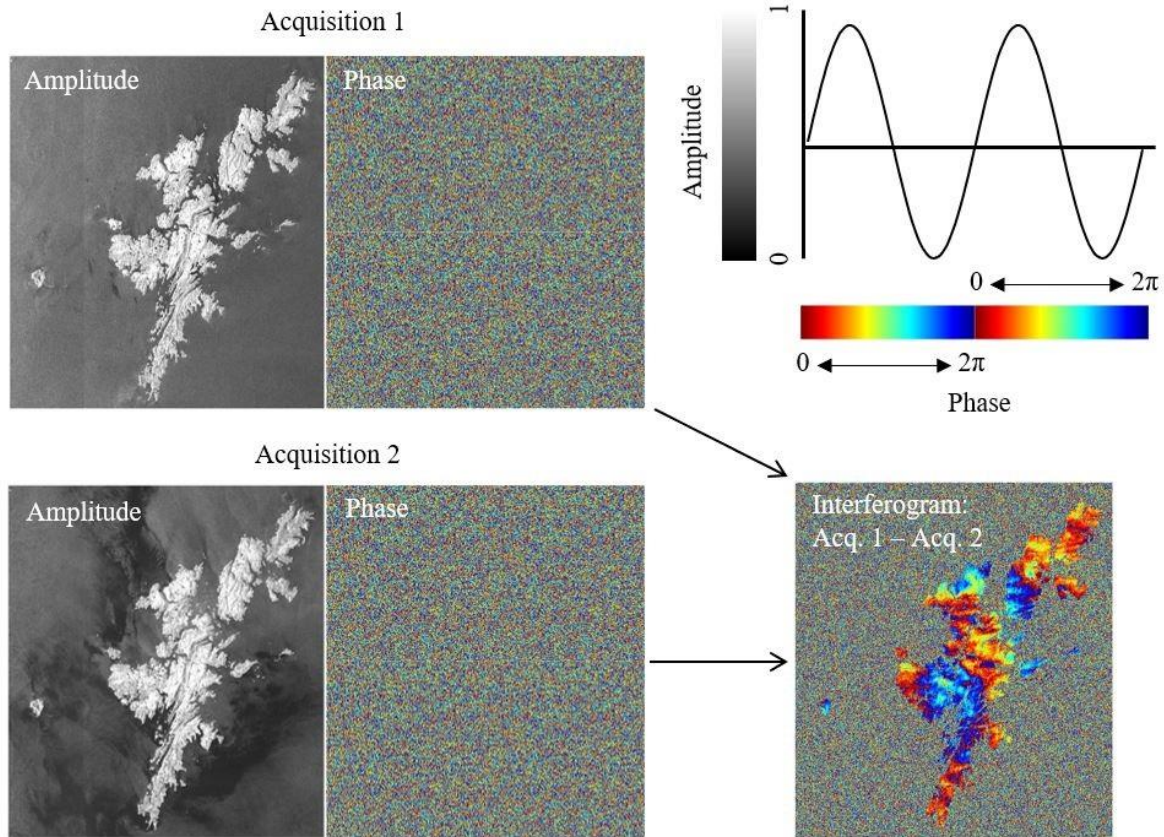


Figure 2.5. Formation of an interferogram. Phase is differenced to form an interferogram.

2.2.1. InSAR Geometry

The geometry of a typical repeat-pass InSAR imaging configuration is shown in Figure 2.6. The phase (φ) of each complex number (s) is equal to the two-way travel of the radar signal divided by the wavelength (λ):

$$\varphi = \frac{2\rho}{\lambda} \quad (2.6)$$

The interferometric signal (Φ), and position of P is derived from the change in range from A_1 and A_2 :

$$\Phi = \rho_1 - \rho_2 \quad (2.7)$$

Where, the phase (φ) of ρ_1 and ρ_2 are:

$$\varphi_{A1} = \frac{(4\pi)}{\lambda} \rho_1 \quad (2.8)$$

and

$$\varphi_{A2} = \frac{(4\pi)}{\lambda} \rho_2 \quad (2.9)$$

hence, the interferometric phase:

$$\Phi = \frac{(4\pi)}{\lambda} (\rho_1 - \rho_2) \quad (2.10)$$

which is wrapped in a modulo 2π environment.

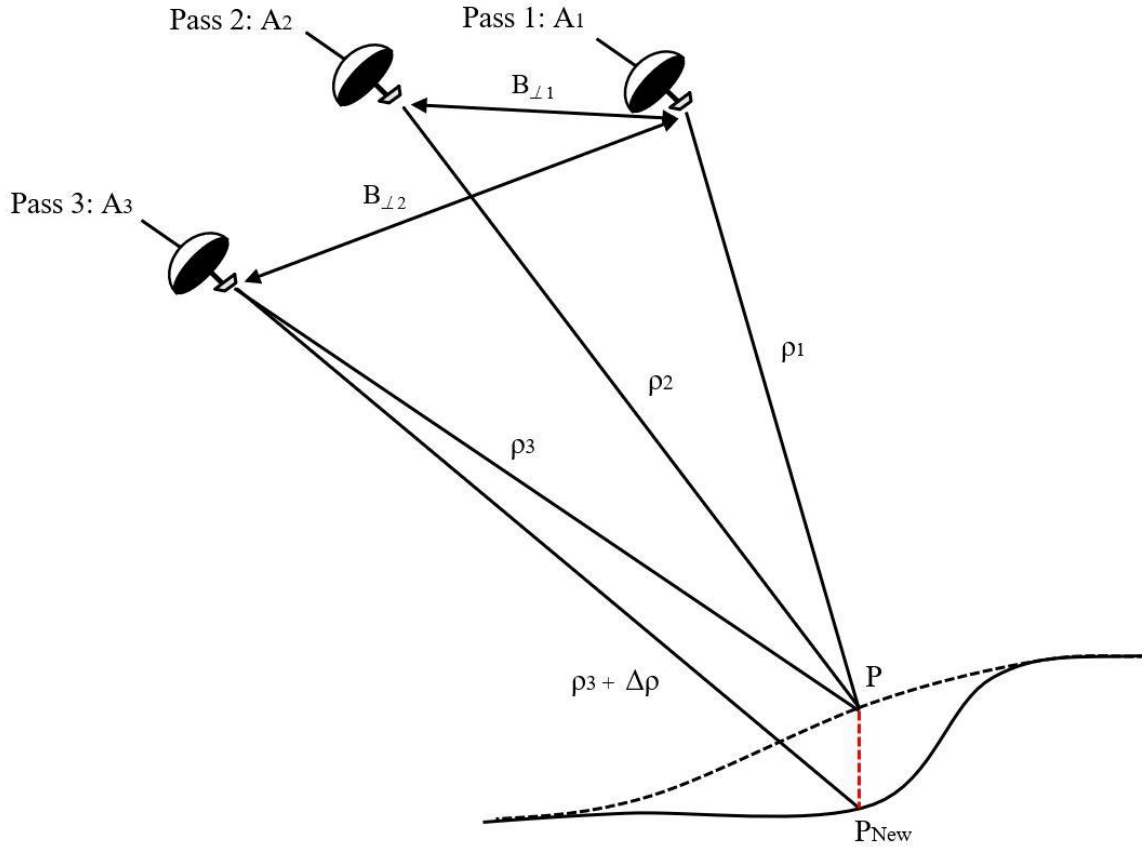


Figure 2.6. The InSAR geometry. The position P represents the point on the Earth's surface at Pass 1 and 2, whilst P_{New} represents the position on Earth's surface at Pass 3, after a deformation event has occurred. ρ₁, ρ₂ and ρ₃ are the range from between P and satellite acquisitions A₁, A₂ and A₃ respectively. Δρ is the additional range from A₃ to P_{New} with respect to A₃ to P.

The phase difference is directly proportional to the wavelength of the signal utilized (Figure 2.7). The achievable deformation gradients measurable by InSAR also depends on the radar band, as well as the ground resolution of the image. Using shorter wavelengths (e.g. X-Band or C-Band) facilitates resolving deformation with greater accuracy, since shorter wavelengths tend to be more sensitive to small changes in surface conditions over time. Conversely, longer wavelengths (e.g. L-Band) are less sensitive, however, larger deformation gradients are measurable. Utilizing higher resolution data also facilitates the measurements of larger deformation gradients, given that the deformation gradient is measured over a smaller pixel size.

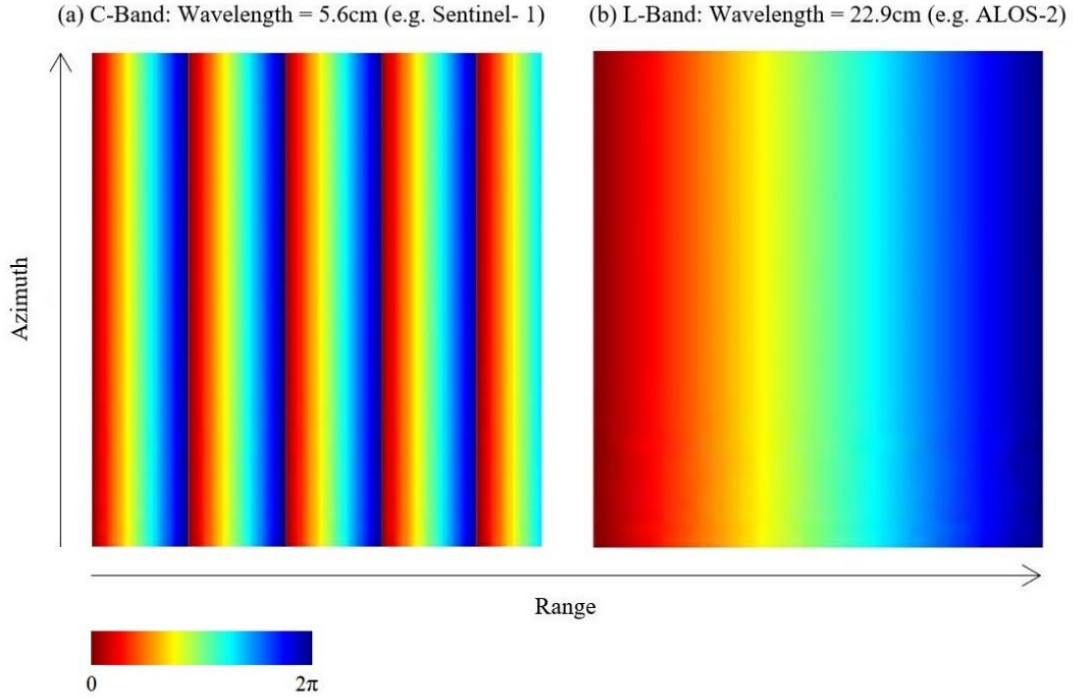


Figure 2.7. Simulated phase difference in the absence of topography at C-Band (5.6cm) and L-Band (22.9cm) wavelengths.

2.2.2. Interferometric Phase Contributions

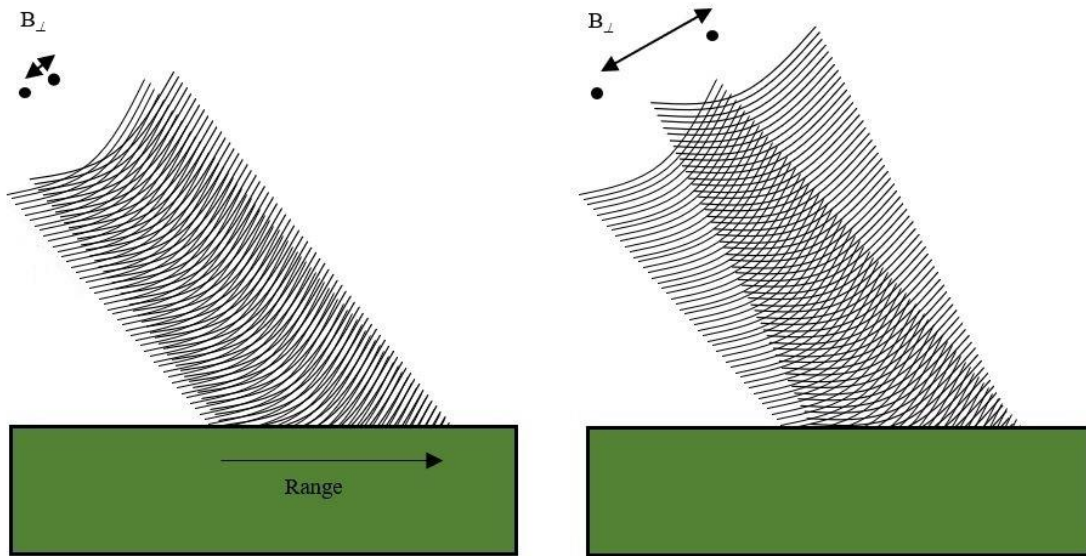
The interferometric phase (Φ) is sum of the contributions of the geometry, topography, atmosphere, noise and ground deformation:

$$\Phi = \varphi_{\text{geometry}} + \varphi_{\text{topography}} + \varphi_{\text{atmosphere}} + \varphi_{\text{noise}} + \varphi_{\text{deformation}} \quad (2.11)$$

2.2.2.1. Geometric

Fringes occur in the interferogram because the two coherent signals are acquired at slightly different locations. The longer the perpendicular baseline (B_{\perp}), the higher the fringe rate and the greater the geometric decorrelation (Figure 2.8). Additionally, the change in range (i.e. distance) from the sensor to the ground between near and far range also induces fringes, a consequence that is heightened by the curvature of the Earth. When the fringe rate exceeds 2π per resolution cell, the critical baseline is exceeded, decorrelation occurs, and such information is not useful for conventional InSAR. Additionally, high fringe rates are more sensitive to the effects of noise (Section 2.2.2.4). The fringes, or phase ramps, are often a large source of the signal; however, phase ramps can be very accurately removed with knowledge of satellites position in space, via the precise orbit determination (POD) information (Hanssen, 2001).

(a) InSAR Geometry



(b) Simulated phase ramps

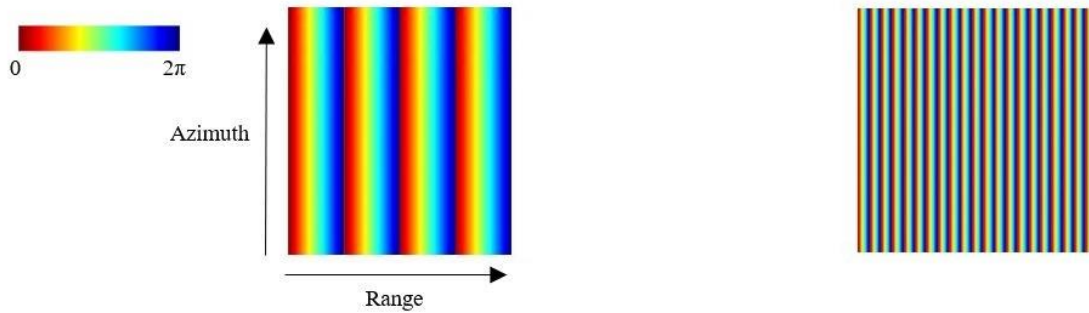


Figure 2.8. Geometric decorrelation. Each curved black line coming from the satellite represents a wavelength. The longer the perpendicular baseline (B_{\perp}) the more fringes introduced into the interferogram.

2.2.2.2. Topographic

The variable topography of the Earth's surface introduces fringes into the phase due to the stereoscopic effect, as is evident in Figure 2.9. With reference to Figure 2.6, if between pass 2 and pass 3 the ground moves (P_{New}), there is a change in range that is related to ground deformation:

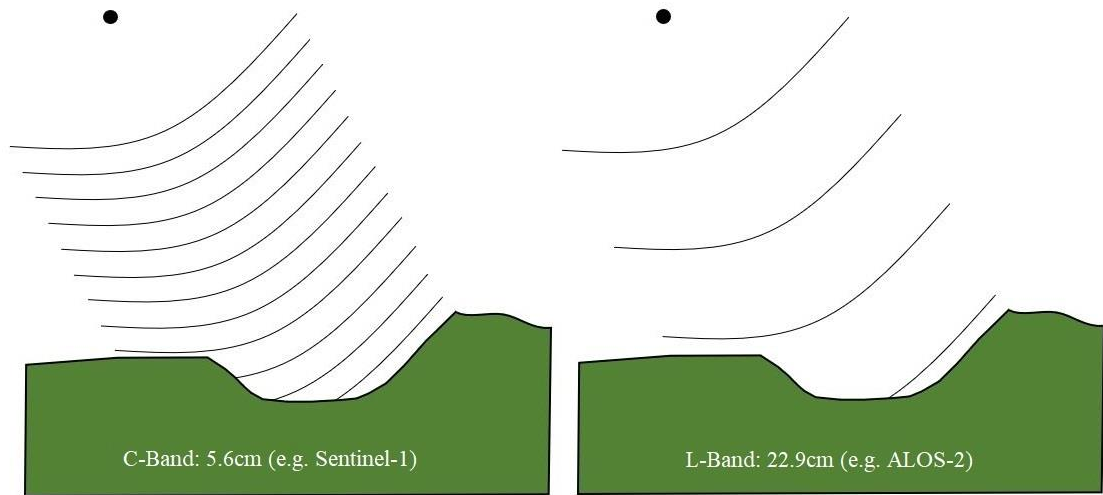
$$\varphi_{A3} = \frac{(4\pi)}{\lambda} (\rho_3 + \Delta\rho) \quad (2.12)$$

Resultantly, the change in phase is:

$$\Phi = \frac{(4\pi)}{\lambda} (\rho_2 - \rho_3) + \frac{(4\pi)}{\lambda} (\Delta\rho) \quad (2.13)$$

The left-hand side of the summation is the phase due to the presence of topography whereas the right-hand term is related to the change in range due to the deformation. Phase

(a) InSAR Geometry



(b) Simulated Phase

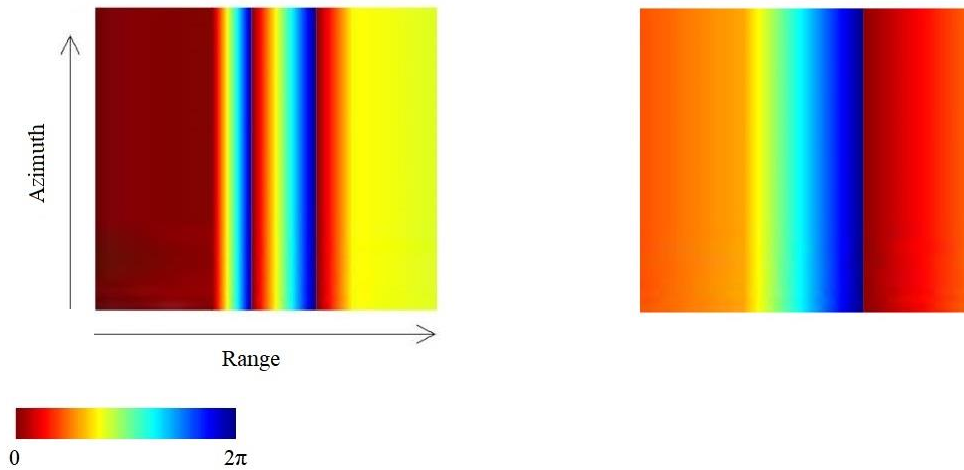


Figure 2.9. Topographic interference. Each curved black line coming from the satellite represents a wavelength. When an interferogram is generated between two images, cycles of phase are introduced due to the topography of the Earth's surface.

associated with topography can be simulated and subtracted, either by simulating an interferogram from a Digital Elevation Model (DEM) (two-pass) or using two interferograms (three or four-pass), to leave phase associated with ground deformation, referred to as the differential phase, or differential InSAR (DInSAR):

$$\Phi = \frac{(4\pi)}{\lambda} (\Delta\rho) \quad (2.14)$$

High-resolution DEMs have been readily available over recent years, for example the Shuttle Radar Topography Mission (SRTM) DEM is available between $\pm 60^\circ$ (Farr *et al.*, 2007) and more recently the global WorldDEM™ from the TanDEM-X mission (Rizzoli *et al.*, 2017). For simulation, the DEM must be transformed into SAR coordinates, resampled to the same resolution and co-registered to the geometry of the master image. Simulating the topographic phase contribution from a DEM has several advantages over the three-pass

approach: there is no atmospheric phase associated with the topographic interferogram; there is no chance of an unforeseen deformation signal being present within the topographic interferogram; phase noise and decorrelation issues are reduced and only a single interferogram requires unwrapping. With reference to Figure 2.6, the phase at P can be derived precisely since the position of A_2 and A_3 are known accurately from the POD information. DEM error ($\varphi_{DEM\ Error}$) occurs when the simulated interferogram (φ_{Sim}) from the DEM does not match the phase (φ) derived from the SAR acquisitions and POD:

$$\varphi_{DEM\ Error} = \varphi - \varphi_{Sim} \quad (2.15)$$

Large baselines are more sensitive to DEM error, whilst smaller baselines are less sensitive, hence, DEM error is proportional to the perpendicular baseline.

Alternatively, topographic phase can be simulated using at least one additional SAR acquisition (Figure 2.6). As previously mentioned, the position of P can be determined accurately from two acquisitions, hence, using a third acquisition, A_1 , an independent interferogram can be utilized to simulate the topographic phase (Eqn. 2.10). Before subtraction the independent interferogram needs to be rescaled as if it was acquired with the same baseline as the first interferogram. The phase contribution for DInSAR once geometric and topographic phase have been subtracted is as follows:

$$\Phi = \varphi_{baseline\ error} + \varphi_{DEM\ error} + \varphi_{atmosphere} + \varphi_{noise} + \varphi_{deformation} \quad (2.16)$$

where any errors resulting from inaccuracies in the orbital or DEM information is transferred into the differential phase.

2.2.2.3. Differences in Atmospheric Propagation Delay

Spatial and temporal inhomogeneities in atmospheric propagation between acquisitions results in irregular artefacts in the interferometric phase (Zebker *et al.*, 1997). In effect, ignoring other phase contributions, the phase (φ) of acquisition A_1 is equal to the two-way travel of the radar signal plus the delay of the radar signal as it passes through the atmosphere:

$$\varphi_{A1} = \frac{(4\pi)}{\lambda} \rho + Atmosphere \quad (2.17)$$

Hence, the interferometric phase between A_1 and A_2 equals:

$$\Phi_{A1-A2} = \frac{(4\pi)}{\lambda} (\rho_1 - \rho_2) + Atmosphere_{1-2} \quad (2.18)$$

The right-hand side of the summation, the atmospheric phase screens, are comprised of 'wet' and 'dry' components. The 'wet' component relates to differences in the turbulent mixing of the atmosphere between acquisitions. Atmospheric delay largely occurs in the troposphere, where the majority of weather occurs. In northern, temperate Europe delays are usually 2-3m which occur principally due to the presence of water vapour, although variations in temperature and pressure also contribute to this effect but are smaller in magnitude (Hanssen, 1998). Only relative delay, rather than absolute delays, between image

pairs can be measured. For example, a localised atmospheric homogeneity at the time of the first acquisition would result in a positive phase change in the interferogram formed with a second image acquired under clear conditions.

The most systematic errors relate to the vertical stratification of the troposphere (i.e. the ‘dry’ component). Differences in vertical refractivity profiles affect the phase difference between arbitrarily selected resolution cells with different topography (Figure 2.10) (Hanssen, 2001). Vertical stratification is a function of topographic height differences, hence, in areas of significant topography the changes in atmospheric conditions due to height could be misinterpreted as the effects of topography.

There are numerous methods for counteracting the phase contribution due to the atmosphere, including: modelling $\varphi_{\text{atmosphere}}$ based upon the topography; modelling $\varphi_{\text{atmosphere}}$ based upon independent observations from GPS, weather models or satellite radiometers; or increasing the signal-to-noise ratio by time-series analysis. For example, with respect to time-series analysis (See Section 2.3.3), by employing a multiple master method which utilizes many observations alongside the assumption that $\varphi_{\text{atmosphere}}$ is random over time and hence Gaussian, atmospheric effects in the derived velocities are considered insignificant. Conversely, this assumption is likely to break down in the case of single master methods when an order of magnitude less observations are utilized and hence, alternative solutions are required (Hanssen, 2001).

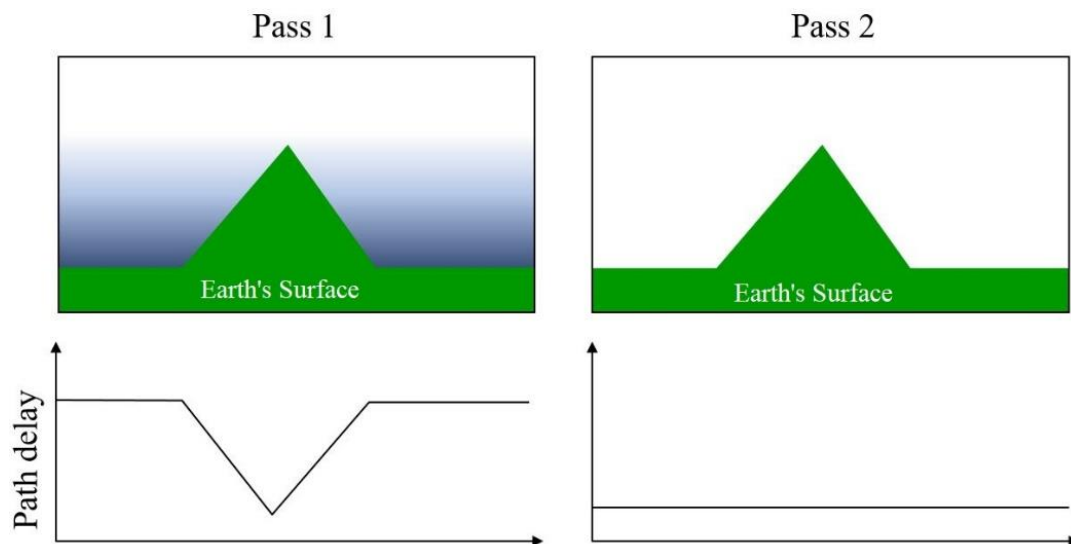


Figure 2.10. The topography of the Earth is shown at the top, whereby at pass 1 there is moisture in the atmosphere (blue). The path delay of the radar signal is shown at the bottom.

2.2.2.4. Noise

2.2.2.4.1. Incoherence

The largest source of noise in the interferometric phase is due to the temporal instability of the imaged target over time. Coherence, γ , is the measure of phase correlation between two

signals, calculated from the cross-correlation coefficient:

$$\gamma_{S_1 S_2} = \left| \frac{\langle S_1 S_2^* \rangle}{\sqrt{\langle |S_1|^2 \rangle \langle |S_2|^2 \rangle}} \right| \quad (2.19)$$

where s_1 and s_2 are the complex pixels for the two acquisitions (A_1 and A_2) and $\langle \rangle$ represent averaging over a finite window. Coherence ranges from 0 to 1, where a value of 0 represents no correlation (i.e., noise) and 1 represents perfect correlation. It is a function of a variety of contributing factors including the land cover of the imaged target, time of year, wavelength of the sensor, temporal and perpendicular baselines and atmospheric conditions.

The deformation signal is only be retrieved for targets which exhibit little phase variability, where the variance of the echoes is small over time. Hence, the best results from DInSAR occur over areas of high coherence, which are typically urban or rocky areas. Conversely, incoherence severely limits the spatial distribution and density of ground deformation measurements outside of urbanised and arid terrain with sparse vegetation cover. This effect is most prevalent in higher frequency radar bands, such as C-band, and incoherence is pervasive over agricultural fields, forests, semi-natural areas and wetlands (Ferretti *et al.*, 2003). Over such environments, due to both natural (e.g. shrink-swell) and anthropogenic (e.g. agricultural) processes, scatterers within resolution elements (pixels) move relative to one another, causing the phase to sum differently (Figure 2.11). Consequently, the integration of phase difference becomes inaccurate if the change in phase is a substantial percentage of the phase cycle (Zebker & Villasenor, 1992).

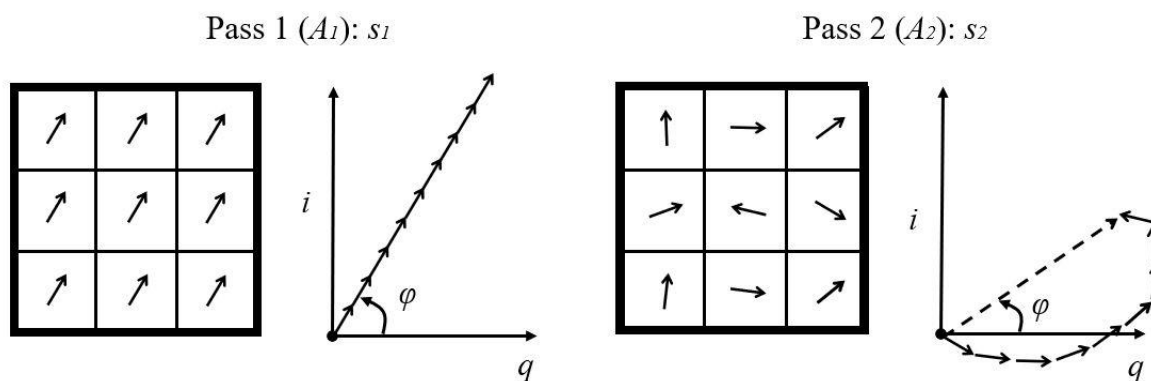


Figure 2.11. An argand diagram representing the change in the sum of scatterers and, hence, phase (φ) within an individual pixel (s) between acquisitions A_1 and A_2 .

2.2.2.4.2. Unwrapping Errors

Deformation information between SAR acquisition is determined from measuring the cumulative angular phase differences between neighbouring cells in the interferogram. The interferometric phase is only known in modulo 2π , hence, if deformation exceeds 2π the ambiguity height is exceeded and the phase becomes wrapped (i.e. constrained between the $[-\pi, \pi]$ or $[0, 2\pi]$) (Figure 2.12).

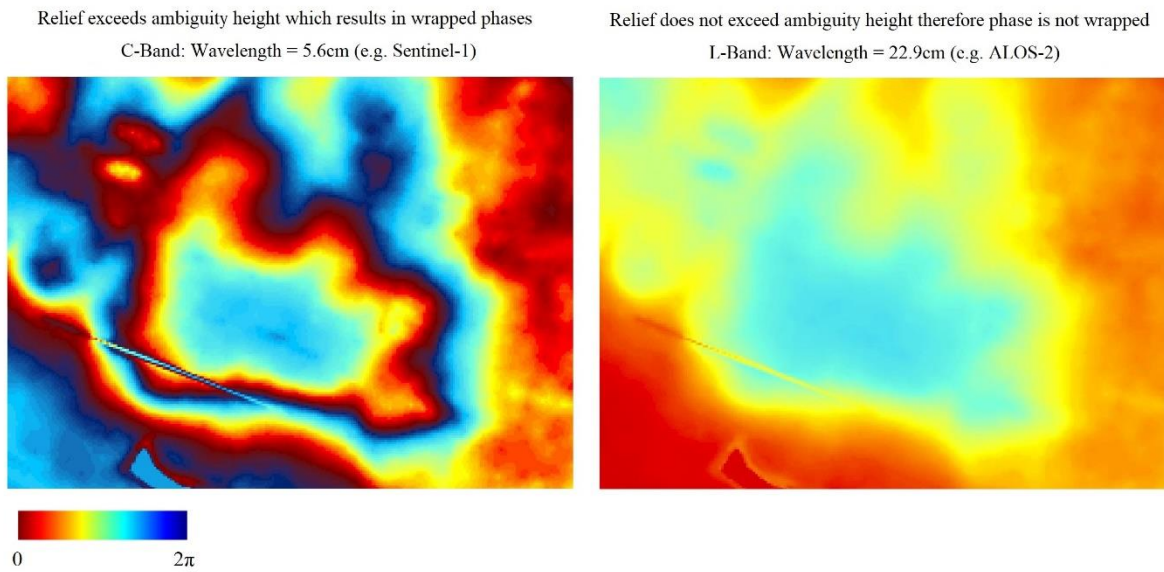


Figure 2.12. Interferograms over in area of topography which demonstrates the relationship between the ambiguity height and the wavelength of the sensor.

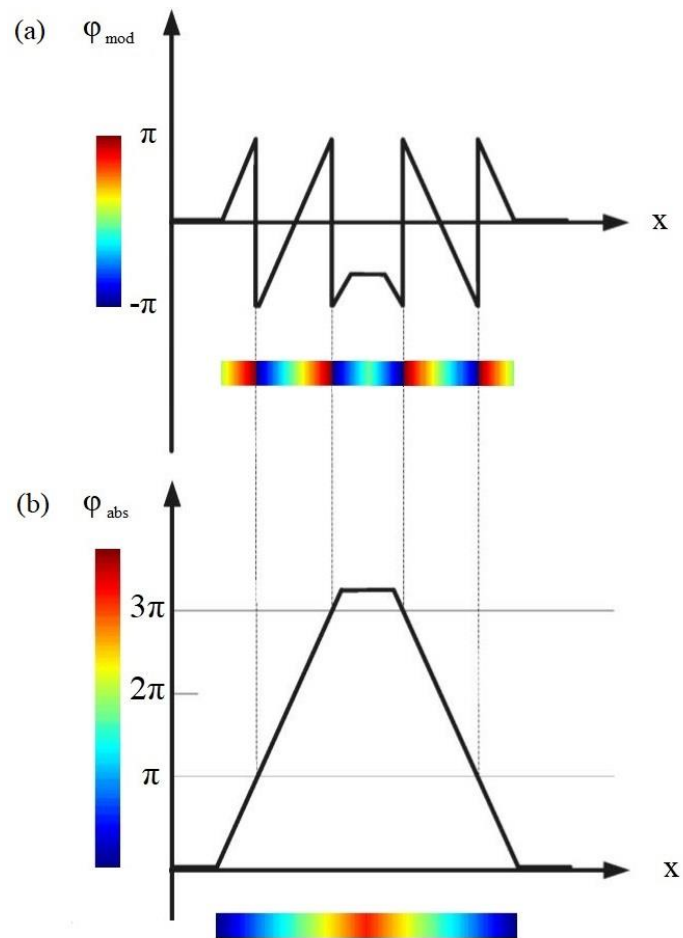


Figure 2.13. The relationship between (a) wrapped, modulo phase and (b) unwrapped absolute phase.

An integer number of phase cycles needs to be added to the wrapped phase in order to derive the absolute phase change. Figure 2.13 depicts a wrapped interferogram where a number of 2π 'sawtooth' jumps are present (a), while (b) shows the absolute phase after unwrapping. Figure 2.13 depicts a simple model case where there are no discontinuities or noise and unwrapping is one dimensional. However, in reality unwrapping occurs in two orthogonal directions where phase gradients between adjacent pixels are computed via integration over a given path relative to a starting point. Hence, phase unwrapping is computationally expensive. Erroneous unwrapping can occur due to discontinuities in the profile, large deformation gradients, atmospheric phase screens, and temporal and perpendicular decorrelation which result from long baselines (Ghiglia & Pritt, 1998). The two main unwrapping methods are residue-based (Goldstein *et al.*, 1988) and least-squares algorithms (Zebker & Lu, 1998). The performance of such methods principally depends on the fringe spacing and the signal-to-noise ratio (SNR) of the interferogram (Zebker *et al.*, 1994).

2.2.2.4.3. *Thermal Noise*

Thermal noise, or system noise, is always present in SAR imagery and is caused by the microscopic motion of electrons due to temperature. This is principally due to the internal circuitry of the satellite. Such effects are random and pervasive at all frequencies, although the levels of noise varies from sensor to sensor and is a function of the SNR of the SAR system. Thermal noise reduces coherence and the spatial averaging of pixels – called multi-looking – is often implemented to improve coherence. Noise decreases and the phase statistics are improved given that phase is proportional to the number of cells over which the mean is computed (Lee *et al.*, 1994). Multi-looking, in turn, improves the reliability of phase unwrapping (Goldstein *et al.*, 1988). Overall, the effect of thermal noise on InSAR measurements are much smaller effects of incoherence and phase unwrapping errors and is not a large issue for modern satellites.

2.2.2.5. *Ground Deformation*

The aim of interferometric processing is to isolate, quantify and minimise the phase contributions of the geometry, topography, atmosphere and noise in order to determine the ground deformation. Once such contributions have been removed, the absolute unwrapped phase is converted into relative ground deformation by multiplying by the wavelength of the sensor. For C-Band missions, 1 fringe equates to 28.3 mm of deformation in the satellite line-of-sight (LOS), which for Sentinel-1 ranges between 29.1° to 46° from near to far range. On the assumption that motion is entirely vertical, LOS deformation can be projected into the vertical by means of dividing by the cosine of the incidence angle. However, where significant lateral motion is present this assumption does not hold. Utilizing measurements calculated over the same time epoch from both ascending (LOS_{Asc}) and descending (LOS_{Desc}) orbits, the deformation vector can be further resolved. Whilst it cannot be resolved for the

vertical (d_{Vert}), north (d_{North}) and east (d_{Hor}) directions, on the assumption that there is negligible motion in the northern direction (i.e., $d_{North} = 0$), the vertical and horizontal components of deformation can be resolved:

$$d_{Vert} = \frac{(-\sin\theta_{Desc} \cdot \cos\phi_{Desc} \cdot LOS_{Asc}) + (-\sin\theta_{Asc} \cdot \cos\phi_{Asc} \cdot LOS_{Desc})}{(-\sin\theta_{Asc} \cdot \cos\phi_{Asc} \cdot \cos\theta_{Desc}) - (\cos\theta_{Asc} \cdot \cos\phi_{Desc} \cdot \sin\theta_{Desc})} \quad (2.20)$$

$$d_{Hor} = \frac{(\cos\theta_{Desc} \cdot LOS_{Asc}) + (-\cos\theta_{Asc} \cdot LOS_{Desc})}{(-\sin\theta_{Asc} \cdot \cos\phi_{Asc} \cdot \cos\theta_{Desc}) - (\cos\theta_{Asc} \cdot \cos\phi_{Desc} \cdot \sin\theta_{Desc})} \quad (2.21)$$

where θ is the incidence angle from surface normal, ϕ is the azimuth track angle and LOS are the line-of-sight velocity measurements. The superscript indicates whether the parameter corresponds to the ascending (*Asc*) or descending (*Desc*) geometry.

2.3. Multi-temporal Differential InSAR

2.3.1. Conventional DInSAR Limitations

Deformation studies have been revolutionised by DInSAR since the first detection of differential motion (Gabriel *et al.*, 1989). An iconic example is of the 1992 magnitude 7.3 Landers earthquake, California, that produced an 85km surface rupture measuring up to 6 m (Massonnet *et al.*, 1993). The coseismic deformation field was evident in an iconic ‘butterfly’ shaped interferogram generated using SAR imagery spanning the event. However, whilst there are many successes of DInSAR, the deformation signal is often concealed by the contributions from nuisance terms (Sections 2.2.2.1 – 2.2.2.4) because many parameters need to be estimated from a small number of observations. Hence, the low SNR makes the detection of small but long-term deformations (i.e. < 1cm over yearly time frames) particularly challenging.

2.3.2. Stacking

To improve the SNR stacking is implemented, which involves chronologically combining multiple interferograms of the same area (Sandwell & Price, 1998). The SNR improves because the deformation signal reinforces, i.e. the unwrapped phase adds up linearly so, for example, interferograms covering two- and three-year periods result in unwrapped phase essentially covering a five year period, whilst the undesired signal does not as it only increases with the square root of the number of observations. The standard deviation of deformation from a single interferogram is inversely proportional to the cumulative time interval, hence, as the cumulative time interval increases, the standard deviation of deformation decreases (Wegmüller *et al.*, 2000).

Furthermore, stacking enables the phase contributions to be filtered and modelled so deformation can be isolated effectively. As Eqn 2.16 states, the differential phase is made up from the sum of contributions from baseline error, DEM error, differences in atmospheric propagation, noise and ground deformation. Baseline errors and atmospheric effects are

both correlated in space but not in time and therefore separation of these effects can be challenging and, in some cases, the atmospheric phase screens might contain some contribution of baseline error (Kampes, 2006). The DEM error is consistent temporally and can be modelled as a function of the individual baselines (Ferretti *et al.*, 2001). Noise is spatially and temporally uncorrelated and can be reduced by filtering. Additionally, often only the highest quality pixels, which characteristically exhibit low noise, are selected, and processed (Hooper, 2006). Deformation is both spatially and temporally correlated and is derived using linear and/or non-linear models of deformation.

Time-series methods first appeared towards the end of the 1990s, around a decade after the first successful use of InSAR. Today, there are many different methods to derive deformation information using multi-temporal DInSAR, which principally follow two main approaches: Persistent Scatterers Interferometry (PSI) (e.g. Ferretti *et al.*, 2001; Werner *et al.*, 2003; Hooper *et al.*, 2004; Kampes, 2005); or Small Baseline (SB) methods (Berardino *et al.*, 2002; Mora *et al.*, 2003; Schmidt & Bürgmann, 2003; Pepe *et al.*, 2005; 2011; Lanari *et al.*, 2007). Alternatively, there are algorithms that combine these approaches (e.g. Hooper *et al.*, 2008; Ferretti *et al.*, 2011).

2.3.3. Time-Series Approaches

2.3.3.1. Persistent Scatterers Interferometry

Persistent Scatterers Interferometry (PSI) targets resolution elements whose echo is dominated by a single scatterer, referred to as persistent scatterers (PS) (Figure 2.14a). PS analyses are based on phase dispersion with stability of the radar response being a necessary assumption. The deformation signal can be retrieved if the variance of the echo over time is small enough. PS points remain highly correlated over extended time periods and discrepancies in look angle have little effect on this variation. The amount of decorrelation is the principal determinant that defines whether a pixel is a PS, which is determined by either modelling deformation over time or determining the spatial correlation of phase terms. Due to the lack of geometric decorrelation, interferograms can be formed over periods that are longer than the critical baseline. For every satellite acquisition, an interferogram is formed with respect to a single common master image, utilizing the maximum number of acquisitions. However, this is at the sacrifice of imaged pixel density; only highly coherent targets are utilized, and their density can be low in many regions, particularly in non-urban areas.

No multilooking is applied as this adds additional scatterers to the phase contribution of the pixel. Since the premise of PSI is based on a dominant scatterer, adding additional non-dominant scatterers introduces noise and, therefore, increases decorrelation. Motion is attributed to a specific scatterer rather than an entire resolution cell, therefore it is an effective method for monitoring local urban regions where the movement of individual hard targets can be analysed to determine, for example, whether one building is moving with respect to another (Hooper *et al.*, 2012).

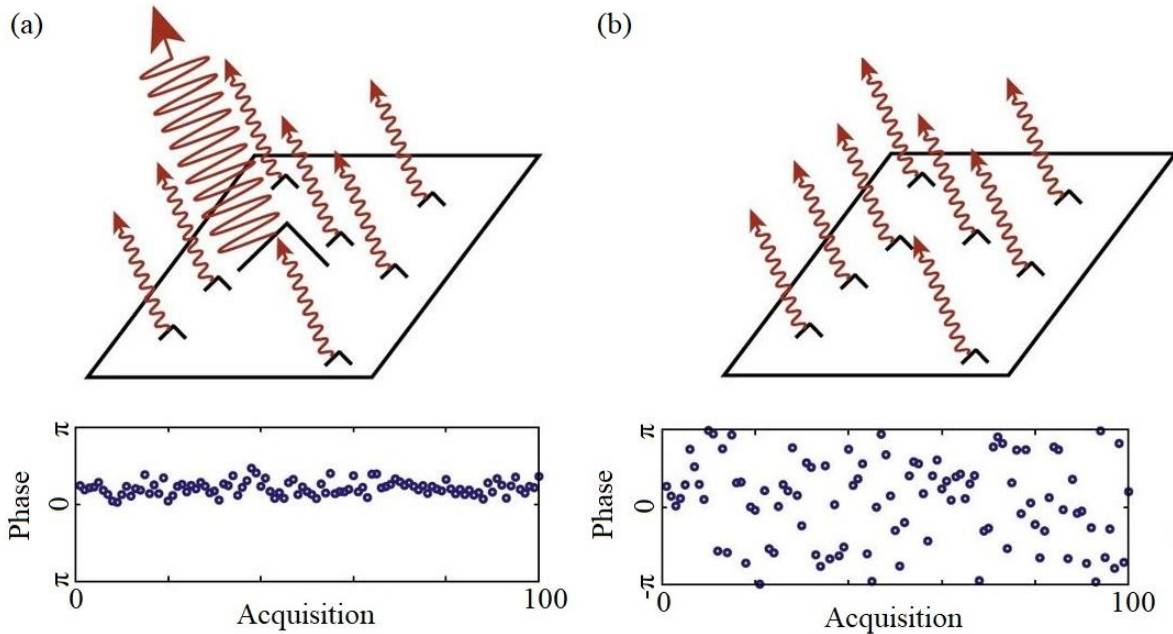


Figure 2.14. Top: A phase simulation the scatterers contributing to a single pixel for (a) a persistent scatterer and (b) a distributed scatterer. Bottom: Phase simulations for 100 acquisitions (Hooper *et al.*, 2012).

2.3.3.2. Small Baseline Methods

For pixels that do not encompass a dominant scatterer, the deformation signal is often concealed by the phase variation due to decorrelation. Scattering is disseminated within the resolution pixel (Figure 2.14b) so small baseline methods form interferograms over short temporal ranges and small perpendicular baselines to restrict deviations in squint and look angle. Effective control of these elements minimizes DEM error and decorrelation so that the deformation signal is still detectable. Multiple master interferograms are formed between all pairs satisfying the spatial and temporal baselines. Spatial multi-looking is implemented to increase phase stability. Provided the signal does not vary dramatically over the multi-looked area, the phase associated with deformation reinforces while environmental noises do not. Small baseline (SB) approaches, therefore, are suited to analysis of spatially correlated deformation over wide expanses (Hooper *et al.*, 2012). Whilst SB methods have been proven to achieve meaningful results outside of areas typically unfavourable for DInSAR analysis (e.g. Lu & Kwoun, 2008), the density and distribution of measurements is still limited (Osmanoğlu *et al.*, 2016).

2.4. Intermittent Small Baseline Subset

2.4.1. SBAS

The Small Baseline Subset (SBAS) method is a low-resolution multi-temporal SB DInSAR method, developed by Berardino *et al.* (2002). It is a widely used method and has shown proficiency to monitor a wide range of natural and anthropogenic hazards (e.g. Tizzani *et al.*, 2007; Liu *et al.*, 2013; Dong *et al.*, 2014; Osmanoğlu *et al.*, 2016). To summarize the

methodology, from an initial co-registered stack of SAR images, multilooked two-pass multiple master interferograms are generated between pairs satisfying the orbital and temporal requirements. Interferograms are unwrapped and linear velocities are derived from a least squares covariance analysis of the unwrapped phase, which also determines height errors and standard errors, calculated from the standard deviation of residuals after fitting. To determine the time-series for each pixel, phase associated with the linear velocities and height errors are removed from the differential interferograms, before being added back after the residual phase components have been unwrapped. The phase velocity between adjacent images are inverted via Singular Value Decomposition. Phase is subsequently integrated to derive the phase at each acquisition interval before an initial spatial low-pass filter and subsequent temporal high-pass filter are employed to derive and remove atmospheric components. Finally, modulo- 2π phase time-series are converted to deformation time-series.

2.4.2. ISBAS

The Intermittent Small Baseline Subset (ISBAS) (Sowter *et al.*, 2013) is an adapted version of the SBAS (Berardino *et al.*, 2002) DInSAR time-series algorithm and has been developed by the University of Nottingham and Terra Motion Limited. The ISBAS method has been designed to improve the density and spatial distribution of survey points so to return measurements in vegetated areas where DInSAR processing algorithms habitually struggle. It is widely acknowledged that phase decorrelation (or incoherence) is a significant limitation of DInSAR, which severely affects the spatial distribution and density of measurements outside of urbanised and arid terrain with sparse vegetation cover (See Section 2.2.2.4.1). This effect is most prevalent in higher frequency radar bands, such as C-band, where incoherence is pervasive over agricultural fields, forests, semi-natural areas and wetlands (Ferretti *et al.*, 2003). This is particularly constraining for both PSI and SB techniques (Osmanoğlu *et al.*, 2016).

Previous work has identified that L-Band (~ 24 cm wavelength) radar is capable of measuring through a forest canopy to map changes in water levels (e.g. Alsdoft *et al.*, 2000; Alsdoft *et al.*, 2000; Wdowinski *et al.*, 2004). The scattering mechanism for L-Band signals was confirmed to be a double-bounce backscatter return, whereby the transmitted signal is initially reflected away from the sensor off the water surface, towards the vegetation trunks and then back to the sensor. This showed that L-Band is capable of penetrating a forest canopy and, thus, interferometric coherence can be maintained for monitoring surface height changes. At shorter wavelengths, such as C-Band (~ 5.6 cm wavelength) or X-Band (~ 3 cm wavelength), measurement is more challenging. However, C-band SAR signals are capable of penetrating through vegetation, although the extent of penetration is dependent upon the density, structure and geometry of the cover (Kornelsen & Coulibaly, 2013). It is understood to be a function of leaf area index (LAI) and incidence angle (Wang *et al.*, 1998). Contrary to common vegetation scattering theories, C-Band has been shown to be able to penetrate forest canopies over long temporal baselines (e.g. Lu & Kwoun, 2008; Hong &

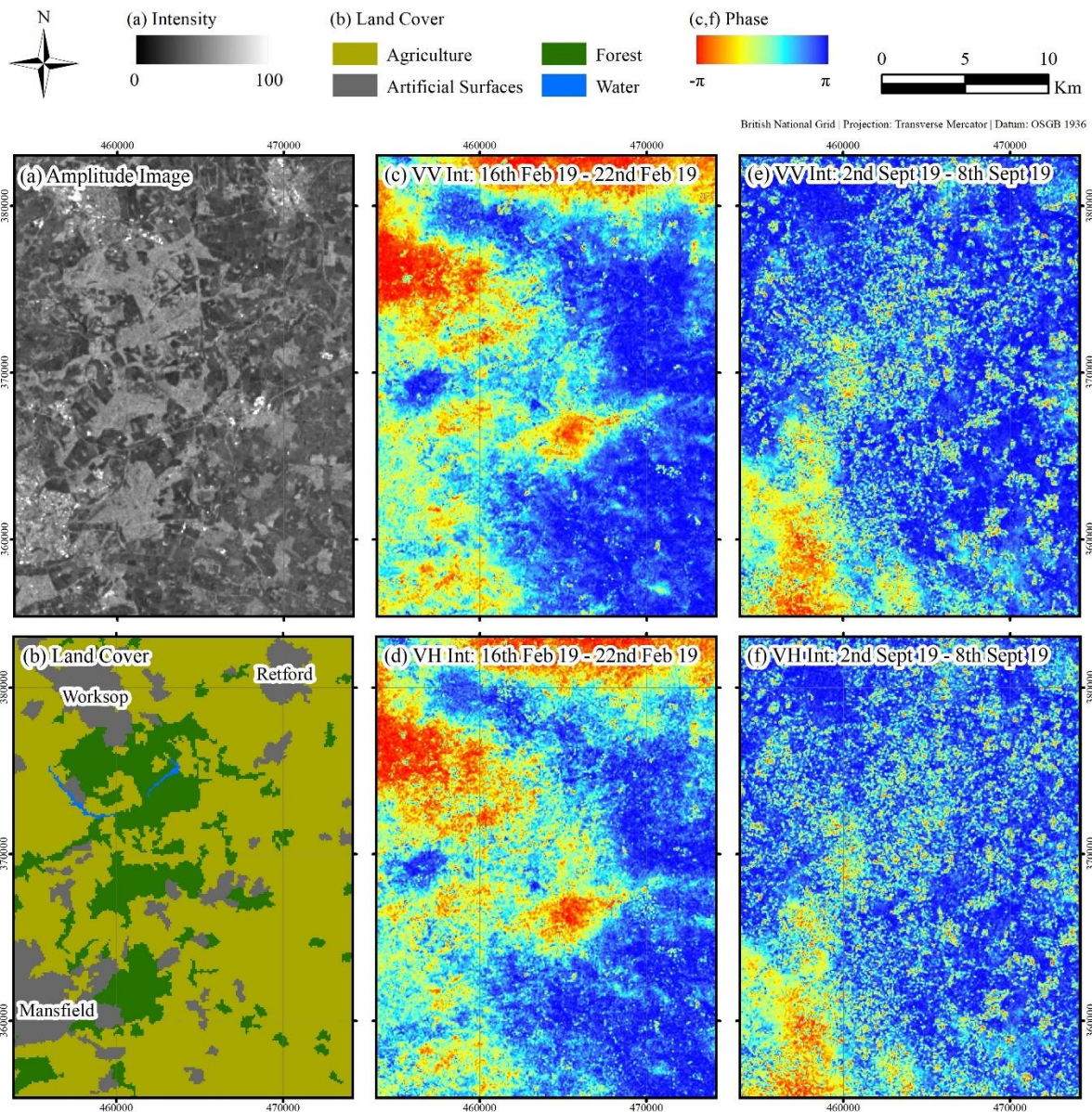


Figure 2.15. Sentinel-1 interferograms over north Nottinghamshire: (a) Amplitude image; (b) CORINE land cover inventory (European Environment Agency, 2012); (c) VV polarized interferogram (16th February 2019 – 22nd February 2019); (d) VH polarized interferogram (16th February 2019 – 22nd February 2019); (e) VV polarized interferogram (2nd September 2019 – 8th September 2019); (f) VH polarized interferogram (2nd September 2019 – 8th September 2019). No filtering has been applied.

Wdowinski, 2013; Brisco *et al.*, 2015). For example, Lu & Kwoun (2008) used ERS-1/2 and Radarsat-1 C-Band data to monitor water level changes through a moderate canopy over swamp forests in southeastern Louisiana, whereby the dominant radar backscattering mechanism was double-bounce backscattering.

Figure 2.15 shows two pairs of C-Band Sentinel-1 interferograms generated over north Nottinghamshire for both VV and VH polarized images. In the interferograms coherence is maintained over both urban and natural surfaces. The VV and VH pairs are very similar which indicates a double bounce scattering mechanism, else if diffuse scattering from the

canopy had occurred the VV and VH interferograms would not be so similar. Double bounce scattering can occur in the canopy; however, coherence is spatially correlated which suggests that the double bounce penetrates the canopy and hits the floor. Thus, this indicates that C-Band radar can measure surface deformation through a canopy, in opportune conditions.

Not all canopies are penetrable, and penetration is less likely in summer when the canopy is likely to be most dense. In temperate climates, interferograms generated over summer months and longer baselines are less likely to be coherent. The ISBAS method utilizes the coherence as a filter to retrieve and utilize the coherent interferograms. Throughout a temporal stack of SAR imagery, the strength of phase correlation between images varies over time, hence, pixels in rural areas are coherent for subsets of the total epoch – i.e., they are intermittently coherent. ISBAS retains intermittently coherent pixels for analysis by modifying the SBAS pixel selection. Once a set of multi-looked small baseline interferograms, satisfying the temporal and perpendicular baseline criteria, have been generated a coherence analysis is employed. Pixels which fulfil the selection criteria are those that exhibit a defined level of coherence in a minimum number of n interferograms, when $n \leq N$, where N is the total number of interferograms. The choice of interferogram threshold, n , determines both the spatial coverage and the precision of the measurement – the standard error, ε . Utilizing a value of $n = N$ is the equivalent to the method of Berardino *et al.* (2002) and minimizes the standard error of velocity. However, this is at the expense of the density of measurements. The choice of n is essentially a trade-off between coverage and quality, hence, the inversely proportional relationship between n and the standard error (i.e. $n \propto 1/\varepsilon$). Velocity errors can be estimated as $\varepsilon = 11/\sqrt{n}$ mm/year (Cigna & Sowter, 2017).

Coherent and intermittently coherent pixels satisfying the criteria are unwrapped from modulo- 2π phase to relative deformation using a statistical-cost network-flow algorithm (Chen & Zebker, 2001) with respect to a reference pixel, assumed to be stable. After unwrapping, the method is in accordance with that of Berardino *et al.* (2002). The linear velocities are derived from a least squares covariance analysis of the unwrapped phase, which also determines DEM height errors. Standard errors associated with both measurements are calculated from the standard deviation of residuals after fitting. To determine the time-series for each pixel, phase associated with the linear velocities and height errors are removed from the differential interferograms, before being added back after the residual phase components have been unwrapped. The phase velocities between adjacent images are inverted through Singular Value Decomposition. It should be noted that to generate the time-series the value of n is required to be at least equal to the number images processed. However, an equal value does not guarantee that there is enough redundancy to invert the interferogram network successfully. The closer n is to N (i.e., the more coherent interferograms) the more likely it is that a full time-series can be reliably generated. Phase is subsequently integrated to derive the phase at each acquisition interval before temporal high-pass and spatial low-pass filters compute and remove atmospheric components. Modulo- 2π phase time-series are then converted to deformation time-series.

The ISBAS method has shown significant capability to increase the spatial distribution of measurements in rural areas for a variety of applications including mining; oil and gas extraction, peatland monitoring, groundwater extraction; civil engineering, permafrost monitoring and landslide detection. Table 2.3 details the full published literature on the ISBAS method at the time of writing, which includes literature in this thesis.

Table 2.3. Published peer reviewed literature on the ISBAS method, excluding conference papers. Up to date as of March 2021.

Author	Satellite	Study Site	Application(s)
Sowter <i>et al.</i> (2013)	ENVISAT	South Derbyshire & Leicestershire, UK	Coal Mining; Groundwater
Bateson <i>et al.</i> (2015)	ERS 1/2	South Wales, UK	Coal Mining; Groundwater
Gee <i>et al.</i> (2016)	ERS 1/2; ENVISAT	Alkmaar, The Netherlands	Oil & Gas
Sowter <i>et al.</i> (2016)	Sentinel-1	Mexico City, Mexico	Ground Water
Novellino <i>et al.</i> (2017a)	Sentinel-1	Multiple, UK	Coal Mining
Gee <i>et al.</i> (2017)	ERS 1/2; ENVISAT; Sentinel-1	Northumberland & Durham, UK	Coal Mining; Groundwater
Cigna & Sowter (2017)	ERS 1/2	Multiple, UK	Coal Mining; Groundwater
Novellino <i>et al.</i> (2017b)	COSMO-SkyMed	Sicily, Italy	Landslides
Sowter <i>et al.</i> (2018)	Sentinel-1	Scotland, UK	Mining; Groundwater; Oil & Gas; Civil Engineering; Peatlands; Landslides
Marshall <i>et al.</i> (2018)	Sentinel-1	Kuala Lumpur, Malaysia	Civil Engineering; Peatlands
Alshammari <i>et al.</i> (2018)	Sentinel-1	Flow Country, Scotland	Peatlands
Gee <i>et al.</i> (2019)	Sentinel-1	The Netherlands	Mining; Groundwater; Oil & Gas; Civil Engineering; Peatlands
Grebbly <i>et al.</i> (2019)	ENVISAT; Sentinel-1	Tengiz, Kazakhstan	Oil & Gas
Jordan <i>et al.</i> (2019)	ERS 1/2; ENVISAT; Sentinel-1	Multiple, UK	Oil & Gas
Alshammari <i>et al.</i> (2020)	Sentinel-1	Flow Country, Scotland	Peatlands
Reinosch <i>et al.</i> (2020)	Sentinel-1	Tibet	Permafrost
Gee <i>et al.</i> (2020)	ENVISAT; Sentinel-1	Nottinghamshire, UK	Coal Mining; Groundwater
Brown <i>et al.</i> (2020)	Sentinel-1	Democratic Republic of Congo	Mining
Grebbly <i>et al.</i> (2021)	Sentinel-1	Brumadinho, Brazil	Mining

2.5. Coal Mining

2.5.1. Mining Subsidence

Mining activity utilizing deep shafts and groundwater pumping in the UK commenced as early as the 14th century, facilitating exploration down to depths of 1000m (Clarke *et al.*, 2006). It has been approximated that 4,800 million tonnes of coal have been extracted from

UK mines, consequently leaving 1000 million cubic metres of voids (Norton, 1996). This has resulted in significant changes to the land surface, including localised catastrophic failures and long-term subsidence over broad expanses. Voids created by underground extraction cause notable changes in the orientation and magnitude of the in-situ stress field, resulting in deformations in both the surrounding rock and remaining coal (Lee & Abel, 1983). Historical indications demonstrate that there remains a risk of ground instability for up to 200 years after pillar and stall and longwall workings have been abandoned. There is potentially no time limit for pillar and stall instability. The delayed onset of motion can be initiated by a number of factors including creep of the overburden, pillar deterioration, collapse of the roof and failure of the floor as a result of seatearth softening. Furthermore, deeper mine activity can trigger events in shallower, often unrecorded, mines (Clarke *et al.*, 2006).

Room and pillar mining, where mined material is extracted across a horizontal plane creating horizontal arrays of pillars and rooms, results in between 15% and 90% of the material being extracted. Consequently, the load on the pillars increases between 60% to 90% which can result in spalling, brittle failure, or ductile failure. The potential for failure depends on the properties of the coal (strength and structure – presence of faults, joints and fractures) and the geometry of the mine (size of extracted area, ratio of seam thickness to pillar width and depth) (Clarke *et al.*, 2006). The collapse of multiple pillars can result in a surface depression, known as areal subsidence (Sizer & Gill, 2000). Deformation can occur in the roof of a room due to the lack of support; it commences during extraction and can continue over time. Natural fractures can open which can weaken intact rock; over time progression of these fractures, and consequent stress changes, can lead to bedding

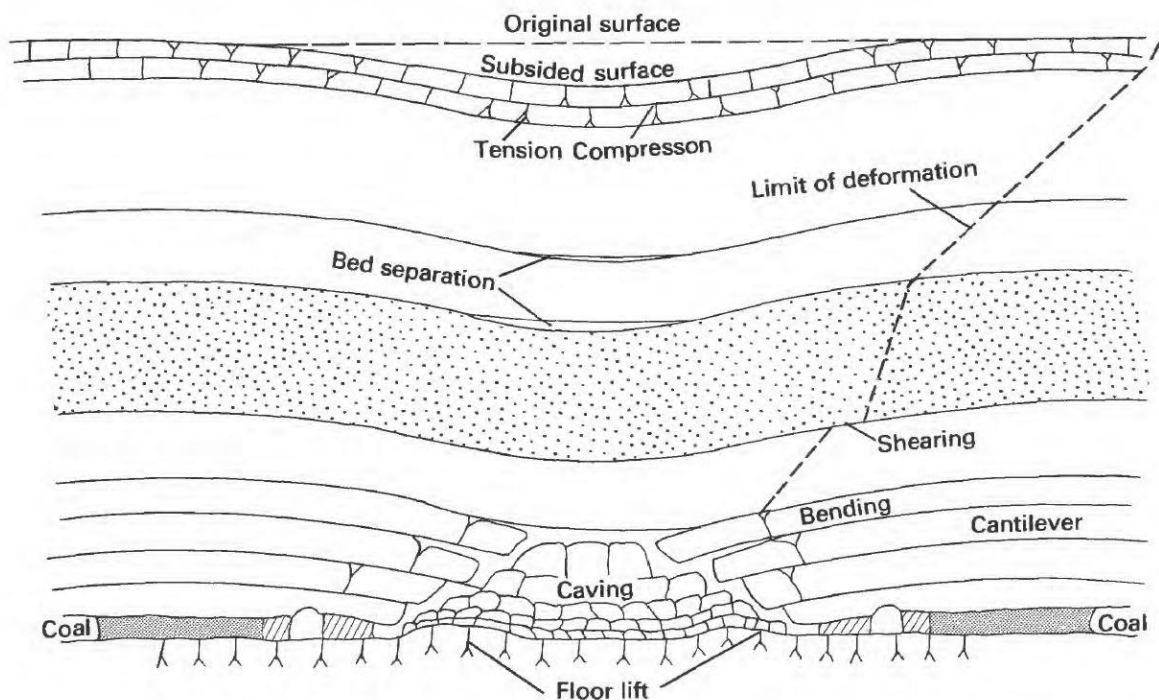


Figure 2.16. Deformations produced in rocks above and below an extracted coal seam (Lee & Abel, 1983).

separation and eventually the collapse of the overlying beds into the room. Under certain circumstances this can lead to the formation of a crown hole (Clarke *et al.*, 2006). Floor failure can occur where a seatearth is exposed below the mined seam. Water is absorbed, leading to swelling and heave of the floor. Where pillars overlie the seatearth, due to the softening of seatearth, coal pillars can 'punch' through it via shear failure (Goodman, 1989).

The mechanical aspects of subsidence produced from longwall mining methods are generally better understood compared with room and pillar mining. The extraction of coal bearing rocks over a wide area result in immediate roof collapse (Figure 2.16). The displacement of rock can result in surface subsidence if the ratio of the width of extracted coal measures to depth of overburden exceeds a value between 0.1-0.5. The structure and strength of the overburden controls the precise ratio value (Lee & Abel, 1983).

2.5.2. Groundwater Rebound

Broadly, coalfields can become associated with stability and contamination issues following abandonment, due to prominent changes in topography and hydrogeological regime (Smith & Underwood, 2000). Deep underground coal extraction requires the pumping of groundwater to maintain safe working conditions within the mine (Younger, 2002). Systematic pumping ordinarily ceases, or significantly reduces, following the abandonment of underground coal mines and groundwater levels begin to rebound. For example, there has been a clear correlation between groundwater rise and the cessation of pumping in the Durham coalfield, UK (Younger, 1993; Younger, 1995). The flooding of abandoned workings can have many detrimental consequences including residual subsidence; the reactivation of existing faults; mine gas migration; slope instability; and can influence the geotechnical properties of the ground (Donnelly, 2006). Individual coalfields may be subject to some or none of the identified issues. Subsidence and slope instability have not been associated with mine water recovery in British coalfields (Coal Authority, 2017).

Rising groundwater creates a complex subsurface environment. As the rock matrix reverts to previously saturated conditions, pore water pressure increases and consequently the rock expands which can produce heave at the surface (Bekendam & Pottgens, 1995). Surface elevation is thought to only represent several percent of any previously identified subsidence during active mining and to occur gradually over a larger area than previous subsidence basins (Wojtkowaik *et al.*, 2000). Water ingress into former workings provides some support pressure inside the mined voids. Ingress is aided by the disturbance, fracturing and disintegration of roof layers and overlying rock mass during mine operation, and consequently permeability and porosity are increased (Bekendam & Pottgens, 1995; Wojtkowaik *et al.*, 2000). However, coal measures rock can lose significant strength on water saturation as a result of mineralogical changes to the clays within the rock matrix, stress corrosion or water absorption (Poulsen *et al.*, 2014) and has been associated with pillar failure in within former mine workings (Knott, 2006; Castellanza *et al.*, 2008). Additionally, the chance of failure can increase as the saturation of soil within the overburden increases vertical stress on the strata (Bekendam & Pottgens, 1995). The risk of surface instability is

substantially higher during the transitory phase of groundwater rise, due to the redistribution of stress within the rock matrix. Risk is reduced once a new hydraulic and hydrogeological equilibrium is reached, following saturation to historical levels (Wotjkowaik *et al.*, 2000). In most cases in the UK, the pre mining hydrogeology is not known but it is assumed rebound is to the pre-mining levels.

2.5.3. Groundwater Modelling

Both numerical and analytical approaches have been previously proposed to model groundwater rebound in abandoned coalfields. There are many freely and commercially available numerical codes used to solve groundwater flow equations which simulate the flow of groundwater through aquifers. For example, MODFLOW (Anderman & Hill, 2000) is an open source a finite-difference model, developed by the U.S. Geological Survey since the early 1980s, which has been applied to mining applications (e.g. Surinaidu *et al.*, 2014; Yu *et al.*, 2007). More recently, GRAM (Groundwater Rebound in Abandoned Mineworkings) (Younger & Adams, 1999), a semi-distributed, non-Darcian groundwater flow model, was developed specifically to simulate the process of mine water rebound in extensive systems of mine-workings. It was designed to overcome the shortcomings of applying standard numerical packages to groundwater rebound in coalfields. The concept central to GRAM is that the coalfield can be divided into discrete ponds, which are groups of mine workings that are thought to be hydraulically analogous with respect the rebound.

The emergence of DInSAR time-series methods in the late 1990s has increased the integration of surface deformation measurements into hydrogeological studies. Subsidence or heave are often indicative areas of groundwater depletion or recharge. Analytical solutions based upon the principle of effective stress (Terzaghi, 1925) and work of Poland (1984) are commonly utilized with DInSAR data to delineate lithological boundaries and map aquifer storage variations and assist characterisation (e.g. Chaussard *et al.*, 2014; Castellazzi *et al.*, 2016; Béjar-Pizarro *et al.*, 2017; Castellazzi *et al.*, 2018). With respect to mine water rebound, spatial distributions of heave in coal measures rocks (e.g. Sowter *et al.*, 2013; Bateson *et al.*, 2015; Sowter *et al.*, 2018; Gee *et al.*, 2019) and temporal correlations between the rise of mine water and deformation time-series (e.g. Cuenca *et al.*, 2013; Gee *et al.*, 2017) have been observed over abandoned coalfields. Perhaps mostly notably, Cuenca *et al.* (2013) used PSI on ERS and ENVISAT data to map mine water dynamics in Limburg, The Netherlands. An attempt was made to model surface heave caused by pore pressure variations using the strain source concept (Geertsma, 1973). Fair agreement was found between the modelled output and observed data, however, it was acknowledged that the use of various point sources does not necessarily realistically reflect or replicate the actual subsurface hydrogeological conditions. Furthermore, the presence of impermeable faults, which act as hydrological barriers preventing water from flowing freely across the coalfield, were observed. Using PSI differential motion was measured over the faults, however, such abrupt changes in groundwater regime could not be identified in the model.

2.6. Summary

Several themes relevant to this thesis have been discussed, starting with Radar, SLAR and SAR. Logically, this progresses onto an overview of InSAR, DInSAR and multi-temporal DInSAR. The methods by which time-series DInSAR is applied, via PSI and SB methods, are discussed, followed by a description of the SBAS and Intermittent SBAS methods. Finally, an overview of mechanisms behind coal mining deformation are provided and the chapter finishes with a summary of methods to model groundwater rebound.

2.7. References

- Alsdorf, D., Birkett, C., Dunne, T., Melack, J. and Hess, L., 2001. Water level changes in a large Amazon lake measured with spaceborne radar interferometry and altimetry. *Geophysical Research Letters*, 28(14), pp.2671-2674. <https://doi.org/10.1029/2001GL012962>
- Alsdorf, D.E., Melack, J.M., Dunne, T., Mertes, L.A., Hess, L.L. and Smith, L.C., 2000. Interferometric radar measurements of water level changes on the Amazon flood plain. *Nature*, 404(6774), pp.174-177. <https://doi.org/10.1038/35004560>
- Alshammari, L., Large, D., Boyd, D., Sowter, A., Anderson, R., Andersen, R. and Marsh, S., 2018. Long-term peatland condition assessment via surface motion monitoring using the ISBAS DInSAR technique over the Flow Country, Scotland. *Remote Sensing*, 10(7), p.1103. <https://doi.org/10.3390/rs10071103>
- Alshammari, L., Boyd, D.S., Sowter, A., Marshall, C., Andersen, R., Gilbert, P., Marsh, S. and Large, D.J., 2020. Use of Surface Motion Characteristics Determined by InSAR to Assess Peatland Condition. *Journal of Geophysical Research: Biogeosciences*, 125(1), p.e2018JG004953. <https://doi.org/10.1029/2018JG004953>
- Anderman, E.R. and Hill, M.C., 2000. MODFLOW-2000, the US Geological Survey modular ground-water model-documentation of the Hydrogeologic-Unit Flow (HUF) Package (No. 2000-342). U. S. Geological Survey. <https://doi.org/10.3133/ofr00342>
- Bamler, R., 1992. A comparison of range-Doppler and wavenumber domain SAR focusing algorithms. *IEEE Transactions on Geoscience and Remote Sensing*, 30(4), pp.706-713. <https://doi.org/10.1109/36.158864>
- Bateson, L., Cigna, F., Boon, D. and Sowter, A., 2015. The application of the Intermittent SBAS (ISBAS) InSAR method to the South Wales Coalfield, UK. *International Journal of Applied Earth Observation and Geoinformation*, 34, pp.249-257. <https://doi.org/10.1016/j.jag.2014.08.018>
- Béjar-Pizarro, M., Ezquerro, P., Herrera, G., Tomás, R., Guardiola-Albert, C., Hernández, J.M.R., Merodo, J.A.F., Marchamalo, M. and Martínez, R., 2017. Mapping groundwater level and aquifer storage variations from InSAR measurements in the Madrid aquifer, Central Spain. *Journal of Hydrology*, 547, pp.678-689. <https://doi.org/10.1016/j.jhydrol.2017.02.011>

- Bekendam, R.F. and Pottgens, J.J., 1995. Ground movements over the coal mines of southern Limburg, The Netherlands, and their relation to rising mine waters. *IAHS Publications-Series of Proceedings and Reports-Intern Assoc Hydrological Sciences*, 234, pp.3-12.
- Berardino, P., Fornaro, G., Lanari, R. and Sansosti, E., 2002. A new algorithm for surface deformation monitoring based on small baseline differential SAR interferograms. *IEEE Transactions on Geoscience and Remote Sensing*, 40(11), pp.2375-2383. <https://doi.org/10.1109/TGRS.2002.803792>
- Brisco, B., Ahern, F., Hong, S.H., Wdowinski, S., Murnaghan, K., White, L. and Atwood, D.K., 2015. Polarimetric decompositions of temperate wetlands at C-band. *IEEE Journal of Selected Topics in Applied Earth Observations and Remote Sensing*, 8(7), pp.3585-3594. <https://doi.org/10.1109/JSTARS.2015.2414714>
- Brown, C., Daniels, A., Boyd, D.S., Sowter, A., Foody, G. and Kara, S., 2020. Investigating the Potential of Radar Interferometry for Monitoring Rural Artisanal Cobalt Mines in the Democratic Republic of the Congo. *Sustainability*, 12(23), p.9834. <https://doi.org/10.3390/su12239834>
- Castellanza, R., Gerolymatou, E. and Nova, R., 2008. An attempt to predict the failure time of abandoned mine pillars. *Rock mechanics and rock engineering*, 41(3), p.377. <https://doi.org/10.1007/s00603-007-0142-y>
- Castellazzi, P., Longuevergne, L., Martel, R., Rivera, A., Brouard, C. and Chaussard, E., 2018. Quantitative mapping of groundwater depletion at the water management scale using a combined GRACE/InSAR approach. *Remote Sensing of Environment*, 205, pp.408-418. <https://doi.org/10.1016/j.rse.2017.11.025>
- Castellazzi, P., Martel, R., Rivera, A., Huang, J., Pavlic, G., Calderhead, A.I., Chaussard, E., Garfias, J. and Salas, J., 2016. Groundwater depletion in Central Mexico: Use of GRACE and InSAR to support water resources management. *Water Resources Research*, 52(8), pp.5985-6003. <https://doi.org/10.1002/2015WR018211>
- Chaussard, E., Bürgmann, R., Shirzaei, M., Fielding, E.J. and Baker, B., 2014. Predictability of hydraulic head changes and characterization of aquifer-system and fault properties from InSAR-derived ground deformation. *Journal of Geophysical Research: Solid Earth*, 119(8), pp.6572-6590. <https://doi.org/10.1002/2014JB011266>
- Chaussard, E., Milillo, P., Bürgmann, R., Perissin, D., Fielding, E.J. and Baker, B., 2017. Remote sensing of ground deformation for monitoring groundwater management practices: Application to the Santa Clara Valley during the 2012–2015 California drought. *Journal of Geophysical Research: Solid Earth*, 122(10), pp.8566-8582. <https://doi.org/10.1002/2017JB014676>
- Chen, C.W. and Zebker, H.A., 2001. Two-dimensional phase unwrapping with use of statistical models for cost functions in nonlinear optimization. *JOSA A*, 18(2), pp.338-351. <https://doi.org/10.1364/JOSAA.18.000338>

- Cigna, F. and Sowter, A., 2017. The relationship between intermittent coherence and precision of ISBAS InSAR ground motion velocities: ERS-1/2 case studies in the UK. *Remote Sensing of Environment*, 202, pp.177-198. <https://doi.org/10.1016/j.rse.2017.05.016>
- Clarke, B.G., Welford, M. and Hughes, D.B., 2006. The threat of abandoned mines on the stability of urban areas. *Engineering Geology for Tomorrow's Cities. Geological Society, London, Engineering Geology Special Publications*, 22.
- Coal Authority, 2017. Review of Northumberland Paper. [letter] (Personal Communication, June 2017).
- Cuenca, M.C., Hooper, A.J. and Hanssen, R.F., 2013. Surface deformation induced by water influx in the abandoned coal mines in Limburg, The Netherlands observed by satellite radar interferometry. *Journal of Applied Geophysics*, 88, pp.1-11. <https://doi.org/10.1016/j.jappgeo.2012.10.003>
- Curlander, J. C., and McDonough, R. N., 1991. *Synthetic aperture radar*. John Wiley & Sons Ltd.
- De Zan, F. and Guarnieri, A.M., 2006. TOPSAR: Terrain observation by progressive scans. *IEEE Transactions on Geoscience and Remote Sensing*, 44(9), pp.2352-2360. <https://doi.org/10.1109/TGRS.2006.873853>
- Dong, S., Samsonov, S., Yin, H., Ye, S. and Cao, Y., 2014. Time-series analysis of subsidence associated with rapid urbanization in Shanghai, China measured with SBAS InSAR method. *Environmental earth sciences*, 72(3), pp.677-691. <https://doi.org/10.1007/s12665-013-2990-y>
- Donnelly, L. 2006. Investigation of Geological Hazards & Mining Risks, Gallowgate, Newcastle-upon-Tyne. *Proceedings of the 10th IAEG International Congress, IAEG2006, Nottingham, UK*.
- European Environment Agency, 2012. *CORINE Land Cover 2012*. Available at: <<https://land.copernicus.eu/pan-european/corine-land-cover/clc-2012/view>> [Accessed 25th August 2019).
- Ferretti, A., Colesanti, C., Perissin, D., Prati, C. and Rocca, F., 2003, Evaluating the effect of the observation time on the distribution of SAR permanent scatterers. In *Proceedings of Fringe*, 1–5 December 2003, ESA-ESRIN, Frascati.
- Ferretti, A., Fumagalli, A., Novali, F., Prati, C., Rocca, F. and Rucci, A., 2011. A new algorithm for processing interferometric data-stacks: SqueeSAR. *IEEE Transactions on Geoscience and Remote Sensing*, 49(9), pp.3460-3470. <https://doi.org/10.1109/TGRS.2011.2124465>
- Ferretti, A., Prati, C. and Rocca, F., 2001. Permanent scatterers in SAR interferometry. *IEEE Transactions on geoscience and remote sensing*, 39(1), pp.8-20. <https://doi.org/10.1109/36.898661>

- Farr, T.G., Rosen, P.A., Caro, E., Crippen, R., Duren, R., Hensley, S., Kobrick, M., Paller, M., Rodriguez, E., Roth, L. and Seal, D., 2007. The shuttle radar topography mission. *Reviews of geophysics*, 45(2). <https://doi.org/10.1029/2005RG000183>
- Gabriel, A.K., Goldstein, R.M. and Zebker, H.A., 1989. Mapping small elevation changes over large areas: differential radar interferometry. *Journal of Geophysical Research: Solid Earth*, 94(B7), pp.9183-9191. <https://doi.org/10.1029/JB094iB07p09183>
- Gee, D., Bateson, L., Grebby, S., Novellino, A., Sowter, A., Wyatt, L., Marsh, S., Morgenstern, R. and Athab, A., 2020. Modelling groundwater rebound in recently abandoned coalfields using DInSAR. *Remote Sensing of Environment*, 249, p.112021. <https://doi.org/10.1016/j.rse.2020.112021>
- Gee, D., Bateson, L., Sowter, A., Grebby, S., Novellino, A., Cigna, F., Marsh, S., Banton, C. and Wyatt, L., 2017. Ground motion in areas of abandoned mining: application of the Intermittent SBAS (ISBAS) to the Northumberland and Durham Coalfield, UK. *Geosciences*, 7(3), p.85. <https://doi.org/10.3390/geosciences7030085>
- Gee, D., Sowter, A., Grebby, S., de Lange, G., Athab, A. and Marsh, S., 2019. National geohazards mapping in Europe: Interferometric analysis of the Netherlands. *Engineering Geology*. 256, pp.1-22. <https://doi.org/10.1016/j.enggeo.2019.02.020>
- Gee, D., Sowter, A., Novellino, A., Marsh, S. and Gluyas, J., 2016. Monitoring land motion due to natural gas extraction: Validation of the Intermittent SBAS (ISBAS) DInSAR algorithm over gas fields of North Holland, the Netherlands. *Marine and Petroleum Geology*, 77, pp.1338-1354. <https://doi.org/10.1016/j.marpetgeo.2016.08.014>
- Ghiglia, D.C. and Pritt, M.D., 1998. *Two-dimensional phase unwrapping: theory, algorithms, and software (Vol. 4)*. New York: Wiley.
- Goldstein, R.M., Zebker, H.A. and Werner, C.L., 1988. Satellite radar interferometry: Two-dimensional phase unwrapping. *Radio science*, 23(4), pp.713-720. <https://doi.org/10.1029/RS023i004p00713>
- Goodman, R.E., 1989. *Introduction to rock mechanics (Vol. 2, p. 576)*. New York: Wiley.
- Grebby, S., Orynassarova, E., Sowter, A., Gee, D. and Athab, A., 2019. Delineating ground deformation over the Tengiz oil field, Kazakhstan, using the Intermittent SBAS (ISBAS) DInSAR algorithm. *International Journal of Applied Earth Observation and Geoinformation*, 81, pp.37-46. <https://doi.org/10.1016/j.jag.2019.05.001>
- Grebby, S., Sowter, A., Gluyas, J., Toll, D., Gee, D., Athab, A. and Girindran, R., 2021. Advanced analysis of satellite data reveals ground deformation precursors to the Brumadinho Tailings Dam collapse. *Communications Earth & Environment*, 2(1), pp.1-9. <https://doi.org/10.1038/s43247-020-00079-2>
- Hanssen, R.F., 1998. *Atmospheric heterogeneities in ERS tandem SAR interferometry*. Delft University Press.

- Hanssen, R.F., 2001. *Radar interferometry: data interpretation and error analysis (Vol. 2)*. Springer Science & Business Media.
- Hong, S.H. and Wdowinski, S., 2013. Double-bounce component in cross-polarimetric SAR from a new scattering target decomposition. *IEEE Transactions on Geoscience and Remote Sensing*, 52(6), pp.3039-3051. <https://doi.org/10.1109/TGRS.2013.2268853>
- Hooper, A., 2006. Persistent scatterer radar interferometry for crustal deformation studies and modeling of volcanic deformation. Doctoral thesis, Stanford University.
- Hooper, A., 2008. A multi-temporal InSAR method incorporating both persistent scatterer and small baseline approaches. *Geophysical Research Letters*, 35(16). <https://doi.org/10.1029/2008GL034654>
- Hooper, A., Bekaert, D., Spaans, K. and Arkan, M., 2012. Recent advances in SAR interferometry time series analysis for measuring crustal deformation. *Tectonophysics*, 514, pp.1-13. <https://doi.org/10.1016/j.tecto.2011.10.013>
- Hooper, A., Zebker, H., Segall, P. and Kampes, B., 2004. A new method for measuring deformation on volcanoes and other natural terrains using InSAR persistent scatterers. *Geophysical research letters*, 31(23). <https://doi.org/10.1029/2004GL021737>
- Jordan, C., Bateson, L. and Novellino, A., 2019. Environmental baseline monitoring for shale-gas development: Insights for monitoring ground motion using InSAR analysis. *Science of The Total Environment*, p.134075. <https://doi.org/10.1016/j.scitotenv.2019.134075>
- Kampes, B., 2005. Displacement Parameter Estimation Using Permanent Scatterer Interferometry. Doctoral thesis. Technische Universiteit Delft.
- Kampes, B.M., 2006. *Radar interferometry*. Springer.
- Kornelsen, K.C. and Coulibaly, P., 2013. Advances in soil moisture retrieval from synthetic aperture radar and hydrological applications. *Journal of Hydrology*, 476, pp.460-489. <https://doi.org/10.1016/j.jhydrol.2012.10.044>
- Knott, D.L., 2006. Assessment of potential subsidence impacts from coal mining using test borings, mine maps and empirical methods. In *Proceedings 2006 interstate technical group on abandoned underground mines meeting* (pp. 1-40).
- Lanari, R., Casu, F., Manzo, M., Zeni, G., Berardino, P., Manunta, M. and Pepe, A., 2007. An overview of the small baseline subset algorithm: A DInSAR technique for surface deformation analysis. *Pure and Applied Geophysics*, 164(4), pp.637-661. <https://doi.org/10.1007/s00024-007-0192-9>
- Lee, J.S., Hoppel, K.W., Mango, S.A. and Miller, A.R., 1994. Intensity and phase statistics of multilook polarimetric and interferometric SAR imagery. *IEEE Transactions on Geoscience and Remote Sensing*, 32(5), pp.1017-1028. <https://doi.org/10.1109/36.312890>

Lee, F.T. and Abel Jr, J.F., 1983. *Subsidence from underground mining: Environmental analysis and planning considerations* (No. USGS-CIRC-876). Colorado School of Mines, Golden (USA). <https://doi.org/10.3133/cir876>

Leighton, J. M., 2010. *GPS and PSI integration for monitoring urban land motion*. Doctoral thesis, University of Nottingham.

Lillesand, T., Kiefer, R.W. and Chipman, J., 2015. *Remote sensing and image interpretation*. 7th Ed. John Wiley & Sons Ltd.

Liu, P., Li, Z., Hoey, T., Kincal, C., Zhang, J., Zeng, Q. and Muller, J.P., 2013. Using advanced InSAR time series techniques to monitor landslide movements in Badong of the Three Gorges region, China. *International Journal of Applied Earth Observation and Geoinformation*, 21, pp.253-264. <https://doi.org/10.1016/j.jag.2011.10.010>

Lu, Z. and Kwoun, O.I., 2008. Radarsat-1 and ERS InSAR analysis over southeastern coastal Louisiana: Implications for mapping water-level changes beneath swamp forests. *IEEE Transactions on Geoscience and Remote Sensing*, 46(8), pp.2167-2184. <https://doi.org/10.1109/TGRS.2008.917271>

Lu, Z., Kwoun, O. and Rykhus, R., 2007. Interferometric synthetic aperture radar (InSAR): its past, present and future. *Photogrammetric engineering and remote sensing*, 73(3), p.217.

Madisetti, V., Williams, D., 1998. *The Digital Signal-Processing Handbook*. CRC Press.

Marshall, C., Large, D.J., Athab, A., Evers, S.L., Sowter, A., Marsh, S. and Sjögersten, S., 2018. Monitoring tropical peat related settlement using ISBAS InSAR, Kuala Lumpur International Airport (KLIA). *Engineering Geology*, 244, pp.57-65. <https://doi.org/10.1016/j.enggeo.2018.07.015>

Massonnet, D. and Feigl, K.L., 1998. Radar interferometry and its application to changes in the Earth's surface. *Reviews of geophysics*, 36(4), pp.441-500. <https://doi.org/10.1029/97RG03139>

Massonnet, D., Rossi, M., Carmona, C., Adragna, F., Peltzer, G., Feigl, K. and Rabaute, T., 1993. The displacement field of the Landers earthquake mapped by radar interferometry. *Nature*, 364(6433), p.138. <https://doi.org/10.1038/364138a0>

Mather, P.M., 2004. *Computer processing of remotely-sensed images: An introduction*. 3rd Ed. John Wiley & Sons Ltd.

Mora, O., Mallorqui, J.J. and Broquetas, A., 2003. Linear and nonlinear terrain deformation maps from a reduced set of interferometric SAR images. *IEEE Transactions on Geoscience and Remote Sensing*, 41(10), pp.2243-2253. <https://doi.org/10.1109/TGRS.2003.814657>

- Norton, P.J., 1996. Mine closure and associated hydrological effects on the environment: some case studies. *Minerals, Metals and the Environment II. The Institution of Mining and Metallurgy*, pp.263-70.
- Novellino, A., Cigna, F., Brahmi, M., Sowter, A., Bateson, L. and Marsh, S., 2017a. Assessing the feasibility of a national InSAR ground deformation map of Great Britain with Sentinel-1. *Geosciences*, 7(2), p.19. <https://doi.org/10.3390/geosciences7020019>
- Novellino, A., Cigna, F., Sowter, A., Ramondini, M. and Calcaterra, D., 2017b. Exploitation of the Intermittent SBAS (ISBAS) algorithm with COSMO-SkyMed data for landslide inventory mapping in north-western Sicily, Italy. *Geomorphology*, 280, pp.153-166. <https://doi.org/10.1016/j.geomorph.2016.12.009>
- Osmanoğlu, B., Sunar, F., Wdowinski, S. and Cabral-Cano, E., 2016. Time series analysis of InSAR data: Methods and trends. *ISPRS Journal of Photogrammetry and Remote Sensing*, 115, pp.90-102. <https://doi.org/10.1016/j.isprsjprs.2015.10.003>
- Pepe, A., Berardino, P., Bonano, M., Euillades, L.D., Lanari, R. and Sansosti, E., 2011. SBAS-based satellite orbit correction for the generation of DInSAR time-series: Application to RADARSAT-1 data. *IEEE Transactions on Geoscience and Remote Sensing*, 49(12), pp.5150-5165. <https://doi.org/10.1109/TGRS.2011.2155069>
- Pepe, A., Sansosti, E., Berardino, P. and Lanari, R., 2005. On the generation of ERS/ENVISAT DInSAR time-series via the SBAS technique. *IEEE Geoscience and Remote Sensing Letters*, 2(3), pp.265-269. <https://doi.org/10.1109/LGRS.2005.848497>
- Poland, J.F., 1984. *Guidebook to studies of land subsidence due to ground-water withdrawal*. UNESCO, Paris, France.
- Poulsen, B.A., Shen, B., Williams, D.J., Huddleston-Holmes, C., Erarslan, N. and Qin, J., 2014. Strength reduction on saturation of coal and coal measures rocks with implications for coal pillar strength. *International Journal of Rock Mechanics and Mining Sciences*, 71, pp.41-52. <https://doi.org/10.1016/j.ijrmms.2014.06.012>
- Reinosch, E., Buckel, J., Dong, J., Gerke, M., Baade, J. and Riedel, B., 2020. InSAR time series analysis of seasonal surface displacement dynamics on the Tibetan Plateau. *The Cryosphere*, 14(5), pp.1633-1633. <https://doi.org/10.5194/tc-14-1633-2020>
- Rizzoli, P., Martone, M., Gonzalez, C., Wecklich, C., Tridon, D.B., Bräutigam, B., Bachmann, M., Schulze, D., Fritz, T., Huber, M. and Wessel, B., 2017. Generation and performance assessment of the global TanDEM-X digital elevation model. *ISPRS Journal of Photogrammetry and Remote Sensing*, 132, pp.119-139. <https://doi.org/10.1016/j.isprsjprs.2017.08.008>
- Sandwell, D.T. and Price, E.J., 1998. Phase gradient approach to stacking interferograms. *Journal of Geophysical Research: Solid Earth*, 103(B12), pp.30183-30204. <https://doi.org/10.1029/1998JB900008>

Schmidt, D.A. and Bürgmann, R., 2003. Time-dependent land uplift and subsidence in the Santa Clara valley, California, from a large interferometric synthetic aperture radar data set. *Journal of Geophysical Research: Solid Earth*, 108(B9). <https://doi.org/10.1029/2002JB002267>

Sizer, K.E. and Gill, M., 2000. Pillar failure in shallow coal mines—a recent case history. *Mining Technology*, 109(3), pp.146-152. <https://doi.org/10.1179/mnt.2000.109.3.146>

Skolnik, M., 1990. *Radar handbook*. McGraw-Hill Professional.

Smith, F.W. and Underwood, B., 2000. Mine closure: the environmental challenge. *Mining Technology*, 109(3), pp.202-209. <https://doi.org/10.1179/mnt.2000.109.3.202>

Sowter, A., 2003. Phase ambiguity determination for the positioning of interferometric SAR data. *The Photogrammetric Record*, 18(104), pp.308-324. <https://doi.org/10.1046/j.0031-868X.2003.00021.x>

Sowter, A., 2010. Orthorectification and interpretation of differential InSAR data over mountainous areas: a case study of the May 2008 Wenchuan Earthquake. *International Journal of Remote Sensing*, 31(13), pp.3435-3448. <https://doi.org/10.1080/01431161003727721>

Sowter, A., Amat, M.B.C., Cigna, F., Marsh, S., Athab, A. and Alshammari, L., 2016. Mexico City land subsidence in 2014–2015 with Sentinel-1 IW TOPS: Results using the Intermittent SBAS (ISBAS) technique. *International Journal of Applied Earth Observation and Geoinformation*, 52, pp.230-242. <https://doi.org/10.1016/j.jag.2016.06.015>

Sowter, A., Athab, A., Novellino, A., Grebby, S. and Gee, D., 2018. Supporting energy regulation by monitoring land motion on a regional and national scale: A case study of Scotland. *Proceedings of the Institution of Mechanical Engineers, Part A: Journal of Power and Energy*, p.0957650917737225. <https://doi.org/10.1177/0957650917737225>

Sowter, A., Bateson, L., Strange, P., Ambrose, K. and Syafiudin, M.F., 2013. DInSAR estimation of land motion using intermittent coherence with application to the South Derbyshire and Leicestershire coalfields. *Remote Sensing Letters*, 4(10), pp.979-987. <https://doi.org/10.1080/2150704X.2013.823673>

Surinaidu, L., Rao, V.G., Rao, N.S. and Srinu, S., 2014. Hydrogeological and groundwater modeling studies to estimate the groundwater inflows into the coal Mines at different mine development stages using MODFLOW, Andhra Pradesh, India. *Water Resources and Industry*, 7, pp.49-65. <https://doi.org/10.1016/j.wri.2014.10.002>

Terzaghi, K., 1925. Principles of soil mechanics, IV—Settlement and consolidation of clay. *Engineering News-Record*, 95(3), pp.874-878.

Tizzani, P., Berardino, P., Casu, F., Euillades, P., Manzo, M., Ricciardi, G.P., Zeni, G. and Lanari, R., 2007. Surface deformation of Long Valley caldera and Mono Basin, California, investigated with the SBAS-InSAR approach. *Remote Sensing of Environment*, 108(3), pp.277-289. <https://doi.org/10.1016/j.rse.2006.11.015>

Torres, R., Snoeij, P., Geudtner, D., Bibby, D., Davidson, M., Attema, E., Potin, P., Rommen, B., Floury, N., Brown, M. and Traver, I.N., 2012. GMES Sentinel-1 mission. *Remote Sensing of Environment*, 120, pp.9-24. <https://doi.org/10.1016/j.rse.2011.05.028>

Ulaby, F. T., Moore, R. K., Fung, A. K., 1982. *Microwave remote sensing: active and passive. Vol. 1. Microwave Remote Sensing Fundamentals and Radiometry*. Addison-Wesley, Reading.

Wang, Y., Day, J.L., Davis, F.W., 1998. Sensitivity of modeled C- and L-band radar backscatter to ground surface parameters in loblolly pine forest. *Remote Sensing of Environment*, 66(3), pp.331–342. [https://doi.org/10.1016/S0034-4257\(98\)00074-1](https://doi.org/10.1016/S0034-4257(98)00074-1).

Wdowinski, S., Amelung, F., Miralles-Wilhelm, F., Dixon, T.H. and Carande, R., 2004. Space-based measurements of sheet-flow characteristics in the Everglades wetland, Florida. *Geophysical Research Letters*, 31(15). <https://doi.org/10.1029/2004GL020383>

Wegmüller, U., 1999. Automated terrain corrected SAR geocoding. In: *IEEE 1999 International Geoscience and Remote Sensing Symposium*. IGARSS'99 Proceedings (Cat. No. 99CH36293). Vol. 3, pp. 1712-1714. <https://doi.org/10.1109/IGARSS.1999.772070>

Werner, C., Wegmuller, U., Strozzi, T. and Wiesmann, A., 2003. Interferometric point target analysis for deformation mapping. In: *IEEE 2003 International Geoscience and Remote Sensing Symposium*. IGARSS'03 Proceedings (Cat. No. 03CH37477). Vol. 7, pp. 4362-4364. <https://doi.org/10.1109/IGARSS.2003.1295516>

Woodhouse, I. H., 2005. *Introduction to microwave remote sensing*. CRC press.

Wojtkowiak, F., Couillet, J.C., Daupley, X. and Tauziede, C., 2000, September. Geotechnical and environmental impacts on the surface of the water rising in French underground coal mines after closure. In 7. *International Mine Water Association Symposium (IMWA 2000)* (pp. 180-194).

Younger, P.L. and Adams, R., 1999. *Predicting mine water rebound*. Environment Agency R&D Technical Report W179. Bristol, UK. 108pp.

Younger, P.L., 2002. Coalfield closure and the water environment in Europe. *Mining Technology*, 111(3), pp.201-209. <https://doi.org/10.1179/mnt.2002.111.3.201>

Younger, P.L., 1995. Hydrogeochemistry of minewaters flowing from abandoned coal workings in County Durham. *Quarterly Journal of Engineering Geology and Hydrogeology*, 28(Supplement 2), pp.S101-S113. <https://doi.org/10.1144/GSL.QJEGH.1995.028.S2.02>

Younger, P.L., 1993. Possible environmental impact of the closure of two collieries in County Durham. *Water and Environment Journal*, 7(5), pp.521-531. <https://doi.org/10.1111/j.1747-6593.1993.tb00881.x>

Yu, M.H., Jefferson, I.F. and Culshaw, M.G., 2007, August. Fault reactivation, an example of environmental impacts of groundwater rising on urban area due to previous mining

activities. In *The Second Half Century of Rock Mechanics, Three Volume Set: 11th Congress of the International Society for Rock Mechanics, 3 VOLUMES+ CD-ROM* (Vol. 1, p. 41). CRC Press.

Zebker, H.A. and Lu, Y., 1998. Phase unwrapping algorithms for radar interferometry: residue-cut, least-squares, and synthesis algorithms. *JOSA A*, 15(3), pp.586-598.
<https://doi.org/10.1364/JOSAA.15.000586>

Zebker, H.A., Rosen, P.A., Goldstein, R.M., Gabriel, A. and Werner, C.L., 1994. On the derivation of coseismic displacement fields using differential radar interferometry: The Landers earthquake. *Journal of Geophysical Research: Solid Earth*, 99(B10), pp.19617-19634.
<https://doi.org/10.1029/94JB01179>

Zebker, H.A., Rosen, P.A. and Hensley, S., 1997. Atmospheric effects in interferometric synthetic aperture radar surface deformation and topographic maps. *Journal of geophysical research: solid earth*, 102(B4), pp.7547-7563. <https://doi.org/10.1029/96JB03804>

Zebker, H.A. and Villasenor, J., 1992. Decorrelation in interferometric radar echoes. *IEEE Transactions on geoscience and remote sensing*, 30(5), pp.950-959.
<https://doi.org/10.1109/36.175330>

3. Ground Motion in Areas of Abandoned Mining

The initial study over the Northumberland and Durham coalfield revisited previous research which applied PSI to ERS and ENVISAT data. The same archive data was processed using the ISBAS method to see whether the increased spatial coverage of ground measurements would aid the geological interpretation. Furthermore, the study was brought up to date using the latest Sentinel-1 data to determine the deformation regime over a 20-year period. The case study afforded the opportunity to examine the potential relationships between surface deformation and the mining, geological and hydrogeological data which would help identify areas for further research.

Article

Ground Motion in Areas of Abandoned Mining: Application of the Intermittent SBAS (ISBAS) to the Northumberland and Durham Coalfield, UK

David Gee ^{1,*} , Luke Bateson ², Andrew Sowter ³ , Stephen Grebby ¹ ,
Alessandro Novellino ², Francesca Cigna ^{2,†} , Stuart Marsh ¹ , Carl Banton ⁴ and Lee Wyatt ⁴

¹ Nottingham Geospatial Institute, University of Nottingham, Triumph Road, Nottingham NG7 2TU, UK; stephen.grebby@nottingham.ac.uk (S.G.); stuart.marsh@nottingham.ac.uk (S.M.)

² British Geological Survey, Keyworth, Nottinghamshire NG12 5GG, UK; lbateson@bgs.ac.uk (L.B.); alessn@bgs.ac.uk (A.N.); francesca.cigna@gmail.com (F.C.)

³ Geomatic Ventures Limited, Nottingham Geospatial Building, Triumph Road, Nottingham NG7 2TU, UK; andrew.sowter@geomaticventures.com

⁴ Coal Authority, 200 Lichfield Lane, Mansfield, Nottinghamshire NG18 4RG, UK; CarlBanton@coal.gov.uk (C.B.); LeeWyatt@coal.gov.uk (L.W.)

* Correspondence: david.gee@nottingham.ac.uk

† Present address: Italian Space Agency (ASI), Via del Politecnico snc, 00133 Rome, Italy.

Received: 20 June 2017; Accepted: 5 September 2017; Published: 13 September 2017

Abstract: In this paper, we investigate land motion and groundwater level change phenomena using differential interferometric synthetic aperture radar (DInSAR) over the Northumberland and Durham coalfield in the United Kingdom. The study re-visits earlier research that applied a persistent scatterers interferometry (PSI) technique to ERS (European Remote Sensing) and ENVISAT (Environmental Satellite) data. Here, the Intermittent Small Baseline Subset (ISBAS) DInSAR technique is applied to ERS, ENVISAT and Sentinel-1 SAR datasets covering the late 1990s, the 2000s and the mid-2010s, respectively, to increase spatial coverage, aid the geological interpretation and consider the latest Sentinel-1 data. The ERS data identify surface depressions in proximity to former collieries, while all three data sets ascertain broad areas are experiencing regional scale uplift, often occurring in previously mined areas. Uplift is attributed to increases in pore pressure in the overburden following the cessation of groundwater pumping after mine closure. Rising groundwater levels are found to correlate to ground motion measurements at selected monitoring sites, most notably in the surrounding area of Ashington. The area is divided by an impermeable EW fault; to the south, surface heave was identified as groundwater levels rose in the 1990s, whereas to the north, this phenomenon occurred two decades later in the 2010s. The data emphasize the complexity of the post-mining surface and subsurface environment and highlight the benefit that InSAR, utilizing the ISBAS technique, can provide in its characterization.

Keywords: ground motion; subsidence; coal mining; DInSAR; Intermittent SBAS

1. Introduction

High precision satellite radar interferometry is an effective and well established technique for monitoring earth surface motion [1]. It is a cost-effective method capable of surveying extensive areas to within millimetre precision regardless of weather and illumination conditions [2]. Differential interferometric synthetic aperture radar (DInSAR) utilizes stacks of high resolution synthetic aperture radar (SAR) data acquired over time from spaceborne platforms. DInSAR utilizes shifts in phase to measure changes in surface height in the satellite line-of-sight (LOS) direction and is capable of

computing both average velocities (linear) and time-series (non-linear) to characterize ground motions occurring over the temporal epoch of image acquisitions [3].

A variety of persistent scatterer and small baseline interferometric techniques have been used to delineate and quantify coal mining related surface phenomena in Europe [4,5] and farther afield [6,7]. However, it is common for temporal gaps to restrict multi-temporal DInSAR analysis in areas subject to historical or active mining [7]. Temporal gaps are common due to large deformation gradients often associated with mining subsidence [8,9] and decorrelation, the loss of coherence, which is common over coal mining areas [10].

Coherence, a by-product of the interferogram formation process, is a measure of phase correlation between two corresponding signals [11]. In areas of high coherence, targets are highly reflective and alter minimally over time. Conversely, in areas of low reflectance, where targets change over time (i.e., from year to year or from season to season), coherence is lost. In temperate, vegetated, rural settings the land surface can be variable due to both natural processes (e.g., soil shrink-swell) and human influences (e.g., agriculture) [12]. As a result, when differential interferograms are stacked, points for which coherence is maintained throughout the stack are generally abundant in urban locations, but sparse if not non-existent in rural areas. The optimum results produced by DInSAR are, therefore, obtained in urban or rocky areas, where coherence is recurrently high.

The Intermittent Small Baseline Subset (ISBAS) [10,13] is an adapted version of the established low resolution SBAS [14] DInSAR time-series algorithm. It has been designed to improve the density and spatial distribution of survey points to return measurements in vegetated areas where DInSAR processing algorithms habitually struggle. The amendment of SBAS is introduced during unwrapping, after a set of low-resolution, two-pass, multi-looked interferograms with small perpendicular baselines have been produced. While SBAS unwraps targets where coherence is above a given threshold in all stacked interferograms, ISBAS considers targets where coherence is above a given threshold in a subset of the total number of interferograms within the stack. The algorithm can retrieve measurements for targets that are intermittently coherent throughout the period of observations. As a consequence, the density of survey points returned is higher and their distribution not limited to urban centres [15]. The ISBAS method has been successfully validated with ground truth over an area of gas production and geostorage in North Holland, the Netherlands [16]. The results demonstrated that the ISBAS technique can be used with confidence over locations where traditional ground-based survey measurements are not available.

Amongst many other applications, the ISBAS technique has previously been used for the monitoring of ground motion related to coal mining in the UK [10,17,18]. Sowter et al. (2013) [10] implemented the ISBAS technique on ENVISAT (Environmental Satellite) data covering the South Derbyshire and North West Leicestershire coalfields. The ISBAS-derived uplift, observed in agricultural and forested areas as well as urban centres, closely matched the outcrop of middle Coal Measures near Swadlincote, appearing bound by existing fault structures and spatially correlated to underground mining works abandoned in the early 1990s. Bateson et al. (2015) [18] applied ISBAS to ERS (European Remote Sensing) data acquired over the South Wales coalfield which has a complex history of surface movement due to coal mining and post-glacial stress relief [19]. Two discrete areas of uplift were observed in the proximity of the towns of Bargoed and Bedwas, again in mixed urban and rural land cover. In both investigations, the mechanism of uplift was not definitively confirmed but was thought to be related to increases in pore water pressure and/or the re-activation of existing faults.

Similar regional patterns of uplift following coalfield closures have been observed over other regions in the UK [20]. In Northumberland, a Persistent Scatterers Interferometry (PSI) analysis, an alternative DInSAR technique, was conducted on ERS and ENVISAT data covering the Northumberland and Durham coalfield and confirmed the changing patterns of ground motion over time [21,22]. Some correlations between the geology and PS derived ground motion products were made; however, in some cases the lack of PSI measurements in rural areas meant that the correlation between the motions and the geological and mining information was not clear.

Accordingly, the principle aim of this paper is to better delineate ground motion on a regional scale in the Northumberland and Durham coalfield by applying the ISBAS technique to the ERS and ENVISAT data in order to extend coverage into areas of low coherence. This will subsequently enable a more comprehensive geological interpretation of the factors and processes associated with the observed ground motion. In addition, the launch of Sentinel-1 in April 2014 provides the opportunity to bring the study up to date by revealing more recent patterns of motion, therefore facilitating an investigation of ground deformation spanning three decades.

2. Northumberland and Durham Case Study

2.1. Land Cover

The area of interest (AOI) is located in the north east region of England and covers the counties of Northumberland, Tyne and Wear and County Durham (Figure 1). The AOI covers 2000 km², 40 km in width and 50 km in length. The north of the AOI extends up to the towns of Ashington and Morpeth and South to the towns of Houghton-le-Spring and Seaham. Agricultural land is most dominant within the AOI, with small pockets of forested and semi natural areas contained within these expanses. Notable urban regions exist along the north east coastline where the cities of Newcastle-upon-Tyne and Sunderland are situated on the banks of the River Tyne and River Wear respectively.

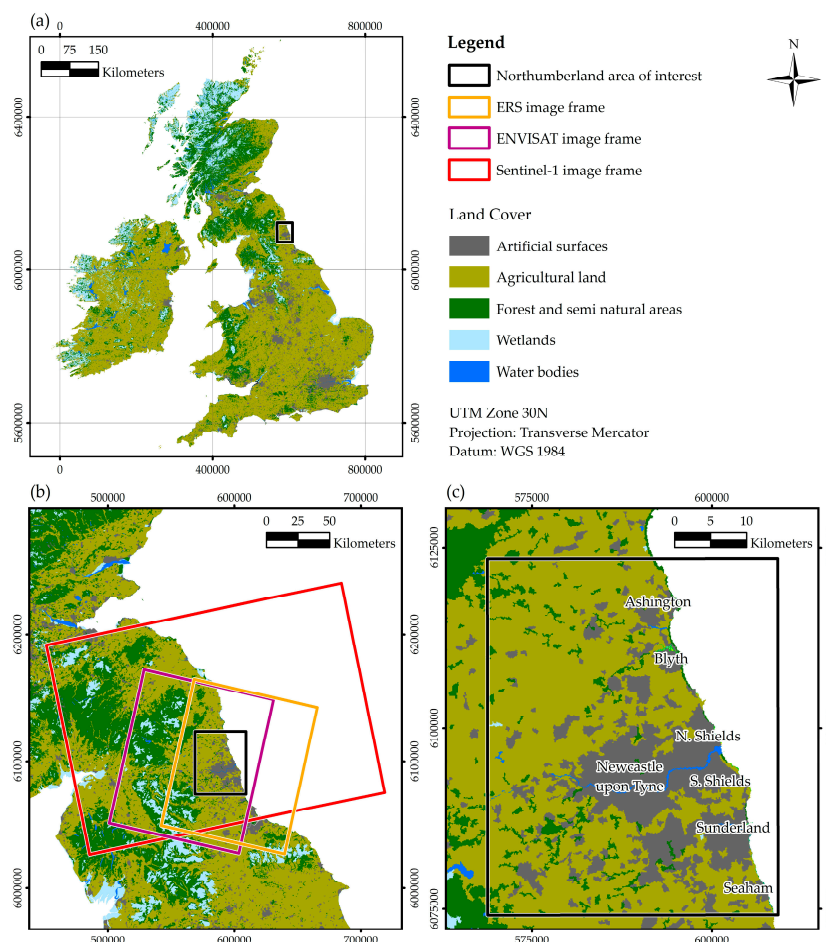


Figure 1. A land cover classification of the United Kingdom and Ireland taken from the 2012 CORINE (Co-ordinated Information on the Environment) Land Cover inventory [23]: (a) A map detailing the location of the Northumberland area of interest (AOI) within the United Kingdom; (b) Footprints of the ERS, ENVISAT and Sentinel-1 image frames; (c) The AOI with major towns and cities labelled. Copyright holder: European Environment Agency (EEA).

2.2. Geological Setting

The geological sequence of interest includes bedrock of Carboniferous strata within the southern sector of the Northumberland Trough: the Yoredale Group (Stainmore and Alston Formation) and the Coal Measures Group (Figure 2). The Northumberland Trough is a major, asymmetrical SW-NE basin bounded to the south by the Stublick and Ninety Fathom faults and by the Cheviot Massif to the north [24]. The Carboniferous rocks dip gently eastwards and are overlaid unconformably by the Permian strata of the basal Yellow Sands Formation and overlying Magnesian limestone formations of the Zechstein Group [25]. The continuity of the outcrops of these units is interrupted by a number of normal faults. The edge of the Zechstein Group outcrop is typically marked by prominent scarp features overlooking the lower lying ground of the Coal Measures Group [22]. Superficial deposits of the Quaternary period, mainly resulting from the last glaciation and subsequent Holocene processes, are present throughout the area and intermittently blanket the bedrock with areas of the Zechstein Group limestone virtually free of cover deposits.

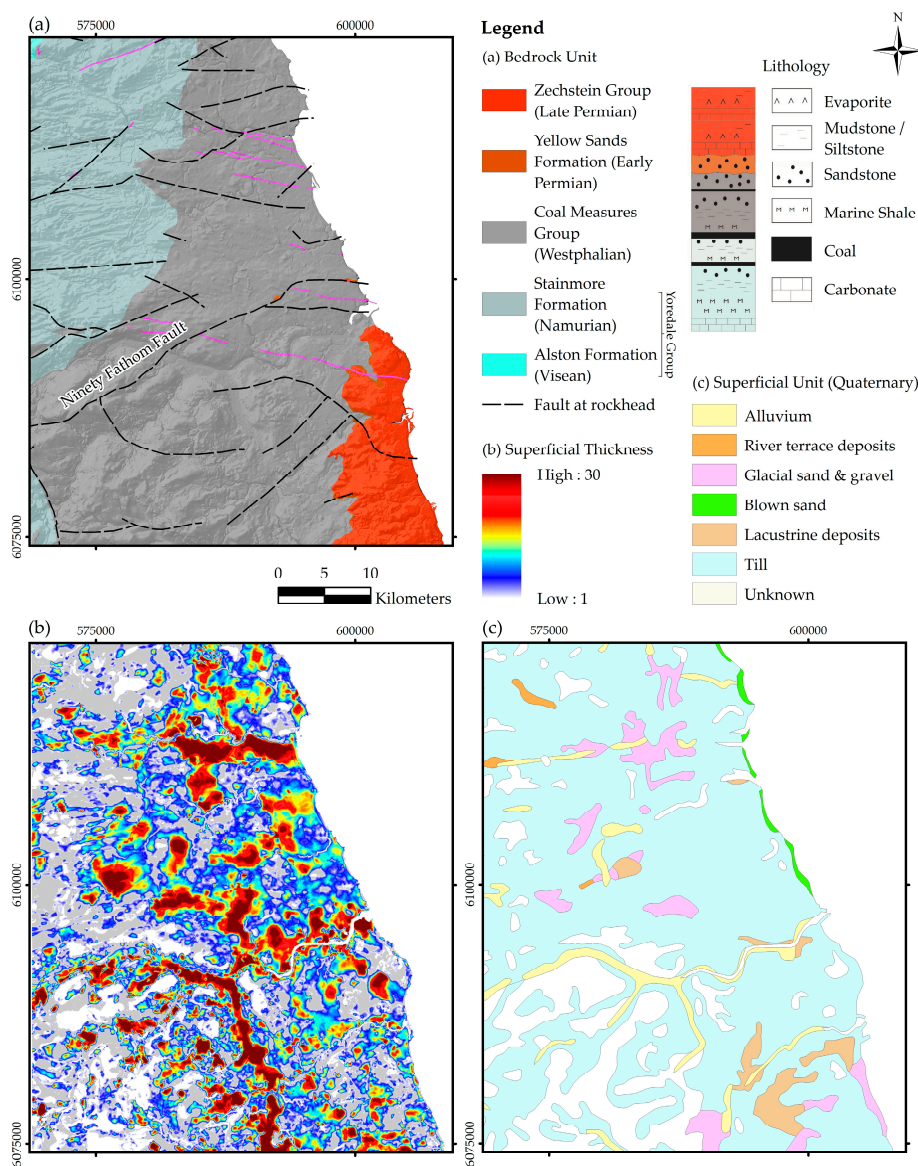


Figure 2. The geology of the AOI: (a) Bedrock geology overlain on topography; (b) Superficial thickness (interpolated from borehole data) [26]; (c) Superficial geology. ‘Reproduced with the permission of the British Geological Survey ©NERC. All rights Reserved’.

2.3. Northumberland and Durham Coalfield

The Northumberland and Durham coalfield has a working history dating back to Roman times. Over twenty coal seams have been mined underground and the coalfield has been one of the major sources of opencast (surface-mined) coal in Great Britain. The coal-bearing strata dip gently to the east, with part of the coalfield concealed beneath the Permian strata to the south of the River Tyne. The geological structure of the area has governed the development of the coalfield with faults serving to divide the area into zones of “take”. Early mining started in areas most accessible (i.e., inland in the west), where seams were often worked from the outcrop [27]. As mining and pumping methods developed, extraction from greater depths became viable; consequently, mining spread towards the eastern coast where deeper seams are situated, eventually advancing under the North Sea.

The coalfield has been extensively worked by both room and pillar and total extraction techniques. Longwall mining, where coal bearing rocks are machine worked from “longwall” faces at right angles from roadways running parallel to the face, is a method of total extraction and results in the immediate collapse of the roof and overlying rock into the void created behind. The displacement of rock can result in surface subsidence if the ratio of the width of extracted coal measures to the depth of the overburden exceeds a value between 0.1 and 0.5, where the structure and strength of the overburden controls the precise ratio value. Room and pillar mining, where mined material is extracted across a horizontal plane creating horizontal arrays of pillars and rooms, results in between 15% and 90% of the material being extracted. Consequently, load on the pillars increases by up to 90% which can result in spalling, brittle failure or ductile failure. The potential for failure depends on the physical properties of the coal and the geometry of the mine; the collapse of multiple pillars can result in a surface depression, known as areal subsidence. The mechanical aspects of subsidence produced from longwall mining methods are generally better understood compared with room and pillar mining [28].

3. SAR Processing

3.1. ERS and ENVISAT

Archive ERS and ENVISAT C-band (5.6 cm wavelength—5.3 GHz frequency) Stripmap SAR products were obtained and processed separately. The Single Look Complex (SLC) image stacks are acquired in the radar line-of-sight (LOS), the incidence angle ranges between 20.1° and 25.9° from near to far range with respect to the surface normal. Twenty-five ERS descending images spanning nearly a five year period from 24 May 1995 to 30 December 1999 (Appendix A) and twenty-one ENVISAT descending images spanning approximately a six year period from 3 December 2002 to 7 October 2008 (Appendix B) were identified for processing as they imaged the AOI with greatest frequency. The complete image frames were processed on both occasions which covers an area of approximately $100 \text{ km} \times 100 \text{ km}$, at a ground spatial resolution of 25 m in range and 5 m in azimuth [29].

The ERS stack was co-registered with respect to the master acquired on 20 November 1997, while the ENVISAT stack was co-registered to the scene acquired on 11 January 2005. Interferograms were generated with restrictions of 4 years on the temporal baseline and 250 m on the perpendicular orbital baseline. These restrictions are common to small baseline surveys using ERS and ENVISAT data, minimizing both temporal and spatial decorrelation in the interferograms and enhancing the quality of phase. Multilooking, applied to reduce noise and increase coherence, was implemented by a factor of 4 in range and 20 in azimuth to produce pixels of approximately $100 \text{ m} \times 100 \text{ m}$. Pixels deemed coherent within each interferogram displayed a coherence ≥ 0.25 .

An ISBAS analysis improves ground coverage by utilizing targets that are not high quality in every interferogram. As detailed by Sowter et al. (2013) [10], the algorithm accepts pixels, termed coherent pixels, which meet a minimum quality standard. Those retained in the analysis displayed a coherence ≥ 0.25 in a minimum number of (m) interferograms, when (m) \leq to the total number of interferograms (N). By unwrapping each interferogram individually the technique accepts intermittently coherent targets throughout the stack. The choice of interferogram threshold (m) is a

trade-off between coverage and quality, the value of which has a direct correlation with the standard error of the derived velocities [30].

The ERS analysis produced 102 multi-looked differential interferograms where an interferogram threshold (m) of 30 was determined. The temporal and orbital baselines of image pairs are plotted relative to the master in Figure 3a. All velocities are computed with respect to a reference point, it is important that this location is both stable and coherent in every interferogram. A reference point in North Shields (55.00° N, -1.46° E) was chosen based upon the data from the British Geological Survey (BGS) GeoSure natural geohazard datasets and its urban location. The control point is in an area of low susceptibility to geohazards and is surrounded by coherent targets which helps to minimize the propagation of errors during phase unwrapping.

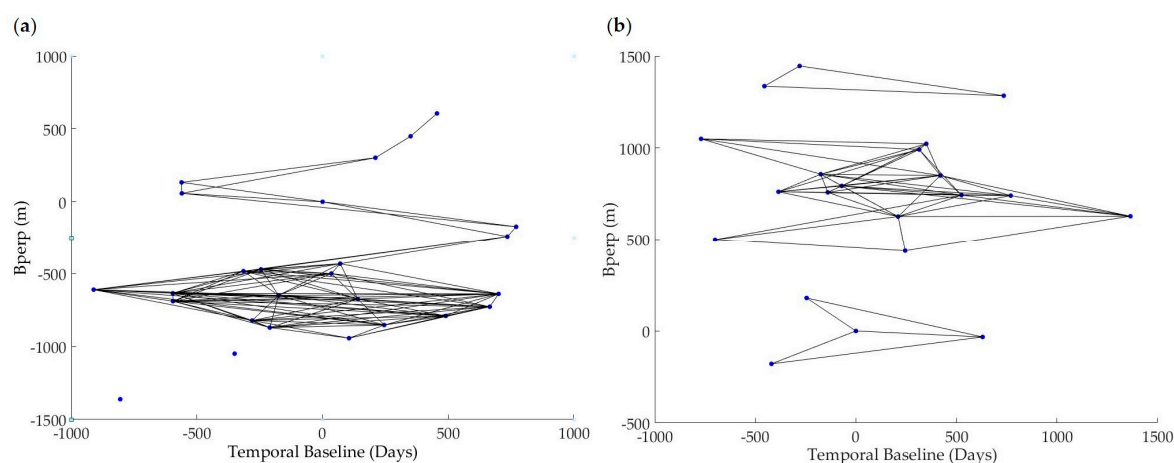


Figure 3. Temporal and perpendicular baselines of image pairs relative to the master. Image acquisitions are represented by points and differential interferograms, satisfying the orbital and temporal requirements, by lines: (a) ERS Synthetic Aperture Radar (SAR) (master: 20 November 1997); (b) ENVISAT Advanced Synthetic Aperture Radar (ASAR) (master: 11 January 2005).

The ENVISAT analysis produced 60 multi-looked differential interferograms (Figure 3b), from which an interferogram threshold (m) of 15 was applied. The reference point was, correspondingly to the ERS analysis, situated in North Shields for the aforementioned reasons.

Topographic phase was removed using a 90 m Shuttle Radar Topography Mission (SRTM) Digital Elevation Model (DEM) [31] and coherent and intermittently coherent pixels within each differential interferogram were unwrapped using a statistical-cost network-flow algorithm [32]. Following the method proposed by Berardino et al. (2002) [14] both linear and non-linear models of deformation were applied to compute average rates of motion and time-series per pixel. Additionally, the standard error for each pixel is computed via a least squares covariance analysis which expresses the goodness-of-fit between the interferogram values and derived linear velocity. Finally, due to the different incidence angles of ERS/ENVISAT (20.1 – 25.9°) and Sentinel-1 (29.1 – 46°), LOS velocities were converted into vertical velocities by means of dividing by the cosine of the incidence angle for each pixel.

3.2. Sentinel-1

Thirty-six Sentinel-1 Interferometric Wide Swath SLC images were identified as most suitable for analysis over the AOI (Appendix C). Radar LOS varies from 29.1° to 46.0° across the swath from near to far range, with a single look resolution of 5 m in range and 20 m in azimuth [33]. The full Sentinel-1 scenes are 250 km in width, in this case much of which is located over North Sea. A subset of the image was processed, approximately $90\text{ km} \times 90\text{ km}$, contained within IWS1 and IWS2.

The nominal repeat cycle of the Sentinel-1 imagery used is 12 days, less than the 35 day repeat cycles of the ERS and ENVISAT satellites. In the period of approximately 12 months, Sentinel-1

acquired more SLC images of the AOI than ENVISAT in its total operational lifetime. This is of great benefit to a DInSAR analysis as more observations generally implies a lower standard deviation of error, as demonstrated for the area of Doncaster in the UK by Novellino et al. (2017) [34]. The C-band (5.555 cm wavelength—5.405 GHz frequency) level-1 images processed were acquired on an ascending geometry; a stack of descending Sentinel-1 imagery were also considered to try and maintain uniformity with the geometries of the ERS and ENVISAT data, however only 26 images covered the full AOI and therefore generated a less reliable result. The ISBAS processing of the Sentinel-1 data followed the approach defined in Sowter et al. (2016) [15].

Coregistration was performed with respect to a master image acquired on 25 January 2016. Multilooking was implemented by a factor of 22 in range and 5 in azimuth which increased pixel size to approximately 90 m in ground range. A dense network of 520 differential interferograms were generated, with restrictions of 250 m on the perpendicular orbital baseline and one year on the temporal baseline, plotted in Figure 4. Comparing against the networks produced from the ERS and ENVISAT analysis (Figure 3) the improved accuracy of Sentinel-1 orbits is evident, designed to operate within a narrow orbital tube radius of 50 m for the majority of its operational lifetime [35]. Consequently, in concurrence with the reduced revisit time and increased number of acquisitions, there is far more redundancy in the network.

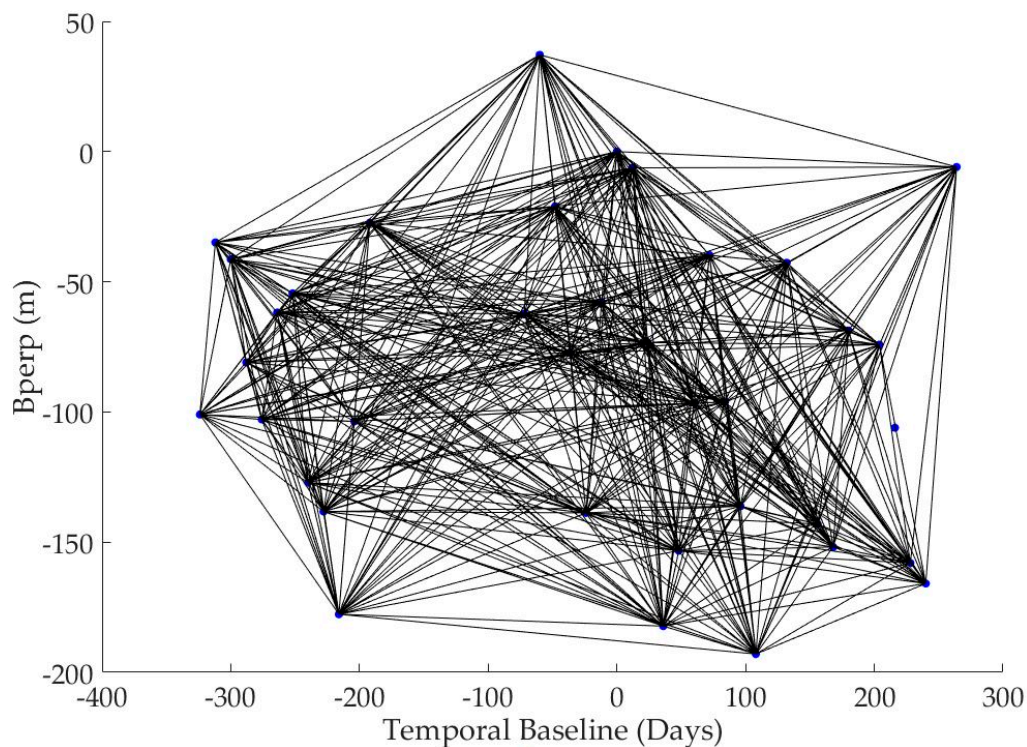


Figure 4. Sentinel-1 Synthetic Aperture Radar (SAR) temporal and perpendicular baselines of image pairs relative to the master acquired on 25 January 2016.

An interferogram threshold of 135 was selected and, following the same approach as for the ERS and ENVISAT processing, the reference point was located in North Shields (55.00° N, -1.46° E), topographic phase was removed using a STRM DEM and SAR orbital parameters, coherent and intermittently coherent pixels were unwrapped to derive linear velocities, standard errors and time-series per pixel which were subsequently projected into the vertical direction.

4. Ground Motion in North East England

4.1. ISBAS Processing Coverage

The analysis covered 99%, 89% and 95% of the land surface area of the full extents processed in the cases of ERS, ENVISAT and Sentinel-1 respectively, providing a broad and complete distribution of velocities over all land cover types (Figure 5). Had velocities been derived for targets where coherence is recurrent in every interferogram, coverage would have only been 7%, 2% and 12% for the respective data sets. Dense coverage was achieved not only in areas of high coherence, but over agricultural land and woodland areas. Standard errors are lowest in urban areas due to increased coherence and consequently more coherent interferograms to derive linear velocities.

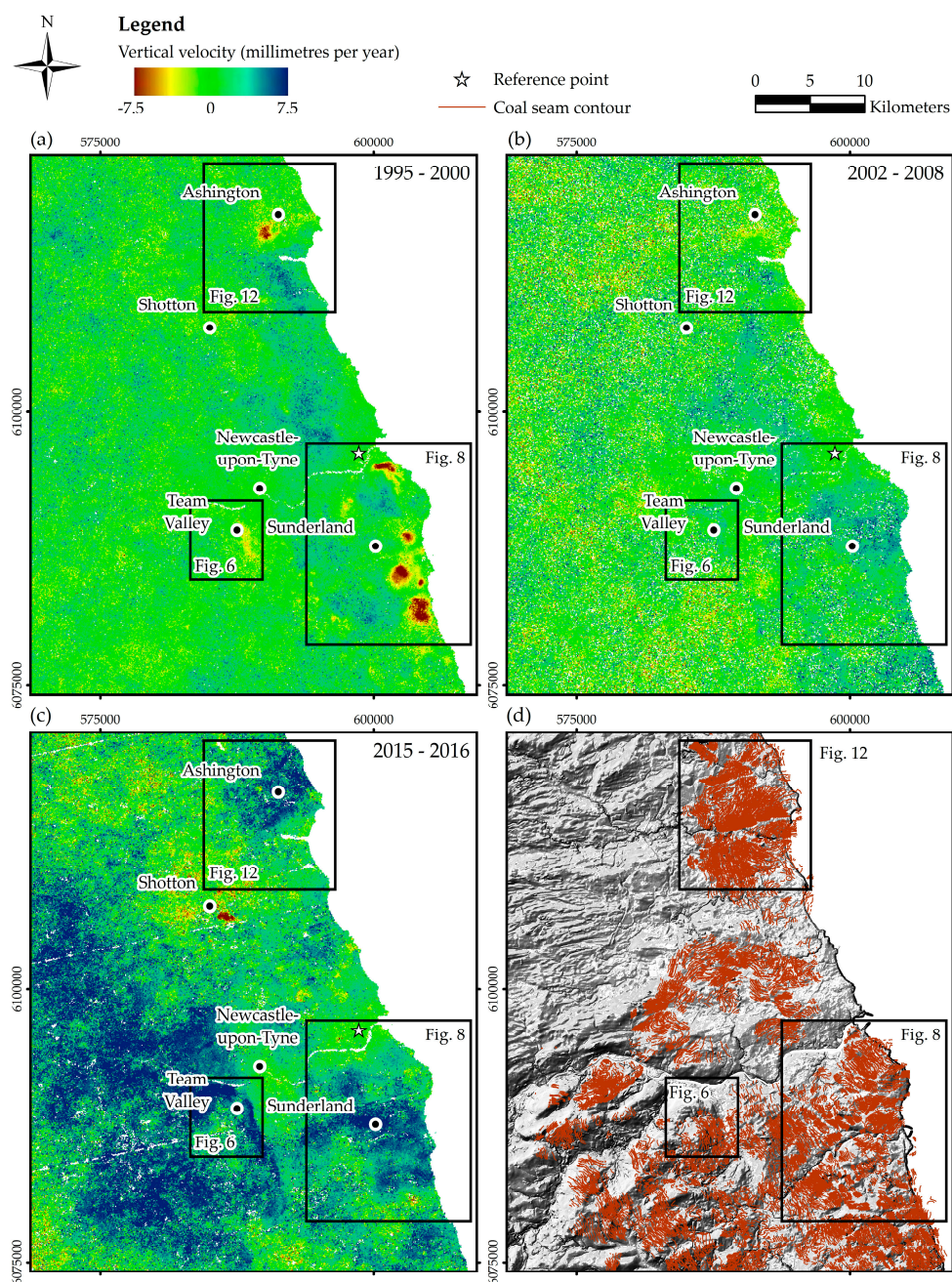


Figure 5. ISBAS average vertical velocities (millimetres per year): (a) ERS (b) ENVISAT (c) Sentinel-1 (d) Coal seam contours and topography.

4.2. Linear Velocities

Several notable areas of localised subsidence were identified along the coastline in the ERS analysis, while uplift occurred in the northern half of the AOI and approximately 5 km inland in the south (Figure 5). Uplift occurs over larger regional areas, while subsidence is localised and of a greater magnitude. There has been a significant change in the spatial patterns of motion between the ERS and ENVISAT data sets; areas of localised subsidence present in the ERS data have stabilised and uplift in the north has reduced in velocity. The results achieved in the ERS and ENVISAT analysis compare well to results produced by FugroNPA using PSI [21]. These were supplied for the TerraFirma Product Interpretation Report: Northumberland (ESRIN/Contract No. 4000101274/10/I-AM) [22] commissioned by the Coal Authority and confirm the findings of a distinct change in velocities between data sets. The Sentinel-1 analysis shows that the trend of regional uplift has strengthened. Uplift occurring around Sunderland during the ENVISAT epoch has increased in velocity, while a large regional pattern of uplift has developed inland in the western half of the AOI.

Table 1 summarizes the statistics of the linear velocities and standard errors. It might be expected, since there are approximately 50% more Sentinel-1 acquisitions than ERS/ENVISAT, that standard errors are lowest for Sentinel-1, which is not the case. However, data acquired over shorter epochs reduces the ability to accurately retrieve the underlying deformation signal. The relatively short time period of the Sentinel-1 analysis (≈ 18 months) is reflected in the amount of noise present in the linear velocities and the standard errors. Atmospheric signal, a prevailing InSAR error source, can be accurately removed via the stacking of numerous acquisitions to retrieve the underlying deformation based upon the assumption that atmospheric delay is random over time. The stratified troposphere is characterized by temporal variations, principally due to precipitation. Interferometric signals, therefore, have a seasonal component which can be aliased by the temporal sampling of SAR acquisitions [36,37]. Furthermore, the TOPS configuration of Sentinel-1 products generates additional difficulties, with respect to stripmap products, and requires a greater amount of acquisitions to accurately sample the atmosphere since constitutive bursts are imaged through different section of the atmosphere [33].

Table 1. A comparison of the statistics of ERS, ENVISAT and Sentinel-1 ISBAS analyses over the Northumberland AOI.

Statistic	ERS SAR	ENVISAT ASAR	Sentinel-1 SAR
Velocity (Millimetres/Year)			
Mean	0.9	0.7	3.5
Minimum	−14.0	−14.5	−16.0
Maximum	10.6	14.6	19.0
Standard Deviation	1.9	2.5	3.4
Standard Error (Millimetres)			
Mean	1.6	2.4	2.2
Minimum	0.5	0.6	0.8
Maximum	4.0	8.0	4.9
Standard Deviation	0.4	0.8	0.7

5. Discussion

As mentioned above, the ground motion results reveal large regional extents of uplift with localized hotspots of subsidence. The following section discusses the link between the observed patterns of ground motion and the geology, history of coal mining and the hydrogeology of the Northumberland region.

5.1. Relationships between Ground Motion and Geology

5.1.1. Bedrock Geology

A number of potential relationships between the velocities and the geology are apparent. However, on the whole, there appears to be no correlation between any of the ERS, ENVISAT or Sentinel-1 velocities and the bedrock geology, with no evidence to indicate that specific geological units are responsible for the observed surface motion.

5.1.2. Superficial Deposits

In general, there is little correlation between any ground motion and the distribution or thickness of superficial deposits, particularly compressible deposits and those with potential for shrink-swell. The exception, however, is in the area of Team Valley, where the land surface changes from subsidence to stability to uplift over the course of the ERS, ENVISAT and Sentinel-1 analyses (Figure 6). Team Valley is a deep buried valley which characterizes the pre-glacial channel of the River Wear. The valley extends downward through Coal Measures to -46 m above ordnance datum and is infilled with an interlensing complex of glacial clays, laminated-clays, silts and sands, overlain by alluvium [38]. Subsidence identified in the ERS data is situated within the deepest parts of the channel, while the glacial till at the margins are stable. Subsidence could be attributed to progressive compaction as the area coincides with an extensive area of industrial development in the Team Valley and Gateshead Metro Centre. Large areas are covered with artificial surfaces sealing the subsurface from rainfall recharge; it is plausible that de-watering of Quarternary sediments in combination with loading, albeit from comparatively light-weight structures, could be significant in creating subsidence.

The ENVISAT data reveals that areas experiencing subsidence in the 1990s, have stabilized, with a small degree of uplift identified further north in the valley. Sentinel-1 velocities indicate this trend has strengthened with strong uplift in the Team Valley. The pumping of mine water within Team Valley could have significant effects on the land surface as a known programme of ground water control is present in this part of the former coalfield.

5.1.3. Geological Structure

When comparing derived velocities to the geological structure, a number of cases emerge for which patterns of motion appear to be associated with major geological faults (Figures 7 and 8). In such cases there is no indication that the faults are directly responsible for the motion, but influence motion by accommodating or constraining it. The constraining of motion appears to be related to both regional patterns of uplift, as well as localised subsidence. Examples of such a relationship in the surrounding areas of Sunderland and Ashington are discussed in more detail in Section 5.4.

5.2. Relationships between Ground Motion and Coal Mining

Subsidence is an inevitable consequence of mining activity [28]. It has been approximated that 4800 million tonnes of coal has been extracted from UK mines, consequently leaving 1000 million cubic metres of voids [39]. Five mines in the AOI were active at some point during the study period; four opencast and one deep mine, Ellington. Ellington was closed in 2005 [40] but there is no spatially correlated subsidence associated with this mine as would be expected since the workings are located under the North Sea (Figure 5). One localized hotspot of deformation is revealed in the Sentinel-1 analysis, corresponding to Shotton opencast coal mine, which was operational throughout the period of Sentinel-1 SAR acquisitions (Figure 5c). A number of potential relationships between ground motion and coal mining were examined including: mine entries; coal seam contours and underground workings.

Within the AOI there are a total 7811 mines entries, the majority of which exist in the Pennine Middle Coal Measures Formation with far fewer located in the Zechstein Formation where Coal Measures are deepest (Figure 2). Areas of subsidence present in the ERS analysis are in proximity

to entries to former collieries, for example at Westoe, Wearmouth, Ryhope in the Sunderland area (Figure 8). However, it is challenging to make correlations with this data since there are many mine entries within the AOI where subsidence is not present.

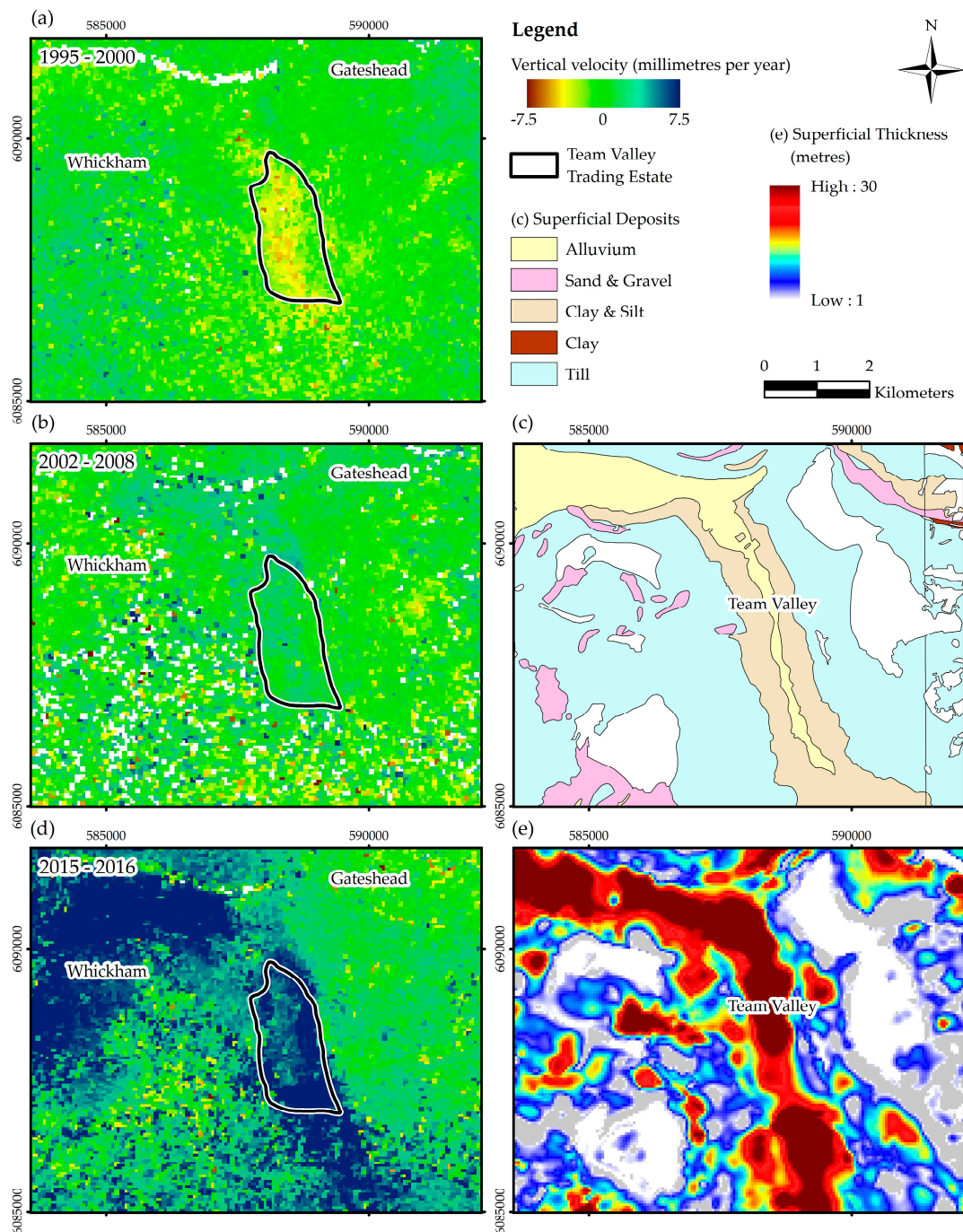


Figure 6. (a) ERS ISBAS vertical velocities (millimetres per year); (b) ENVISAT ISBAS vertical velocities (millimetres per year); (c) Superficial geology; (d) Sentinel-1 ISBAS vertical velocities (millimetres per year); (e) Superficial thickness. ‘Reproduced with the permission of the British Geological Survey ©NERC. All rights Reserved’.

There is a relationship between areas of motion and seam contours at many locations in all three data sets (Figure 5). As faults often delimit Coal Measures it is perceptible that areas of motion are delimited by these boundaries. An example of such a relationship occurs in the surrounding area of Ashington, with evidence to suggest uplift has been caused by former mining activities (Figure 5c,d). The majority of mining and resultant ground motion would have been completed long before the satellite data was acquired, therefore subsidence associated with surface hazards or pillar collapse are localized. No relationships were observed when analysing any ground motion in conjunction with coal seams categorised by depth or working dates.

There is no distinct relationship between underground workings and ground motion in any of the SAR observations. Nonetheless, establishing relationships with these data is challenging because the majority of Coal Measures in the AOI have been worked extensively, at multiple depths by both pillar and stall and total extraction techniques. Coal mine abandonment plans were not a requisite in the United Kingdom until 1859, hence not all mining has been documented. Additionally, old mine plans are often inaccurate due to poor surveying techniques and pillar robbing [41].

5.3. Relationships between Ground Motion and Ground Water Levels

Groundwater rebound is the reasoned cause of regional-scale surface uplift [42,43]. Surface heave phenomena has previously been identified by geodetic levelling [44–46] and radar interferometry [10,13,17,18,20–22,47–51] above a number of abandoned coalfields in different geographies. Deep underground coal extraction requires the pumping of groundwater to maintain safe working conditions within the mine [52]. Systematic pumping ordinarily ceases following the abandonment of underground coal mines and groundwater levels begin to rebound. Monitoring by the Coal Authority in the Durham Coalfield clearly identifies mine water recovery, although part of the coalfield is still controlled by pumping. As the rock matrix reverts back to previously saturated conditions, pore water pressure increases and consequently the rock expands which can produce an expression at the surface [43]. Surface elevation is thought to only represent several percent of any previously identified subsidence during active mining and to occur gradually over a larger area than previous subsidence basins [53].

Broadly, coalfields can become associated with a number of stability and contamination issues following abandonment, due to prominent changes in topography and hydrogeological regime [54]. The rise of mine water and flooding of abandoned workings can have some detrimental consequences including: residual subsidence; the reactivation of existing faults; mine gas migration; slope instability; and influence the geotechnical properties of the ground [55]. Individual coalfields may be subject to some or none of the identified issues. Subsidence and slope instability have not been associated with mine water recovery in British coalfields.

Historical indications demonstrate that there remains a risk of ground instability long after pillar and stall and longwall workings have been abandoned. The delayed onset of motion can be initiated by a number of factors including creep of the overburden, pillar deterioration, collapse of the roof and failure of the floor as a result of seatearth softening. There is potentially no time limit for pillar and stall instability. Furthermore, deeper mine activity can trigger events in shallower, often unrecorded, mines [28]. The risk of surface instability is substantially higher during the transitory phase of groundwater rise, due to the redistribution of stress within the rock matrix. Risk is reduced once a new hydraulic and hydrogeological equilibrium is reached, following saturation to historical levels [53]. In most cases in the UK, the pre mining hydrogeology is not known but it is assumed rebound is to the pre-mining levels.

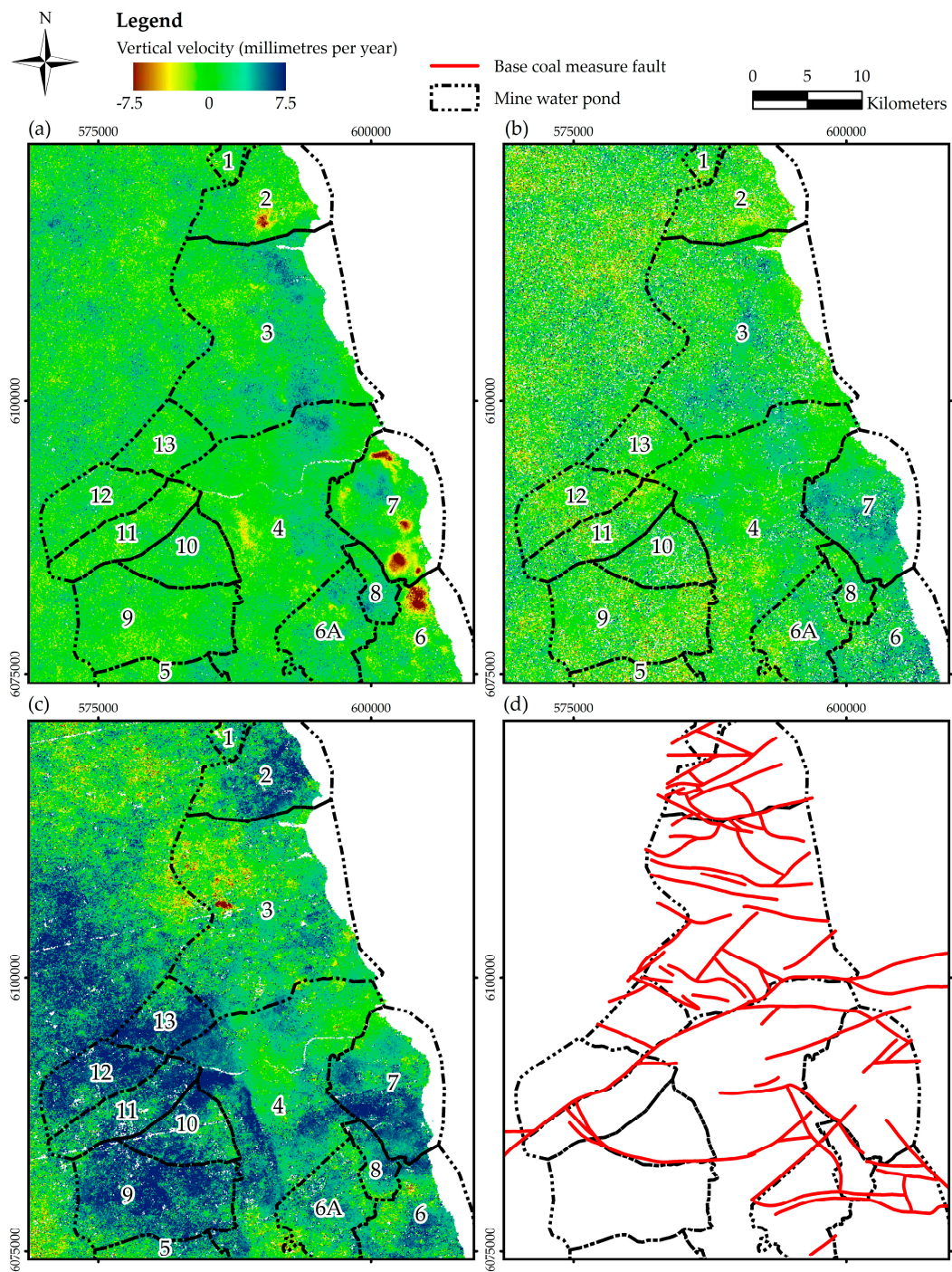


Figure 7. ISBAS vertical velocities (millimetres per year) with minewater ponds overlaid: (a) ERS (b) ENVISAT (c) Sentinel-1; (d) Minewater ponds and base coal measure faults.

Rising groundwater creates a complex subsurface environment. Water ingress into former workings does provide some support pressure inside the mined voids. Ingress is aided by the disturbance, fracturing and disintegration of roof layers and overlying rock mass during mine operation, consequently permeability and porosity are increased [44,53]. However, Coal Measures rocks can lose significant strength on water saturation as a result of mineralogical changes to the clays within the rock matrix, stress corrosion or water absorption [56] and has been associated with pillar failure in within former mine workings [57,58]. Additionally, the chance of failure can increase as the saturation of soil within the overburden increases vertical stress on the strata [44].

Fault reactivation is a further consequence of rising minewater [59]. The incidence of fluids within fault zones have been shown to induce seismicity [60,61]. An increase in fluid pore pressure reduces fault plane shear strength. Reactivation can occur if the reduction in shear strength counterpoises the normal stress acting across the fault [62]. Since Coal Measures sandstones in the Durham coalfield possess very little intergranular permeability, groundwater movement is principally through fractures in the sandstone [63]. Mining has extensively disrupted and complicated the hydrogeology and increased permeability. Rising groundwater levels have previously been associated with incidences of fault reactivation in the Durham Coalfield [64].

In the area of study, rather than abruptly turn off all pumps in the abandoned coalfield, the Coal Authority have continued to pump minewater from a number of sites as part of a strategy to control the rise of water levels. Since mining was operational there has been a reduction in the number of operational pumping sites and, consequently, groundwater levels in some eastern parts of the coalfield have recovered to levels close to the base of the Permian rocks. However, in more recent years (≈ 10 years) the number of operational sites may have increased; active management of groundwater is important so to prevent potential contamination of important aquifers within these rocks. For example, it is known that approximately 4 km south of the study area that groundwater pumping began at a new facility at the former Horden Colliery in July 2004 [65].

Newcastle University, the Environment Agency and Coal Authority have conducted previous work over the AOI to better understand the hydrogeological regime and the effects of altering pumping regimes following mine closure [21,22,66–70]. Modelling studies have previously attempted to predict minewater rebound. The coalfield is divided into “ponds”, considered single hydraulic units which homogeneously rise or fall principally depending on ground water pumping. Some of these ponds are connected (hydraulically) to other ponds, whilst some are not. Some of the connections between ponds are unclear and can change over time. The connections can be at different depths, hence some ponds can become joined or isolated with groundwater level changes. From the information made available, the location of these ponds appears to be controlled in many cases by the geological structure, specifically by geological faults (Figure 7). The ponds, which cover a greater area than the AOI, are thought to refill in increasing numerical order defined in Figure 7.

The filling of ponds in numerical order is largely supported by the Sentinel-1 data (Figure 7c). The rates of uplift have increased over time in ponds 4–13. Pond “2” does not support this premise, experiencing strong uplift in the Sentinel-1 analysis; however, it does support the proposition of mine water ponds moving homogeneously, with the extents of motion defined by the pond. One potential contributory factor could be the accuracy of the divisions between ponds. For example, pond “4”, which extends from Newcastle to Durham, is considered to be sub-divided into further blocks. There are three major pumping stations within this block, the relationships between these pumping stations are complex and not well understood. Surface motion in the Sentinel-1 data supports the premise that pond “4” might be further divided into moving blocks. The results show InSAR can provide new information to help determine these boundaries.

For further scrutiny, comparisons are made in the following section between groundwater levels and ground motion at specific monitoring sites.

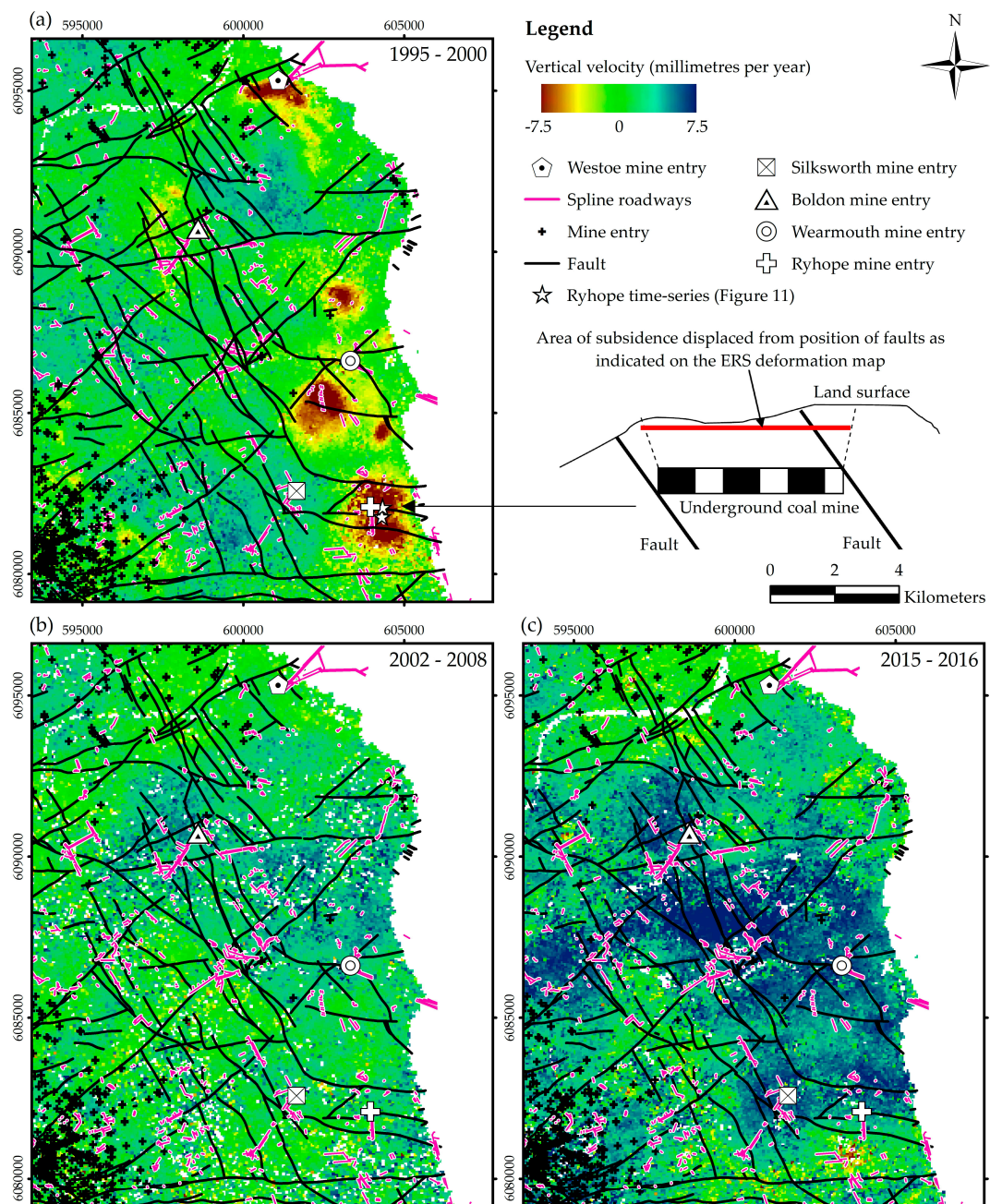


Figure 8. ISBAS vertical velocities (millimetres per year) in the surround area of Sunderland with faults, mine entries and spline roadways overlaid: (a) ERS (b) ENVISAT (c) Sentinel-1.

5.4. Case Studies

5.4.1. Sunderland

It was not until 1788, as exploration methods reached greater depths, that serious prospecting began in the Durham coastal limestone. Wearmouth colliery struck coal in 1834 at 480 m below sea level, making it the deepest coal mine in the world at the time. The Wearmouth Coal Company subsequently undermined most of the Sunderland area and in 1912 were calculating how much they could extract from underneath churches, hospitals, schools and St George’s square before subsidence claims offset profits. In 1958, Wearmouth was identified as a ‘super pit’ from which 500 million tonnes of coal were extracted from under the North Sea, until the colliery was closed in 1993 [71]. Other

smaller mines, just outside Sunderland, were later founded such as Ryhope (1859–1966), Boldon (1869–1982), Silksworth (1873–1971) and Westoe (1909–1993) [40].

The ERS analysis indicates a complex environment, identifying hotspots of deformation as well as areas of uplift (Figure 8). The most prominent subsidence identified in the ERS analysis spatially correlates to the collieries at Westoe, Wearmouth and Ryhope. Westoe and Wearmouth collieries shut in 1993, shortly before the period of ERS imagery (1995–2000), while, curiously, Ryhope closed in 1966, nearly four decades before the ERS analysis. The later ENVISAT data indicates a reversal in the velocities, with uplift present in some areas where subsidence was previously identified. By 2015–2016, the Sentinel-1 data reveal that uplift has both strengthened and spread out over a greater area.

Neighbouring time-series and linear velocities from ENVISAT and Sentinel-1 data correlate with rising groundwater monitored at Westoe, Wearmouth and Boldon, as shown in Figures 9 and 10. The ENVISAT time series are the noisiest due to the reduced amount of data acquisitions. There is a lack of correlation at Westoe and Wearmouth during the ERS time period where localised subsidence is identified; no groundwater data is available at Ryhope. From data provided by the Coal Authority and Harrison et al. (1989) [72] it is known that groundwater levels were rising sharply, through former workings, at Westoe and Wearmouth in the 1990s (Figures 9 and 10). Levels rose approximately 240 m at Westoe during this decade and approximately 315 m at Wearmouth between 1989 and 2002. It would be expected that if there is a collapse, for example caused by pillar failure, that strong localised subsidence will dominate the deformation signal over any moderate uplift caused by a rise in groundwater.

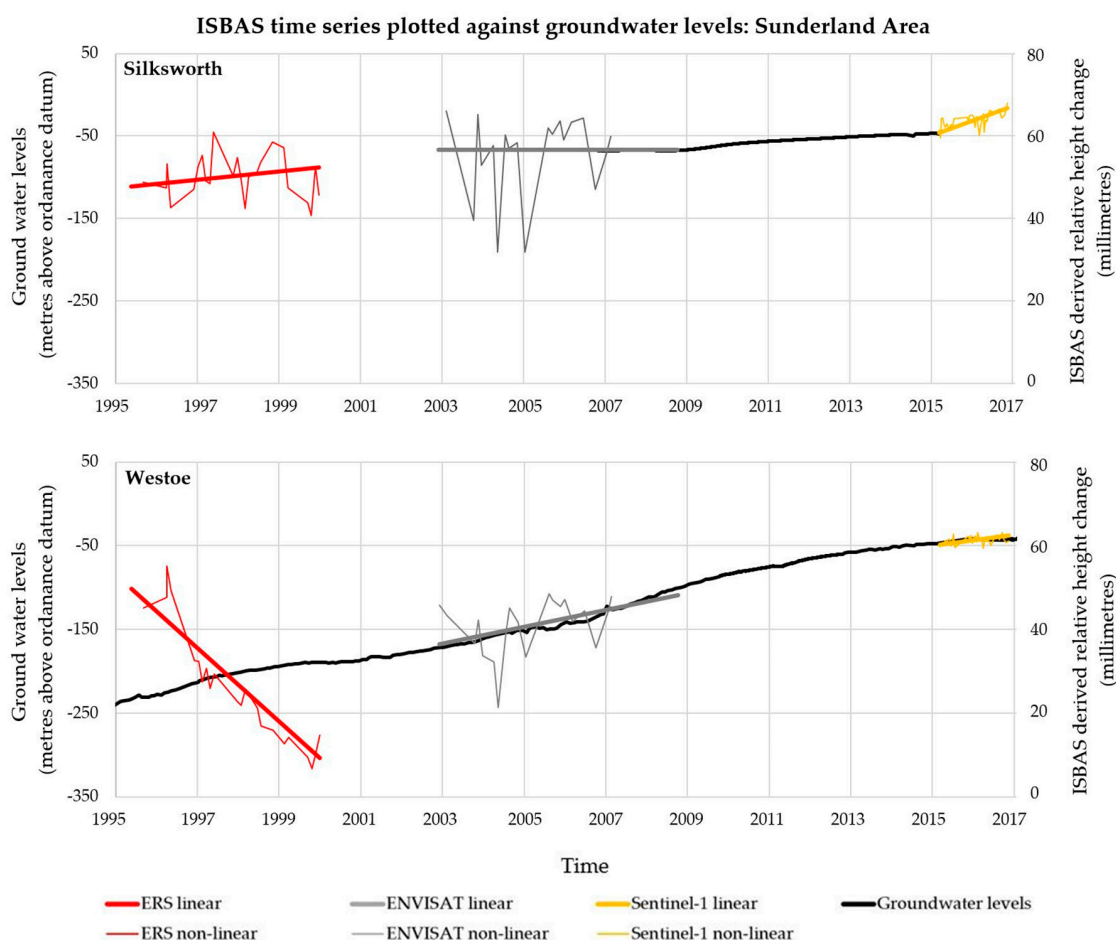


Figure 9. Groundwater levels plotted against neighbouring ISBAS time-series and linear velocities (derived separately) at Silksworth and Westoe, the locations of which are marked on Figure 8.

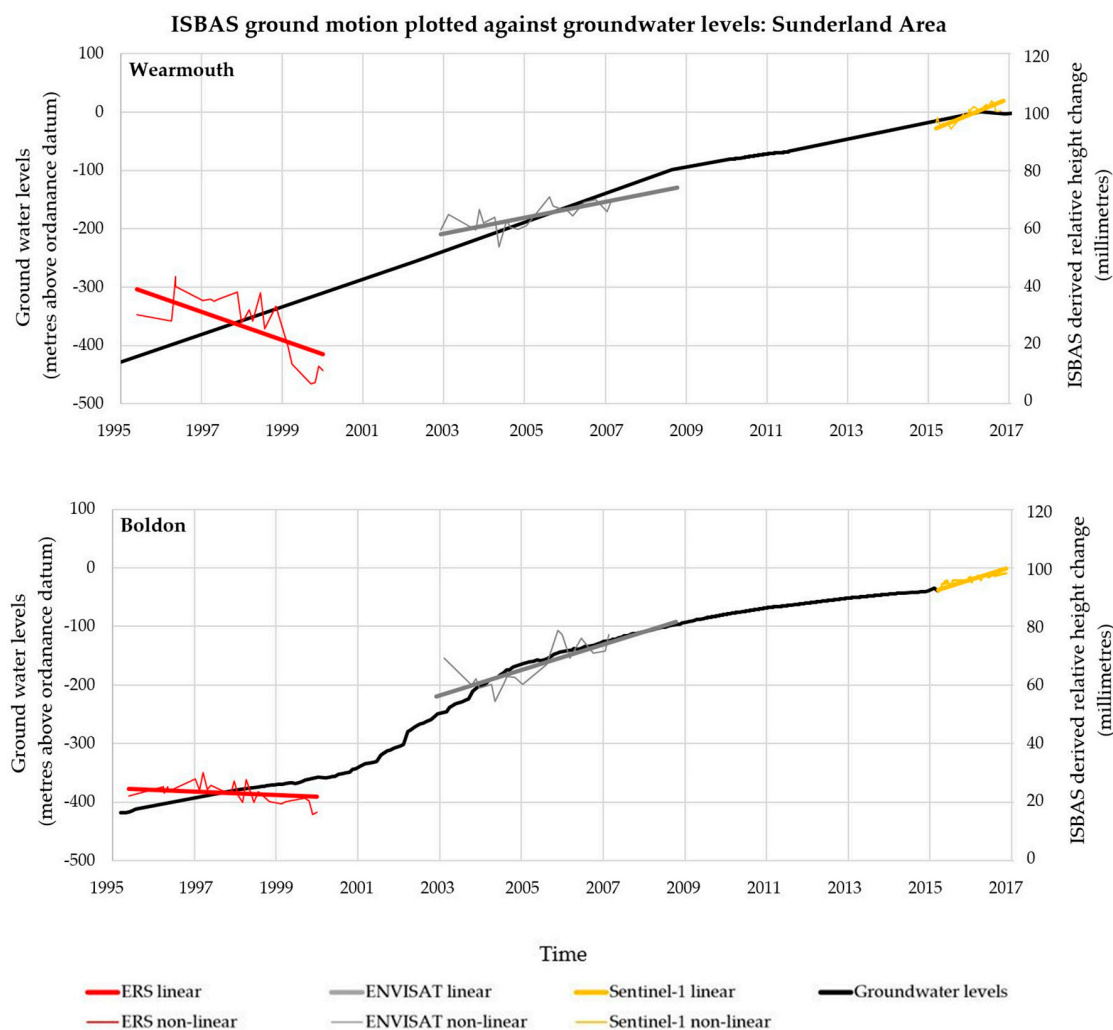


Figure 10. Groundwater levels plotted against neighbouring ISBAS time-series and linear velocities (derived separately) at Wearmouth and Boldon, the locations of which are marked on Figure 8.

Between 1998 and 1999, 20 earth tremors in the Ryhope area were reported over a 12 month period, with local residents from 14 different streets reporting vibrations [19]. Following an inconclusive investigation into the cause, four possible rationale were put forward: neotectonic processes; collapse of sub-surface cavities in the Magnesian limestone that overlies the Coal Measures; residual mining subsidence or rising mine water; the displacement of mine gases along the fault zone [73]. ERS time-series at Ryhope indicate an acceleration in the subsidence from July 1998, shortly before the period when the tremors were felt as shown in Figure 11.

A geological justification for the apparent offset of subsidence to faults thought to be controlling the motion is given in Figure 8. Subsidence at Ryhope, for example, appears bound by two east-west trending faults, albeit displaced slightly to the south with respect to the faults. The apparent offset of the subsidence to the bounding faults is likely due to the dip of the faults, with the assumed southward dipping fault planes intersecting the rockhead (or ground surface) at a more northerly point than that at which it confines the coal seam being mined at depth.

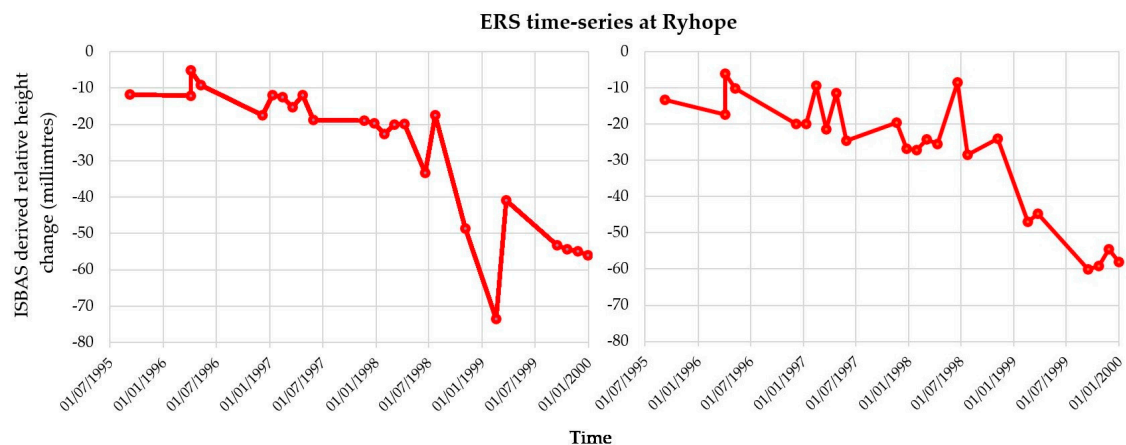


Figure 11. Selected ERS ISBAS time-series in the Ryhope subsidence depression, marked on Figure 8.

5.4.2. Ashington

The Ashington area has been extensively mined since the Bothal mining shaft was sunk in 1867, situated just over 3 km to the west of the Ashington shafts. Collieries quickly developed in the Ashington area remaining active until the rapid decline of the UK coal industry in the 1970s and 1980s, including: Ashington (1867–1986); Ellington (1905–2005); Woodhorn (1894–1981); Bates (1932–1986) and Bedlington (1838–1971) [40].

The land surface around Ashington is highly dynamic, where patterns of motion change significantly over the sequence of satellite acquisitions (Figure 12). During the ERS period of observations a localised hotspot of deformation spatially correlates with Ashington colliery, where seven mine entry shafts are connected to areas of underground workings via spline roadways. Groundwater levels at Ashington rose 30 m through former workings during this period of collapse. Further south, a large area of uplift is present, bound to the north by the ENE to WSW Stakeford fault, where differential motion is present over the fault. The southern tip of this area of uplift also appears delimited by faults. Subsidence occurring over Ashington has reduced during the ENVISAT period of observations, appearing less spatially correlated and distinct. To the south uplift is still present but the size and velocity has reduced. The Sentinel-1 analysis indicates the region to the north of the Stakeford fault, is homogeneously uplifting. Similarly to the temporal evolution of motion occurring around Sunderland, uplift in the Sentinel-1 analysis occurs over a broader area than previously identified subsidence. Motion is constrained by faults, most notably to the south by the Stakeford fault, and uplift correlates strongly with mined Coal Measures. South of the Stakeford fault, uplift has ceased, with the ground surface reaching approximate equilibrium.

Neighbouring time-series and linear velocities were compared against groundwater levels at former collieries to the south of the Stakeford fault, at Bates and Bedlington, and to the north, at Ellington and Woodhorn (Figure 13). These areas belong to separate mining blocks which the Stakeford fault delimits; there are no known connections through this boundary. At Bates and Bedlington, rising groundwater during the 1990s correlates with upward surface motion, a relationship which continues as groundwater levels return to the level of the ordnance datum in the early 2000s and the surface reaches equilibrium.

Subsidence had previously been identified at Bedlington, which occurred between 1990 and 1994 and produced a subsidence trough with a maximum settlement of 260 mm at the centre [74]. This resulted in the demolishing of Cloverdale terrace due to subsidence damage. Borehole investigations took place in 1994 and 1997; less than half of those drilled that were expected to encounter coal did. The boreholes identified much evidence of roof collapse and suggested that the pillars had deteriorated badly with time or had been reworked on retreat. It is thought areal subsidence was caused by small scale pillar failure, here, and at a similar nearby case study [75]. Mining at Bedlington ceased in 1971,

long before the identified motion. From the groundwater levels provided by the Coal Authority and those published in Harrison et al. (1989) [72] it is known that groundwater levels rose approximately 150 m during the course of the 1990s; uplift is present during the ERS analysis in the latter half of the 1990s (Figure 12a).

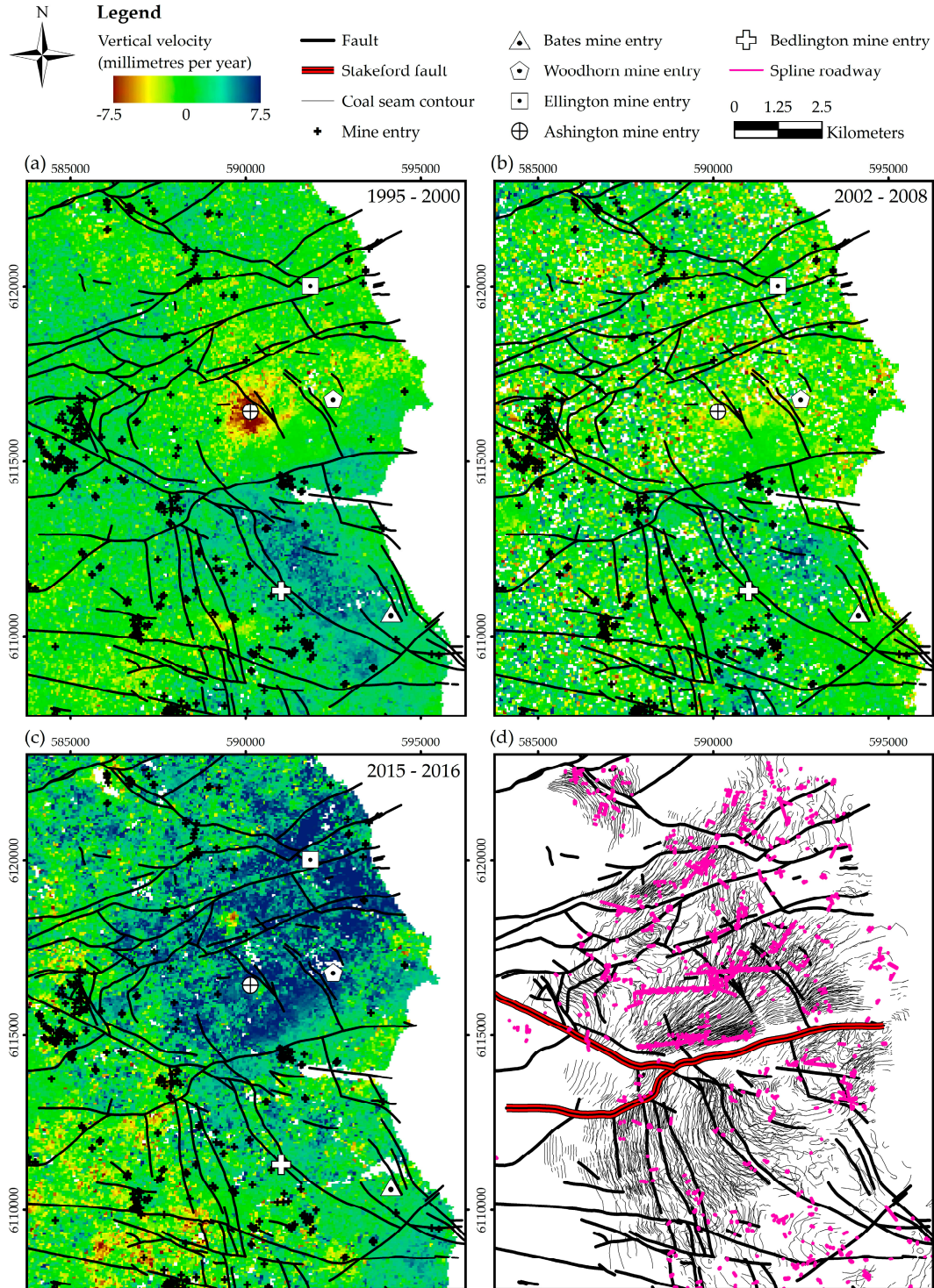


Figure 12. ISBAS vertical velocities (millimetres per year) in the surrounding area of Ashington with faults and mine entries overlaid: (a) ERS; (b) ENVISAT; (c) Sentinel-1; (d) Coal seam contours, faults and spline roadways.

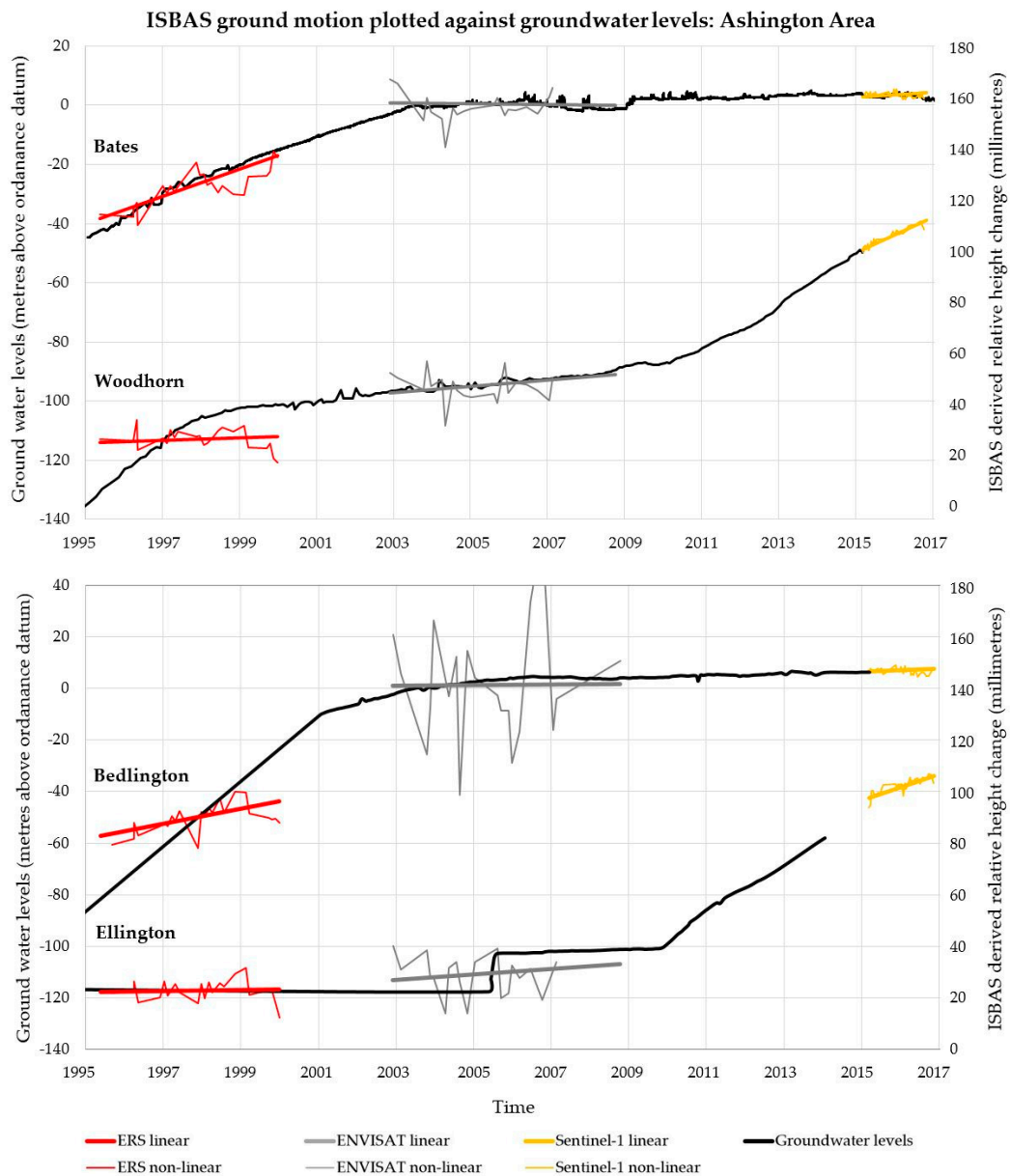


Figure 13. Groundwater levels plotted against neighbouring ISBAS time-series and linear velocities (derived separately) at Bates, Woodhorn, Bedlington and Ellington, the locations of which are marked on Figure 12.

At Ellington and Woodhorn the relationship between rising groundwater and surface velocities continues as strong uplift is identified in the Sentinel-1 data (Figure 13). The rate of groundwater recovery increases after approximately 2010, which is reflected in surface uplift in the Sentinel-1 analysis. Although groundwater data at these locations do not continue over the period of Sentinel-1 observations, on the assumption that levels continue to rebound as they have over the previous five years, a correlation between rising groundwater and the surface is present. Relative stability is identified at Ellington and Woodhorn during the ERS and ENVISAT observations.

Curiously, groundwater levels were rising at Woodhorn during the ERS time period, however the surface was relatively stable. It is, therefore, too simplistic to suggest surface uplift will occur in the surrounding locations where groundwater levels are rising. The volume of void space present in the coalfield could be one plausible explanation for the where there is no correlation. A rise in groundwater

might only influence the surface when it is confined within the mine, i.e., once the void space in the mine has been filled, groundwater has reached the roof and is rising through the overburden. The depth to groundwater could also be a consideration; for example, it might be expected that a rise of 10 m in groundwater has less of an impact on the surface at a depth of -400 m AOD, than it will at -30 m AOD. Further research might also consider the potential effects aquifer groundwater levels could have on surface motion.

It should be noted that making a direct correlation between groundwater levels and deformation time-series here is challenging; at the majority of the sites investigated in this study groundwater measurements do not cover the epoch of InSAR acquisitions with sufficient frequency, particularly for ERS and Sentinel-1. For example, at Bedlington there is over a ten year gap (1989 and 2001) between groundwater measurements and only three out of eight sites investigated cover the entire Sentinel-1 period. At Bates, there is sufficient data to cover the all three InSAR acquisition periods; surface deformation is plotted against groundwater levels for the ERS time period (1995–2000) in Figure 14. Here, the coefficient of determination demonstrates that $\approx 65\%$ of surface deformation is predicted by a rise in groundwater and that under these geological conditions a rise of 10m in groundwater induces surface uplift of 8mm.

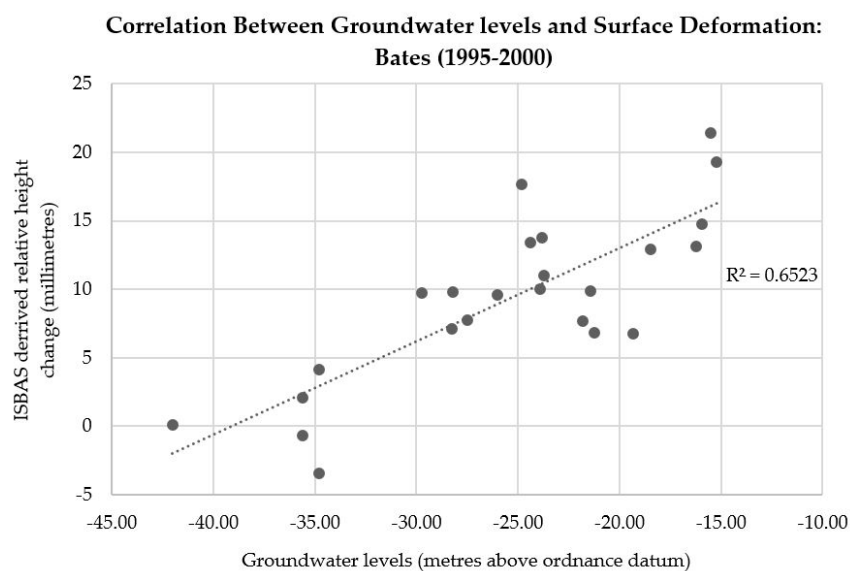


Figure 14. A linear regression between groundwater levels and surface deformation at Bates (Figure 12) for the ERS time period.

6. Conclusions

This study was undertaken to better delineate ground motion in the Northumberland and Durham coalfield over a 20-year time period. The ISBAS algorithm employed provides ground motion measurements that are consistent with those previously obtained using persistent scatterers interferometry on ERS and ENVISAT data, although the ISBAS approach provides a more complete spatial coverage of measurements.

The results show that unexpected amounts of ground motion are present in areas of former mining, occurring long after coal extraction has ceased. Localized subsidence has been identified over former mines during the late 1990s, with subsidence hotspots identified in proximity to former collieries. Regional patterns of uplift are present in all three data sets occurring over a larger spatial extent than any previously observed subsidence, often correlating with mined Coal Measures. An association was ascertained in proximity to former collieries that rising groundwater can be significant in influencing surface motion. The degree of influence rising mine water has on the surface requires further scrutiny in different geographies.

This is important for the post-mining environment, and demonstrates that InSAR can provide a cost-effective regional outlook for making informed decisions to mitigate detrimental environmental effects in abandoned coalfields. The data shows how multifaceted post-closure ground deformation regimes can be with a complex interaction between the local stress field, regional groundwater recovery and accommodation and delimiting of motion by faults.

Acknowledgments: The work conducted here has been funded by the GeoEnergy Research Centre (GERC) and Geomatic Ventures Limited. The authors would like to acknowledge ESA for the provision of ERS, ENVISAT and Sentinel-1 SAR data; the Coal Authority for mining and hydrogeological data; the British Geological Survey for geological data and Chris Satterley for his role in the co-ordination of the study. Alessandro Novellino, Luke Bateson and Francesca Cigna publish with the permission of the Executive Director of BGS.

Author Contributions: David Gee, Andrew Sowter, Alessandro Novellino, Luke Bateson, Stephen Grebby Stuart Marsh and Chris Satterley conceived and designed the experiments; David Gee performed the experiments; all the authors analysed the data; David Gee, Luke Bateson and Stephen Grebby wrote the paper.

Conflicts of Interest: The authors declare no conflict of interest.

Appendix A

ERS SAR image dates and perpendicular baselines B_{\perp} (m) in reference to the master image on 20 November 1997.

Image Date	B_{\perp} (m)	Image Date	B_{\perp} (m)
20 November 1997	0	29 January 1998	−431
24 May 1995	−610	5 March 1998	−943
7 September 1995	−1361	9 April 1998	−674
3 April 1996	−634	18 June 1998	302
4 April 1996	−689	23 July 1998	−852
8 May 1996	133	5 November 1998	449
9 May 1996	58	18 February 1999	606
9 January 1997	−483	25 March 1999	−790
13 February 1997	−821	16 September 1999	−727
20 March 1997	−470	21 October 1999	−639
24 April 1997	−870	25 November 1999	−240
29 May 1997	−649	30 December 1999	−172
25 December 1997	−499		

Appendix B

ENVISAT ASAR image dates and perpendicular baselines B_{\perp} (m) in reference to the master image on 11 January 2005.

Image Date	B_{\perp} (m)	Image Date	B_{\perp} (m)
11 January 2005	0	9 August 2005	627
3 December 2002	1050	13 September 2005	437
11 February 2003	500	22 November 2005	991
14 October 2003	1336	27 December 2005	1023
18 November 2003	−179	7 March 2006	850
23 December 2003	762	20 June 2006	744
6 April 2004	1446	3 October 2006	−33
11 May 2004	179	16 January 2007	1284
20 July 2004	857	20 February 2007	741
24 August 2004	759	7 October 2008	629
2 November 2004	794		

Appendix C

Sentinel-1 IW SAR image dates and perpendicular baselines B_{\perp} (m) at scene centre in reference to the master image on 25 January 2006.

Image Date	B_{\perp} (m)	Image Date	B_{\perp} (m)
25 January 2016	0	13 January 2016	−58
7 March 2015	−101	6 February 2016	−6
19 March 2015	−35	18 February 2016	−73
31 March 2015	−41	1 March 2016	−182
12 April 2015	−81	13 March 2016	−153
24 April 2015	−103	25 March 2016	−97
6 May 2015	−62	6 April 2016	−40
18 May 2015	−55	18 April 2016	−96
30 May 2015	−127	30 April 2016	−136
11 June 2015	−138	12 May 2016	−193
23 June 2015	−178	5 June 2016	−43
5 July 2015	−104	29 June 2016	−143
17 July 2015	−27	11 July 2016	−152
14 November 2015	−62	23 July 2016	−69
26 November 2015	37	16 August 2016	−74
8 December 2015	−21	9 September 2016	−158
20 December 2015	−77	21 September 2016	−166
1 January 2016	−139	15 October 2016	−6

References

- Rosen, P.A.; Hensley, S.; Joughin, I.R.; Li, F.K.; Madsen, S.N.; Rodriguez, E.; Goldstein, R.M. Synthetic aperture radar interferometry. *Proc. IEEE* **2000**, *88*, 333–382. [[CrossRef](#)]
- Massonnet, D.; Feigl, K.L. Radar interferometry and its application to changes in the Earth's surface. *Rev. Geophys.* **1998**, *36*, 441–500. [[CrossRef](#)]
- Hooper, A.; Bekaert, D.; Spaans, K.; Arkan, M. Recent advances in SAR interferometry time series analysis for measuring crustal deformation. *Tectonophysics* **2012**, *514*, 1–3. [[CrossRef](#)]
- Colesanti, C.; Mouelic, S.L.; Bennani, M.; Raucoules, D.; Carnec, C.; Ferretti, A. Detection of mining related ground instabilities using the Permanent Scatterers technique—A case study in the east of France. *Int. J. Remote Sens.* **2005**, *26*, 201–207. [[CrossRef](#)]
- Herrera, G.; Tomás, R.; López-Sánchez, J.M.; Delgado, J.; Mallorqui, J.J.; Duque, S.; Mulas, J. Advanced DInSAR analysis on mining areas: La Union case study (Murcia, SE Spain). *Eng. Geol.* **2007**, *90*, 148–159. [[CrossRef](#)]
- Du, Z.; Ge, L.; Li, X.; Ng, A.H. Subsidence monitoring over the Southern Coalfield, Australia using both L-Band and C-Band SAR time series analysis. *Remote Sens.* **2016**, *8*, 543. [[CrossRef](#)]
- Yang, Z.; Li, Z.; Zhu, J.; Yi, H.; Hu, J.; Feng, G. Deriving dynamic subsidence of coal mining areas using InSAR and logistic model. *Remote Sens.* **2017**, *9*, 125. [[CrossRef](#)]
- Kratzsch, H. *Mining Subsidence Engineering*; Springer: Berlin/Heidelberg, Germany, 1983.
- Peng, S.S.; Ma, W.; Zhong, W. *Surface Subsidence Engineering*; Society for Mining, Metallurgy, and Exploration: Littleton, CO, USA, 1992.
- Sowter, A.; Bateson, L.; Strange, P.; Ambrose, K.; Syafiudin, M.F. DInSAR estimation of land motion using intermittent coherence with application to the South Derbyshire and Leicestershire coalfields. *Remote Sens. Lett.* **2013**, *4*, 979–987. [[CrossRef](#)]
- Zebker, H.A.; Villasenor, J. Decorrelation in interferometric radar echoes. *IEEE Trans. Geosci. Remote Sens.* **1992**, *30*, 950–959. [[CrossRef](#)]
- Ferretti, A.; Colesanti, C.; Perissin, D.; Prati, C.; Rocca, F. Evaluating the effect of the observation time on the distribution of SAR permanent scatterers. In Proceedings of the FRINGE 2003 Workshop, Frascati, Italy, 1–5 December 2003; pp. 1–5.

13. Cigna, F.; Sowter, A. The relationship between intermittent coherence and precision of ISBAS InSAR ground motion velocities: ERS-1/2 case studies in the UK. *Remote Sens. Environ.* **2017**. [[CrossRef](#)]
14. Berardino, P.; Fornaro, G.; Lanari, R.; Sansosti, E. A new algorithm for surface deformation monitoring based on small baseline differential SAR interferograms. *IEEE Trans. Geosci. Remote Sens.* **2002**, *40*, 2375–2383. [[CrossRef](#)]
15. Sowter, A.; Amat, M.B.; Cigna, F.; Marsh, S.; Athab, A.; Alshammari, L. Mexico City land subsidence in 2014–2015 with Sentinel-1 IW TOPS: Results using the Intermittent SBAS (ISBAS) technique. *Int. J. Appl. Earth Obs. Geoinf.* **2016**, *52*, 230–242. [[CrossRef](#)]
16. Gee, D.; Sowter, A.; Novellino, A.; Marsh, S.; Gluyas, J. Monitoring land motion due to natural gas extraction: Validation of the Intermittent SBAS (ISBAS) DInSAR algorithm over gas fields of North Holland, the Netherlands. *Mar. Pet. Geol.* **2016**, *77*, 1338–1354. [[CrossRef](#)]
17. Novellino, A.; Athab, A.D.; bin Che Amat, M.A.; Syafiudin, M.F.; Sowter, A.; Marsh, S.; Cigna, F.; Bateson, L. *Intermittent SBAS Ground Motion Analysis in Low Seismicity Areas: Case Studies in the Lancashire and Staffordshire Coalfields, UK, Seismology from SPACE: Geodetic Observations and Early Warning of Earthquakes*; Royal Astronomical Society, Burlington House: London, UK, 2014.
18. Bateson, L.; Cigna, F.; Boon, D.; Sowter, A. The application of the Intermittent SBAS (ISBAS) InSAR method to the South Wales Coalfield, UK. *Int. J. Appl. Earth Obs. Geoinf.* **2015**, *34*, 249–257. [[CrossRef](#)]
19. Donnelly, L.J. A review of coal mining induced fault reactivation in Great Britain. *Q. J. Eng. Geol. Hydrogeol.* **2006**, *39*, 5–50. [[CrossRef](#)]
20. Culshaw, M.G.; Tragheim, D.; Bateson, L.; Donnelly, L.J. Measurement of ground movements in Stoke-on-Trent (UK) using radar interferometry. In Proceedings of the 10th Congress of the International Association for Engineering Geology and the Environment, IAEG2006, Nottingham, UK, 6–10 September 2006; Geological Society: London, UK, 2006; pp. 1–10.
21. Banton, C.; Bateson, L.; McCormack, H.; Holley, R.; Watson, I.; Burren, R.; Lawrence, D.; Cigna, F. Monitoring post-closure large scale surface deformation in mining areas. In Proceedings of the Mine Closure 2013, Eighth International Conference on Mine Closure 2013, Australian Centre for Geomechanics, Perth Eden Project, Cornwall, UK, 18–20 September 2013.
22. Bateson, L.; Lawrence, D. TerraFirma Product: Interpretation Report. V1. 1: Northumberland. Available online: <http://nora.nerc.ac.uk/21035/1/OR12054.pdf> (accessed on 8 September 2017).
23. Copernicus Land Monitoring Service. Available online: <http://land.copernicus.eu/pan-european/corine-land-cover/clc-2012/view> (accessed on 15 May 2017).
24. Clarke, S.M. *The Geology of NY76NW (S), Cawfields, Northumberland*; British Geological Survey Open Report, OR/07/034; British Geological Survey: Nottingham, UK, 2007; p. 28.
25. Stone, P.; Millward, D.; Young, B.; Merritt, J.W.; Clarke, S.M.; McCormack, M.; Lawrence, D.J.D. *British Regional Geology: Northern England*, 5th ed.; British Geological Survey: Nottingham, UK, 2010.
26. Lawley, R.; Garcia-Bajo, M. *The National Superficial Deposit Thickness Model (Version 5)*; British Geological Survey Internal Report, OR/09/049; British Geological Survey: Nottingham, UK, 2009; p. 18.
27. Smailes, A.E. The development of the Northumberland and Durham coalfield. *Scott. Geogr. Mag.* **1935**, *51*, 201–214. [[CrossRef](#)]
28. Clarke, B.G.; Welford, M.; Hughes, D.B. The threat of abandoned mines on the stability of urban areas. In Proceedings of the 10th Congress of the International Association for Engineering Geology and the Environment, IAEG2006, Nottingham, UK, 6–10 September 2006; Geological Society: London, UK, 2006.
29. European Space Agency: SAR Image Mode. Available online: <https://earth.esa.int/web/guest/missions/esa-operational-eo-missions/ers/instruments/sar/design> (accessed on 15 May 2017).
30. Cigna, F.; Rawlins, B.G.; Jordan, C.J.; Sowter, A.; Evans, C. Intermittent Small Baseline Subset (ISBAS) InSAR of rural and vegetated terrain: A new method to monitor land motion applied to peatlands in Wales, UK. In Proceedings of the EGU General Assembly, Vienna, Austria, 27 April–2 May 2014.
31. Farr, T.G.; Rosen, P.A.; Caro, E.; Crippen, R.; Duren, R.; Hensley, S.; Kobrick, M.; Paller, M.; Rodriguez, E.; Roth, L.; et al. The shuttle radar topography mission. *Rev. Geophys.* **2007**, *45*. [[CrossRef](#)]
32. Chen, C.W.; Zebker, H.A. Two-dimensional phase unwrapping with use of statistical models for cost functions in nonlinear optimization. *J. Opt. Soc. Am. A Opt. Image Sci. Vis.* **2001**, *18*, 338–351. [[CrossRef](#)] [[PubMed](#)]

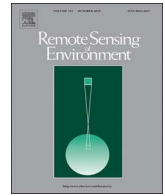
33. European Space Agency: Interferometric Wide Swath. Available online: <https://sentinel.esa.int/web/sentinel/user-guides/sentinel-1-sar/acquisition-modes/interferometric-wide-swath> (accessed on 15 May 2017).
34. Novellino, A.; Cigna, F.; Brahmi, M.; Sowter, A.; Bateson, L.; Marsh, S. Assessing the feasibility of a national InSAR ground deformation map of Great Britain with Sentinel-1. *Geosciences* **2017**, *7*, 19. [[CrossRef](#)]
35. Davidson, G.; Mantle, V.; Rabus, B.; Williams, D.; Geudtner, D. Implementation of TOPS mode on RADARSAT-2 in support of the Sentinel-1 mission. In Proceedings of the Living Planet Symposium, Edinburgh, UK, 9–13 September 2013; pp. 1–22.
36. Jolivet, R.; Grandin, R.; Lasserre, C.; Doin, M.P.; Peltzer, G. Systematic InSAR tropospheric phase delay corrections from global meteorological reanalysis data. *Geophys. Res. Lett.* **2011**, *38*. [[CrossRef](#)]
37. González, P.J.; Fernandez, J. Error estimation in multitemporal InSAR deformation time series, with application to Lanzarote, Canary Islands. *J. Geophys. Res. Solid Earth* **2011**, *116*. [[CrossRef](#)]
38. Mills, D.A.; Holliday, D.W. *Geology of the District around Newcastle upon Tyne, Gateshead and Consett: Memoir for 1:50,000 Geological Sheet 20 (England and Wales)*; British Geological Survey: Nottingham, UK, 1998; p. 20.
39. Norton, P.J. Mine closure and associated hydrological effects on the environment: Some case studies. In *Minerals, Metals and the Environment II. Institute of Mining and Metallurgy*; Elsevier Applied Science: London, UK, 1996; pp. 263–270.
40. Durham Mining Museum: Collieries. Available online: <http://www.dmm.org.uk/colliery/> (accessed on 15 May 2017).
41. Bell, F.G.; Genske, D.D. The influence of subsidence attributable to coal mining on the environment, development and restoration; some examples from Western Europe and South Africa. *Environ. Eng. Geosci.* **2001**, *7*, 81–99. [[CrossRef](#)]
42. Pöttgens, J.J. Uplift as a result of rising mine waters (in German). The Development Science and Art of Minerals Surveying. In Proceedings of the 6th International Congress of the International Society for Mine Surveying, Harrogate, UK, 9–13 September 1985; Volume 2, pp. 928–938.
43. Donnelly, L.J. A review of international cases of fault reactivation during mining subsidence and fluid abstraction. *Q. J. Eng. Geol. Hydrogeol.* **2009**, *42*, 73–94. [[CrossRef](#)]
44. Bekendam, R.F.; Pottgens, J.J. Ground movements over the coal mines of southern Limburg, The Netherlands, and their relation to rising mine waters. *IAHS Publ.-Ser. Proc. Rep.-Int. Assoc. Hydrol. Sci.* **1995**, *234*, 3–12.
45. Chen, C.T.; Hu, J.C.; Lu, C.Y.; Lee, J.C.; Chan, Y.C. Thirty-year land elevation change from subsidence to uplift following the termination of groundwater pumping and its geological implications in the Metropolitan Taipei Basin, Northern Taiwan. *Eng. Geol.* **2007**, *95*, 30–47. [[CrossRef](#)]
46. Devleeschouwer, X.; Declercq, P.Y.; Flamion, B.; Brixko, J.; Timmermans, A.; Vanneste, J. Uplift revealed by radar interferometry around Liège (Belgium): A relation with rising mining groundwater. In Proceedings of the Post-Mining Symposium, Nancy, France, 6–8 February 2008; pp. 6–8.
47. Cuenca, M.C.; Hooper, A.J.; Hanssen, R.F. Surface deformation induced by water influx in the abandoned coal mines in Limburg, The Netherlands observed by satellite radar interferometry. *J. Appl. Geophys.* **2013**, *88*, 1–11. [[CrossRef](#)]
48. Samsonov, S.; d'Oreye, N.; Smets, B. Ground deformation associated with post-mining activity at the French–German border revealed by novel InSAR time series method. *Int. J. Appl. Earth Obs. Geoinf.* **2013**, *23*, 142–154. [[CrossRef](#)]
49. Graniczny, M.; Colombo, D.; Kowalski, Z.; Przyłucka, M.; Zdanowski, A. New results on ground deformation in the Upper Silesian Coal Basin (southern Poland) obtained during the DORIS Project (EU-FP 7). *Pure Appl. Geophys.* **2015**, *172*, 3029–3042. [[CrossRef](#)]
50. Przyłucka, M.; Herrera, G.; Graniczny, M.; Colombo, D.; Béjar-Pizarro, M. Combination of conventional and advanced DInSAR to monitor very fast mining subsidence with TerraSAR-X Data: Bytom City (Poland). *Remote Sens.* **2015**, *7*, 5300–5328. [[CrossRef](#)]
51. Vervoort, A.; Declercq, P.Y. Surface movement above old coal longwalls after mine closure. *Int. J. Min. Sci. Technol.* **2017**, in press. [[CrossRef](#)]
52. Younger, P.L. Coalfield closure and the water environment in Europe. *Min. Technol.* **2002**, *111*, 201–209. [[CrossRef](#)]

53. Wojtkowiak, F.; Couillet, J.C.; Daupley, X.; Tauziede, C. Geotechnical and environmental impacts on the surface of the water rising in French underground coal mines after closure. In Proceedings of the 7th International Mine Water Association Symposium (IMWA 2000), Ustron, Poland, 11–15 September 2000; pp. 180–194.
54. Smith, F.W.; Underwood, B. Mine closure: The environmental challenge. *Min. Technol.* **2000**, *109*, 202–209. [[CrossRef](#)]
55. Donnelly, L. Investigation of Geological Hazards & Mining Risks, Gallowgate, Newcastle-upon-Tyne. In Proceedings of the 10th IAEG International Congress, (IAEG 2006), Nottingham, UK, 6–10 September 2006.
56. Poulsen, B.A.; Shen, B.; Williams, D.J.; Huddleston-Holmes, C.; Erarslan, N.; Qin, J. Strength reduction on saturation of coal and coal measures rocks with implications for coal pillar strength. *Int. J. Rock Mech. Min. Sci.* **2014**, *71*, 41–52. [[CrossRef](#)]
57. Knott, D.L. Assessment of potential subsidence impacts from coal mining using test borings, mine maps and empirical methods. In Proceedings of the 2006 Interstate Technical Group on Abandoned Underground Mines Meeting, Rochester, NY, USA, 14–16 June 2006; pp. 1–40.
58. Castellanza, R.; Gerolymatou, E.; Nova, R. An attempt to predict the failure time of abandoned mine pillars. *Rock Mech. Rock Eng.* **2008**, *41*, 377. [[CrossRef](#)]
59. Smith, J.; Colls, J.J. Groundwater rebound in the Leicestershire Coalfield. *Water Environ. J.* **1996**, *10*, 280–289. [[CrossRef](#)]
60. Raleigh, C.B.; Healy, J.H.; Bredehoeft, J.D. An experiment in earthquake control at Rangely, Colorado. *Science* **1976**, *191*, 1230–1237. [[CrossRef](#)] [[PubMed](#)]
61. Ingebritsen, S.E.; Sanford, W.E. *Groundwater in Geologic Processes*; Cambridge University Press: Cambridge, UK, 1999.
62. Donnelly, L.J. Reactivation of geological faults during mining subsidence from 1859 to 2000 and beyond. *Min. Technol.* **2000**, *109*, 179–190. [[CrossRef](#)]
63. Younger, P.L. Hydrogeochemistry of minewaters flowing from abandoned coal workings in County Durham. *Q. J. Eng. Geol. Hydrogeol.* **1995**, *28* (Suppl. 2), S101–S113. [[CrossRef](#)]
64. Yu, M.H.; Jefferson, I.F.; Culshaw, M.G. Fault reactivation, an example of environmental impacts of groundwater rising on urban area due to previous mining activities. In Proceedings of the 11th Congress of the International Society for Rock Mechanics, Lisbon, Portugal, 9–13 July 2007.
65. Environment Agency. *Personal Communication*; Environment Agency: Bristol, UK, 2012.
66. Sherwood, J.M.; Younger, P.L. Modelling groundwater rebound after coalfield closure: An example from County Durham, UK. In Proceedings of the 5th International Mine Water Congress, University of Nottingham and IMWA, Nottingham, UK, 18–23 September 1994; pp. 767–777.
67. Younger, P.L.; Adams, R. *Predicting Mine Water Rebound: Research & Development Technical Report W179*; Environment Agency: Bristol, UK, 1999. [[CrossRef](#)]
68. Adams, R.; Younger, P.L. A strategy for modeling ground water rebound in abandoned deep mine systems. *Ground Water* **2001**, *39*, 249–261. [[CrossRef](#)] [[PubMed](#)]
69. Kortas, L.; Younger, P.L. Using the GRAM model to reconstruct the important factors in historic groundwater rebound in part of the Durham Coalfield, UK. *Mine Water Environ.* **2007**, *26*, 60–69. [[CrossRef](#)]
70. Adams, R. A Review of mine water rebound predictions from the VSS–NET model. *Mine Water Environ.* **2014**, *33*, 384–388. [[CrossRef](#)]
71. Victoria County History: Coal-Mining. Available online: <https://www.victoriacountyhistory.ac.uk/sites/default/files/work-in-progress/coal-mining.pdf> (accessed on 15 May 2017).
72. Harrison, R.; Scott, W.B.; Smith, T. A note on the distribution, levels and temperatures of minewaters in the Northumberland and Durham coalfield. *Q. J. Eng. Geol. Hydrogeol.* **1989**, *22*, 355–358. [[CrossRef](#)]
73. IMC Consulting Engineers Ltd. *Report on Earth Tremors at Ryhope*; The Coal Authority: Mansfield, UK, 1999.
74. Sizer, K.E.; Gill, M. Pillar failure in shallow coal mines—A recent case history. *Min. Technol.* **2000**, *109*, 146–152. [[CrossRef](#)]
75. Coal Authority. *Personal Communication*; Coal Authority: Mansfield, UK, 2017.



4. Modelling Groundwater Rebound in Coalfields

The main conclusion from the initial study over Northumberland and Durham was that heave was caused by the rise of groundwater. This suggested that surface deformation measurements could be used to infer changes in groundwater levels. However, the amount of surface deformation per unit of groundwater rise was different at each of the borehole locations, hence, using such simple correlations were not wholly appropriate to map groundwater changes. This is because of differences across the coalfield in the geology (i.e. the physical properties and confinement of the geological units) and hydrogeology (i.e. depth at which groundwater is rising). Here, we attempt to map groundwater change using InSAR data by generating a model to account for the heterogeneous geology and groundwater regime across the coalfield, so to be able to infer groundwater changes more realistically. The Nottinghamshire coalfield was chosen as a demonstration site since heave had been previously observed here, there was appropriate SAR, hydrogeological and mining data available and it is a coalfield that is relatively well understood by the Coal Authority.



Modelling groundwater rebound in recently abandoned coalfields using DInSAR



David Gee^{a,b,*}, Luke Bateson^c, Stephen Grebby^a, Alessandro Novellino^c, Andrew Sowter^b, Lee Wyatt^d, Stuart Marsh^a, Roy Morgenstern^e, Ahmed Athab^b

^a Nottingham Geospatial Institute, University of Nottingham, Nottingham NG7 2TU, UK

^b Terra Motion Limited, Ingenuity Centre, Nottingham NG7 2TU, UK

^c British Geological Survey, Natural Environment Research Council, Keyworth NG12 5GG, UK

^d Coal Authority, 200 Lichfield Lane, Mansfield, Nottinghamshire NG18 4RG, UK

^e Geotechnical Institute, TU Bergakademie Freiberg, Saxony 09599, Germany

ARTICLE INFO

Keywords:

Surface deformation
DInSAR
Intermittent SBAS
Groundwater modelling
Coal mining
Dewatering
Heave
Hydrogeology

ABSTRACT

Advances in differential interferometric synthetic aperture radar (DInSAR) processing algorithms, such as the Intermittent Small Baseline Subset (ISBAS), and increased data availability from SAR systems, such as Sentinel-1, provide the opportunity to increase the spatial and temporal density of ground deformation measurements. Such measurements, when combined with modelling, have the potential to make a significant cost-effective contribution to the progressive abandonment strategy of recently closed coalfields. Applications of DInSAR over coalfields have observed heave in coal measures rocks and temporal correlations between the rise of mine water and deformation time-series. The cessation of systematic dewatering can have a variety of detrimental impacts and knowledge of the time-scales (i.e. the rate of rebound) and structure of the mine system are crucial to the remediation strategy. Although mine plans and borehole measurements provide vital information in this regard, mine plans are often incomplete or inaccurate, whereas monitoring boreholes are spatially sparse. Consequently, groundwater can flow in unanticipated directions via goaf, mine shafts and roadways, making it difficult to determine where the impacts of rebound are likely to occur. In this study, ground deformation data obtained using ISBAS DInSAR on ENVISAT (2002–2009) and Sentinel-1 (2015–2019) data are used to develop a simple method to model groundwater rebound in abandoned coalfields. A forward analytical model based upon the principle of effective stress and mine water ponds is first implemented to estimate surface heave in response to changes in groundwater levels measured in monitoring boreholes. The forward model is then calibrated and validated using the ground deformation data. The DInSAR data were subsequently inverted to map the change in groundwater levels in greater detail across the coalfield and forecast surface discharges in order to support mitigation strategies.

1. Introduction

Deep underground coal mining almost always extends below the natural water table (Younger, 2016). Accordingly, extensive dewatering of coal measures rocks is required to ensure dry and safe working conditions in collieries, with strategic pumping stations located around the complex network of mine workings (Dumpleton et al., 2001). After colliery closure, the cessation of dewatering results in the progressive rise of groundwater and flooding of old workings and surrounding rock, as the rock matrix begins to revert back to saturated conditions. Acid mine water drainage (AMD) is water that becomes polluted through contact with former workings. AMD can have many adverse

consequences, which are listed in order of environmental significance and frequency (Younger and Adams, 1999):

- (i) surface water pollution;
- (ii) localised flooding of agricultural, industrial or residential areas;
- (iii) loss of dilution for other pollutants in surface waters where former pumped discharges have ceased;
- (iv) overloading and clogging of drains and sewers;
- (v) pollution of overlying aquifers by upward movement of mine water (principally from sulphate and chloride);
- (vi) temporarily increased emissions of mine gases, driven ahead of rising mine water;

* Corresponding author at: Nottingham Geospatial Institute, University of Nottingham, Nottingham NG7 2TU, UK.

E-mail address: david.gee@nottingham.ac.uk (D. Gee).

- (vii) ground deformation due to renewed mining subsidence and re-activation of faults (Donnelly, 2006);
- (viii) adverse effects on landfills – possible damage to lining, leakage of leachate and increased gas emissions.

Methods to estimate the spatial extent and timescales (i.e. the rate of rebound) of mine water rise are vital to generate rational policies and a cost-benefit remediation strategy for progressive mine abandonment (Younger and Adams, 1999; Younger, 2016). Mine plans provide crucial information in the prediction of the directional and structural control of groundwater flow. When above the water table, groundwater flows down-dip through permeable stratigraphic horizons, such as the fractured or jointed sandstones, goaf, collapsed strata and mining roadways. Down-dip flow will stop and groundwater will pond once it reaches a hydraulic barrier such as an intact coal pillar or fault. Water levels will rise until a new overflow point is reached in the form of a drainage adit at the surface or a connection to a neighbouring colliery. However, the prediction of flow is often challenging due to incomplete and inaccurate information regarding inter-seam connections within collieries, as well as connections between adjacent collieries from mine plans that might have been drawn more than a century ago. Flow can therefore occur in unanticipated directions which can lead to surface discharges and pollution in areas not thought to be vulnerable (Younger and Adams, 1999). In addition, monitoring boreholes are expensive and often spatially sparse, providing only a limited overview of mine water levels in complex and often vast mine systems.

Many studies have recognised the impact of changing groundwater levels on the compaction of strata and deformation at the surface (e.g. Hoffmann et al., 2001; Galloway and Hoffmann, 2007; Bell et al., 2008; Chaussard et al., 2017; Motagh et al., 2017). As groundwater levels change, compaction or expansion of the subsurface strata occurs due to a change in hydrostatic pressure (Bekendam and Pöttgens, 1995). Conventional monitoring methods for mapping surface deformation, such as precise levelling, close range photogrammetry and GPS, can be laborious, expensive and offer limited spatial coverage. Remote differential interferometric synthetic aperture radar (DInSAR) is a cost-effective wide-area method to measure sub-centimetre rates of surface deformation. In particular, the emergence of time-series methods in the late 1990s has increased the integration of surface deformation measurements into hydrogeological studies. DInSAR data facilitate the identification of areas of groundwater depletion or recharge, and so provide the means to calibrate groundwater models, delineate lithological boundaries and map aquifer storage variations and assist characterisation (e.g. Chaussard et al., 2014; Castellazzi et al., 2016; Béjar-Pizarro et al., 2017; Castellazzi et al., 2018). Additionally, DInSAR measurements have previously been utilized to calibrate and/or validate models of surface deformation associated with anthropogenic fluid injection or extraction (e.g. Rutqvist et al., 2010; Pearse et al., 2014; Gee et al., 2016). Initial applications over mining areas also confirmed the capability of DInSAR to measure mining induced subsidence (e.g. Carnec et al., 1996; Wright and Stow, 1999). More recently, spatial distributions of heave in coal measures rocks (e.g. Sowter et al., 2013; Bateson et al., 2015; Sowter et al., 2018; Gee et al., 2019) and temporal correlations between the rise of mine water and deformation time-series (e.g. Cuenca et al., 2013; Gee et al., 2017) have been observed over abandoned coalfields.

The monitoring of groundwater rebound in abandoned coalfields requires a dense, regular spatiotemporal sampling of ground deformation measurements. This is because the response to hydrostatic pressure changes caused by pumping can be highly spatially variable due to differences in the compressibility, thickness and confinement of the aquifer volume (Castellazzi et al., 2018). However, the obtained spatial distribution and density of DInSAR measurements can be severely affected by phase decorrelation or incoherence (Crosetto et al., 2016). This effect is most prevalent in higher frequency radar bands (e.g. C-

band) and incoherence is pervasive over agricultural land, forests, semi-natural areas and wetlands. This is particularly constraining for both persistent scatterer interferometry (PSI) and small baseline techniques. Small baseline methods have proven to achieve meaningful results in areas typically unfavourable for DInSAR analysis (e.g. Lu & Kwon, 2008), however, the density and distribution of measurements is still limited (Osmanoğlu et al., 2016). Furthermore, data availability has been an additional historical limitation where it is crucial to have sufficient data acquisitions spanning a deformation event at an appropriate revisit time for a reliable analysis.

The potential of DInSAR has continued to improve over time with many advancements in processing algorithms and increasing data availability from SAR orbital systems. In this regard, two notable advances are the development of the Intermittent Small Baseline Subset (ISBAS) (Sowter et al., 2013; Sowter et al., 2016) processing method and the launch of the Sentinel-1 satellite. The ISBAS method is an adapted version of the SBAS method (Berardino et al., 2002) that is capable of computing velocities over unfavourable land cover types to return a spatially distributed set of deformation measurements with near complete ground coverage (Cigna and Sowter, 2017). Sentinel-1 is a two-satellite constellation carrying a C-Band (5.5 cm wavelength — 5.4 GHz) SAR payload which provides conflict-free data every 6 days in Europe and at least 12 days for the majority of the global landmasses (Torres et al., 2012).

Characterising and predicting the rise of AMD is a global challenge facing parts of Europe (Gee et al., 2017), Africa (Van Tonder et al., 2007), Asia (Liu et al., 2020), Australia (Wright et al., 2018) and the Americas (Gammons et al., 2010), particularly as the demand for coal declines in favour of more sustainable energy sources. With this in mind, this study aims to propose a cost-effective method to model groundwater rise in recently abandoned coalfields using DInSAR for the purpose of identifying where problems associated with mine water rebound may manifest. The specific objectives are to:

- (i) generate a forward analytical model to predict the change in thickness of the strata and, hence, determine surface movement, based upon measurements of groundwater change from monitoring boreholes;
- (ii) calibrate and validate the model using ISBAS DInSAR;
- (iii) invert the DInSAR measurements to provide an estimate of the change in groundwater levels with detailed and near-complete spatial coverage across the coalfield;
- (iv) utilize the inverted rates to estimate the time it will take for groundwater to discharge out of the Coal Measures rock.

These objectives provide the structural sub-headings used in the following Methods and Results and Discussions sections.

2. Study site & materials

2.1. Land Cover

The study site comprises ~2000 km² and covers the counties of Derbyshire and Nottinghamshire, UK (Fig. 1). Land cover is largely rural, dominated by agricultural land (50%) with patches of pastures (21%), forests (7%), semi-natural areas (< 2%), and wetlands (< 1%) (European Environment Agency, 2012). Artificial surfaces (20%) predominantly correspond to the city of Nottingham in the south and towns of Mansfield and Chesterfield in the centre and north-west, respectively. Water bodies make up less than 1% of the total land cover. Topographically, the study site is located between the Peak District at the southern end of Pennines hill and mountain range in the west, where the elevation reaches a maximum of 380 m above ordnance datum (AOD), and the midlands plains to the east at mean sea level.

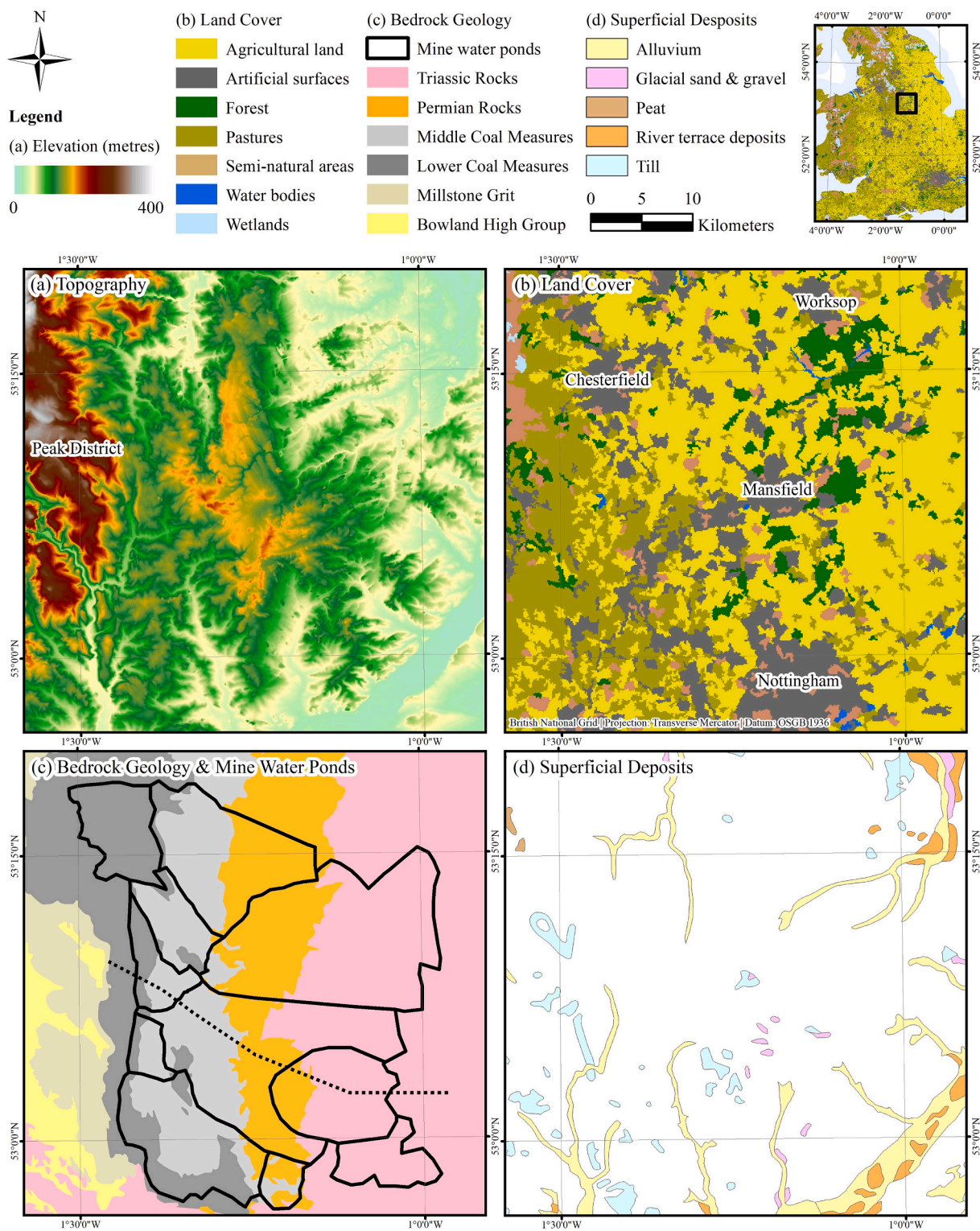


Fig. 1. (a) Topography – NEXTMap® DTM at 10 m resolution; (b) CORINE land cover inventory (European Environment Agency, 2012); (c) Bedrock geology at 1:625,000 scale, from BGS Geology 625 k (DiGMapGB-625) data; and (d) Superficial deposits at 1:625,000 scale, from BGS Geology 625 k (DiGMapGB-625) data. The dashed black line in (c) shows the location of the cross-section in Fig. 2. NEXTMap® Britain © 2003, Intermap Technologies Inc. European Environment Agency © 2012. Reproduced with the permission of the British Geological Survey © NERC. All rights Reserved.

2.2. Geology

The study area lies to the east of the Pennine Dinantian-Namurian anticlinal ridge (Figs. 1 and 2). The Coal Measures Group (CMG) are dominated by argillaceous strata with alternations of sandstone, grey

siltstone and grey mudstone with frequent coal seams and seatearth horizons. Groundwater movement largely occurs via secondary permeability through fractures, given that the carboniferous strata are extensively faulted which act to either increase permeability or prevent hydraulic connectivity (Holliday, 1986). The Nottinghamshire

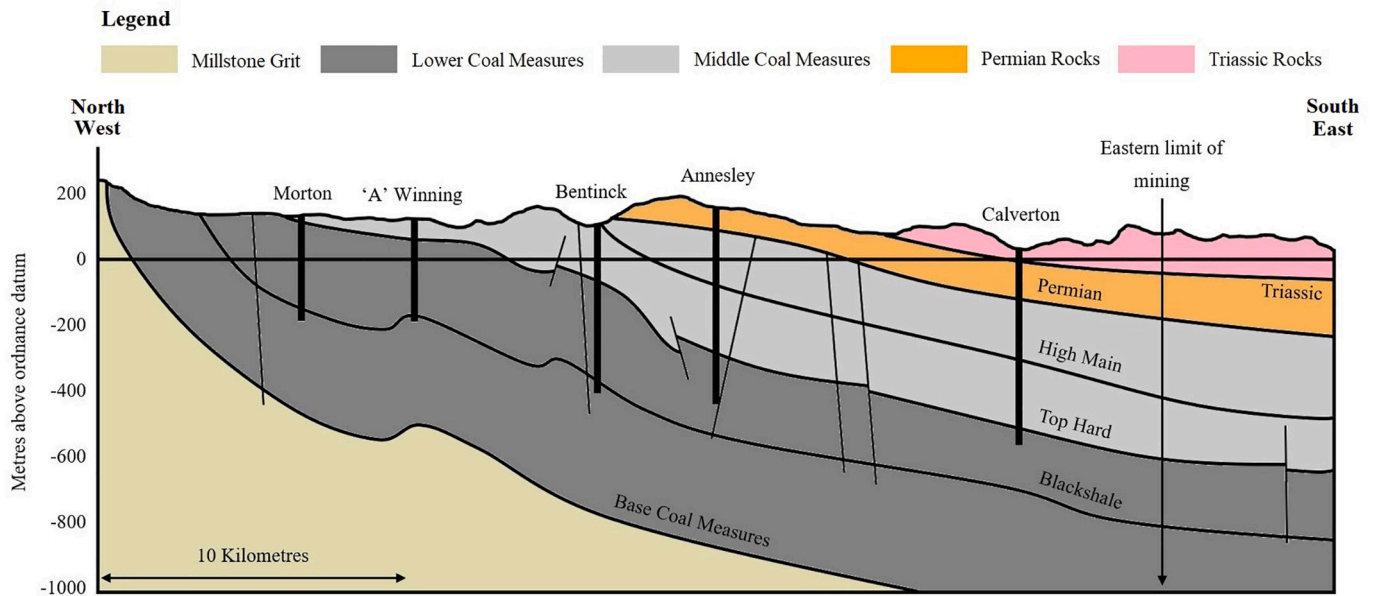


Fig. 2. Cross-section of the Nottinghamshire Coalfield. The location is marked on Fig. 1c. The thick vertical black lines represent shaft locations and thinner vertical black lines represent faults. The high main seam demarcates the upper limit of mining. The base of the Top Hard and Blackshale seams for the areas east and west of Annesley-Bentinck, respectively, indicates the base of the zone of enhanced permeability due to mining induced fractures (adapted from Dumbleton et al., 2001).

Coalfields have been extensively worked since the early 1800s until the last deep mine, Thoresby, was closed in July 2015. Over thirty separate seams have been mined, and the extraction of large volumes of coal and adjacent rock, associated fracturing and collapse of in situ strata, generation of roadways and entry shafts, and areas of goaf generate a complex combination of disturbed and undisturbed strata. The most exploited horizon is the Top Hard seam and neighbouring collieries are frequently linked via the working of this seam from different directions (Dumbleton et al., 2001). The CMG dip regionally east under the East Midlands shelf, which is formed of Permian and Triassic strata and ranges between 50 m to 200 m in thickness from west to east. The bedrock is overlain with superficial deposits that are only up to a few metres thick (Charsley et al., 1990).

The geological parameters required for establishing a groundwater model are the porosity and compression index of the CMG. The porosity was determined as 0.134, calculated as the mean of 236 measurements of the Pennine CMG from the National Geotechnical Properties Database of the British Geological Survey (BGS). No laboratory samples were available to determine the compression index, therefore a value for dense sand of 0.005 was defined according to the literature (Jain et al., 2015). In addition, a digital elevation model (NEXTMap® DTM) and the 3D extent of the top of the Middle Coal Measures formation (Fig. 2) was required, with the latter taken from the BGS 1:250,000 3D geological models of the Pennine Basin (Hulbert and Terrington, 2014a, 2014b).

2.3. Hydrogeology

Mining activities have substantially altered the permeability of the CMG, whereby hydraulic connectivity has been generated between previously isolated horizons and abandoned saturated workings (Banks, 1997). The Nottinghamshire Coalfield is divided by the NW–SE Hardsoft-Mansfield anticline into northern and southern fault-bound sections, which can be further sub-divided into mine water ponds (Fig. 3). Younger and Adams (1999) introduced the Groundwater Rebound in Abandoned Mineworkings (GRAM) modelling concept, within which the coalfield is simplified into discrete ponds that represent groups of mine workings that are – with respect to rebound – hydraulically

analogous. Connectivity within the ponds can be extensive and, hence, these are expected to subside or uplift uniformly at the surface dependant on the associated groundwater regime. Some of the ponds are known to contain sub-ponds which have not been resolved due to a lack of mine water information. Hydraulic connectivity between ponds occurs at different levels between permeable geological features, mining roadways, existing boreholes and areas where adjoining goaf panels collapse. As the groundwater rises, the ponds fill until a connection to another pond is reached and water decants into the neighbouring pond. Connections between ponds alter at depth and therefore ponds can become isolated or connected at different stages of abandonment. Fig. 3 shows the expected schematic of groundwater flow. The workings of the deepest mines in the east were very dry, however, they are connected via an extensive network of workings up-dip which receive considerable ingress from rainfall and surface runoff (Rae, 1978). Little is known about the amount of flow, if any, between the deepest mines, since mine water accumulating in shallower workings was pumped to prevent the build-up of water against hydraulic barriers and therefore reduce the risk of inrushes.

Hydrogeological data was provided by the Coal Authority and was available for 21 and 24 boreholes coinciding with the ENVISAT and Sentinel-1 periods, respectively (Table 1). The number and frequency of groundwater measurements vary and where borehole data was incomplete across the epoch, it was linearly interpolated to fit the time-period provided that it covered more than three quarters of the epoch; otherwise it was discarded. Spatially, groundwater measurements are relatively sparse, with no information on levels in the Chesterfield, North Deep, Swanick or Gedling ponds for either time epochs.

2.4. Earth observation data

Thirty-nine ENVISAT C-Band Stripmap Level-1 single look complex (SLC) Image Mode products in VV polarisation from descending track 366 were available over the study site (Table 2). There were insufficient acquisitions from the ascending geometry for a reliable analysis. The descending data has a median revisit time of 35 days over a seven-year period (November 2002 – November 2009) regularly distributed throughout the epoch. The incidence angle ranges between 20.1° and 25.9° from near to

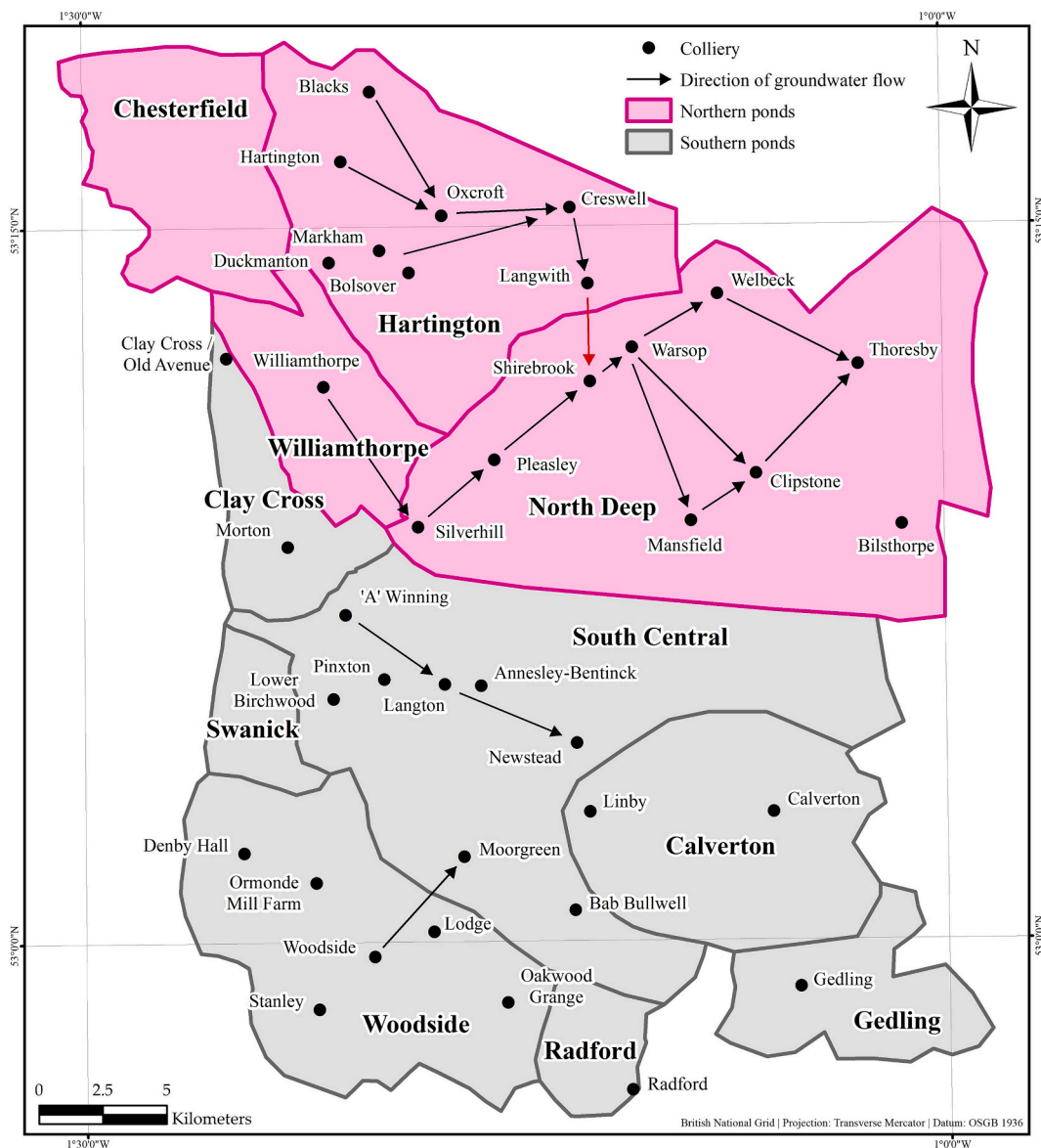


Fig. 3. Mine water ponds and expected schematic of flow of groundwater for the Nottinghamshire Coalfield. The red arrow between Langwith and Shirebrook indicates that at present there is very little or no flow between this barrier. (For interpretation of the references to colour in this figure legend, the reader is referred to the web version of this article.)

far range with respect to the surface normal. The products have a pixel spacing of 8 m in slant range and 4 m in azimuth, corresponding to an approximate ground spatial resolution of 25 m in range and 5 m in azimuth. In addition, 185 Sentinel-1 C-Band Terrain Observation with Progressive Scans SAR Interferometric Wide (IW) SLC VV polarized images from descending track 154 and 176 images from ascending track 132 (May 2015 – April 2019) were utilized (Table 2). The median revisit time is much reduced with respect to the ENVISAT data at 6 days. The Sentinel-1 IW products have a pixel spacing of 2.3 m in slant range and 13.9 m in azimuth, corresponding to a spatial resolution 5 m in ground range and 20 m in azimuth at scene centre. The incidence angle varies from 29.1° to 46° across the swaths from near to far range.

3. Methods

3.1. Generation of forward model using borehole measurements

The forward model applies the principle of effective stress (Terzaghi, 1925) and mine water ponds (Younger and Adams, 1999) to

calculate the increase in bed thickness (i.e. heave) that occurs for a given rise in groundwater level. Separate models were set up for the ENVISAT (2002–2009) and Sentinel-1 (2015–2019) epochs since the two stacks of SAR data were processed separately. The model is treated as a homogeneous matrix, where the initial bed thickness (b_0) (m) was calculated as the depth from the surface to the groundwater level at the start of the modelling epoch (Table 1). The bed thickness was interpolated for each pond based on the borehole measurements. The structure of mines or any of the interseam connections were not considered as their inclusion would introduce an undesired level of complexity to the model that would exceed the scope of the simple approach presented here. As groundwater levels fluctuate over the time-epochs but remain confined to the CMG unit, the model calculates the change in bed thickness of only the CMG unit. It does not consider any compaction of the overlying Permo-Triassic formation. For each pond, to determine the rise in groundwater, or change in piezometric head (Δh) (m), across the coalfield over the modelling epoch, the borehole measurements were interpolated (Table 1). For ponds where only one measurement was available, a uniform surface was utilized.

Table 1
Groundwater data for the ENVISAT (November 2002 – November 2009) and Sentinel-1 (May 2015 – April 2019) periods.

Coalfield	Pond	Borehole	ENVISAT (2002–2009)					Sentinel-1 (2015–2019)			
			No. Measurements	Start Height (Metres AOD)	End Height (Metres AOD)	Head Change (Metres)	Coefficient of Determination (R ²)	Mean Start (Metres AOD)	Mean End (Metres AOD)		
North	Chesterfield	Blacks	77	2.6	2.8	–	–	–	–	–	
		Hartington	288	–140.9	–142.6	0.2	0.09	–139.4	–	–120.3	
		Duckmanton	39	69.7	69.8	0.1	0.16	–	–	–	
	Hartington	Markham	3	–341.4	201.1	140.3	0.98	–	–	–	
		Oxcroft No.2	161	1.5	–11.8	–13.2	0.82	–	–	–	
	Williamthorpe	Creswell	162	–300.3	–301.4	–1.1	0.26	–	–	–	
		Langwith	158	–266.9	–257.9	9.0	0.31	–	–	–	
		Williamthorpe	280	–143.7	–147.4	–3.7	0.00	–143.7	–	–147.4	
		North Deep	–	–	–	–	–	–	–	–	
		Clay Cross	183	33.8	78.3	44.5	0.95	57.9	–	78.5	
South	Clay Cross	Clay Cross 1	168	56.5	77.4	20.9	0.94	–	–	–	
		Clay Cross 2	161	56.5	76.9	20.4	0.94	–	–	–	
	Clay Cross	Old Avenue 3	939	65.2	78.1	12.9	0.74	–	–	–	
		Old Avenue 4	166	77.4	81.8	4.4	0.55	–	–	–	
	South Central	'A' Winning	162	–41.8	44.3	86.1	0.99	–175.5	–	–21.1	
		Lower	–	–	–	–	–	–	–	–	
	Swanick	Woodside	Birchwood	–	–	–	–	–	–	–	–
			Pinxton	–	–	–	–	–	–	–	–
		Woodside	Langton	82	–309.2	–86.5	222.7	0.98	–	–	–
			Newstead	–	–	–	–	–	–	–	–
Woodside		Moorgreen	–	–	–	–	–	–	–	–	
		Babington	–	–	–	–	–	–	–	–	
Woodside		Bulwell	–	–	–	–	–	–	–	–	
		Denby Hall	788	78.2	85.5	7.2	0.22	46.0	–	50.9	
Woodside		Ormonde (Mill Farm)	565	64.4	68.7	4.3	0.64	–	–	–	
		Woodside	301	16.5	0.3	–16.2	0.00	–	–	–	
Woodside	Stanley	1098	53.5	58.9	5.4	0.27	–	–	–		
	Oakwood	1231	17.3	41.0	23.7	0.74	–	–	–		
Woodside	Grange	–	–	–	–	–	–	–	–		
	Radford	–	–	–	–	–	–	–	–		
Woodside	Calverton	38	–408.9	–377.9	30.0	0.94	–408.9	–	–377.9		
	Gedling	–	–	–	–	–	–	–	–		

(continued on next page)

Table 1 (continued)

Coalfield	ENVISAT (2002–2009)		Sentinel-1 (2015–2019)									
	Mean Head Change (Metres)	No. Measurements	Start Height (Metres AOD)	End Height (Metres AOD)	Head Change (Metres)	Coefficient of Determination (R ²)	Mean Start (Metres AOD)	Mean End (Metres AOD)	Mean Head Change (Metres)			
North	19.1	12	2.7	15.9	13.2	0.65	-82.3	-29.4	52.9			
		30	-58.5	14.5	72.9	0.98						
		5	-10.2	15.9	26.1	0.97						
		4	-172.5	-95.0	77.6	0.97						
	-3.7	23	-172.9	-98.4	74.5	0.99						
		11	-49.0	20.3	69.3	0.91	-49.0	20.3	69.3			
		25	88.4	84.8	-3.6	0.16	82.6	82.2	-0.4			
		12	79.9	81.7	1.8	0.23						
		12	79.5	79.5	0.0	0.20						
		19	80.3	80.2	-0.1	0.02						
		21	84.9	85.0	0.1	0.18						
South	154.4	162	47.3	36.1	-11.2	0.02	23.5	35.6	12.1			
		10	55.6	55.1	-0.5	0.15						
		142	27.8	44.7	16.9	0.11						
		155	25.7	44.5	18.8	0.97						
		146	22.5	41.1	18.5	0.96						
		141	10.4	34.6	24.2	0.84						
		132	-25.1	-7.0	18.1	0.83						
	4.9	13	88.8	94.1	6.1	0.33	67.4	66.7	-0.7			
		9	70.9	76.3	5.4	0.69						
		82	38.5	10.9	-27.6	0.34						
		17	91.7	101.6	9.9	0.20						
	14	47.9	50.6	2.7	0.17	25.1	25.1	0.0				
31.0	14	25.1	25.1	0.0	0.00							

Table 2
Earth Observation data and ISBAS processing parameters.

Satellite	Geometry	Track	N° of Images	Date Range	Median Revisit (Days)	Max. Orbital Baseline (Metres)	Min. Temp. Baseline (Days)	Max. Temp. Baseline (Days)	Mean Temp. Baseline (Days)	Multilooking (Azimuth: Range)	Coherence Threshold	N° of Interferograms	Interferogram Threshold	Reference Point
ENVISAT	Desc.	366	40	30/Nov/2002–28/Nov/2009	35	250	0	1460	618	20: 4	0.25	240	70	Nottingham City Centre
Sentinel-1	Desc.	154	185	08/May/2015–17/Apr/2019	6	45	365	673	673	6: 21	3603	3603	370	
	Asc.	132	175	06/May/2015–15/Apr/2019		50		674	674			3558		

The strata is subject to a level of geostatic pressure (p) (kPa), which increases as more material is overlain over time. Geostatic pressure is resisted by the intergranular (effective) stress (p_s) of the rock matrix and the fluid pressure of pore water (p_w) (Poland, 1984):

$$p = p_s + p_w \quad (1)$$

Equilibrium must be maintained in Eq. (1), thus, an increase in piezometric head increases the pore fluid pressure and decreases the effective stress on the strata. This results in expansion of the strata until equilibrium is again reached. The stress transfer from fluid to rock matrix per unit change in piezometric head was calculated at 10 kPa/m by Poland (1984). The geostatic pressure was calculated from the initial bed thickness (b_0) as:

$$p = 10 \cdot b_0 \quad (2)$$

Poland (1984) estimated for an unconfined aquifer that geostatic pressure is divided as 60% effective stress and 40% pore fluid pressure, whereas for a confined aquifer this is divided as 75% effective stress and 25% pore fluid pressure. In the western exposed coalfield only a single formation exists (the CMG), whilst in the east the CMG is overlain by the Permo-Triassic strata. To account for this, in the western exposed coalfield the CMG is considered unconfined, whereas it is treated as a confined formation where the coalfield is overlain by Permo-Triassic rocks. In the confined formation in the thinnest area of cover the pore fluid pressure is at 25%, which decreased linearly with cover thickness to 10% in the east where cover is thickest.

Following the change in head (Δh), the new pore fluid pressure (p_w) is calculated as:

$$p_w = p_{w0} + 10 \cdot \Delta h \quad (3)$$

and by maintaining the equilibrium in Eq. (1), the new effective stress (p_s) is:

$$p_s = p - p_w \quad (4)$$

hence, the change in effective stress (Δp_s) can be expressed as a function of the initial geostatic pressure (Eq. (1)) and change in piezometric head:

$$\Delta p_s = p_s - p_{s0}$$

$$\Delta p_s = p - p_w - p_{s0}$$

$$\Delta p_s = p - p_{w0} - 10 \cdot \Delta h - p_{s0} \quad (5)$$

The initial void ratio (e_0) is calculated from the initial porosity (n_0):

$$e_0 = \frac{n_0}{1 - n_0} \quad (6)$$

and after a change in effective stress a new void ratio (e) is calculated:

$$e = e_0 - c_c \cdot \log\left(\frac{p_s}{p_{s0}}\right) \quad (7)$$

as expressed as a function of the initial void ratio (e_0), the compression index (c_c) and the initial (p_{s0}) and new effective stress (p_s). The compression index is a dimensionless parameter that determines the compressibility of the stratigraphic bed and considers the elastic properties of the unit.

The coefficient of volume compressibility (m_v) relates the coefficient of compressibility (a_v) and the initial void ratio (e_0):

$$m_v = \frac{a_v}{1 + e_0} \quad (8)$$

where,

$$a_v = \frac{\Delta e}{\Delta p_s} \quad (9)$$

and Δe is the difference in void ratio.

The change in bed thickness (Δb) is caused by the change in

effective stress (Δp_s) and is calculated as a function of the coefficient of volume compressibility (m_v) and the initial thickness of the unit (b_0):

$$\Delta b = s \cdot \Delta p_s \cdot m_v \cdot b_0 \quad (10)$$

where s is a scaling factor to account for predicted inelastic (non-recoverable) deformation. The response of the strata to changes in piezometric head are dependent on historical pressure changes. Small-scale variations in head (e.g. seasonal effects) are elastic and recoverable so the strata expand and contract in equal measure. When variations in head are greater, the expansion and contraction is bigger which results in inelastic, and non-recoverable deformation, therefore limiting future expansion and contraction. Coarse grained strata (e.g. sand, gravel) are more likely to maintain equilibrium under increased effective stress due to their rigid skeletal matrix, however, fine-grained material (e.g. clays) are susceptible to high rates of potential compaction due to their plastic nature (Hiscock, 2009). Given the extensive and often variable dewatering regime that has occurred to great depths over many decades in the Nottinghamshire Coalfields and dominance of argillaceous strata within the CMG, it is assumed that the majority of previous compaction is inelastic.

3.2. Calibration & validation of forward model using ISBAS DInSAR observations

To calibrate the models and calculate the scaling factors, two sets of ground deformation measurements were generated from the ENVISAT and Sentinel-1 data (Table 2). The three stacks, processed separately, were co-registered to a common slant-range coordinate system using an amplitude-based Fast Fourier Transform method (Guizar-Sicairos et al., 2008). In the case of Sentinel-1, each image was deburst and merged prior to co-registration. Short orbital perpendicular baseline differential interferograms were generated following the method proposed by Bernardino et al. (2002). For ENVISAT, employing a maximum perpendicular baseline of 250 m and maximum temporal baseline of 4 years generated 270 interferograms with a mean temporal baseline of 618 days (Table 2). For the Sentinel-1 analysis, a maximum perpendicular baseline of 45 m and 50 m were applied to the descending and ascending data sets. The baseline was more stringent for the descending dataset to ensure a consistent number of interferograms were generated for both stacks despite the difference in the number of available images. A minimum temporal baseline of 1 year and no maximum was applied to achieve a similar mean temporal baseline as the ENVISAT stack. A total of 3603 and 3558 interferograms were generated, which have a mean temporal baseline of 673 and 674 days for the descending and ascending stacks, respectively.

An Intermittent Small Baseline Subset (ISBAS) (Sowter et al., 2013; Sowter et al., 2016) analysis was employed due to the dominance of the non-urban land cover. ISBAS is based upon the method of Bernardino et al. (2002), with a modification in the selection of pixels for analysis. The modification facilitates the retention of pixels which are coherent for only a subset of the total number of interferograms, which is common outside of urban areas. Pixels that fulfil the selection criteria exhibit a defined level of coherence in a minimum number of interferograms. The choice of interferogram threshold determines both the spatial coverage and the precision of the measurement – the standard error. Utilizing an interferogram threshold equal to the total number of interferograms is the equivalent to the method of Bernardino et al. (2002) and minimizes the standard error of velocity, but at the expense of the density of measurements. The choice of interferogram threshold is a trade-off between coverage and quality, hence, the inversely proportional relationship between the interferogram threshold and the standard error (Cigna and Sowter, 2017). A coherence analysis was employed on the small baseline interferograms, considering all of the image permutations meeting the baseline criteria. No spatial filtering was applied, and coherence was calculated over a multi-looked window of 4 in range and 20 in azimuth for ENVISAT and 21 in range and 6 in

azimuth for Sentinel-1. In ground range, the resultant pixels have an approximate pixel spacing of 90 m. A minimum of 70 and 370 interferograms that exhibited coherence > 0.25 were utilized for the ENVISAT and Sentinel-1 analyses, respectively.

Phase ramps attributed to orbital errors were subtracted and phase associated with topography was removed using a 90 m Shuttle Radar Topography Mission (SRTM) DEM (Farr et al., 2007). Coherent and intermittently coherent pixels satisfying the criteria were unwrapped from modulo- 2π phase to relative deformation using a statistical-cost network-flow algorithm (Chen and Zebker, 2001) with respect to a reference point located in Nottingham City centre. The same reference point was used for all data sets and was assumed to be stable due to its urban characteristics and abundant cluster of coherent pixels. After unwrapping, the method is in accordance with that of Bernardino et al. (2002). The linear velocities are derived from a least squares covariance analysis of the unwrapped phase, which also determines DEM height errors. Standard errors associated with both measurements are calculated from the standard deviation of residuals after fitting. To determine the time-series for each pixel, phase associated with the linear velocities and height errors were removed from the differential interferograms, before being added back after the residual phase components had been unwrapped. The phase velocities between adjacent images were inverted through Singular Value Decomposition. Phase was subsequently integrated to derive the phase at each acquisition interval before temporal high-pass and spatial low-pass filters compute and remove atmospheric components. Modulo- 2π phase time-series are then converted to deformation time-series.

Sufficient ENVISAT data was only available from the descending geometry so, on the assumption that horizontal motion is negligible, the ENVISAT deformation data were projected into the vertical by means of dividing by the cosine of the incidence angle. For Sentinel-1, the descending time-series were linearly interpolated to the dates of the ascending data before the vertical (d_{vert}) and horizontal (d_{hor}) components of motion were resolved for both the average velocities and time-series, on the assumption that there is negligible motion in the north-south direction:

$$d_{vert} = \frac{(-\sin\theta_{Desc} \cdot \cos\varnothing_{Desc} \cdot LOS_{Asc}) + (-\sin\theta_{Asc} \cdot \cos\varnothing_{Asc} \cdot LOS_{Desc})}{(-\sin\theta_{Asc} \cdot \cos\varnothing_{Asc} \cdot \cos_{Desc}) - (\cos\theta_{Asc} \cdot \cos\varnothing_{Desc} \cdot \sin_{Desc})} \quad (11)$$

$$d_{hor} = \frac{(\cos\theta_{Desc} \cdot LOS_{Asc}) + (-\cos\theta_{Asc} \cdot LOS_{Desc})}{(-\sin\theta_{Asc} \cdot \cos\varnothing_{Asc} \cdot \cos_{Desc}) - (\cos\theta_{Asc} \cdot \cos\varnothing_{Desc} \cdot \sin_{Desc})} \quad (12)$$

where θ is the incidence angle from surface normal, \varnothing is the azimuth track angle and LOS are the line-of-sight velocity measurements. The superscript indicates whether the parameter corresponds to the ascending (Asc) or descending (Desc) geometry.

The DInSAR average velocities were utilized to calibrate the forward model. Where there is a notable rise in groundwater, the rise is observed to occur linearly over time. For example, over the ENVISAT and Sentinel-1 epochs the coefficient of determination (R^2) is on average 0.93 and 0.94, respectively, for cases where groundwater rises more than 20 m. Similarly, the time-series data showed that in areas of heave the DInSAR measurements were principally linear which also provides an indication that the observed heave is attributable to groundwater rise. Accordingly, it is appropriate to utilize the average velocities for comparison and calibration (Table 1). In this study, an attempt was not made to utilize the time-series to account for variable pumping rates, however, this could be implemented on a pointwise basis at the borehole locations (e.g. Bateson et al., 2009). To perform calibration, a 1D forward model was generated at each borehole – excluding those located in areas of mining subsidence. The scaling factor (s) that minimised the root mean square error (RMSE) between the modelled measurements and 95th percentile of the DInSAR average velocities within the surrounding 1 km of the borehole were calculated. The mean scaling factor was taken for each pond. Whilst this approach achieved realistic results in most ponds, some scaling factors were

manually adjusted to account for the fact that heave caused by a change in groundwater does not always directly manifest at the borehole location. Instead, it can arise elsewhere within the mine complex and failure to account for this could lead to erroneous calibration. It was clear that when the scaling factor was too low, the average velocities generated by the forward model were too small and, consequently, the inverse map of groundwater rise was unrealistically high. Conversely, when the scaling factor was too high, the velocities in the forward model were similarly too high and the inverse map improbably small. Finally, to provide a quantitative comparison between the forward model and DInSAR average velocities the residuals were calculated by subtracting the modelled deformation from the DInSAR measurements.

3.3. Inversion of ISBAS DInSAR observations to estimate groundwater rise

To provide a quantitative estimate of groundwater rise (Δh) across the entire coalfield, an inversion of both the average DInSAR velocities and the displacement time-series was implemented as:

$$\Delta h = \frac{1}{10. s} \left(p - p_{so} - p_{wo} - \left(\frac{\Delta b}{m_v \cdot b_0} \right) \right) \quad (13)$$

where the DInSAR measurements are utilized to determine the change in bed thickness (Δb). The change in bed thickness was calculated by multiplying the average velocities by the length of the DInSAR time epoch to determine the cumulative deformation, whereas for the time-series each relative height change was inverted. In addition, the cumulative standard errors of the average velocities were inverted to provide an estimate of how the measurement error of the DInSAR translates into error in the estimate of groundwater rise.

3.4. Estimate of time until discharge using inverted map of groundwater rise

The inverted average rate of rise of the Sentinel-1 data was utilized to calculate the time it would take for groundwater to reach the top of the CMG and either discharge at the surface, where the CMG is unconfined, or infiltrate the Permo-Triassic formation. Groundwater recovery curves in most hydrogeological environments, including studies of mine water rebound, follow a shape that conforms to an exponential function. The recovery of mine water is a non-linear process because as the head difference between the formerly dewatered and now recovering strata and surrounding aquifers reduces, the head-dependant inflow also reduces. Hence, the rate of rebound decreases exponentially with time (Younger and Adams, 1999).

It is possible to predict mine water rebound by fitting an exponential curve to early rebound data, however, this is particularly challenging as it assumes that the reduction in head-dependant inflow into the voids of the recovering strata occurs at the same rate for entire rebound period. This assumption rarely holds – for instance, the curve might be fit to data for a period when an extensively worked lower seam of relatively high specific yield was flooding. In this case, once the mine water reaches the roof and proceeds into the strata of lower permeability, rebound would accelerate and thus deviate from the assumed exponential function. Rebound might take on an exponential function again once it reaches a higher seam, however, rebound will ultimately occur sooner than predicted. Alternatively, if the curve is fit to data related to the rapid filling of a seam interval, then rebound will occur later than predicted (Younger and Adams, 1999). Accounting for such processes requires detailed geological, mining and hydrogeological data, which are often unavailable.

In Britain, linear projections are utilized by the Coal Authority for the management of mine water, as this provides a scenario towards the worst-case; one in which rebound occurs more rapidly than in reality, which affords more time to implement pumping and treatment schemes. Such an estimate is preferable over an exponential projection that might erroneously indicate an area is not at risk. In line with this,

the estimate of time until discharge was calculated by dividing the depth of the groundwater from the top of the CMG at the end of the Sentinel-1 period by the inverted yearly rate of groundwater rise. The depth of groundwater at the end of the Sentinel-1 period was interpolated from the boreholes for each pond.

4. Results & discussion

4.1. Generation of forward model using borehole measurements

The results from the initial models showed good spatial agreement with areas of heave identified in the DInSAR data, however, large differences occurred in the magnitude of deformation. Such differences occur due to the choice of parameters; for example, whilst the value of porosity has been taken from real samples, the extraction of vast areas of strata and resultant void space will act to likely increase this value. The compression index was taken from literature and even had actual measurements been utilized, the CMG is a highly variable complex multilayer aquifer so samples may not be representative of the entire formation. Additionally, the response of the strata to pressure changes is also dependant on historical elastic and inelastic deformation, the degree of which is unknown, hence, leading to uncertainties.

4.2. Calibration & validation of forward model using ISBAS DInSAR observations

The average annual velocities identified over the ENVISAT and Sentinel-1 periods are shown in Fig. 4. The near complete spatial coverage (~94%) of the ISBAS measurements facilitates a comprehensive characterisation of the deformation occurring over the coalfield. Areas of spatially correlated heave are measured in both data sets and occur because of rising groundwater. The temporal evolution of deformation between the ENVISAT and Sentinel-1 data concur with the timeframes of coalfield abandonment. For example, rebound in the northern coalfield has only recently commenced. Over the ENVISAT period the area is relatively stable, and pumping was performed in the west of the Hartington and Williamthorpe ponds to prevent infiltrated groundwater migrating down-dip. Following the closure of Welbeck in May 2010, pumping has gradually been reduced allowing the deeper easterly mine workings to flood. At present there is very little flow across the barrier between the Langwith and Shirebrook, located in the North Deep pond. As a result, mine water is rising at Creswell and Langwith and heave is identified in the Sentinel-1 DInSAR. The barrier between Williamthorpe and Silverhill is known to leak and is allowing some flow into the North Deep pond, as evidenced from modelling by the Coal Authority in 2016/17. When Thoresby was closed in 2015, aside from the expected flow and flooding from the make of water from the mine workings, there was no evidence for notable large or increased flows coming from Williamthorpe, suggesting that pumping at Williamthorpe had prevented significant down-dip decant. Rebound is soon expected in the North Deep pond, however, no heave is observed over the period 2015–2019. This suggests that the connections with the westerly ponds are not present as anticipated, or that the groundwater levels have not yet reached the depth of the connections. Future DInSAR monitoring of this area will help to identify such a change, where groundwater has not yet reached the bottom of the monitoring borehole in the North Deep pond. In the southern coalfield, the most easterly up-dip measures around Morton and 'A' Winning recovered during the 2000s where heave is identified, and are subsequently stable once recovered and pumped in the 2010s.

At the regional scale of the entire coalfield, the calibrated forward models of heave show good agreement with the DInSAR surface deformation measurements (i.e. heave is observed in ponds where groundwater is rising) (Fig. 5). Over the ENVISAT epoch (2002–2009), the modelled heave primarily occurs in the southern coalfield, within the South Central pond, driven by rebound at 'A' Winning and Langton.

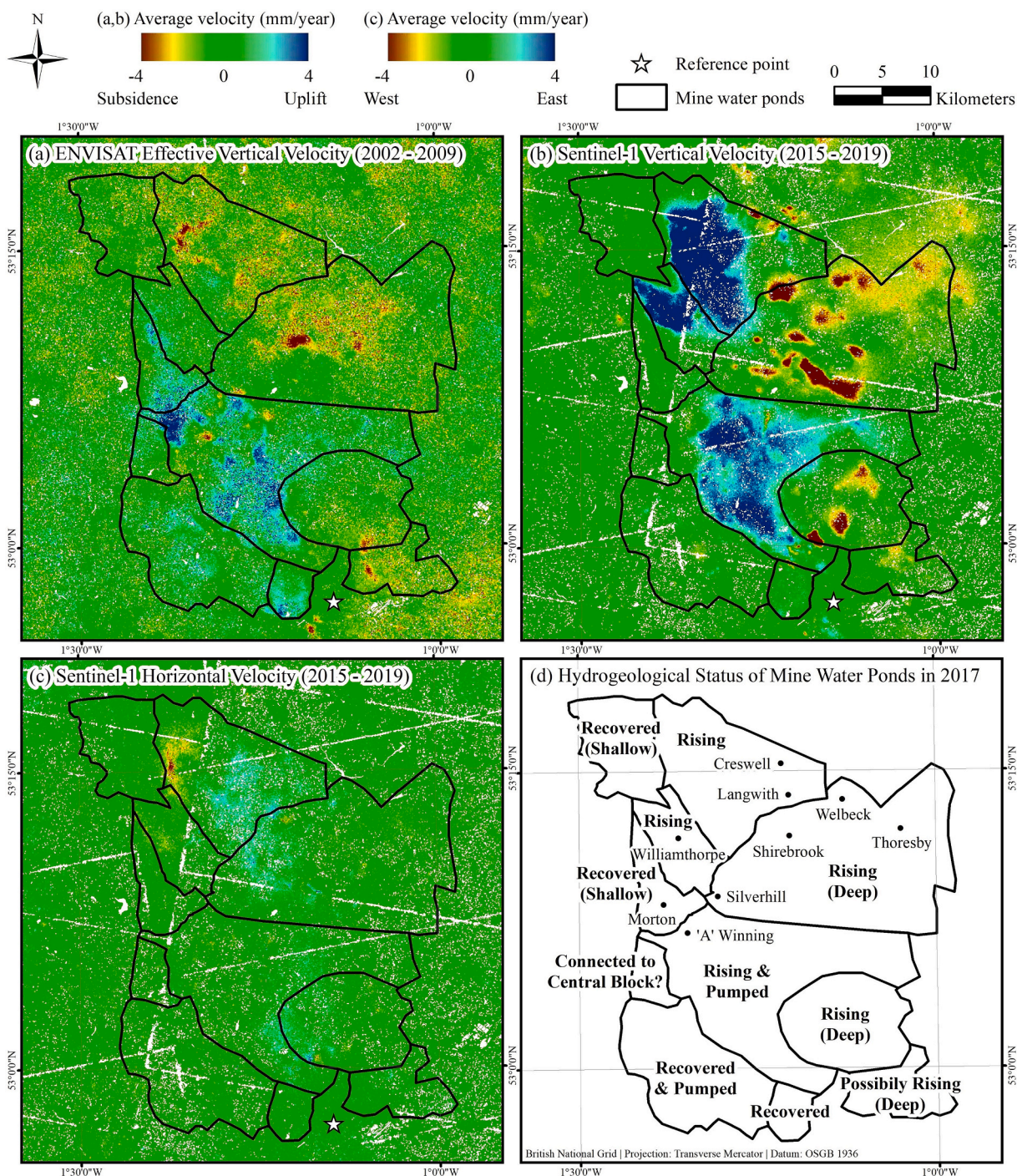


Fig. 4. (a) ENVISAT effective vertical velocities (mm/year); (b) Sentinel-1 vertical velocity (mm/year); (c) Sentinel-1 horizontal velocity (mm/year); and (d) Hydrogeological status of mine water ponds in 2017.

The DInSAR similarly identifies heave in South Central, although the rates are spatially variable in this relatively large pond suggesting South Central could contain sub-ponds. This evidences the simplification that the concept of ponds are relative to the actual geological setting. In the north the modelled heave is small. The DInSAR indicate that this pond is relatively stable, although there is a region of subsidence over the Markham borehole with an area of heave further to the south.

Over the Sentinel-1 epoch (2015–2019), heave occurs in the north coalfield within the Hartington and Williamthorpe ponds, in areas experiencing some of the largest recovery of groundwater (Fig. 5). Hydraulic connectivity within the Hartington and Williamthorpe ponds is

extensive. The DInSAR measurements concur with the modelled deformation, showing that heave is geologically bound by the outcropping of Pennine Middle Coal Measures. Most significantly, within the Hartington pond both the DInSAR and modelled deformation show that surface heave is of a lower velocity where the coal measures dip under the Permo-Triassic horizon. Where the CMG is confined, the DInSAR identifies lesser movement, mostly in close proximity to the boreholes at Creswell and Langwith where groundwater is rising. Crucial to this verification was the near-complete coverage (~94%) of the ISBAS DInSAR measurements in an area dominated by agricultural land where coherence is intermittent. If a conventional SBAS analysis had been

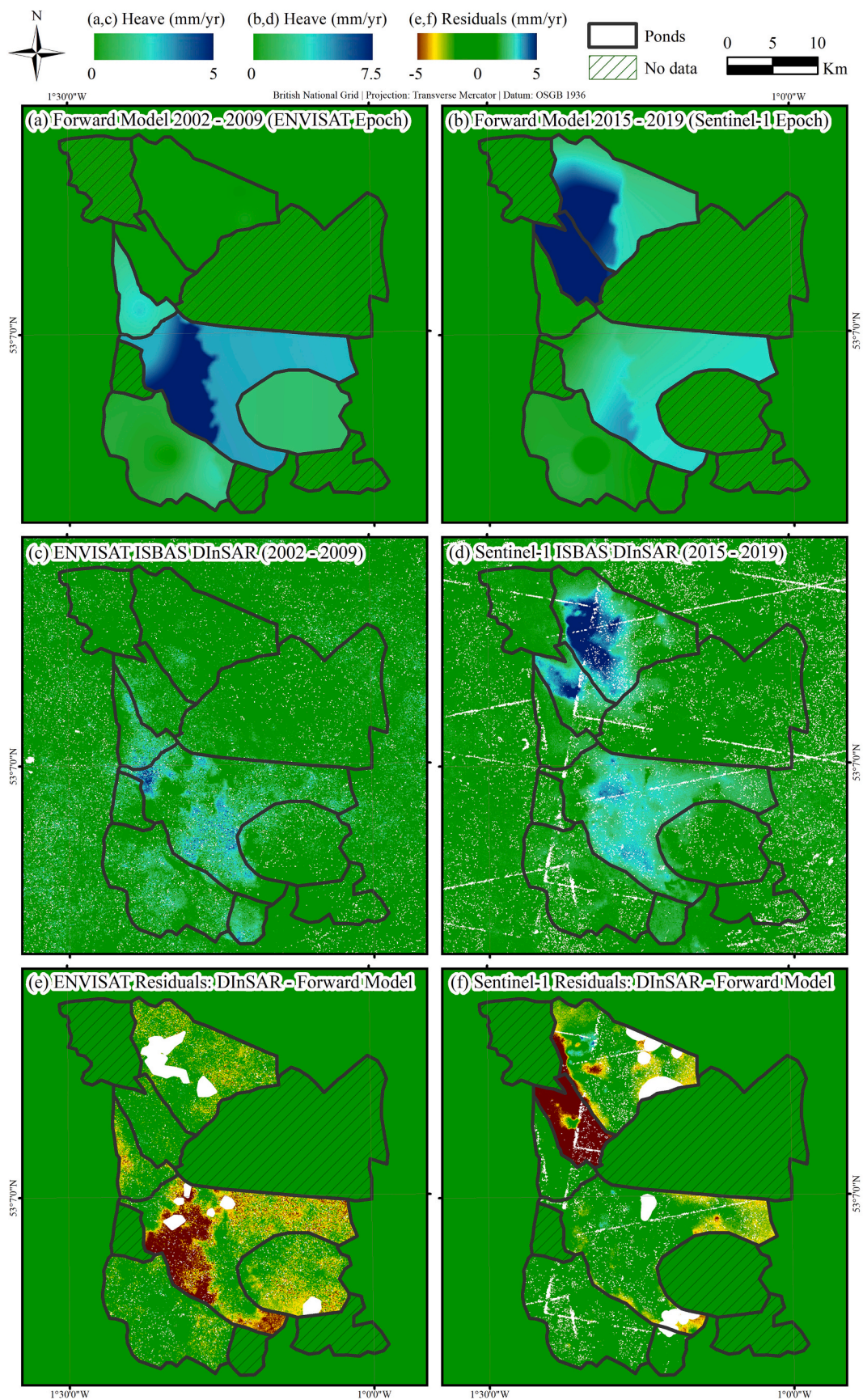


Fig. 5. Calibrated forward models for the: (a) ENVISAT and (b) Sentinel-1 time epochs. Intermittent SBAS DInSAR analysis for the: (c) ENVISAT and (d) Sentinel-1 time epochs. Residuals between ISBAS DInSAR and forward models for the: (e) ENVISAT and (f) Sentinel-1 time epochs. Red and blue indicate respective underestimation and overestimation of heave by the DInSAR relative to the model. Areas of notable subsidence identified by the DInSAR have been masked from the residuals. (For interpretation of the references to colour in this figure legend, the reader is referred to the web version of this article.)

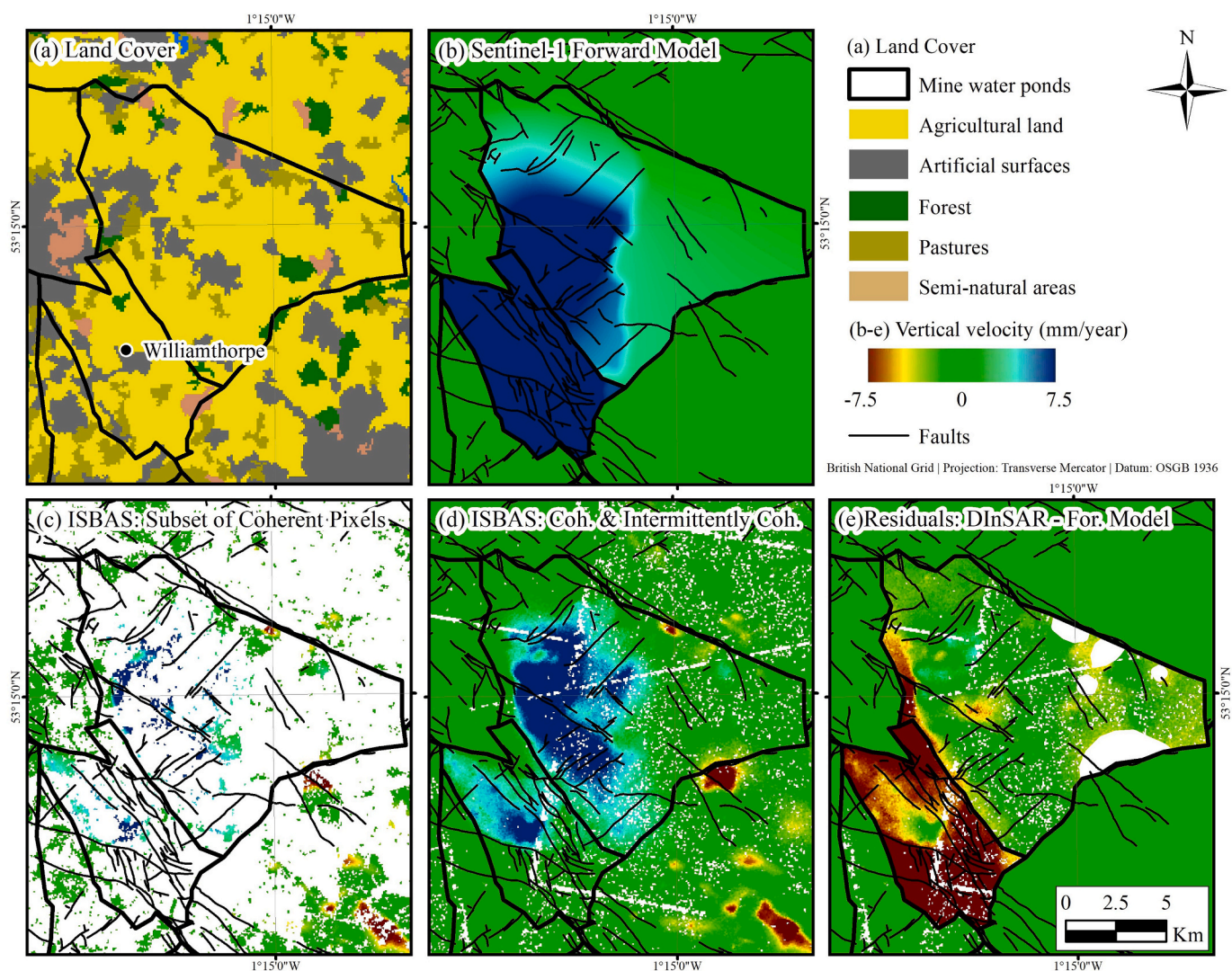


Fig. 6. Fault-bound motion and variable deformation within the Hartington and Williamthorpe ponds, measured over the Sentinel-1 period: (a) CORINE land cover inventory (European Environment Agency, 2012); (b) Forward model (mm/year); (c) Sentinel-1 average vertical velocities (mm/year) for the subset of coherent pixels only; (d) Sentinel-1 average velocities (mm/year) for all pixels (coherent and intermittently coherent); and (e) Residuals between ISBAS DInSAR and forward models. Red indicates underestimation of heave by the DInSAR relative to the model and blue indicates and overestimation by the DInSAR relative to the model. Areas of notable subsidence identified by the DInSAR have been masked from the residuals. European Environment Agency © 2012. (For interpretation of the references to colour in this figure legend, the reader is referred to the web version of this article.)

utilized, the ground measurement coverage would not have been sufficient to validate the change in rate of heave of the forward model where the CMG becomes confined (Fig. 6). Furthermore, calibration of the model would have been more challenging because 70% of the boreholes are situated within intermittently coherent pixels.

Heave also occurs in the DInSAR and the model in the South Central pond, in which groundwater levels are rising. To the west of the pond heave is not measured in the DInSAR in proximity of 'A' Winning where pumping occurs up-dip to control the levels at Langton and Newstead. In South Central heave is bound to the north by Hardsoft-Mansfield anticline which divides the northern and southern coalfields, to the south by a narrow but complex anticlinal zone which divides the South Central pond from the Woodside and Radford ponds (Dumpleton et al., 2001), and to the east by the Calverton pond, despite significant mine water pressure on the barriers (> 200 m). As expected, the recovered ponds of Clay Cross, Radford and Woodside are characterised as stable by the DInSAR and the model. Some heave is identified by the DInSAR in close proximity to the boreholes at Denby Hall, Ormonde Mill Farm and Lodge Erewash within the Woodside pond, which is indicative that whilst Woodside has recovered, it is still pumped to prevent mine water

discharging at the surface and/or flowing into South Central.

Unfortunately, no ground truth with sufficient spatial and temporal sampling at the required accuracy and precision is available to verify the DInSAR results. However, one of the great advantages of DInSAR is the ability to provide historical and current ground deformation measurements in areas where there is limited or no ground truth data. Prior ISBAS measurements have been validated in urban and rural environments, providing confidence in the method (e.g. Gee et al., 2016; Alshammari et al., 2019; Gee et al., 2019; Grebby et al., 2019). Over the Nottinghamshire Coalfields, the temporal evolution of deformation between the ENVISAT and Sentinel-1 data and the quantitative comparison between the deformation measured by the forward models and DInSAR confirm that the heave is caused by the recovery of mine water. No groundwater data is available to generate the forward model in several ponds, however, given the agreement between the DInSAR and model, the DInSAR can be utilized to infer the status of rebound. For instance, during the ENVISAT epoch heave is measured in Radford although no borehole measurements are available for this period (Fig. 5). The pond is known to have rebounded by the Sentinel-1 epoch (Table 1; Fig. 4d) so the DInSAR indicate that recovery occurred partly or wholly

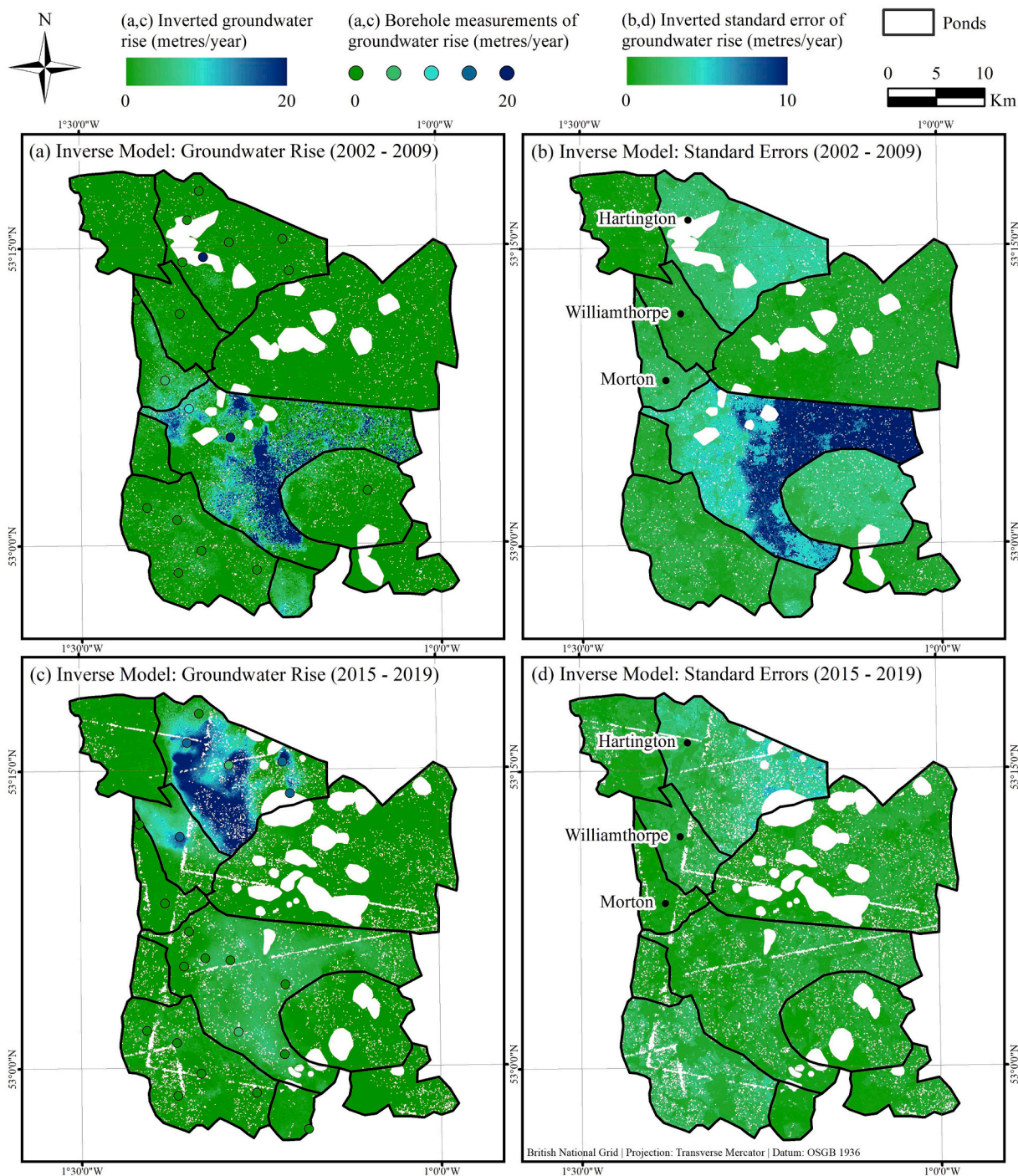


Fig. 7. Average change in groundwater levels per year as derived via the inverse model from: (a) ENVISAT ISBAS DInSAR; (b) ENVISAT standard errors; (c) Sentinel-1 ISBAS DInSAR and (d) Sentinel-1 standard errors.

between 2002 and 2009.

4.3. Inversion of ISBAS DInSAR observations to estimate groundwater rise

The adoption of ponds to characterise rebound in the coalfield is a practical, albeit necessary, simplification of the actual hydrogeological setting for the forward modelling. Whilst at the regional coalfield scale the forward models show a good level of agreement with the DInSAR measurements, the variability in groundwater rise has to be interpolated, or a single value input for an entire pond where only a single borehole exists. The complex and extensive network of mine workings

and poor spatial sampling of the boreholes means that groundwater rise between boreholes is not likely to be realistically characterised. For example, over the Sentinel-1 period within the Williamthorpe pond there is variability in the groundwater levels where heave is confined due to the presence of impermeable faults (Fig. 6d,e). The residuals between the forward model and DInSAR observations tend towards zero in the area surrounding the borehole, however, because of the variability in groundwater levels large residuals, up to -10 mm/year, occur in the south of the pond. Similarly, due to the variability of rebound within South Central over the ENVISAT epoch residuals of up to -8 mm/year are measured (Fig. 5). The near-complete spatial sampling

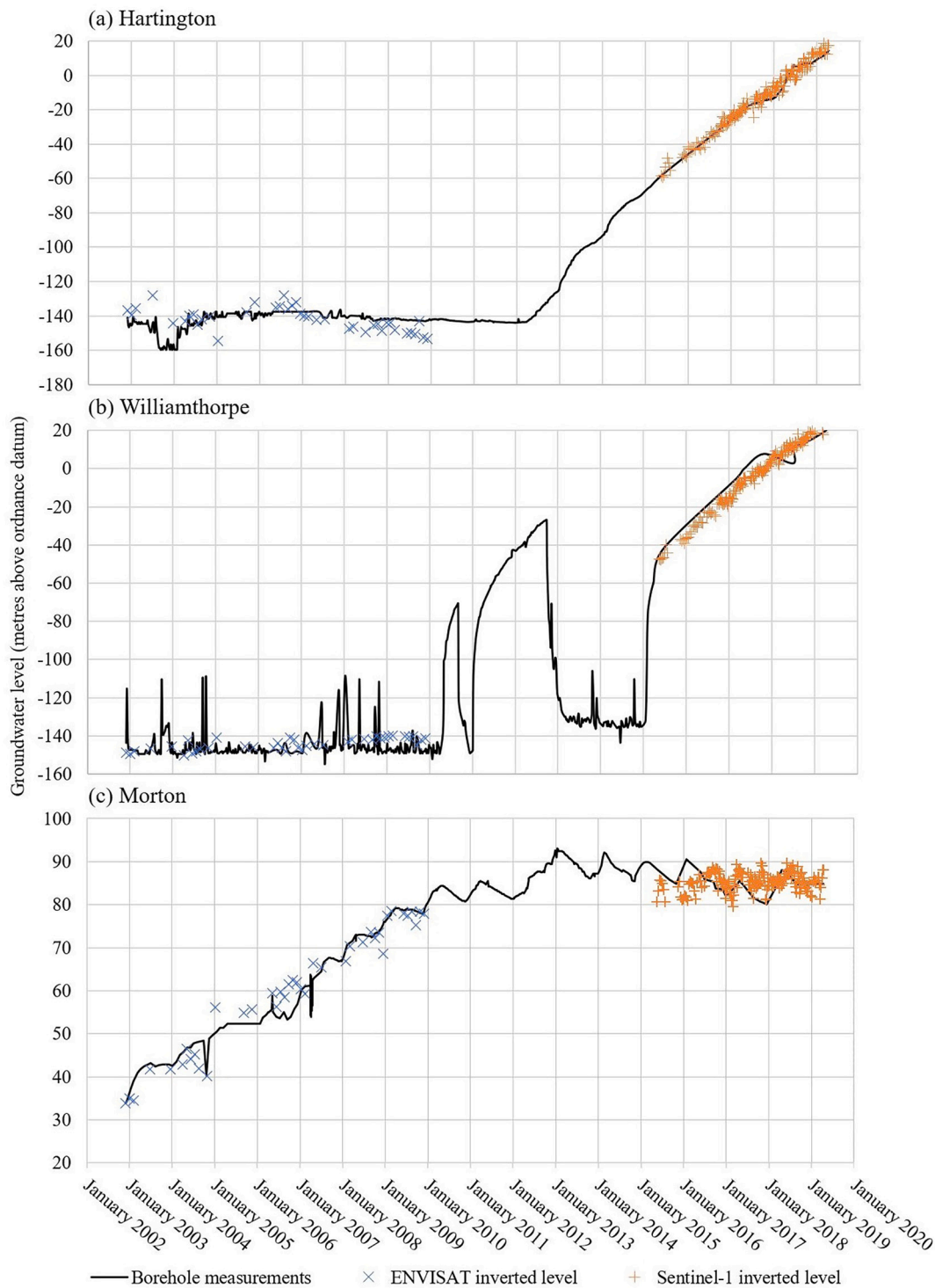


Fig. 8. Measured groundwater rise from monitoring boreholes and calibrated inverted groundwater rise from ENVISAT and Sentinel-1 data: (a) Hartington; (b) Williamthorpe; and (c) Morton. The locations of the boreholes are shown in Fig. 7.

of the ISBAS DInSAR surface measurements can capture the groundwater variability, hence, once inverted the change in groundwater levels are characterised in greater detail than the boreholes can solely achieve across the coalfield.

The inverted DInSAR measurements assume that heave occurs solely as a result of rising groundwater, which may not always be the only cause of the observed ground motions. However, it is a reasonable assumption given that the spatially correlated heave is delimited by the structural geology and has been validated by the forward models

(Section 4.2). The model can be theoretically utilized to predict a drop in groundwater levels. Notably, there are areas where subsidence occurs due to groundwater depletion at boreholes where groundwater has been pumped, for example, in close proximity to Woodside and 'A' Winning over the Sentinel-1 period (~ -2 mm/year). However, groundwater depletion does not cause many of the detrimental problems associated with rebound (e.g. surface water pollution, localised flooding, pollution of overlying aquifers), hence, the purpose of the study is to identify where the problems associated with rebound may

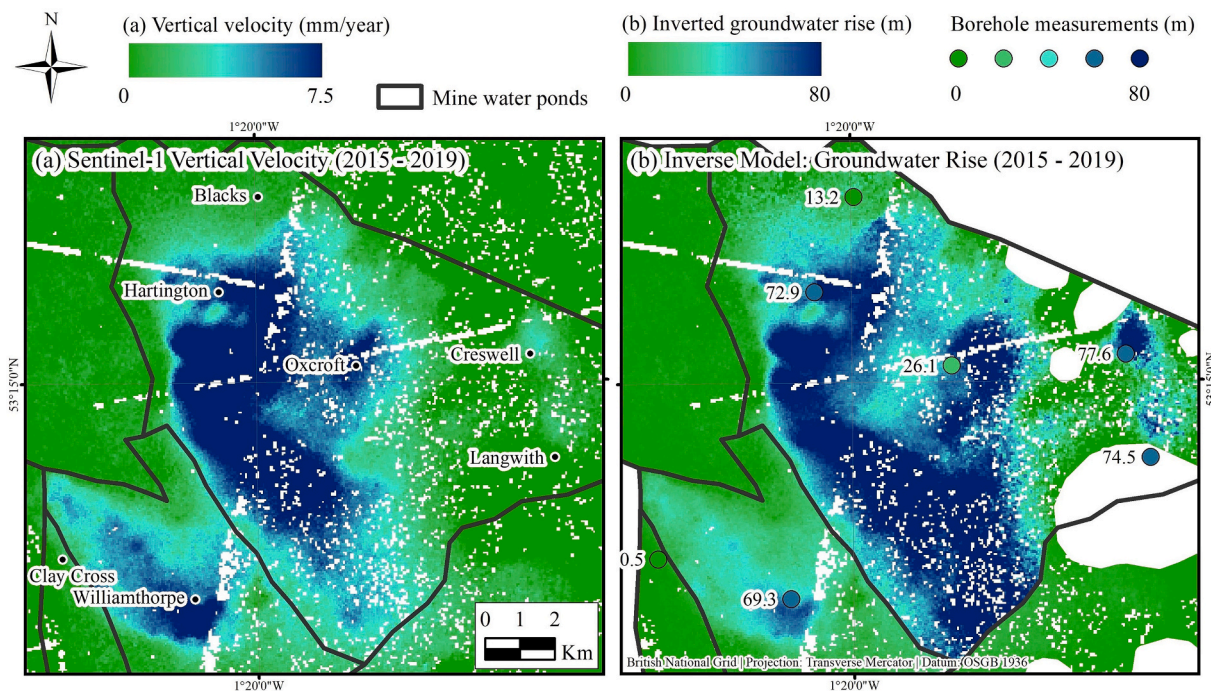


Fig. 9. (a) Sentinel-1 vertical velocity (mm/year); and (b) cumulative inverted groundwater rise (m) and borehole measurements over the Sentinel-1 period. Areas of notable subsidence identified by the DInSAR have been masked from the inverse map.

manifest. There are also localised hotspots of subsidence that are either known to be or likely to be related to mining induced collapses (e.g. the North Deep and Calverton ponds). Where such subsidence processes are transpiring an estimate of groundwater rise cannot be generated and so these areas are not considered and were masked from the inverse model.

The average inverted rates are shown in Fig. 7 and the average of all the inverted time-series in the surrounding 1 km of the boreholes of Hartington, Williamthorpe and Morton are shown in Fig. 8. The

inverted measurements provide a more realistic estimate of the rise in groundwater than previous simple correlations that universally determine a value of groundwater rise per unit of surface deformation (e.g. Banton et al., 2013). A change in bed thickness within the CMG would plausibly have less of an effect at the surface when the CMG is overlain by successive strata and, similarly, a rise in groundwater closer to the surface would be expected to have a greater control on surface deformation than a rise that occurs at depth. The value of groundwater rise per unit of surface deformation is different for every pixel since the

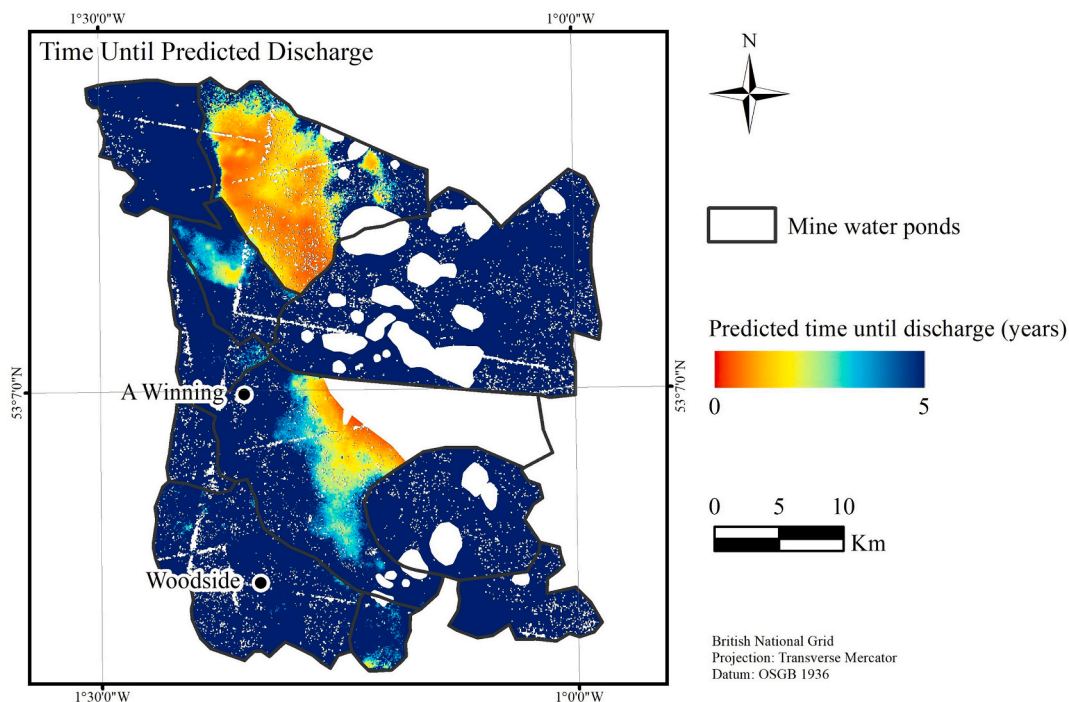


Fig. 10. Predicted time until discharge out of the Coal Measures Group, either at the surface or into the Permo-Triassic strata.

inverted estimate considers both the geology and the depth at which mine water is rising. For example, over the Sentinel-1 period heave measures up to ~ 10 mm/year around the Williamthorpe borehole which is in a shallow unconfined area, whereas at Creswell, in a deeper confined area, heave is ~ 3 mm/year (Fig. 9a). If only the surface deformation data was considered, it might be erroneously interpreted that groundwater levels are rising ~ 3 -times as fast at Williamthorpe than Creswell. The inverted measurements consider the geology and depth of groundwater and, hence, correctly determines that over the course of the Sentinel-1 epoch groundwater levels rose faster at Creswell (77.6 m) than Williamthorpe (69.3 m) (Fig. 9b).

The standard errors associated with the inverted rates are shown in Fig. 7b,d. The inverted standard errors are largest when a relatively small rate of heave translates into a large rise in groundwater (i.e. in deep confined areas such as the east of South Central pond over the ENVISAT period and east of the Hartington pond over the Sentinel-1 period). The standard error of the ISBAS velocities are controlled by the number of coherent interferograms, which is in turn predominantly controlled by the land cover. Coherence is less likely to be maintained outside of urban areas, hence, there are less coherent interferograms and the standard errors of velocities are higher. The standard errors of the Sentinel-1 velocities are on average less than the ENVISAT velocities, as a result of the greater number of images available and smaller perpendicular orbital baselines between images. Hence, the inverted standard errors of groundwater rise are controlled by the quantity and quality of SAR data, land cover, the confinement of the CMG, and depth and rate of change of the groundwater.

Again, the near complete ground coverage of the DInSAR measurements afforded by the ISBAS method has been crucial to the inverse mapping. In previous studies where DInSAR has been utilized to map groundwater level variations, decorrelation over non-urban land cover meant that measurements had to be interpolated to achieve complete coverage before inversion (e.g. Béjar-Pizarro et al., 2017). Whilst the density of measurements is important for modelling, for spatially correlated deformation, achieving a balanced spatial sampling can be more important to successfully characterise the signal of interest (Hanssen et al., 2008). Spatial interpolation is not required to achieve both a high density and regular spatial sampling with the ISBAS method, ultimately leading to a more accurate characterisation of the changes in groundwater levels.

4.4. Estimate of time until discharge using inverted map of groundwater rise

Fig. 10 displays the estimated time until discharge out of the CMG for the worst-case scenario. This assumes that the groundwater regime of the previous four years continues (i.e. the Sentinel-1 period), which might not be the case if a connection to a neighbouring mine is reached or if the Coal Authority decide to pump or stop pumping at selected boreholes. Nevertheless, it is indicative of where mine water discharges will occur under the current management and can be used to help prevent pollution at the surface or of the overlying Triassic Sherwood Sandstone aquifer, which is a major source of public water supply for the region. Such an approach could only be implemented effectively for areas where the depth of the groundwater is known at the end of the Sentinel-1 period (April 2019) and requires a regular sampling of borehole measurements, particularly in areas where the CMG dip relatively steeply. This is not the case in the eastern portion of the South Central pond which was, therefore, excluded. The results show that the west of the Hartington and centre of the South Central ponds are predicted to discharge first, in as little six months under the current groundwater regime. In the Williamthorpe pond, discharge is predicted in approximately 18 months at the centre of the pond. Conversely, the effects of pumping are clear in the areas surrounding the 'A' Winning borehole and the entire Woodside pond which are not at risk of discharge.

5. Conclusion

Characterisation and prediction of hydraulic flow in recently abandoned coalfields is particularly challenging due to inaccurate or incomplete mine plans and sparse monitoring boreholes. In this study, a method based upon the principle of effective stress and concept of mine water ponds was implemented to map variations in groundwater levels using DInSAR. The near complete coverage of the ISBAS deformation measurements was critical to calibrate the model, verify the outputs and provide a spatial quantitative estimate of the rate of groundwater rebound and an estimate of the time it will take for groundwater to discharge out of the Coal Measures rock. Given that many shafts are backfilled following coalfield closure and drilling new deep monitoring boreholes is expensive, the method proposed can provide a valuable cost-effective input into the abandonment strategy to help identify where pumping might be required. It is relatively straightforward to apply and requires few parameters to be estimated, and so, with the aid of the Sentinel-1 archive, has the potential to be readily applied over other recently abandoned coalfields.

Declaration of Competing Interest

The authors declare no conflicts of interest.

Acknowledgements

The research was funded by the GeoEnergy Research Centre (GERC) and Terra Motion Limited. ENVISAT and Sentinel-1 SAR data were provided by the European Space Agency, geological data by the British Geological Survey and hydrogeological data by the Coal Authority. The authors would like to thank Christopher Satterley for his role in the coordination of this research and Andrew Barkwith for useful comments at the beginning of the study. The authors would also like to thank four anonymous reviewers and the Remote Sensing of Environment editorial team who helped to improve the quality of the manuscript. L. Bateson and A. Novellino published with the permission of the Executive Director of BGS.

References

- Alshammari, L., Boyd, D.S., Sowter, A., Marshall, C., Andersen, R., Gilbert, P., Marsh, S., Large, D.J., 2019. Use of surface motion characteristics determined by InSAR to assess peatland condition. *J. Geophys. Res. Biogeosci.* 125 (1), 1–15. <https://doi.org/10.1029/2018JG004953>.
- Banks, D., 1997. Hydrogeochemistry of millstone grit and coal measures groundwaters, South Yorkshire and north Derbyshire, UK. *Q. J. Eng. Geol. Hydrogeol.* 30 (3), 237–256. <https://doi.org/10.1144/GSL.QJEG.1997.030.P3.06>.
- Banton, C., Bateson, L., McCormack, H., Holley, R., Watson, I.A., Burren, R., Lawrence, D., Cigna, F., 2013. Monitoring post-closure large scale surface deformation in mining areas. In: *Proceedings of the Eighth International Seminar on Mine Closure*. Australian Centre for Geomechanics, pp. 97–108.
- Bateson, L.B., Barkwith, A.K.A.P., Hughes, A.G., Aldiss, D., 2009. *TerraFirma: London H-3 Modelled Product. Comparison of PS data with the results of a groundwater abstraction related subsidence Model*. British Geological Survey Commissioned Report, OR/09/032. (47pp).
- Bateson, L., Cigna, F., Boon, D., Sowter, A., 2015. The application of the intermittent SBAS (ISBAS) InSAR method to the South Wales coalfield, UK. *Int. J. Appl. Earth Obs. Geoinf.* 34, 249–257. <https://doi.org/10.1016/j.jag.2014.08.018>.
- Béjar-Pizarro, M., Ezquerro, P., Herrera, G., Tomás, R., Guardiola-Albert, C., Hernández, J.M.R., Merodo, J.A.F., Marchamalo, M., Martínez, R., 2017. Mapping groundwater level and aquifer storage variations from InSAR measurements in the Madrid aquifer, Central Spain. *J. Hydrol.* 547, 678–689. <https://doi.org/10.1016/j.jhydrol.2017.02.011>.
- Bekendam, R.F., Pöttgens, J.J., 1995. Ground movements over the coal mines of southern Limburg, The Netherlands, and their relation to rising mine waters. In: *Land Subsidence (Proc. Fifth Int. Symp. On Land Subsidence, The Hague, October 1995)*, pp. 3–12 IAHS Publ. no. 234.
- Bell, J.W., Amelung, F., Ferretti, A., Bianchi, M., Novali, F., 2008. Permanent scatterer InSAR reveals seasonal and long-term aquifer-system response to groundwater pumping and artificial recharge. *Water Resour. Res.* 44 (2). <https://doi.org/10.1029/2007WR006152>.
- Berardino, P., Fornaro, G., Lanari, R., Sansosti, E., 2002. A new algorithm for surface deformation monitoring based on small baseline differential SAR interferograms.

- IEEE Trans. Geosci. Remote Sens. 40 (11), 2375–2383. <https://doi.org/10.1109/TGRS.2002.803792>.
- Carnec, C., Massonnet, D., King, C., 1996. Two examples of the use of SAR interferometry on displacement fields of small spatial extent. *Geophys. Res. Lett.* 23 (24), 3579–3582. <https://doi.org/10.1029/96GL03042>.
- Castellazzi, P., Martel, R., Rivera, A., Huang, J., Pavlic, G., Calderhead, A.I., Chaussard, E., Garfias, J., Salas, J., 2016. Groundwater depletion in Central Mexico: use of GRACE and InSAR to support water resources management. *Water Resour. Res.* 52 (8), 5985–6003. <https://doi.org/10.1002/2015WR018211>.
- Castellazzi, P., Longuevergne, L., Martel, R., Rivera, A., Brouard, C., Chaussard, E., 2018. Quantitative mapping of groundwater depletion at the water management scale using a combined GRACE/InSAR approach. *Remote Sens. Environ.* 205, 408–418. <https://doi.org/10.1016/j.rse.2017.11.025>.
- Charsley, T.J., Rathbone, P.A., Lowe, D.J., 1990. Nottingham: A geological background for planning and development. In: *British Geological Survey Technical Report, WA/90/1*.
- Chaussard, E., Bürgmann, R., Shirzaei, M., Fielding, E.J., Baker, B., 2014. Predictability of hydraulic head changes and characterization of aquifer-system and fault properties from InSAR-derived ground deformation. *J. Geophys. Res. Solid Earth* 119 (8), 6572–6590. <https://doi.org/10.1002/2014JB011266>.
- Chaussard, E., Milillo, P., Bürgmann, R., Perissin, D., Fielding, E.J., Baker, B., 2017. Remote sensing of ground deformation for monitoring groundwater management practices: application to the Santa Clara Valley during the 2012–2015 California drought. *J. Geophys. Res. Solid Earth* 122 (10), 8566–8582. <https://doi.org/10.1002/2017JB014676>.
- Chen, C.W., Zebker, H.A., 2001. Two-dimensional phase unwrapping with use of statistical models for cost functions in nonlinear optimization. *JOSA A* 18 (2), 338–351. <https://doi.org/10.1364/JOSAA.18.000338>.
- Cigna, F., Sowter, A., 2017. The relationship between intermittent coherence and precision of ISBAS InSAR ground motion velocities: ERS-1/2 case studies in the UK. *Remote Sens. Environ.* 202, 177–198. <https://doi.org/10.1016/j.rse.2017.05.016>.
- Crosetto, M., Monserrat, O., Cuevas-González, M., Devanthéry, N., Crippa, B., 2016. Persistent scatterer interferometry: a review. *ISPRS J. Photogramm. Remote Sens.* 115, 78–89. <https://doi.org/10.1016/j.isprsjprs.2015.10.011>.
- Cuenca, M.C., Hooper, A.J., Hanssen, R.F., 2013. Surface deformation induced by water influx in the abandoned coal mines in Limburg, the Netherlands observed by satellite radar interferometry. *J. Appl. Geophys.* 88, 1–11. <https://doi.org/10.1016/j.jappgeo.2012.10.003>.
- Donnelly, L.J., 2006. A review of coal mining induced fault reactivation in Great Britain. *Q. J. Eng. Geol. Hydrogeol.* 39 (1), 5–50. <https://doi.org/10.1144/1470-9236/05-015>.
- Dumpleton, S., Robins, N.S., Walker, J.A., Merrin, P.D., 2001. Mine water rebound in south Nottinghamshire: risk evaluation using 3-D visualization and predictive modelling. *Q. J. Eng. Geol. Hydrogeol.* 34 (3), 307–319. <https://doi.org/10.1144/qjegh.34.3.307>.
- European Environment Agency, 2012. CORINE Land Cover 2012. Available at: < <https://land.copernicus.eu/pan-european/corine-land-cover/clc-2012/view> > [Accessed 25th August 2019].
- Farr, T.G., Rosen, P.A., Caro, E., Crippen, R., Duren, R., Hensley, S., Kobrick, M., Paller, M., Rodriguez, E., Roth, L., Seal, D., 2007. The shuttle radar topography mission. *Rev. Geophys.* 45 (2). <https://doi.org/10.1029/2005RG000183>.
- Galloway, D.L., Hoffmann, J., 2007. The application of satellite differential SAR interferometry-derived ground displacements in hydrogeology. *Hydrogeol. J.* 15 (1), 133–154. <https://doi.org/10.1007/s10040-006-0121-5>.
- Gammons, C.H., Duaiame, T.E., Parker, S.R., Poulson, S.R., Kennelly, P., 2010. Geochemistry and stable isotope investigation of acid mine drainage associated with abandoned coal mines in Central Montana, USA. *Chem. Geol.* 269 (1–2), 100–112. <https://doi.org/10.1016/j.chemgeo.2009.05.026>.
- Gee, D., Sowter, A., Novellino, A., Marsh, S., Gluyas, J., 2016. Monitoring land motion due to natural gas extraction: validation of the intermittent SBAS (ISBAS) DInSAR algorithm over gas fields of North Holland, the Netherlands. *Mar. Pet. Geol.* 77, 1338–1354. <https://doi.org/10.1016/j.marpetgeo.2016.08.014>.
- Gee, D., Bateson, L., Sowter, A., Grebby, S., Novellino, A., Cigna, F., Marsh, S., Banton, C., Wyatt, L., 2017. Ground motion in areas of abandoned mining: application of the Intermittent SBAS (ISBAS) to the Northumberland and Durham Coalfield, UK. *Geosciences* 7 (3), 85. <https://doi.org/10.3390/geosciences7030085>.
- Gee, D., Sowter, A., Grebby, S., de Lange, G., Athab, A., Marsh, S., 2019. National geohazards mapping in Europe: interferometric analysis of the Netherlands. *Eng. Geol.* 256, 1–22. <https://doi.org/10.1016/j.enggeo.2019.02.020>.
- Grebby, S., Orynbassarova, E., Sowter, A., Gee, D., Athab, A., 2019. Delineating ground deformation over the Tengiz oil field, Kazakhstan, using the Intermittent SBAS (ISBAS) DInSAR algorithm. *Int. J. Appl. Earth Obs. Geoinf.* 81, 37–46. <https://doi.org/10.1016/j.jag.2019.05.001>.
- Guizar-Sicairos, M., Thurman, S.T., Fienup, J.R., 2008. Efficient subpixel image registration algorithms. *Opt. Lett.* 33 (2), 156–158. <https://doi.org/10.1364/OL.33.000156>.
- Hanssen, R.F., Van Leijen, F.J., Van Zwieten, G.J., Dortland, S., Bremmer, C.N., Kleuskens, M., 2008. Validation of PSI results of Alkmaar and Amsterdam within the Terrafirma validation project. In: *Proceedings of FRINGE 2007*, pp. 26–30.
- Hiscock, K.M., 2009. *Hydrogeology: Principles and Practice*. John Wiley & Sons.
- Hoffmann, J., Zebker, H.A., Galloway, D.L., Amelung, F., 2001. Seasonal subsidence and rebound in Las Vegas Valley, Nevada, observed by synthetic aperture radar interferometry. *Water Resour. Res.* 37 (6), 1551–1566. <https://doi.org/10.1029/2000WR900404>.
- Holliday, D.W., 1986. Devonian and carboniferous basins. In: Downing, R.A., Gray, D.A. (Eds.), *Geothermal Energy: The Potential in the United Kingdom*. 27. British Geological Survey, HMSO, London, pp. 84–109.
- Hulbert, A.G., Terrington, R.L., 2014a. Metadata report for the East Midlands region of the Pennine Basin 1:250 000 resolution geological model. In: *British Geological Survey Open Report, OR/14/026*, (14pp).
- Hulbert, A.G., Terrington, R.L., 2014b. Metadata report for the south-west Pennine Basin and adjacent area 1:250 000 resolution geological model. In: *British Geological Survey Open Report, OR/14/027*, (14pp).
- Jain, V.K., Dixit, M., Chitra, R., 2015. Correlation of plasticity index and compression index of soil. *Int. J. Innov. Eng. Technol.* 5, 263–270.
- Liu, P., Gao, Y., Shang, M., Yi, X., 2020. Predicting water level rises and their effects on surrounding karst water in an abandoned mine in Shandong, China. *Environmental Earth Sciences* 79 (1), 51. <https://doi.org/10.1007/s12665-019-8798-7>.
- Lu, Z., Kwoun, O.I., 2008. Radarsat-1 and ERS InSAR analysis over southeastern coastal Louisiana: Implications for mapping water-level changes beneath swamp forests. *IEEE Transactions on Geoscience and Remote Sensing* 46 (8), 2167–2184. <https://doi.org/10.1109/TGRS.2008.917271>.
- Motagh, M., Shamshiri, R., Haghighi, M.H., Wetzel, H.U., Akbari, B., Nahavandchi, H., Roessner, S., Arabi, S., 2017. Quantifying groundwater exploitation induced subsidence in the Rafsanjan plain, southeastern Iran, using InSAR time-series and in situ measurements. *Eng. Geol.* 218, 134–151. <https://doi.org/10.1016/j.enggeo.2017.01.011>.
- Osmanoglu, B., Sunar, F., Wdowinski, S., Cabral-Cano, E., 2016. Time series analysis of InSAR data: Methods and trends. *ISPRS Journal of Photogrammetry and Remote Sensing* 115, 90–102. <https://doi.org/10.1016/j.isprsjprs.2015.10.003>.
- Pearse, J., Singhroy, V., Samsonov, S., Li, J., 2014. Anomalous surface heave induced by enhanced oil recovery in northern Alberta: InSAR observations and numerical modelling. *J. Geophys. Res. Solid Earth* 119 (8), 6630–6649. <https://doi.org/10.1002/2013JB010885>.
- Poland, J.F., 1984. *Guidebook to Studies of Land Subsidence Due to Ground-Water Withdrawal*. UNESCO, Paris, France.
- Rae, G.W., 1978. *Groundwater resources in the coalfields of England and Wales*. In: *B the Yorkshire Coalfield. Technical Note*. Central Water Planning Unit, Reading.
- Rutqvist, J., Vasco, D.W., Myer, L., 2010. Coupled reservoir-geomechanical analysis of CO₂ injection and ground deformations at in Salah, Algeria. *Int. J. Greenh. Gas Control* 4 (2), 225–230. <https://doi.org/10.1016/j.ijggc.2009.10.017>.
- Sowter, A., Bateson, L., Strange, P., Ambrose, K., Syafudin, M.F., 2013. DInSAR estimation of land motion using intermittent coherence with application to the south Derbyshire and Leicestershire coalfields. *Remote Sens. Lett.* 4 (10), 979–987. <https://doi.org/10.1080/2150704X.2013.823673>.
- Sowter, A., Amat, M.B.C., Cigna, F., Marsh, S., Athab, A., Alshammari, L., 2016. Mexico City land subsidence in 2014–2015 with Sentinel-1 IW TOPS: results using the intermittent SBAS (ISBAS) technique. *Int. J. Appl. Earth Obs. Geoinf.* 52, 230–242. <https://doi.org/10.1016/j.jag.2016.06.015>.
- Sowter, A., Athab, A., Novellino, A., Grebby, S., Gee, D., 2018. Supporting energy regulation by monitoring land motion on a regional and national scale: a case study of Scotland. *Proc. Inst. Mech. Eng. Part A: J. Power Energy* 232 (1), 85–99. <https://doi.org/10.1177/0957650917737225>.
- Terzaghi, K., 1925. *Principles of soil mechanics, IV—settlement and consolidation of clay*. *Eng. News Record* 95 (3), 874–878.
- Torres, R., Snoeij, P., Geudtner, D., Bibby, D., Davidson, M., Attema, E., Potin, P., Rommen, B., Flourey, N., Brown, M., Traver, I.N., 2012. GMES Sentinel-1 mission. *Remote Sensing of Environment* 120, 9–24. <https://doi.org/10.1016/j.rse.2011.05.028>.
- Van Tonder, G.J., Usher, B.H., Dennis, I., Vermeulen, P.D., 2007. Predicting rebound in a deep colliery in South Africa. *Mine Water Environ.* 26 (2), 79–87. <https://doi.org/10.1007/s10230-007-0154-6>.
- Wright, P., Stow, R., 1999. Detecting mining subsidence from space. *Int. J. Remote Sens.* 20 (6), 1183–1188. <https://doi.org/10.1080/014311699212939>.
- Wright, I.A., Pacuszkiewicz, K., Belmer, N., 2018. Increased water pollution after closure of Australia's longest operating underground coal mine: a 13-month study of mine drainage, water chemistry and river ecology. *Water, Air, & Soil Pollution* 229 (3), 55. <https://doi.org/10.1007/s11270-018-3718-0>.
- Younger, P.L., 2016. A simple, low-cost approach to predicting the hydrogeological consequences of coalfield closure as a basis for best practice in long-term management. *Int. J. Coal Geol.* 164, 25–34. <https://doi.org/10.1016/j.coal.2016.06.002>.
- Younger, P.L., Adams, R., 1999. *Predicting mine water rebound*. In: *Environment Agency R&D Technical Report W179*. Bristol, UK, (108pp).

5. National Geohazards Mapping in Europe

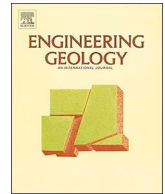
A secondary conclusion from the Northumberland and Durham study was that the ability to concatenate Sentinel-1 frames together was required. Over time the divisions between Sentinel-1 frames change, hence, using only a single image for each date can result in areas that are not imaged throughout the time-series. This leaves areas which cannot be surveyed. The modification of the software enabled the concatenation of scenes so to be able to create a seamless strip of imagery. Such capability facilitates wide-area mapping and, hence, the potential and challenges of generating deformation measurements at the national scale was evaluated over the Netherlands. The Netherlands was chosen as it is a relatively small country and is subject to many natural and anthropic hazards. Furthermore, the quantification and delineation of subsidence is particularly significant given that parts of the country lie below sea level.



ELSEVIER

Contents lists available at ScienceDirect

Engineering Geology

journal homepage: www.elsevier.com/locate/enggeo

National geohazards mapping in Europe: Interferometric analysis of the Netherlands

David Gee^{a,b,*}, Andrew Sowter^b, Stephen Grebby^a, Ger de Lange^c, Ahmed Athab^b, Stuart Marsh^a^a Nottingham Geospatial Institute, University of Nottingham, Nottingham NG7 2TU, United Kingdom^b Geomatic Ventures Limited, Nottingham Geospatial Building, Nottingham NG7 2TU, United Kingdom^c Deltares, Post box 85467, 3508 AL Utrecht, the Netherlands

ARTICLE INFO

Keywords:

National geohazard mapping
 Surface deformation
 Interferometric SAR
 Intermittent SBAS
 Sentinel-1
 Copernicus programme

ABSTRACT

The launch of Copernicus, the largest Earth Observation program to date, is significant due to the regular, reliable and freely accessible data to support space-based geodetic monitoring of physical phenomena that can result in natural hazards. In this study, wide area interferometric synthetic aperture radar (InSAR) capability is demonstrated by processing 435 Copernicus Sentinel-1 C-Band SAR images (May 2015–May 2017) using the Intermittent Small Baseline Subset (ISBAS) method to produce a wide-area-map (WAM) covering 53,000 km² of the Netherlands, Belgium and Germany. The ISBAS-WAM contains over 19 million measurements, achieving a ground coverage of 94%. The retrieval of measurements over soft surfaces (i.e. agricultural fields, forests and wetlands) was crucial due the dominance of non-urban land cover. A statistical analysis of the velocities reveals that intermittently coherent measurements in rural areas can provide reliable, additional deformation information with a very high degree of confidence (5σ), which spatially correlates to known deformation features associated with compressible soils, infrastructure settlement, peat oxidation, gas production, salt mining and underground and opencast mining. The spatial distribution of deformations concurs with independent data sources, such as previous persistent scatterer interferometry (PSI) deformation maps, models of subsidence and settlement susceptibility, and quantitatively with GPS measurements over the Groningen gas field.

Remotely derived deformation products, with near complete spatial coverage, provide a powerful screening tool for mitigation and remediation of geological and geotechnical issues to help in the protection of assets, property and life. The ISBAS-WAM demonstrates that routine generation of such products on a continental scale is now theoretically achievable, given the establishment of the Copernicus programme and the development of state-of-the-art InSAR methods, such as ISBAS.

1. Introduction

In Europe, the European Space Agency (ESA) and the European Union (EU) have supported a large range of projects that have demonstrated the feasibility of space technologies to monitor geohazards across the continent, although primarily those affecting cities. Examples of such projects include ESA-TerraFirma (2003–2012) (Adam et al., 2009), EU-FP7-Subcoast (2010–2013) (Grujters and van der Krogt, 2013), EU-FP7-PanGeo (2011–2014) (Capes, 2012) and EU-FP7-PROTHEGO (2015–2018) (Themistocleous et al., 2016). Satellite-based interferometric synthetic aperture radar (InSAR) has played a central role in all of these projects as it is capable of measuring and monitoring a wide range of geohazards including landslides (Bayer et al., 2017), tectonics (Colesanti et al., 2003) and volcanology (Hooper et al., 2004), in addition to ground motion associated with anthropogenic activity

such as oil and gas operations (Castelletto et al., 2013), carbon capture and storage (Rohmer et al., 2015), mining (Gee et al., 2017), civil engineering works (Marshall et al., 2018) and groundwater abstraction (Bonì et al., 2015).

The success of the value-added products derived from the aforementioned ESA and EU projects demonstrate that InSAR has reached a level of maturity where national-scale land motion maps are now feasible. There have been a number of demonstrations of wide-area mapping capability (e.g. Adam et al., 2011; Chaussard et al., 2013; Chaussard et al., 2014), and full maps of the Netherlands (Cuenca et al., 2011; Hanssen and Cuenca, 2012) and Italy (Costantini et al., 2017) have been generated using persistent scatterer interferometry (PSI) techniques. However, PSI solutions are primarily limited to mapping surface deformation in urbanised areas, which comprise only 12% and 5% of the surface area of the Netherlands and Italy, respectively

* Corresponding author at: Nottingham Geospatial Institute, University of Nottingham, Nottingham NG7 2TU, United Kingdom
 E-mail address: david.gee@nottingham.ac.uk (D. Gee).

<https://doi.org/10.1016/j.enggeo.2019.02.020>

Received 13 November 2018; Received in revised form 18 February 2019; Accepted 19 February 2019

Available online 20 February 2019

0013-7952/ © 2019 Elsevier B.V. All rights reserved.

(European Environment Agency, 2012). Furthermore, at the time of these earlier studies, ample SAR data was generally not available and, in some cases, marginal for reliable InSAR analysis. Consequently, the PSI results required interpolation and/or assimilation with ancillary data to achieve nationwide coverage. For example, Cuenca et al. (2011) utilized ERS 1/2 and ENVISAT SAR data alongside supplementary geodetic measurements from levelling and GPS for the period 1992–2011. Since then, advances have been made in state-of-the-art InSAR processing techniques, such as the Intermittent Small Baseline Subset (ISBAS) method (Sowter et al., 2013; Sowter et al., 2016), which can derive ground motion measurements over urban and rural environments alike. Moreover, the availability and accessibility of SAR data has also vastly improved with the launch of the Copernicus programme.

Copernicus is an EU programme, managed and coordinated by the European Commission, which was founded to develop European information services based on in situ and satellite Earth Observation (EO) data. Copernicus is served via a group of satellite missions (Sentinels) which deliver regular, reliable, near real-time data that are provided freely to all end users (i.e. commercial and institutional). It will eventually be served by twenty satellites as part of 6 missions, the first of which, Sentinel-1a, was launched in April 2014. Sentinel-1 is an imaging radar mission carrying a C-Band (5.405 GHz) SAR instrument at an altitude of 693 km in a near-polar sun-synchronous orbit. The two-satellite constellation currently maintains a conflict-free repeat pass of 6 days over Europe, representing a significant improvement in reliability and revisit time over legacy SAR missions (Torres et al., 2012). The technical and operational capabilities of the mission fully support interferometric processing and it therefore has potential to underpin cost-effective, wide area geohazard mapping across Europe and, indeed, anywhere in the world, for the foreseeable future.

Sentinel-1 is already showing significant promise in supporting national geohazard programmes, which require products like maps of surface deformation to be generated in a systematic semi-automated process and methodically kept up to date with new data (Van der Meulen et al., 2013). This necessitates the operational processing of large volumes of EO data on a regular basis. Currently, over 8 Petabytes per year are acquired, processed and disseminated by the Copernicus programme which presents new challenges in the era of big EO data. The volume, frequency, variety and complexity of data outstrips conventional computing and storage capabilities and therefore new solutions are required to support EO applications.

Given this abundance of new EO data and the need for a semi-automated operational approach to generating national-scale surface displacement information, this study aims to demonstrate the potential of Copernicus Sentinel-1 SAR data for geohazard mapping and monitoring in Europe. This is achieved through the generation of an Intermittent Small Baseline Subset Wide-Area-Map (ISBAS-WAM) covering the Netherlands and extending into neighbouring areas of Belgium and Germany (totalling 53,000 km²), without the need for interpolation or integration with ancillary data. The ISBAS-WAM highlights ground deformation associated with a range of potential geohazards capable of posing a risk to both infrastructure and society, which are subsequently discussed in detail. Finally, the processing requirements for a full Europe-wide deformation map are calculated to determine the opportunity and challenges Copernicus presents for future operational monitoring services.

2. The Netherlands

2.1. Land cover

The Netherlands has a total land mass of ~33,500 km² and is dominated by rural areas which comprise 86% of the total surface area

(Fig. 1). Agriculture (73%) dominates land use in the rural landscape, with the remainder comprising various forested and semi-natural areas (12%) and wetlands (1%). Artificial surfaces in the form of housing, built structures and transport infrastructure make up 14% of the total land cover, evident in pockets of distinct urban clusters. Urban developments are most prominent between Amsterdam and Rotterdam in the Randstad megalopolis in the west, with notably less development in the eastern and northern provinces.

2.2. Geology

The Netherlands is located on the south-eastern edge of the Cenozoic North Sea basin and consists of three distinct domains: a Holocene coastal barrier formed of sand dunes in the west, a lowland coastal and fluvial plain, and a relatively higher inland area of Pleistocene deposits that extends to the east (De Mulder, 1994; Fig. 2). Covering about half of the country, the coastal and fluvial plain lies approximately at and below sea level and consists mainly of sand, clay and peat. Peat beds, which can be up to 8 m thick, are geotechnically the weakest part of the Holocene succession. Such deposits, along with younger soft Holocene clays, are particularly predisposed to settlement and compaction. Holocene sands deposited in tidal channels are very loosely packed and often exhibit porosities > 40%, consequently, such sands can be unstable and prone to liquefaction (De Mulder, 1994). The Pleistocene deposits in the east are predominantly sandy soils that are glacial, fluvial and aeolian in origin. While generally flat, these deposits gently slope upwards to an elevation of 20 m above mean sea level in the east and south, although ice-pushed ridges can locally reach heights of 100 m (De Mulder, 1994; Van der Meulen et al., 2013).

2.3. Geohazards in the Netherlands

Due to its low-lying geographical setting and sedimentary composition, flooding and land subsidence are the predominant geohazards in the Netherlands. Deformations can be broadly classified into two categories: shallow Holocene motions (up to 30 m deep) induced by peat oxidation, sediment compaction and dewatering; and deeper sources driven by gas production, mining, tectonics and underground water pumping (Hanssen and Cuenca, 2012). The combination of sea level rise and land subsidence increases the risk of flooding, salt water contamination of low-lying aquifers and surface water and the cost of maintaining drained agricultural farmland in low-lying coastal areas. If it were not for anthropogenic (e.g. dikes and water pumps) and natural defences (i.e. sand dunes), over 60% of the country would be submerged at high tide and most of the sub-datum area would inundate due to upward seepage (De Mulder, 1994). Soil compaction increases the need for pumping, which in turn increases rates of subsidence, hence, the detrimental circle the Netherlands is locked into. Differential motion of soils in the shallow subsurface are hazardous to built structures and surface and sub-surface infrastructure. Damage severity depends on the velocity of differential motions which is controlled by the spatial distribution and thickness of soft soil layers, groundwater regime and the presence or state of foundations (Peduto et al., 2017). Furthermore, the peatlands that dominate the Dutch lowlands act as large carbon stores, and drainage of such environments contributes to increasing global temperatures and climate change (Erkens et al., 2016).

Secondary hazards include induced seismicity from the extraction of natural gas, which has caused recent public concern following the 2012 magnitude 3.6 Huizinge earthquake in Groningen (Van Thienen-Visser et al., 2018). Reservoir compaction is considered to be a driving force of induced seismicity in the Groningen field (Bourne et al., 2014). Accordingly, there are extensive legal, technical and organizational frameworks to ensure subsidence remains within predefined limits and is

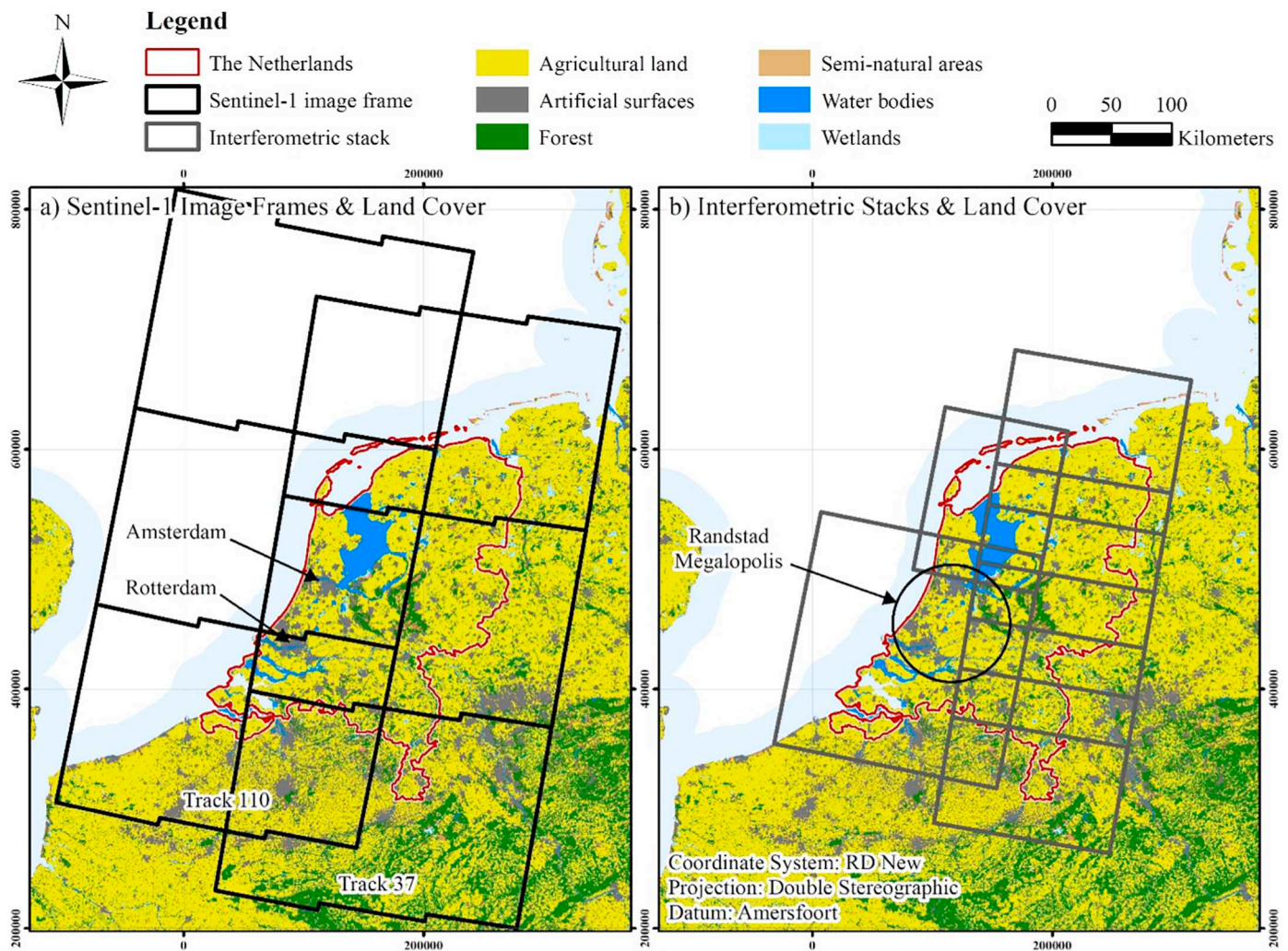


Fig. 1. CORINE Land Cover inventory (European Environment Agency, 2012): (a) Sentinel-1 image frames (b) Interferometric stacks. European Environment Agency © 2012.

openly communicated to the public (de Waal et al., 2012).

3. Processing

3.1. The ISBAS method

A variety of PSI (e.g. Ferretti et al., 2001; Hooper et al., 2004) and small baseline methods (e.g. Berardino et al., 2002) have been shown to produce very accurate profiles of deformation over hard targets such as rocky or urban areas. However, a principal limitation of InSAR analysis is decorrelation, whereby the scattering properties of the imaged target change over time. This is common over rural settings where, due to processes such as shrink-swell and agricultural practises, scatterers within resolution elements move relative to one another. Consequently, the integration of phase difference becomes inaccurate if the change in phase is a substantial percentage of the phase cycle (Zebker and Villasenor, 1992). Approximately 86% of the surface of the Netherlands is comprised of vegetated surfaces, which constitutes a significant hindrance to obtaining a high density of surface displacement measurements and, therefore, achieving detailed spatial characterisation of deformation processes (Crosetto et al., 2010).

Since the introduction of the first multi-temporal InSAR method in the late 1990's, there have been new processing algorithms that have

successfully managed to increase the number and spatial density of returned InSAR measurements (e.g. Hooper, 2008; Ferretti et al., 2011). The ISBAS method (Sowter et al., 2013; Sowter et al., 2016) is a recent development that extends the coverage of deformation measurements into rural environments to provide near complete coverage. It is an adapted version of the low-resolution SBAS algorithm (Berardino et al., 2002), which computes solutions for pixels which exhibit coherence in all stacked interferograms (coherent pixels). In contrast, ISBAS relaxes the need for coherence to be maintained across all interferograms. It computes solutions for coherent pixels and pixels which exhibit coherence for a specified subset of the total multiple master interferograms (intermittently coherent pixels). The ISBAS method was employed here due to the predominance of vegetation cover, and since it has been proven to achieve accurate validated results in parts of the Netherlands (Gee et al., 2016) and to enable national deformation mapping elsewhere (Sowter et al., 2018). For a Sentinel-1 Interferometric Wide (IW) image with a nominal spatial resolution better than 25 m, the ISBAS solution is of approximately 90 m resolution.

3.2. Data processing

A total of 435 Sentinel-1 Level-1 IW Single Look Complex (SLC) products (May 2015–May 2017) from descending tracks 110 and 37

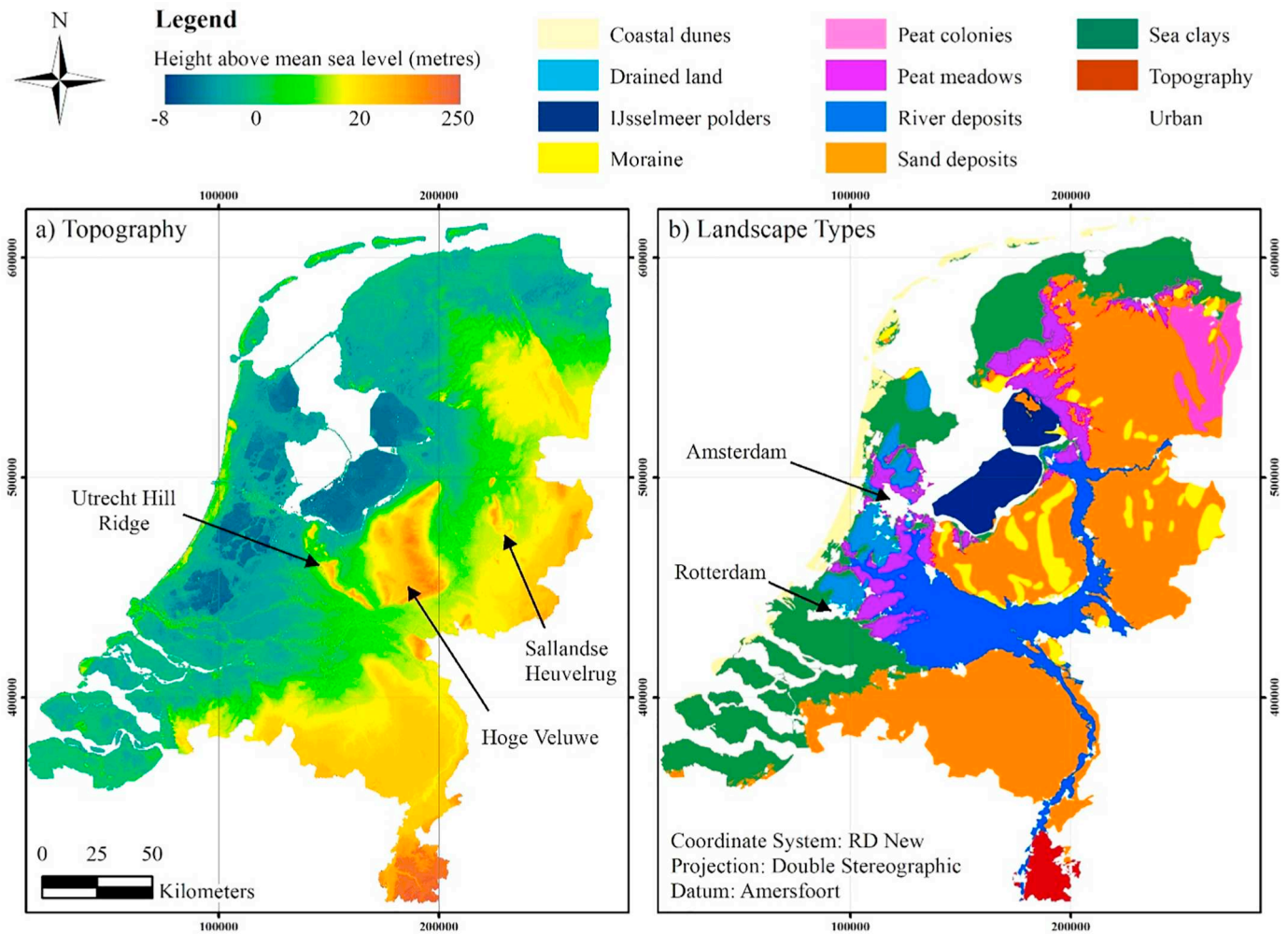


Fig. 2. (a) Topography and (b) Landscape types of the Netherlands.

were utilized (Table 1; Fig. 1a). The flow diagram in Fig. 3 outlines the implemented deformation mapping approach, in accordance with that of Sowter et al. (2018). Readers are referred to Sowter et al. (2013, 2016) for further details on the ISBAS algorithm and its application to Sentinel-1 data. Six interferometric stacks (Fig. 1b) were processed separately, whereby at least 30 km overlap was maintained between both neighbouring stacks in azimuth and neighbouring tracks to aid subsequent mosaicking. Two-pass low-resolution differential interferograms were generated between image pairs with restrictions of 150 m on the perpendicular orbital baseline and 365 days on the temporal baseline (Table 1). Deformation velocities were computed for pixels for which coherence (> 0.25) was maintained in ≥ 400 and 340 interferograms for tracks 110 and 37, respectively. Phase ramps attributed to orbital errors were calculated and removed, and a 90 m SRTM DEM was used to simulate and subtract phase associated with topography. Reference points were chosen in major cities where there was an abundance of highly coherent points (Fig. 4a). Using a linear model of deformation, line-of-sight velocities for the time period were computed and then projected into the vertical direction by means of dividing by the cosine of the incidence angle. Whilst feasible for regional areas (e.g. Gee et al., 2017), the generation of time-series at the national scale is not currently achievable due to the computational and storage demands for such a large volume of pixels generated by the ISBAS method. Software developments are ongoing to address this matter in future mosaics. A seamless deformation map was generated by mosaicking the six subsets. Individual mosaics were first generated from the two stacks in track 110 and four stacks in track 37, followed

subsequently by the mosaicking of the two tracks to generate the ISBAS-WAM.

4. Results

4.1. Average velocities – national deformation product

The mosaicked deformation product (ISBAS-WAM) covers an area of 53,000 km² and reveals the average vertical ground motion for each pixel for the period May 2015–May 2017 (Fig. 4a). The pixels cover 94% of the total land surface available, with velocities computed over hard targets in towns and cities (artificial surfaces) and over soft targets in rural areas (agricultural land, forests, semi-natural areas and wetlands). It is estimated that had velocities been solely derived for coherent pixels (i.e. pixels where coherence is maintained in every differential interferogram), coverage would have only been 13% and restricted to just urban areas and transport infrastructure (Fig. 4c). Fig. 4d shows the velocities for the subset of intermittently coherent pixels, which evidences the crucial additional characterisation of deformation that the ISBAS method provides.

The mean density of measurements in the ISBAS-WAM is 374 solutions/km² (Table 2), greatest over artificial surfaces (387 solutions/km²) and lowest over forested areas (291 solutions/km²). With respect to computing measurements over forested areas, although often dominated by diffuse scattering from the canopy, the ability of C-band radar to penetrate a canopy and scatter from the ground is well-known and understood to be a function of leaf area index (LAI) and incidence angle

Table 1
Sentinel-1 satellite data and processing parameters used to generate the ISBAS-WAM.

Geometry	Track	N° Frames	Acquisitions per frame	Start date	End date	Max. orbital baseline (metres)	Max. temporal baseline (days)	Multilooking (azimuth: range)	Coherence threshold	N° of interferograms	Interferogram threshold
Descending	110	3	77	5th May 2015	12th May 2017	150	365	5: 22	0.25	1984	400
	37	3	68	12th May 2015	13th May 2017					1670	340

(Wang et al., 1998). Indeed, InSAR has been applied successfully to monitor water level change through a moderate canopy over swamp forests (Lu and Kwoun, 2008) and the ISBAS method has previously shown to return measurements over forested areas and map the underlying deformation (e.g. Sowter et al., 2013).

4.2. Standard errors

The standard error for each measurement expresses the goodness-of-fit between interferogram values and the computed linear velocity and is derived via a least-squares covariance analysis. No outlier rejection was performed in the calculation. The mean standard error was 1.02 mm/year, revealing millimetre precision across the Netherlands (Table 2; Fig. 4b). Coherent pixels exhibit the lowest standard errors, on average 0.62 mm/year, while the mean standard error for intermittently coherent pixels is 1.12 mm/year. With respect to land cover types, artificial surfaces on average have the lowest standard error given the likelihood of more coherent interferograms per pixel to derive velocities; however, pixels located in agricultural and semi-natural areas exhibit approximately millimetre precision.

4.3. Statistically significant velocities

Observed velocities are considered reliable (i.e. ‘real’ and not attributed to noise) if there is a statistically significant difference between them and the population mean for a given level of confidence. Velocities that lie outside ± 3 , 4 and 5 standard errors (σ) away from the population mean were determined (Table 3; Fig. 5), which identifies pixels with a 99.73% (3σ), 99.994% (4σ) and 99.99994% (5σ) confidence that the velocity does not occur by chance. This corresponds to an expected frequency outside of the range of 1 in every 370, 15,787 and 1,744,278 measurements, respectively. At the 3σ , 4σ , 5σ confidence levels 2,816,698, 1,355,775 and 699,802 velocity measurements, respectively, were deemed significant, of which 57%, 48% and 43% are pixels that are characteristically intermittently coherent. Such measurements are retrieved over agricultural land, forests, semi-natural areas and wetlands as well as over artificial surfaces, and spatially correlate to known areas of deformation, as is discussed below.

5. Overview of identified hazards

5.1. Compressible soils

The entirety of the Netherlands is known to be deforming in some way, whereby some areas heave but for the most part soil subsides, much of which occurs as a result of water management practises (Climate Impact Atlas, 2019). Motions in the ISBAS-WAM, in certain instances, show a high degree of spatial correlation to the Netherlands subsidence prognosis map (De Lange et al., 2011; Climate Impact Atlas, 2019; Fig. 6b). It identifies areas most susceptible to soil deformation under current environmental circumstances as calculated with empirical models based on the interpolation of measurements from levelling and benchmarks located in the Holocene layer. The models predict the effects of dewatering on the assumption that, despite subsidence, level indexation is followed (i.e. water levels in drainage ditches remain at a consistent level with respect to ground level) for the period 2000–2050, although higher rates of peat oxidation and subsidence are predicted to occur under warming climate conditions. As the predictive map covers a significantly longer time period than the ISBAS-WAM, a direct quantitative comparison requires some caution as susceptibility is an indication of potential subsidence rather than observed subsidence – which may be controlled or prevented by effective management.

Nonetheless, a close agreement is observed in the Flevoland polders, in the northern Noordoostpolder north-west of Emmeloord (Fig. 6d,e), north-east of Dronten in the Eastern Flevoland polder and most notably

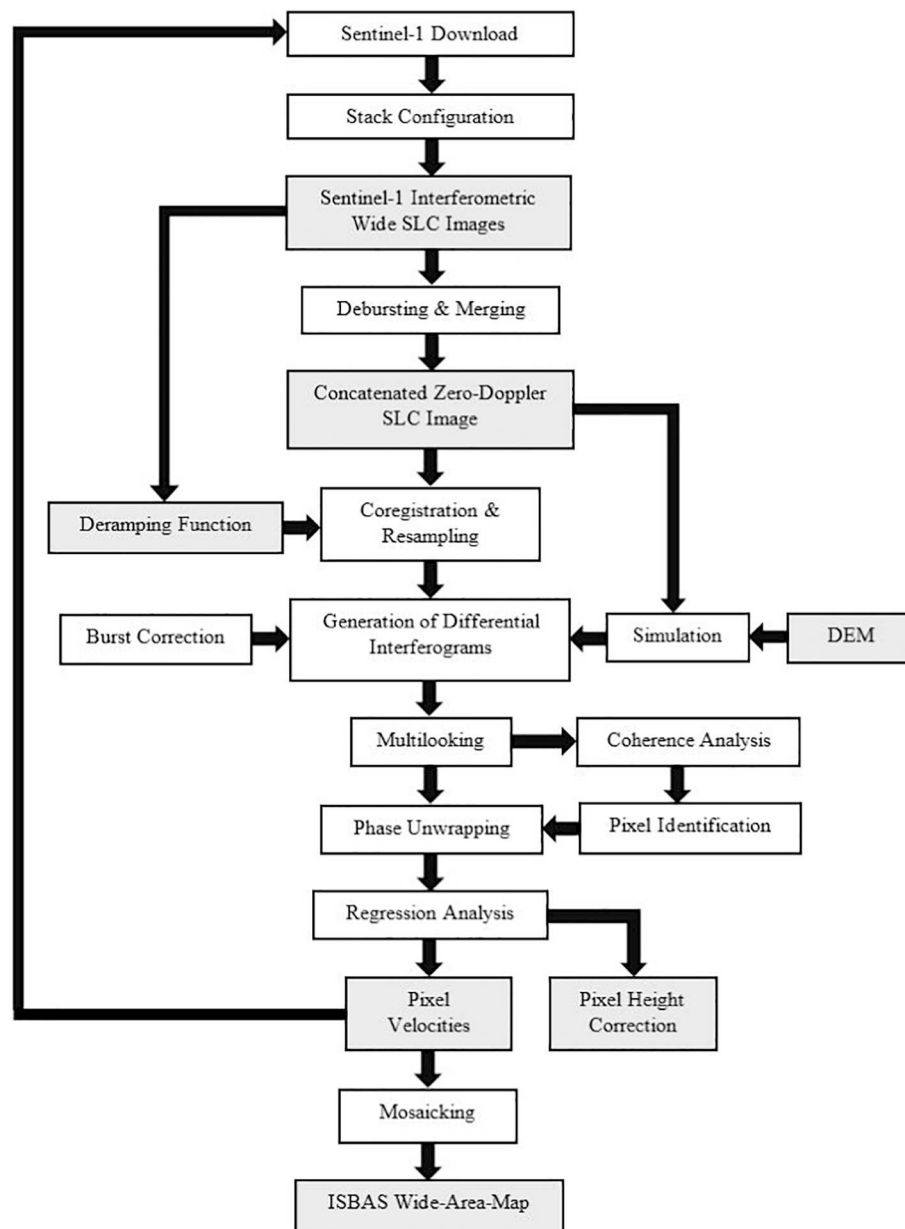


Fig. 3. The deformation mapping processing chain.

in the Southern Flevoland polder near Almere (Fig. 7). Eastern and Southern Flevoland is divided by a dike which runs across from Harderwijk perpendicular to the coastline west of Lelystad. The Southern Flevoland polder is more susceptible to subsidence due to the difference in age of the reclamation and the thickness of the compressible layer, which is reflected in the observed velocities in the ISBAS-WAM. Fig. 7c,d demonstrates the importance of intermittently coherent pixels in characterising soil deformation with a high degree of certainty (4 σ and 5 σ confidence levels).

The ISBAS measurements in the ‘Green Hart’ (Groene Hart), a large rural area within the Dutch Randstad characterised by peat, clay and sandy soils, reveal relative stability and in cases uplift, which is contrary to predicted subsidence patterns (Fig. 6a,b). Previous PSI studies (e.g. Cuenca and Hanssen, 2008) also found that this area was relatively stable in comparison with independent subsidence estimates. The predictive map is based upon susceptibility, and water levels in such low-lying areas are heavily controlled for agriculture and habitation by a complex system of drainage ditches, canals and pumping stations. The ISBAS-WAM suggests such water management practises have been

effective for the period May 2015–May 2017, likely accounting for the discrepancy with the predicted subsidence.

The identification of ground motion in wetlands using traditional geodetic techniques is challenging. In the Netherlands, there is a lack of shallow benchmarks in the vicinity of benchmarks founded in the Pleistocene base (the base for the NAP datum system) and it is notoriously difficult to find consistent levelling stations of surface deformation outside of urban areas. Furthermore, attempts to monitor peat compaction utilizing PSI, such as in Cuenca and Hanssen (2008), have been hindered by decorrelation effects. The low-resolution ISBAS method does not suffer the problems of traditional geodetic methods, nor does it rely on the presence of a persistent scatterer. Hence, the retrieval of measurements on soft targets illustrates the potential to monitor and quantify the effects of water management practises on such areas – which is very valuable for policy makers defining water management strategy (Vönhögen et al., 2012). The Holocene areas of the Netherlands are subject to periodicity in the ground level due to seasonal variations in ground water levels. Ground water levels are lower in the summer when soil dehydration and associated shrinkage,

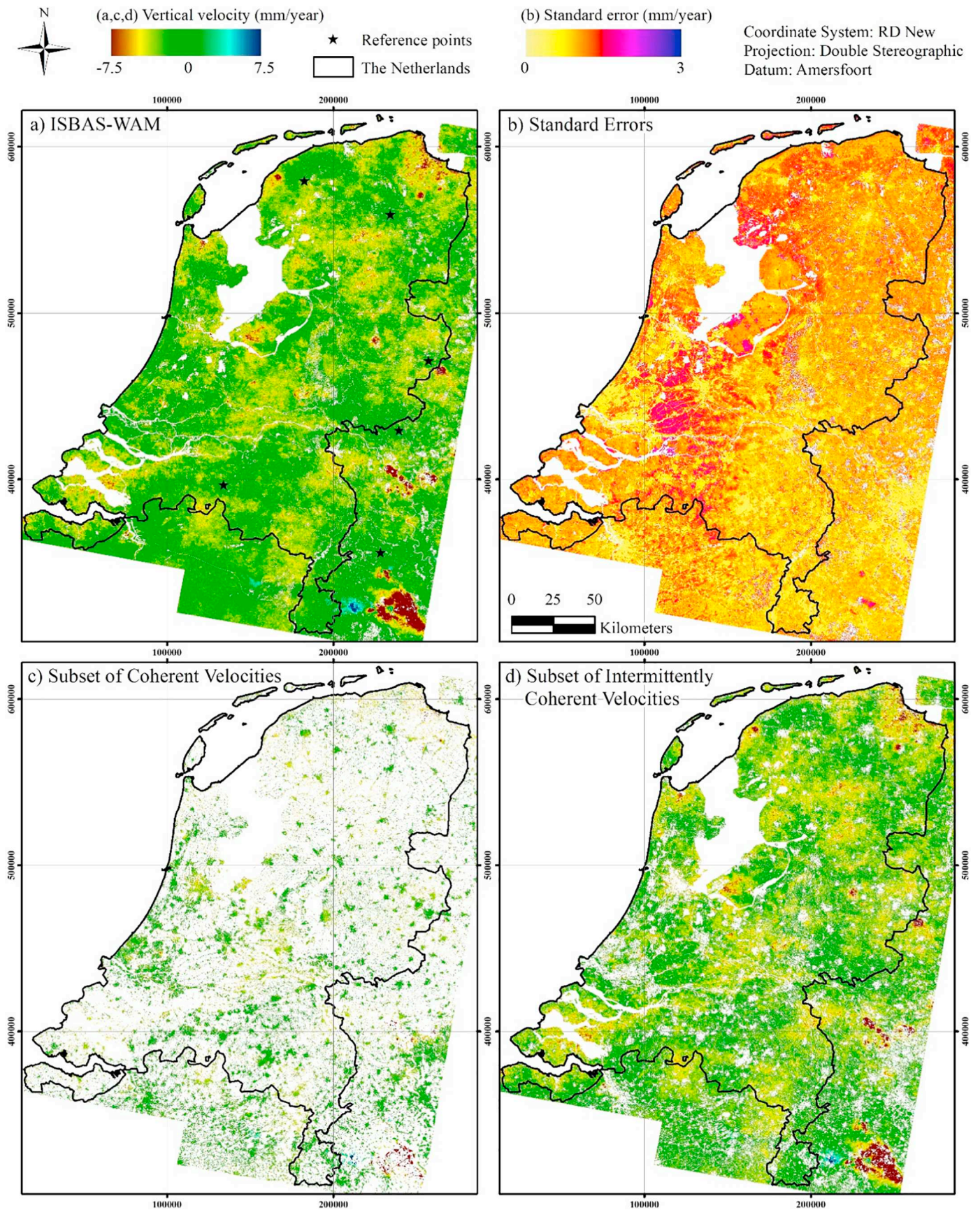


Fig. 4. (a) ISBAS-WAM vertical velocities (mm/year) (b) Standard errors (mm/year) (c) Vertical velocities for the subset of coherent pixels (mm/year) (d) Vertical velocities for the subset of intermittently coherent pixels (mm/year). The complete ISBAS-WAM (a) comprises both coherent and intermittently coherent pixels.

Table 2
Ground coverage and standard errors of velocities.

Statistic	ISBAS-WAM	Coherent pixels	Intermittently coherent pixels	Agricultural land	Artificial surfaces	Forest	Semi-natural areas	Wetlands
Ground coverage								
N° solutions	19,775,110	3,995,561	15,779,549	13,842,700	3,642,577	1,598,758	459,437	231,638
Density (solutions/km ²)	374	75	299	386	387	291	351	335
Standard error (millimetres/year)								
Mean	1.02	0.62	1.12	1.06	0.72	1.25	1.05	1.30
Standard deviation	0.31	0.13	0.25	0.26	0.26	0.29	0.32	0.32
Minimum	0.38	0.38	0.40	0.39	0.38	0.39	0.42	0.44
Maximum	4.60	3.50	4.60	4.30	3.51	3.77	4.60	3.78

Table 3
The number of statistically significant measurements at different levels of confidence.

Confidence level	N° of statistically significant measurements							
	ISBAS-WAM	Coherent pixels	Intermittently coherent pixels	Agricultural land	Artificial surfaces	Forest	Semi-natural areas	Wetlands
3 σ (99.73%)	2,816,698	1,207,956	1,608,742	1,601,233	992,646	124,972	79,314	18,533
4 σ (99.994%)	1,355,775	708,343	647,432	679,471	579,406	49,248	40,082	7568
5 σ (99.99994%)	699,802	396,175	303,627	326,749	326,431	23,128	20,183	3311

oxidation and deeper subsidence are most likely to occur (Vönhögen et al., 2012). In this respect, InSAR time-series data is central to affirming a relationship between ground water and soft soil deformation, as is being as is being demonstrated by ongoing research efforts (e.g. UKRI, 2018).

5.2. Infrastructure settlement

Surface deformations in Holocene areas also relate to the compaction of sediments on which infrastructure has been built (i.e. settlement). Almost all new developments in areas of soft soils (peat, clay) are drained and raised before they are built on. Embankment is also employed to existing structures. Soil consolidates when it is raised with sand, which mainly occurs within the first months to years of placement, although residual settlement can occur decades after construction. The occurrence of soil subsidence itself is often, but not always, the reason for embankment, and such drops in elevation momentarily speed up the deformation process again due to the increased load. As a result of this self-perpetuating cycle, a layer a few metres thick has been generated in areas of weak soils in many historic city centres (Climate Impact Atlas, 2019).

Deformations in the ISBAS-WAM correlate with the susceptibility to surcharge map (De Lange et al., 2012; Climate Impact Atlas, 2019; Fig. 6a,c) which identifies areas susceptible to settlement after embankment. The amount of settlement after a 40-year period under a uniform load of 1 m thick sand fill is modelled; a fictitious situation which is designed to identify areas where taxing the weak subsoil has the greatest consequences, for instance to buried conduits or archaeological remains. Similarly, as with the subsidence prognosis map, a quantitative comparison is not appropriate.

There are numerous instances of deformation related to transport infrastructure, the largest areas of which occur when infrastructure crosses areas highly susceptible to settlement (Figs. 8 and 9). Differential settlements often occur at the intersection of piled and embanked foundations. A 10 km stretch of deformation occurs along the railway to the north of Lelystad (Fig. 8a-c). Notably, the characteristics of deformation change as the route exits north of the city and travels eastward into rural areas. Through the rural environment, the influence of the infrastructure appears to be distributed over the wider surroundings whereby deformation spreads out from the track, over 600 m in some instances. This may be attributed to the drainage system that was put in place with the embankment and the draining character of the sand embankment itself. Interestingly, this suggests that the zone of

influence in a subsidence prone area extends beyond the zone of surcharge settlement. Conversely, as the track enters urban Lelystad from the north, the subsidence is confined to within a 100 m proximity of the track. This is likely due to the fact the railway embankment is surrounded by an urban area that was developed by employing a surface surcharge itself and consists of structures on piled foundations. Other notable examples occur in south Rotterdam (Fig. 9c,d) and along a 10 km stretch of track between Abcoude and Breukelen (Fig. 9e,f).

The longest near-continuous stretch of settlement occurs along an 80 km stretch of the Betuweroute, between Gorinchem and Elst (Fig. 9a,b). The Betuweroute is a major double track freight railway running from Rotterdam to Germany. The track is built on clay, peat, gravel and sandy soils of the Rhine-Meuse-Scheldt river delta, which is particularly susceptible to compaction and settlement. Along the entire route deformation occurs in areas less susceptible to settlement, in the area to the east of Gorinchem (Figs. 6c; 9a,b). This section crosses the alluvial plain of the Rhine, which contains more clay and less peat layers than the area west of Gorinchem. In the western areas, between Gorinchem and Rotterdam, the Betuweroute was constructed with attention to the characteristically settlement-prone soils and less settlement is observed here. Conversely, residual settlement in the clay-dominated fluvial plane area has resulted in noticeable vertical movements. These may develop in unwanted differential settlements, especially where buried sand-filled river valleys are crossed.

Full resolution PSI has previously been utilized for monitoring the structural health of rail infrastructure in the Netherlands, demonstrating the potential to offer a cost-effective alternative to in-situ measurements from survey trains, levelling or GPS (e.g. Peduto et al., 2016; Chang et al., 2017). Chang et al. (2017) used Radarsat-2 imagery (2010–2015) to detect differential motion over the entire rail network and, although the Sentinel-1 and Radarsat-2 analysis do not coincide in time, the spatial distribution of deformations is largely consistent. Whilst PSI returns measurements of the track itself, the ISBAS method is capable of ubiquitously measuring deformations in the surrounding environment which can provide additional insight into the cause of deformation; whether that be the repeated loading of the infrastructure by passing trains, soil compaction in the adjacent land or deeper processes such as salt mining.

There are also cases of deformation relating to other infrastructure (Fig. 8d-g). In Rotterdam, residual settlement affects a 15 km stretch of the A15, which was recently widened (Fig. 8d,e). The project was completed in early 2014 and ran significantly over budget due to doubts over the reliability of the foundations. In Amsterdam, a 9 km

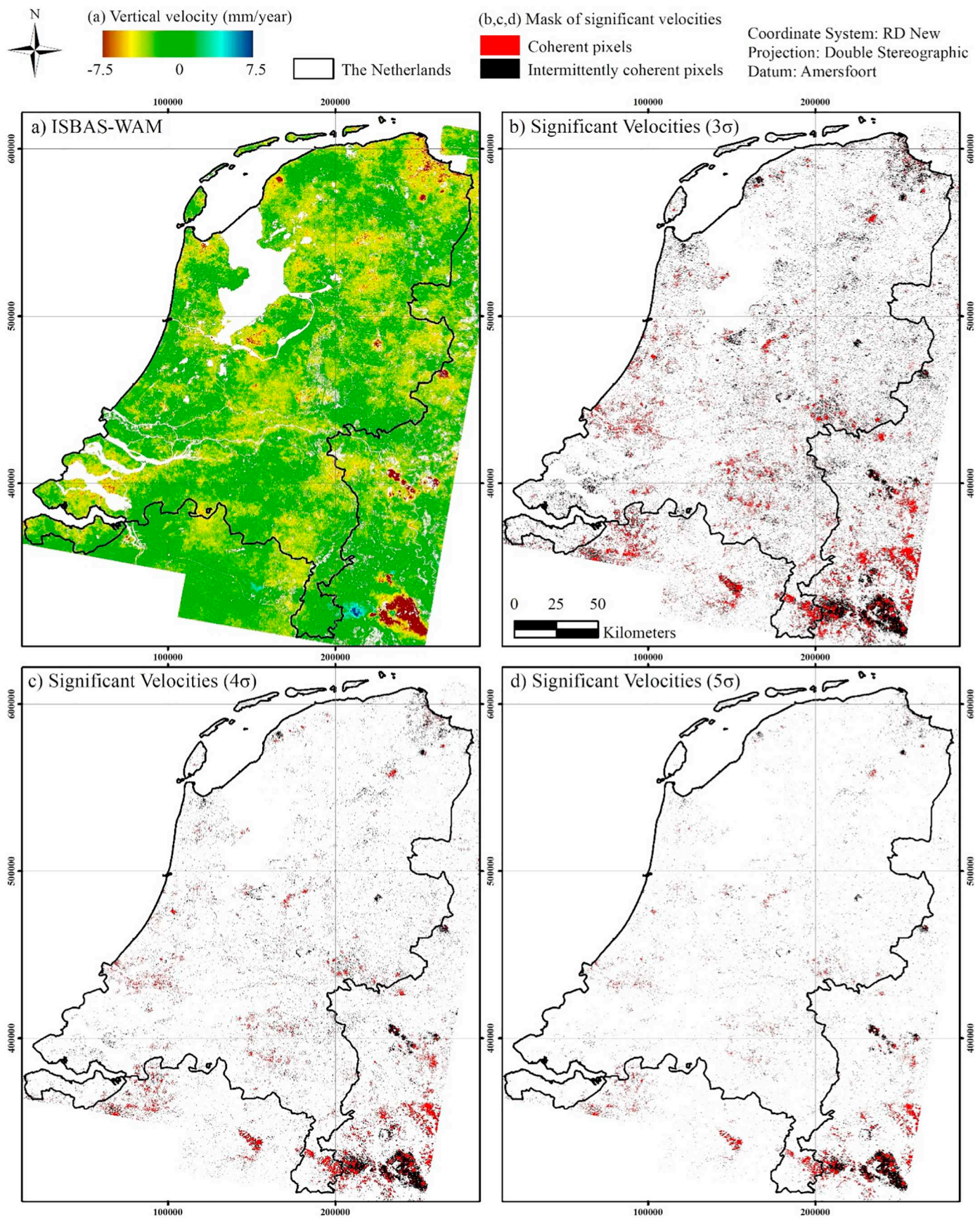


Fig. 5. (a) ISBAS-WAM vertical velocities (mm/year). Mask of statistically significant velocities at: (b) 3σ (99.73%) (c) 4σ (99.994%) (d) 5σ (99.99994%) confidence levels.

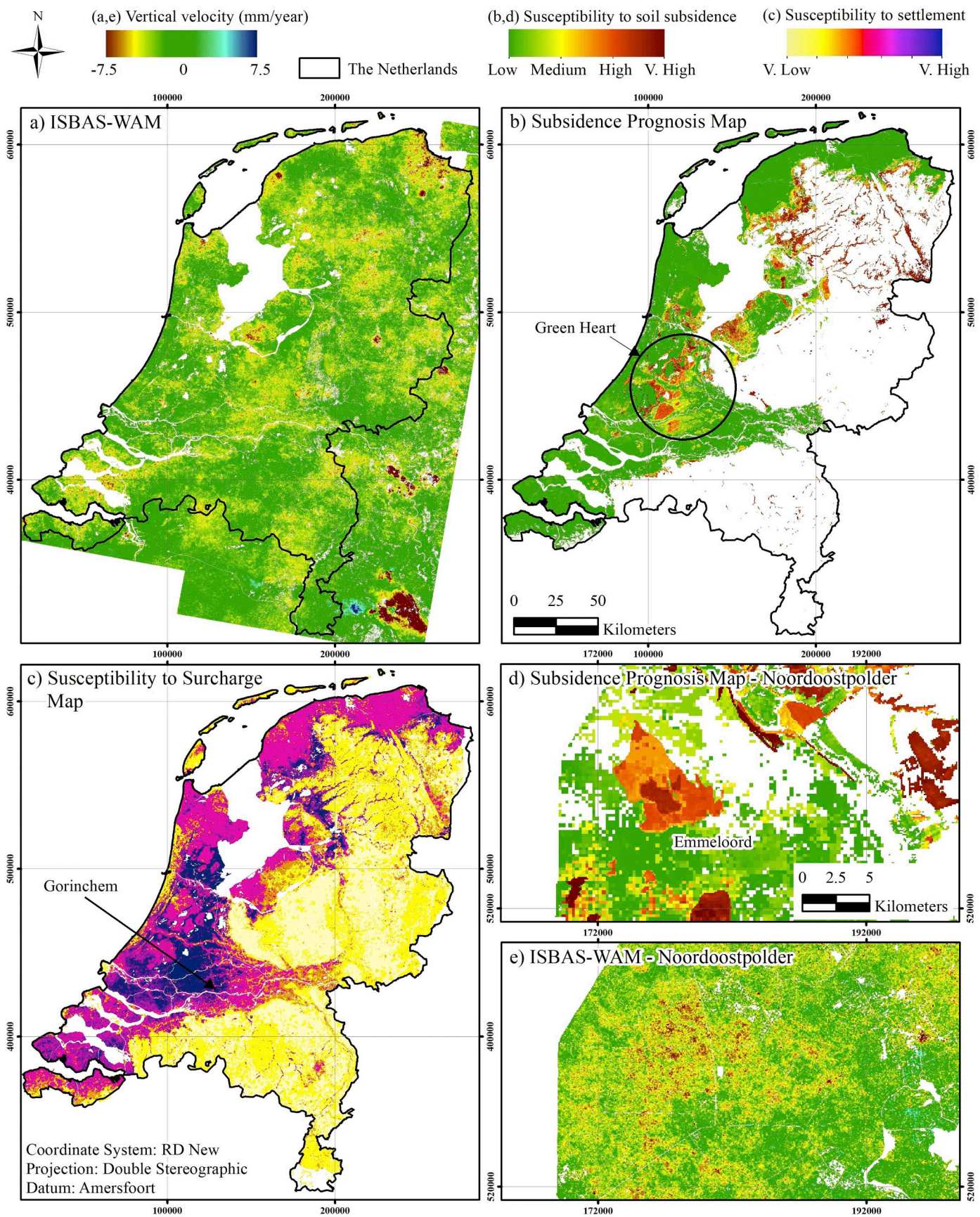


Fig. 6. (a) ISBAS-WAM vertical velocities (mm/year), (b) subsidence prognosis map (De Lange et al., 2011; Climate Impact Atlas, 2019) and (c) susceptibility to surcharge map of the Netherlands (De Lange et al., 2012; Climate Impact Atlas, 2019). (d) Subsidence prognosis map (De Lange et al., 2011; Climate Impact Atlas, 2019) and (e) ISBAS-WAM vertical velocities (mm/year) of the Noordoostpolder, Flevoland. Climate Impact Atlas © 2019.

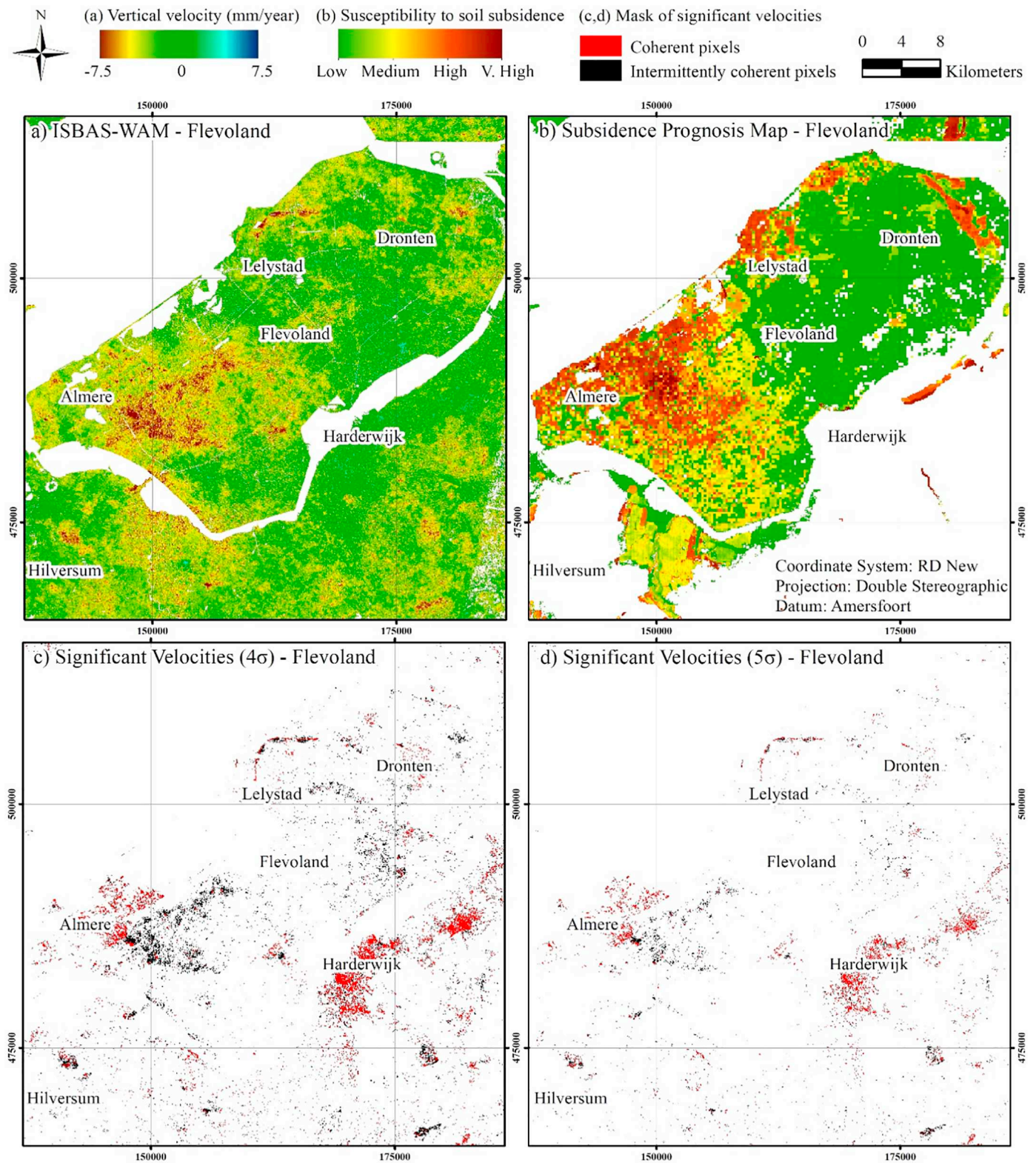


Fig. 7. Flevoland: (a) ISBAS-WAM vertical velocities (mm/year) and (b) subsidence prognosis map (De Lange et al., 2011; Climate Impact Atlas, 2019). Mask of statistically significant velocities at: (c) 4σ (99.994%) (d) 5σ (99.99994%) confidence levels. Climate Impact Atlas © 2019.

stretch of settlement is identified along the A5 motorway, which was opened in December 2012 (Fig. 8f,g). A further example is at Vopak Terminal Amsterdam Westpoort, an oil storage terminal opened in 2011, where deformation correlates to an area of highest settlement susceptibility (Fig. 8f,g).

5.3. Peat oxidation

Subsidence occurs over areas of heathland located on elevated glacial deposits, including the Utrecht Hill Ridge, Hoge Veluwe National Park and perhaps most notably over the Sallandse Heuvelrug National Park (Fig. 10). The Sallandse Heuvelrug national park is

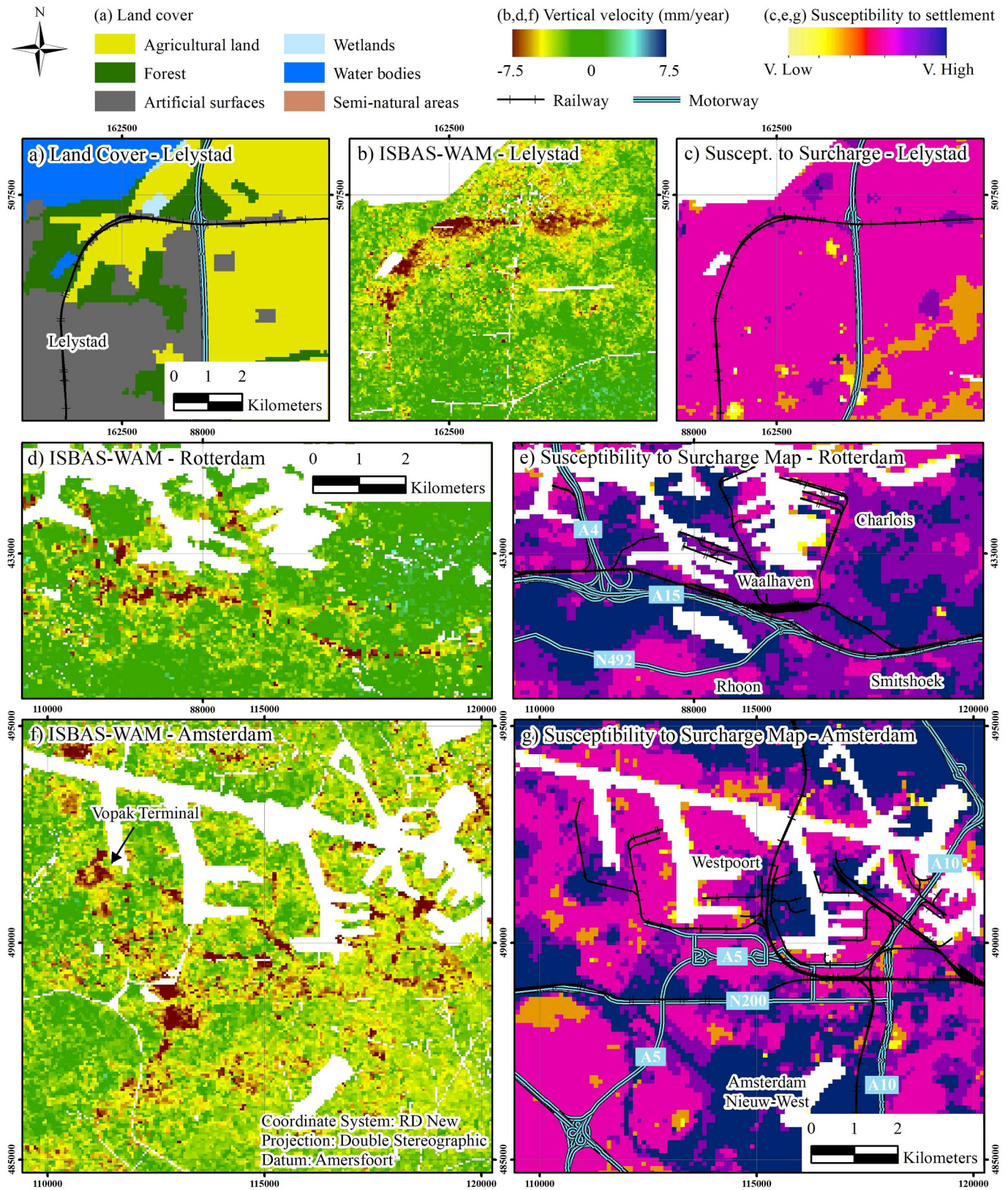


Fig. 8. Infrastructure induced settlement: (a) CORINE Land Cover inventory (European Environment Agency, 2012) and transport infrastructure, (b) ISBAS-WAM vertical velocities (mm/year) and (c) susceptibility to surcharge map (De Lange et al., 2012; Climate Impact Atlas, 2019) and transport infrastructure at Lelystad. (d) ISBAS-WAM vertical velocities (mm/year) and (e) susceptibility to surcharge map (De Lange et al., 2012; Climate Impact Atlas, 2019) and transport infrastructure at Rotterdam. (f) ISBAS-WAM vertical velocities (mm/year) and (g) susceptibility to surcharge map (De Lange et al., 2012; Climate Impact Atlas, 2019) and transport infrastructure at Amsterdam. European Environment Agency © 2012, Climate Impact Atlas © 2019.

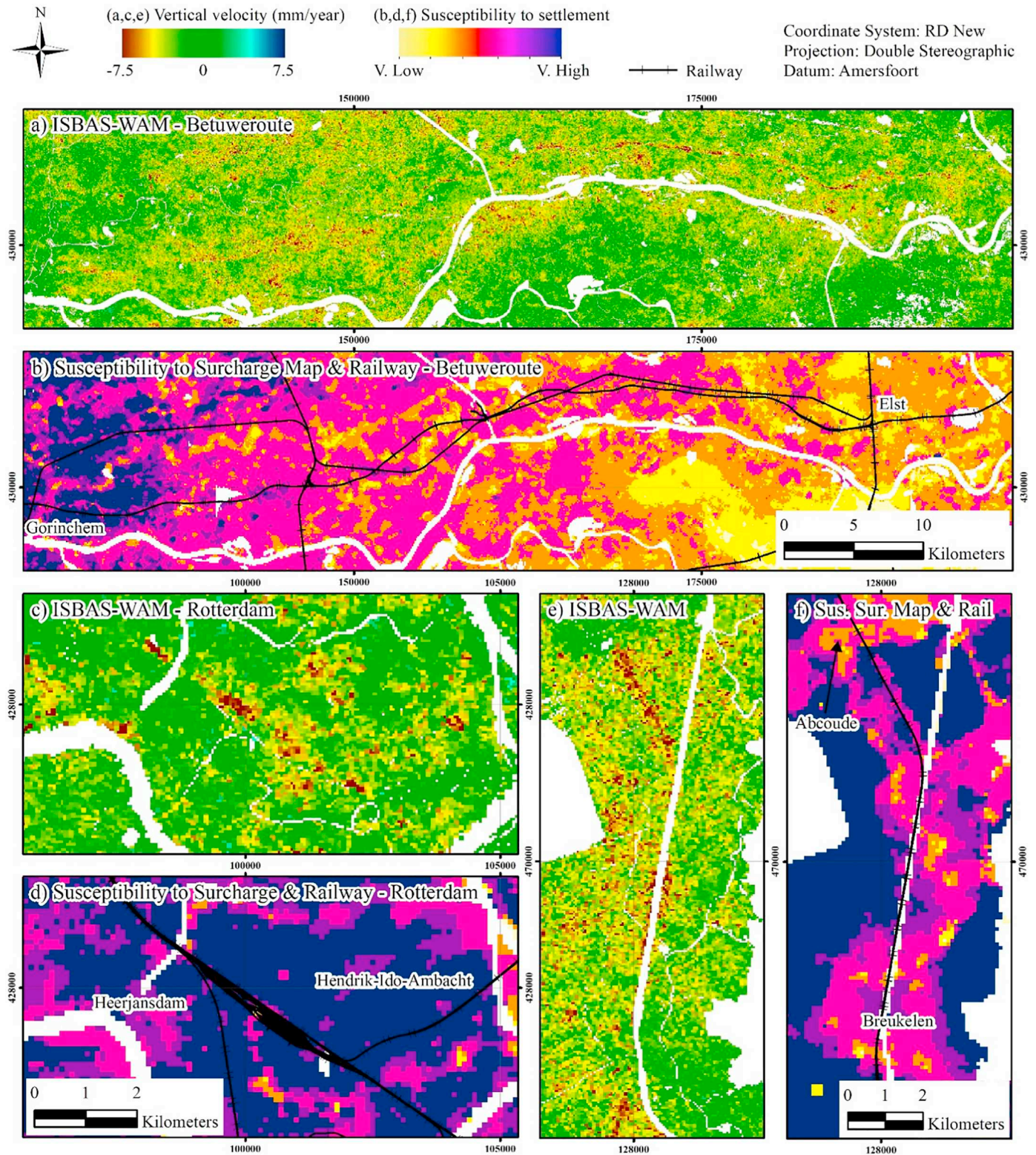


Fig. 9. Settlement along rail routes: (a) ISBAS-WAM vertical velocities (mm/year) and (b) susceptibility to surcharge map (De Lange et al., 2012; Climate Impact Atlas, 2019) of the Betuweroute. (c) ISBAS-WAM vertical velocities (mm/year) and (d) susceptibility to surcharge map (De Lange et al., 2012; Climate Impact Atlas, 2019) of south east Rotterdam. (e) ISBAS-WAM vertical velocities (mm/year) and (f) susceptibility to surcharge map (De Lange et al., 2012; Climate Impact Atlas, 2019) on the route between Amsterdam and Utrecht. Climate Impact Atlas © 2019.

comprised of dry heathland and mixed deciduous-coniferous woodland. The heath landscape has changed substantially over the preceding 100 years due to anthropic influences; wet heath was dewatered and the top soil was removed to be utilized as fertilizer for agriculture, and

dry heath was forested for wood production and to prevent erosion and sand-drifting. The park is now intensely managed to ensure degradation does not continue (Sallandse Heuvelrug, 2018).

Given these deformations are in areas of elevated topography

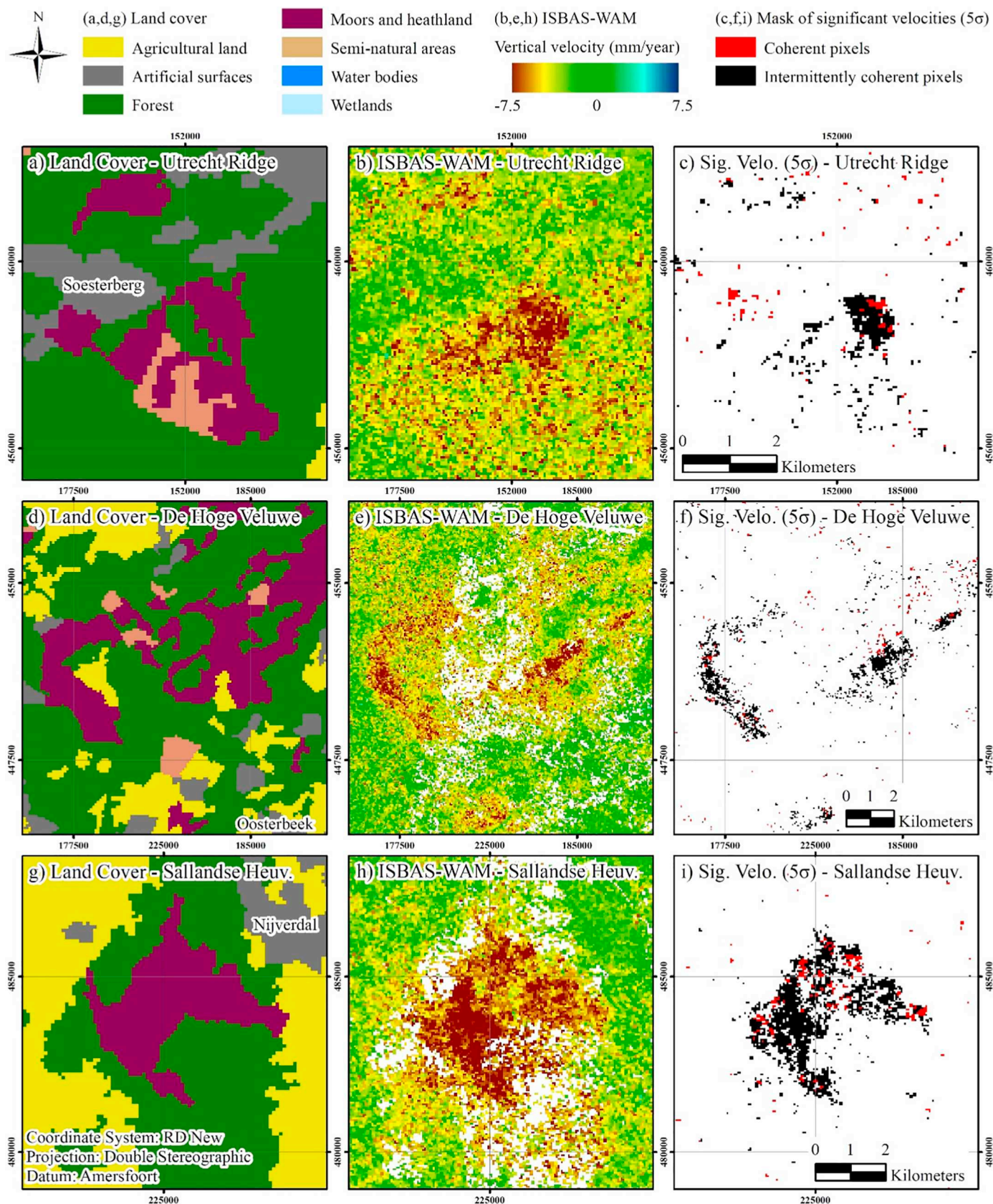
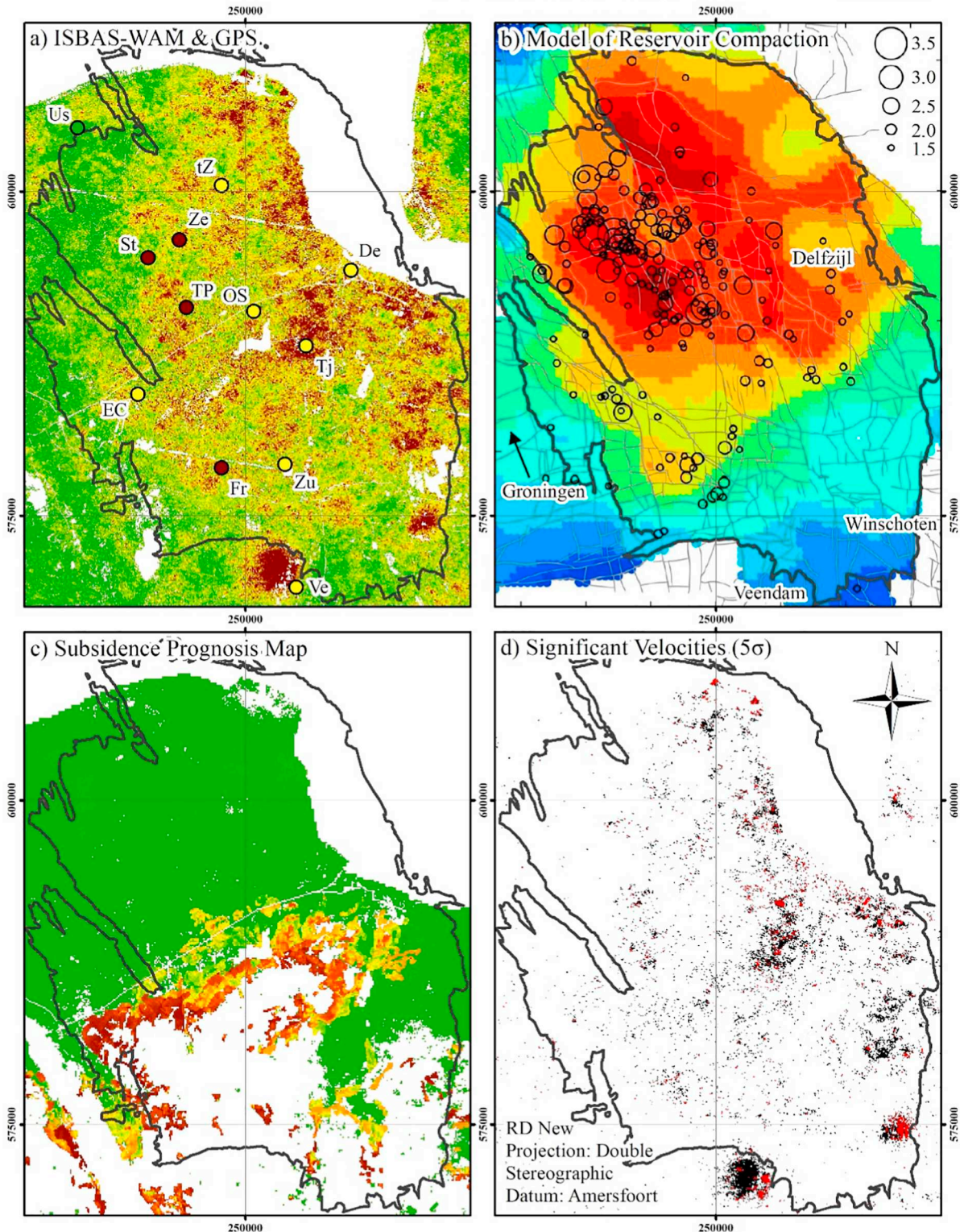
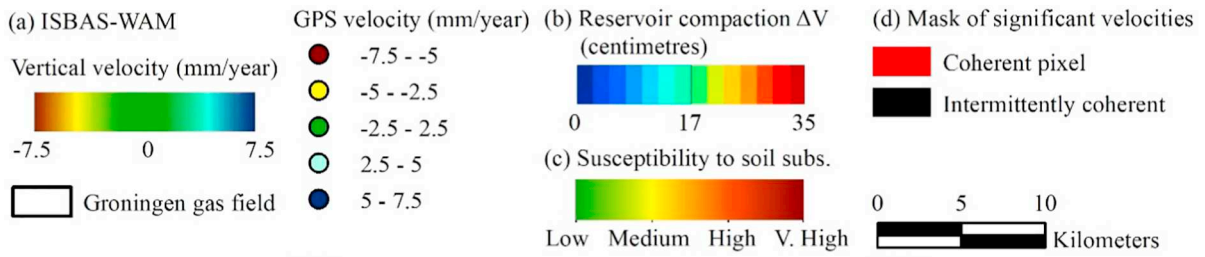


Fig. 10. Heathland deformation: (a) CORINE Land Cover inventory (European Environment Agency, 2012), (b) ISBAS-WAM vertical velocities (mm/year) and (c) Mask of statistically significant deformations at 5σ (99.99994%) confidence level at Utrecht Hill Ridge. (d) CORINE Land Cover inventory (European Environment Agency, 2012), (e) ISBAS-WAM vertical velocities (mm/year) and (f) Mask of statistically significant deformations at 5σ (99.99994%) confidence level at Hoge Veluwe National Park. (g) CORINE Land Cover inventory (European Environment Agency, 2012), (h) ISBAS-WAM vertical velocities (mm/year) and (i) Mask of statistically significant deformations at 5σ (99.99994%) confidence level at Sallandse Heuvelrug National Park. European Environment Agency © 2012.



(caption on next page)

Fig. 11. Subsidence over the Groningen field: (a) ISBAS-WAM vertical velocities, GPS velocities and Groningen gas field, (b) Model of reservoir compaction from 1960 to 2012, earthquake epicentres for $M_L \geq 1.5$ from 1995 to 2012 and Groningen gas field (adapted with permission from Bourne et al., 2014), (c) Subsidence prognosis map and Groningen gas field (De Lange et al., 2011; Climate Impact Atlas, 2019) and (d) Mask of statistically significant velocities at 5 σ (99.99994%) confidence level and Groningen gas field. Climate Impact Atlas © 2019.

(Fig. 2a) and that dry heath is unaffected by variations in the phreatic surface (Sallandse Heuvelrug, 2018), deformation might be attributed to the erosion of the subsurface of coarse sand and the top layer of fine sand. Management practises such as the mowing and burning of heath might also contribute to this effect. Subsidence in these areas spatially correlates to the areas of heathland and these measurements, which almost entirely relate to intermittently coherent pixels, are reliable at the 5 σ level (Fig. 10c,f,i).

5.4. Gas extraction

The subsidence observed within the perimeter of the Groningen gas field in the north-east of the Netherlands (Fig. 11) has been well documented (Ketelaar, 2009; de Waal et al., 2015). Subsidence has previously been identified over the gas field by applying PSI to ERS and ENVISAT data, with rates in the range of 4–7 mm/year for the period 1992–2007 (Ketelaar, 2009). Slightly higher subsidence rates were calculated at some 7–8 mm/year as of 2015 (Pijpers and van der Laan, 2015; Van Thienen-Visser and Breunese, 2015). However, production was restricted from 54 billion m³ in 2013 to 27 billion m³ in 2015/16 (Van 't Hof, 2017; Van Thienen-Visser et al., 2018) because of a correlation established between rates of production and the frequency and magnitude of earthquakes (Bourne et al., 2014). The estimated maximum predicted subsidence due to gas production up to 2050, as calculated in the 2015 Nederlandse Aardolie Maatschappij status report (NAM, 2015), is 45 cm (13.3 mm/year). The ISBAS-WAM reveals that the mean velocity within the perimeter the Groningen field for 2015–2017 is -4.07 ± 1.07 mm/year, which has a standard deviation of 2.03 mm. Fig. 11d shows that much of this deformation is significant at the 5 σ confidence level, even though located in a largely rural area where coherence is typically intermittent.

As an additional validation of the ISBAS-WAM, velocities from a sample of 12 GPS stations (NAM, 2018) for the same period of Sentinel-1 acquisitions over the Groningen area were compared to the corresponding nearest neighbour ISBAS velocity (Table 4; Fig. 11a). The average GPS velocity was -4.44 ± 0.78 mm/year (at the 95% confidence level) while the average velocity for the corresponding locations in the ISBAS-WAM was -4.67 ± 1.18 mm/year, indicating that the two sets of deformation measurements concur. Estimated rates and

Table 4
Comparison of GPS and nearest neighbour ISBAS-WAM velocities over the Groningen gas field for the period 12th May 2015–13th May 2017. The locations of GPS monitoring stations are shown in Fig. 11a.

GPS monitoring station	GPS average velocity (mm/year)	ISBAS-WAM average velocity (mm/year)	Error difference (mm/year)
Delfzijl (De)	-4.05	-6.14	2.09
Ems Canal (EC)	-4.35	-2.61	-1.74
Froombosch (Fr)	-5.10	-3.93	-1.17
Over-shielded (OS)	-4.45	-4.40	-0.05
Stedum (St)	-5.15	-3.30	-1.85
Ten Post (TP)	-5.75	-4.75	-1.00
Tjuchem (Tj)	-4.00	-8.62	4.62
Usquert (Us)	-0.90	-1.40	0.50
Veendam (Ve)	-4.85	-5.30	0.45
't Zandt (tZ)	-4.75	-5.24	0.49
Zuiderveen (Zu)	-4.45	-6.12	1.67
Zeerijp (Ze)	-5.5	-4.25	-1.25
Mean	-4.44	-4.67	0.23
RMSE	-	-	1.82

patterns of deformation in the north Netherlands are complex given the contributions of deformation from shallow Holocene-related (i.e. peat) and deep sources (i.e. gas production) (Hanssen and Cuenca, 2012) and, despite agreement, it is still important to note that GPS and ISBAS measurements are not wholly comparable. GPS antennae are usually attached to built structures which are likely to have foundations that extend deeper than the Holocene layer. Therefore, any movement of such antenna is most likely associated with deeper sources of motion, such as gas production from Groningen. Conversely, the ISBAS measurements capture the combined deformation signal originating from both Holocene and deeper sources. An example of the incompatibility of the two measurements is at the Tjuchem station, located in an area of peat soil between Groningen and Delfzijl which is highly susceptibility to soil subsidence, where the ISBAS measurement is over twice the magnitude of that measured by GPS (Table 4; Fig. 11a,c). Further, the GPS measures the velocity of a point target, whereas the ISBAS velocity is representative of the sum of motions of a 90×90 m area, which can contain a mixture of hard and soft targets.

5.5. Salt mining

Subsidence in the north of the Netherlands also relates to underground salt mining. Two subsidence bowls coincide with salt mines in the Veendam concession, specifically within the bounds of the Veendam and Adolf van Nassau II & III license areas (Fig. 12a). The maximum subsidence over Veendam between 1993 and 2004 was measured as 170 mm (on average corresponding to ~ 15 mm/year) by levelling and 155 mm (~ 14 mm/year) by PSI on ERS data (Humme, 2007). The Sentinel-1 analysis indicates subsidence in the region continued into 2015–2017, the majority of which occurs in a rural area and is predominantly characterised by intermittently coherent pixels with a high degree of confidence (5 σ) (Fig. 12b,c). A maximum rate of subsidence of -18.32 ± 0.96 mm/year and -18.06 ± 0.86 mm/year is observed over Veendam and Adolf van Nassau II & III respectively.

Deformation also occurs in Friesland within the Barradeel II license area, centred on borehole BAS-4 which has been utilized for solution mining since 2006 (Fig. 12d). Subsidence reaches a maximum of -13.77 ± 1.42 mm/year and is characterised with a high degree of confidence (5 σ) over agricultural fields (Fig. 12e,f). Subsidence was previously identified over BAS-1 and BAS-2 using PSI in conjunction with ERS and ENVISAT data (Humme, 2007). BAS-1 is now utilized as a reserve cavern, while BAS-2 ceased operation in 2004. As expected, a well-defined subsidence bowl is no longer present over this area given that salt production has all but ceased. Some deformation is observed but this is more likely to be related to soil subsidence rather than deeper geological processes given that it is less spatially correlated than would be expected of a typical subsidence bowl overlying a salt mine.

5.6. Coal mining

The largest resources of Dutch coal exist in the southern province of Limburg, which were exploited extensively until 1965. Long term extraction can result in subsidence following the collapse of mine galleries and groundwater pumping. Once abandoned, pumping regimes cease and uplift often occurs when pore pressure of the overburden increases as groundwater flows back to hydrostatic equilibrium (Bekendam and Pöttgens, 1995). Uplift (or heave) of up to approximately 5 mm/year is identified over the Roer Valley Rift System in the south east of the Netherlands (Fig. 13). Surface heave has been previously identified between 1992 and 2009 using PSI, ranging from 1 to 8 mm/year and

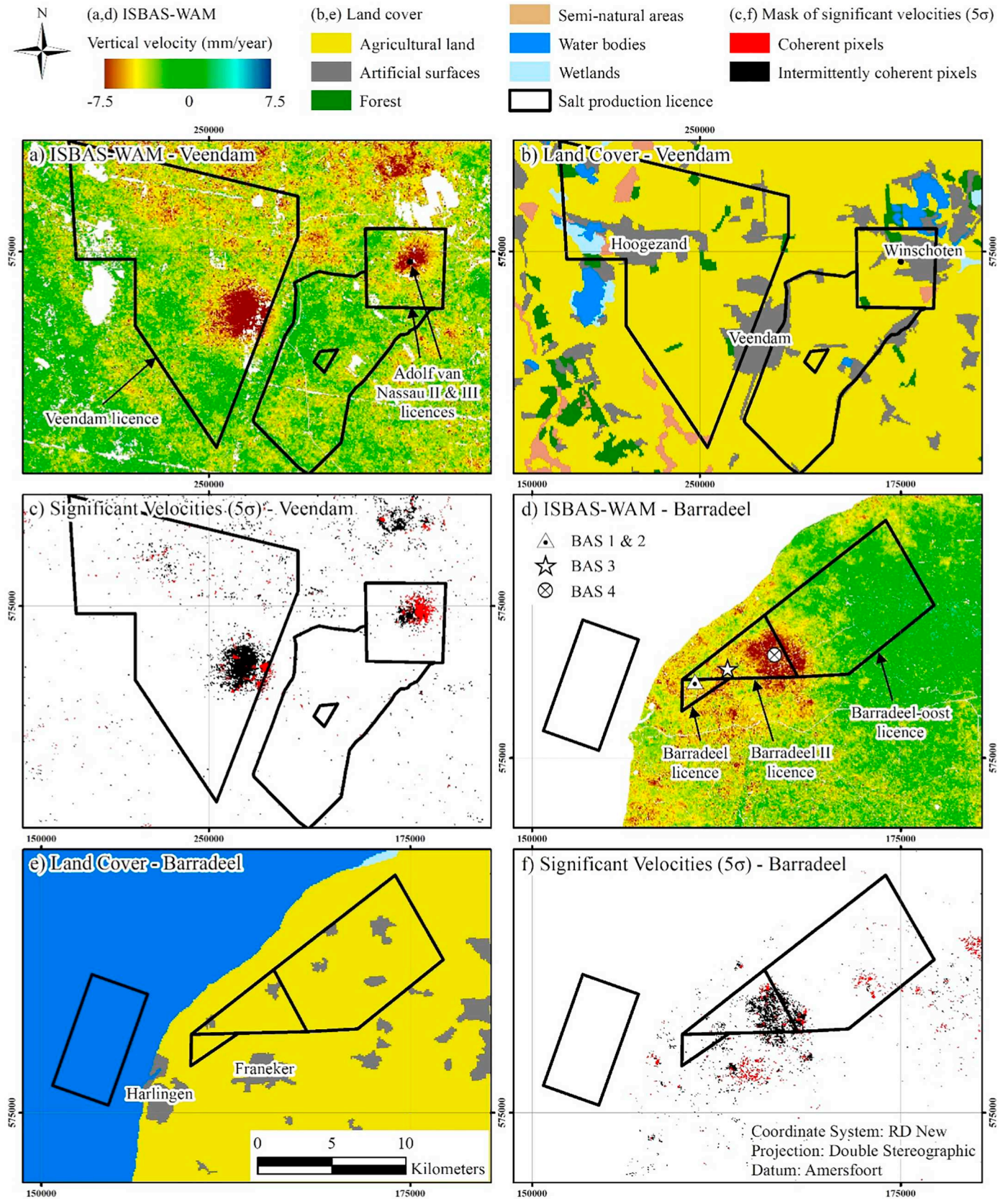


Fig. 12. Subsidence attributed to salt mining in the north of the Netherlands: (a) ISBAS-WAM vertical velocities (mm/year), (b) CORINE Land Cover inventory (European Environment Agency, 2012) and (c) Mask of statistically significant deformations at 5σ (99.99994%) confidence level over the Veendam concession, Groningen. (d) ISBAS-WAM vertical velocities (mm/year), (e) CORINE Land Cover inventory (European Environment Agency, 2012) and (f) Mask of statistically significant deformations at 5σ (99.99994%) confidence level over the Barradeel concession, Franeker. European Environment Agency © 2012.

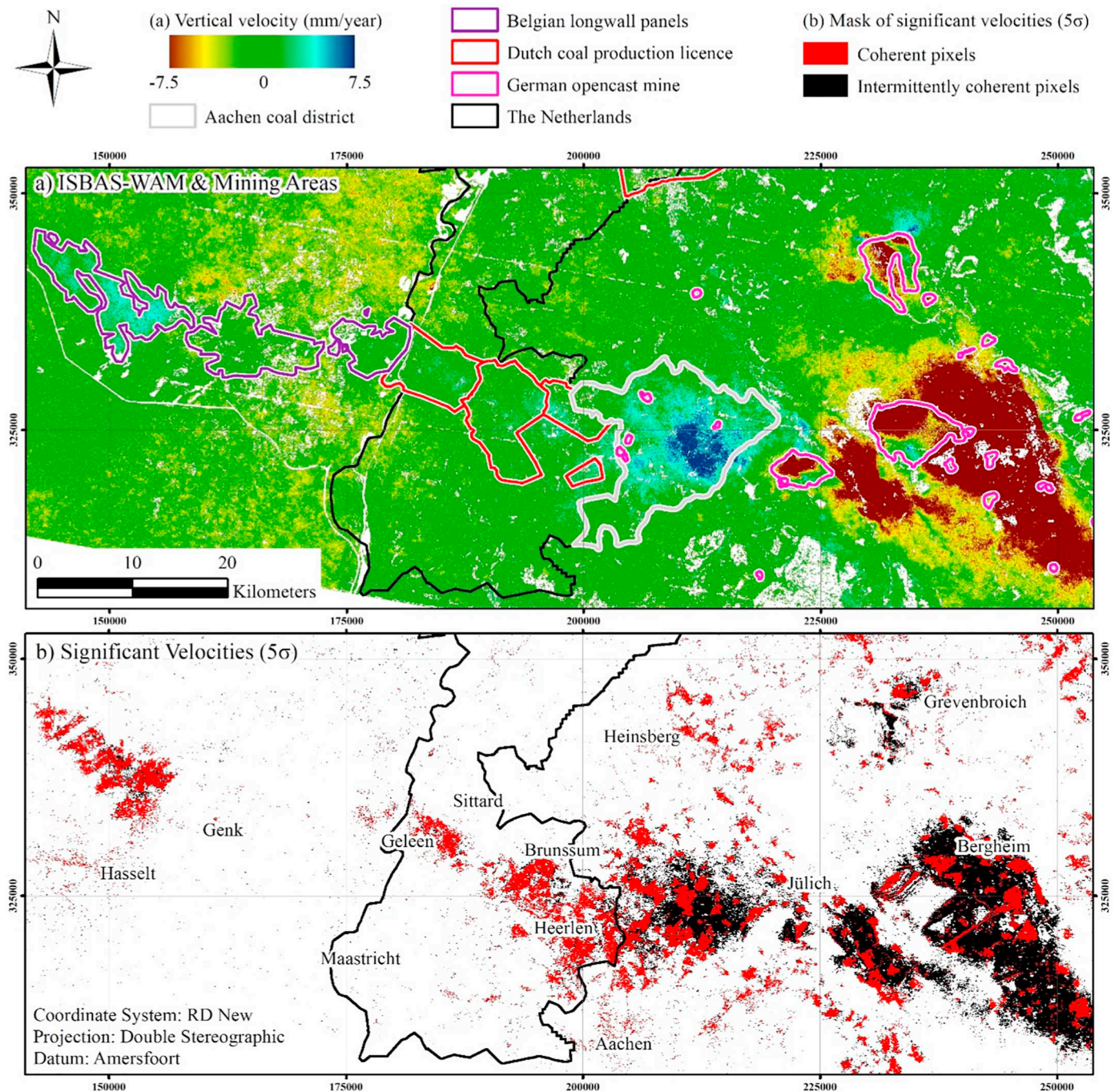


Fig. 13. Mining related deformations covering Belgium, the Netherlands and Germany: (a) ISBAS-WAM vertical velocities (mm/year) and mining areas and (b) Mask of statistically significant deformations at 5σ (99.99994%) confidence level.

significantly correlated to rising groundwater following the cessation of pumping in the early 1990s (Cuenca et al., 2013). Uplift over the course of the 1990s and 2000s was greatest around Geleen towards the western half of the mine concession and to a lesser extent in the east towards Brunssum. The ISBAS-WAM shows that this trend has reversed, with uplift now greater in the eastern part.

Uplift also occurs in the neighbouring Aachen coal district in Germany and the Belgian Campine Basin (Fig. 13). In the Aachen district, greater rates of uplift of up to 11 mm/year occur, suggesting that the rates of groundwater rebound for the period May 2015–May 2017 are greater in the Aachen district than in the Netherlands. The Belgian mines were closed between 1966 and 1992; however, no measurements of ground-water levels have been taken since closure (Vervoort and

Declercq, 2017). Nonetheless, using ERS and ENVISAT data, Vervoort and Declercq (2017) identified residual subsidence in the west of the Campine Basin for a period of ~ 10 years after closure, whilst the uplift was found in the east in 1992, 4–5 years after closure. Surface uplift in Belgium is now of a greater magnitude in the west, up to 6 mm/year, indicating that groundwater levels are now rising faster in the west.

Large areas of subsidence are associated with the Rhineland lignite mining region, as also previously detected using PSI (Cuenca et al., 2011; Hanssen and Cuenca, 2012). The subsidence within open cast mines corresponds to erosion of the surfaces due to extraction and the effects of dewatering programmes. Subsidence here is typically between -10 mm/year and -15 mm/year and deformation extends far beyond the extents of the mines due to groundwater pumping (Fig. 13).

Table 5

Data requirements for an average velocity European deformation map for a two-year period using Sentinel-1 data.

Statistic	Ascending Europe-WAM
Land surface area (km ²)	4,914,364
N° of frames	293
N° of images	35,160
Vol. of imagery (Terabytes)	141
N° interferometric stacks	440
Vol. of processed interferometric stacks (Terabytes)	396
Cumulative processing time (days)	1320
Modelled N° of solutions	1,706,145,321
Modelled density (solutions/km ²)	347
Modelled ground coverage (%)	87
Modelled mean standard error (mm/year)	1.10

6. Operational monitoring outlook

Although InSAR is now a mature technology, it is still far less established in comparison to more conventional surveying techniques such as GPS-GNSS, total stations and levelling. Whilst Italy has had a national PSI database for several years (Costantini et al., 2017), Copernicus has been the catalyst for other European countries, such as Norway, France, Denmark, Germany and the Netherlands (ESA, 2017; Oyen, 2017; NGU, 2019), to transition from ad hoc surveys into systematic operational nationwide monitoring. The results presented here demonstrate that the processing flow has the potential to be scaled for methodical production. However, such production is expensive in relation to storage, memory and computational power and presents a variety of challenges with respect to tasking capability and big data. This challenge is illustrated by the calculation of the feasibility of a single geometry European-wide product, which highlights the substantial quantity of imagery required, volume of intermediate data to be produced and the number of measurements which will be computed (Table 5; Fig. 14). Furthermore, to generate the absolute vertical and horizontal components of motion, solutions from both ascending and descending geometries are required, and to determine time-series for each pixel, residual phase components need to be unwrapped, which are significant additional computational loads.

The migration of the required software onto a Cloud computing environment provides a viable solution to negate volume and efficiency issues and have already demonstrated the potential to deliver efficient multi-user services for InSAR (e.g. De Luca et al., 2017). Central to efficient processing is automation; computation via the ISBAS method currently requires relatively minimal operator interaction, such that only relatively minor modifications would be required to fulfil this objective. Automated processing in combination with regular, near global, systematic acquisitions from the Sentinel-1 mission would be a potentially unprecedented resource of ‘big’ InSAR data which could be transformational for the downstream EO community.

The quality of such a volume of autonomously derived data is central to ensure deformation information is reliable. In this study it has been demonstrated that on average millimetre precision was achieved for nearly 20 million ISBAS solutions. The Netherlands has an abundance of geodetic infrastructure (e.g. gravimeter network, GNSS reference stations, Normaal Amsterdams Peil height reference system, regular national-scale airborne LiDAR) for which to corroborate spaceborne InSAR measurements. However, elsewhere in Europe, the availability of such accurate and precise ground truth data with sufficient spatial and temporal sampling is less common. Despite not performing any absolute referencing, ISBAS measurements concur with independent GPS data over Groningen. This indicates that reliable results can be achieved without referencing, which bodes well for forthcoming products in countries where geodetic ground truth is unavailable.

Future operational services need to be a multi-disciplinary

undertaking, where InSAR specialists work alongside engineers, geologists, geophysicists and alike to combine InSAR datasets with ancillary information, such as lithological maps, land cover/use, DEMs, spatial development data and landslide inventories, to produce individual application-based products where deformations are evaluated and interpreted by geologists. For example, by combining information on the spatial distribution and severity of recorded infrastructure damages with concurrent satellite-derived deformation measurements, an empirical cause-effect relationship can be established and validated to produce damage forecasting models (e.g. Peduto et al., 2018). Determining subsidence and settlement risk is a difficult and complex task that technical and scientific communities responsible for land-use planning and urban management rely upon (Peduto et al., 2017). Such accurate risk and vulnerability information on a continental scale have enormous potential for providing information on potential geohazards.

7. Conclusion

The Netherlands has been subject to a multitude of initial studies that have highlighted the potential of InSAR to make monitoring strategies more cost-effective and efficient (e.g. Dentz et al., 2006; Dheenathayalan et al., 2011; Hopman et al., 2013; Peduto et al., 2016; Chang et al., 2017). This study demonstrates that, by utilizing large volumes of Sentinel-1 C-Band SAR data, national scale ground motion maps are now achievable following the establishment of the Copernicus programme. The ISBAS-WAM was produced from a total of 435 Sentinel-1 images through the computation of average velocities from six individual interferometric stacks, which were subsequently combined into a seamless mosaic. By utilizing the ISBAS method, 94% of the land surface area was surveyed, achieving unprecedented coverage solely using InSAR. The retrieval of low-resolution measurements over soft surfaces was crucial in achieving this, due the dominance of non-urban land cover in the Netherlands. The resulting ubiquitous spatial coverage aided the delineation and quantification of deformation features. A statistical analysis of velocities demonstrates that intermittently coherent measurements can provide reliable (5 σ), additional deformation information outside of urban areas. The main causes of deformation were attributed to compressible soils, infrastructure settlement, peat oxidation, gas production, salt mining and underground and opencast mining. Across the mosaic, the spatial distribution of deformation concurs with independent sources of data, such as previous PSI-based deformation maps (e.g. Cuenca et al., 2011; Hanssen and Cuenca, 2012; Chang et al., 2017; Oyen, 2017), models of subsidence and settlement susceptibility (De Lange et al., 2011; De Lange et al., 2012; Climate Impact Atlas, 2019), and quantitatively with GPS measurements over the Groningen gas field.

Nationwide deformation products are a powerful and cost-effective tool for informing risk mitigation strategies against geological issues resulting from natural and anthropogenic phenomena. Although cost estimations related to ground motion are not straightforward, damage associated with deformation in the Netherlands was estimated at over €3.5 billion in 2006 (Erkens et al., 2015). Attempts to mitigate this cost rely upon early identification and implementation of intermediary measures to prevent damage becoming considerably more serious. Examples have shown there can be an order of magnitude difference between reaching an asset in time to conduct repairs and having to undertake emergency works (Environment Agency, 2018). The delineation and quantification of subsidence at broader spatial scales is, therefore, crucial for the sustainable management of the environment and Earth resources (Van der Meulen et al., 2013) and is fundamentally embedded within Dutch government policy (Erkens et al., 2015).

Dense survey data of ground motions is vital to better comprehend the impact of ground heterogeneities (Ngan-Tillard et al., 2010). The ISBAS-WAM, which uniquely has near complete ground coverage, can be analysed to readily screen and identify affected regions, which may require more detailed local-scale follow-up geological and geotechnical

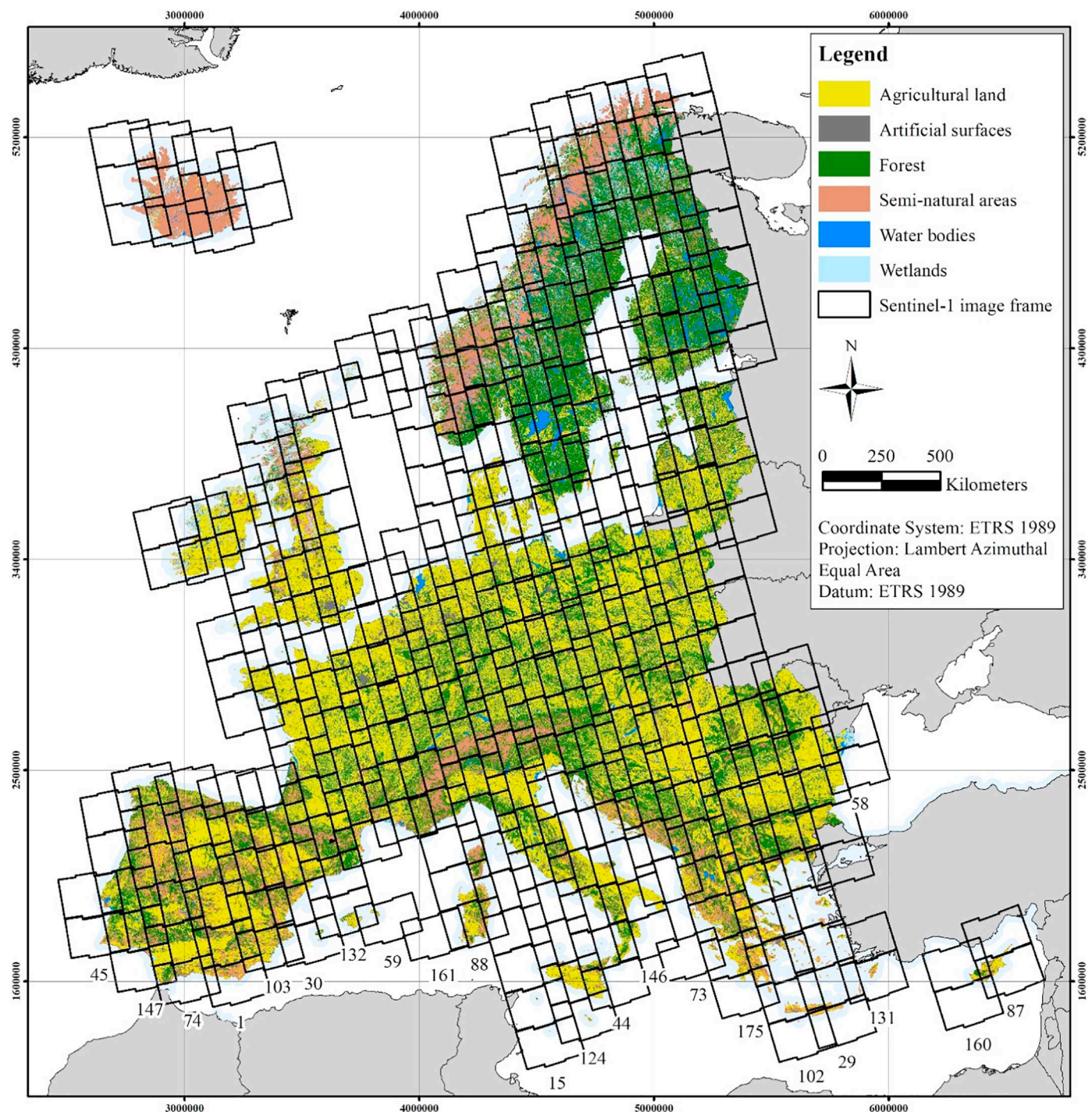


Fig. 14. Footprints of Sentinel-1 frames required to cover mainland Europe, encompassing the European Economic Area, Switzerland and the western Balkan countries, in an ascending geometry and CORINE Land Cover inventory (European Environment Agency, 2012). Labels define each relative orbital track. European Environment Agency © 2012.

investigation. The product provides critical information on Earth-structure interactions which can be utilized to inform the location, design, construction, operation and maintenance of infrastructure (e.g. Peduto et al., 2016). Such data can also be of use for optimising renovations to subsurface utilities, climate change adaption, as well as for insurance, engineering, road and rail companies, and local authorities, amongst others.

The only practical approach from which timely, reliable, systematic geohazard information can be derived throughout Europe is through the use of remote sensing. In this regard, the product generated over the

Netherlands clearly demonstrates the potential of the ISBAS method for providing precise deformation information on that scale. However, it is clear that the generation of regularly updated national or European products will not be simple due to computational challenges related to scaling-up the processing and the characteristics of the environment. In relation to computing, developing a systematic semi-automated production platform requires algorithmic, data management and product development challenges to be addressed. From an EO perspective, deriving velocities over complex topography (e.g. fjords and mountains) and non-urban areas – comprising 94% of the land cover in Europe

(European Environment Agency, 2012) – is challenging. Areas characterised by highly variable topography will require careful assimilation of results from multiple geometries; nonetheless, as demonstrated here, the ISBAS method offers an effective algorithmic solution for reliably monitoring deformation over vegetated environments with a high degree of confidence.

Declarations of interest

None.

Acknowledgements

The work conducted here was funded by the GeoEnergy Research Centre and Geomatic Ventures Limited. Sentinel-1 SAR data was sourced from the Copernicus Open Access Hub (<https://scihub.copernicus.eu/dhus/#/home>); mining and oil and gas data from NLOG (<http://www.nlog.nl/en/files-interactive-map>); topographic map, rail and roads from PDOK (<https://www.pdok.nl/en/producten/pdok-services/overzicht-urls>); landscape types and the subsidence and settlement susceptibility maps from the Climate Impact Atlas (<http://www.klimaat-effectatlas.nl/en/>); and GPS data from NAM (<https://nam-feitenencijfers.data-app.nl/>). Belgian longwall panels and the Aachen coal district were digitized from publicly available sources. The authors would like to acknowledge the anonymous reviewers who helped to improve the quality of the manuscript.

References

- Adam, N., Parizzi, A., Eineder, M., Crosetto, M., 2009. Practical persistent scatterer processing validation in the course of the Terrafirma project. *J. Appl. Geophys.* 69 (1), 59–65. <https://doi.org/10.1016/j.jappgeo.2009.07.002>.
- Adam, N., Gonzalez, F.R., Parizzi, A., Liebhart, W., 2011. Wide area persistent scatterer interferometry. In: *Geoscience and Remote Sensing Symposium (IGARSS)*, 2011 IEEE International. IEEE, pp. 1481–1484. <https://doi.org/10.1109/IGARSS.2011.6049347>.
- Bayer, B., Simoni, A., Schmidt, D., Bertello, L., 2017. Using advanced InSAR techniques to monitor landslide deformations induced by tunneling in the Northern Apennines, Italy. *Eng. Geol.* 226, 20–32. <https://doi.org/10.1016/j.enggeo.2017.03.026>.
- Bekendam, R.F., Pöttgens, J.J., 1995. Ground movements over the coal mines of southern Limburg, The Netherlands, and their relation to rising mine waters. In: *Land Subsidence (Proc. Fifth Int. Symp. On Land Subsidence, The Hague, October 1995)*. IAHS Publ. no. 234, pp. 3–12.
- Berardino, P., Fornaro, G., Lanari, R., Sansosti, E., 2002. A new algorithm for surface deformation monitoring based on small baseline differential SAR interferograms. *IEEE Trans. Geosci. Remote Sens.* 40 (11), 2375–2383. <https://doi.org/10.1109/TGRS.2002.803792>.
- Boni, R., Herrera, G., Meisina, C., Notti, D., Béjar-Pizarro, M., Zucca, F., González, P.J., Palano, M., Tomás, R., Fernández, J., Fernández-Merodo, J.A., 2015. Twenty-year advanced DInSAR analysis of severe land subsidence: the Alto Guadalentín Basin (Spain) case study. *Eng. Geol.* 198, 40–52. <https://doi.org/10.1016/j.enggeo.2015.08.014>.
- Bourne, S.J., Oates, S.J., Elk, J.V., Doornhof, D., 2014. A seismological model for earthquakes induced by fluid extraction from a subsurface reservoir. *J. Geophys. Res. Solid Earth* 119 (12), 8991–9015. <https://doi.org/10.1002/2014JB011663>.
- Capes, R., 2012, September. PanGeo: enabling access to geological information in support of GMES. In: 1st EAGE/GRSG Remote Sensing Workshop, <https://doi.org/10.3997/2214-4609.20143281>.
- Castelletto, N., Ferronato, M., Gambolati, G., Janna, C., Marzorati, D., Teatini, P., 2013. Can natural fluid pore pressure be safely exceeded in storing gas underground? *Eng. Geol.* 153, 35–44. <https://doi.org/10.1016/j.enggeo.2012.11.008>.
- Chang, L., Dollevoet, R.P., Hanssen, R.F., 2017. Nationwide railway monitoring using satellite SAR interferometry. *IEEE J. Sel. Top. Appl. Earth Obs. Remote Sens.* 10 (2), 596–604. <https://doi.org/10.1109/JSTARS.2016.2584783>.
- Chaussard, E., Amelung, F., Abidin, H., Hong, S.H., 2013. Sinking cities in Indonesia: ALOS PALSAR detects rapid subsidence due to groundwater and gas extraction. *Remote Sens. Environ.* 128, 150–161. <https://doi.org/10.1016/j.rse.2012.10.015>.
- Chaussard, E., Wdowinski, S., Cabral-Cano, E., Amelung, F., 2014. Land subsidence in Central Mexico detected by ALOS InSAR time-series. *Remote Sens. Environ.* 140, 94–106. <https://doi.org/10.1016/j.rse.2013.08.038>.
- Climate Impact Atlas, 2019. Soil Subsidence. Available at: <http://www.klimaat-effectatlas.nl/en/story-map-drought>, Accessed date: 20 March 2018.
- Colesanti, C., Ferretti, A., Prati, C., Rocca, F., 2003. Monitoring landslides and tectonic motions with the Permanent Scatterers Technique. *Eng. Geol.* 68 (1–2), 3–14. [https://doi.org/10.1016/S0013-7952\(02\)00195-3](https://doi.org/10.1016/S0013-7952(02)00195-3).
- Costantini, M., Ferretti, A., Minati, F., Falco, S., Trillo, F., Colombo, D., Novali, F., Malvarosa, F., Mammone, C., Vecchioli, F., Rucci, A., 2017. Analysis of surface deformations over the whole Italian territory by interferometric processing of ERS, Envisat and COSMO-SkyMed radar data. *Remote Sens. Environ.* 202, 250–275. <https://doi.org/10.1016/j.rse.2017.07.017>.
- Crosetto, M., Monserrat, O., Iglesias, R., Crippa, B., 2010. Persistent scatterer interferometry. *Photogramm. Eng. Remote Sens.* 76 (9), 1061–1069. <https://doi.org/10.14358/PERS.76.9.1061>.
- Cuenca, M.C., Hanssen, R., 2008. Subsidence due to peat decomposition in the Netherlands, kinematic observations from radar interferometry. In: *Proceedings Fringe 2007 Workshop, Frascati, Italy Workshop*, pp. 1–6.
- Cuenca, M.C., Hanssen, R., Hooper, A., Arikian, M., 2011. Surface deformation of the whole Netherlands after PSI analysis. In: *Proceedings Fringe 2011 Workshop, Frascati, Italy*, pp. 19–23.
- Cuenca, M.C., Hooper, A.J., Hanssen, R.F., 2013. Surface deformation induced by water influx in the abandoned coal mines in Limburg, the Netherlands observed by satellite radar interferometry. *J. Appl. Geophys.* 88, 1–11. <https://doi.org/10.1016/j.jappgeo.2012.10.003>.
- De Lange, G., Oosthoek, J.T., Gunnink, J.L.T., 2011. Maaiveldalings prognose voor 2050, onderdeel van de scenario's van het Deltamodel. In: *Deltascenario's, Report 1205747-000-veb-0005 (in Dutch)*. Technical Report. Deltare, Utrecht.
- De Lange, G., Bakr, M., Gunnink, J.L., Huisman, D.J., 2012. A predictive map of compression-sensitivity of the Dutch archaeological soil archive. *Conserv. Manag. Archaeol. Sites* 14 (1–4), 284–293. <https://doi.org/10.1179/1350503312.00000000024>.
- De Luca, C., Zinno, I., Manunta, M., Lanari, R., Casu, F., 2017. Large areas surface deformation analysis through a cloud computing P-SBAS approach for massive processing of DInSAR time series. *Remote Sens. Environ.* 202, 3–17. <https://doi.org/10.1016/j.rse.2017.05.022>.
- De Mulder, E.F.J., 1994. The Netherlands without engineering geology: no lands. *Eng. Geol.* 37 (1), 5–14. [https://doi.org/10.1016/0013-7952\(94\)90077-9](https://doi.org/10.1016/0013-7952(94)90077-9).
- Dentz, F., van Halderen, L., Pospel, B., Eshahny, S.S., Slobbe, C., Wortel, T., 2006. On the Potential of Satellite Radar Interferometry for Monitoring Dikes of the Netherlands. Geomatics, Faculty of Aerospace Engineering, Delft University of Technology Available at: https://d1rkab7tlqy5f1.cloudfront.net/TUDeft/Onderwijs/Opleidingen/Master/MSc_Geomatics/2006_Geomatics_Synthesis_Project.pdf, Accessed date: 21 January 2017.
- Dheenathayalan, P., Cuenca, M.C., Hanssen, R., 2011. Different approaches for PSI target characterization for monitoring urban infrastructure. In: *8th International Workshop on Advances in the Science and Applications of SAR Interferometry*. Frascati (Italy).
- Environment Agency, 2018. Space Derived Condition Assessment Tool for Critical National Infrastructure Structural Risk Management. (Personal Communication, Great George Street, London, 19th November 2018).
- Erkens, G., Bux, T., Dam, R., De Lange, G., Lambert, J., 2015. Sinking coastal cities. *Proc. Int. Assoc. Hydrol. Sci.* 372, 189–198. <https://doi.org/10.5194/piahs-372-189-2015>.
- Erkens, G., van der Meulen, M.J., Middelkoop, H., 2016. Double trouble: subsidence and CO 2 respiration due to 1,000 years of Dutch coastal peatlands cultivation. *Hydrogeol. J.* 24 (3), 551–568. <https://doi.org/10.1007/s10040-016-1380-4>.
- ESA, 2017. Fringe 2017 Workshop: Advances in the Science and Applications of SAR Interferometry and Sentinel-1 InSAR. Aalto University, Helsinki, Finland Available at: http://fringe.esa.int/files/Fringe2017_Abstract_Book_FINAL.pdf >, Accessed date: 24 November 2018.
- European Environment Agency, 2012. CORINE Land Cover 2012. Available at: <https://land.copernicus.eu/pan-european/corine-land-cover/clc-2012/view>, Accessed date: 21 January 2018.
- Ferretti, A., Prati, C., Rocca, F., 2001. Permanent scatterers in SAR interferometry. *IEEE Trans. Geosci. Remote Sens.* 39 (1), 8–20. <https://doi.org/10.1109/36.898661>.
- Ferretti, A., Fumagalli, A., Novali, F., Prati, C., Rocca, F., Rucci, A., 2011. A new algorithm for processing interferometric data-stacks: SqueeSAR. *IEEE Transactions on Geoscience and Remote Sensing* 49 (9), 3460–3470. <https://doi.org/10.1109/TGRS.2011.2124465>.
- Gee, D., Sowter, A., Novellino, A., Marsh, S., Gluyas, J., 2016. Monitoring land motion due to natural gas extraction: Validation of the Intermittent SBAS (ISBAS) DInSAR algorithm over gas fields of North Holland, the Netherlands. *Mar. Pet. Geol.* 77, 1338–1354. <https://doi.org/10.1016/j.marpetgeo.2016.08.014>.
- Gee, D., Bateson, L., Sowter, A., Grebby, S., Novellino, A., Cigna, F., Marsh, S., Banton, C., Wyatt, L., 2017. Ground motion in areas of abandoned mining: application of the Intermittent SBAS (ISBAS) to the Northumberland and Durham Coalfield, UK. *Geosciences* 7 (3), 85. <https://doi.org/10.3390/geosciences7030085>.
- Grujters, S., van der Krogt, R., 2013. TerraFirma and SubCoast: using satellite data for flood related issues and ground subsidence. In: *EGU General Assembly Conference Abstracts*. vol. 15.
- Hanssen, R.F., Cuenca, M.C., 2012. Absolute Wide Scale Subsidence Map of the Netherlands. European Commission Research Executive Agency, Brussels, Belgium (October 2012). 27p. Available at: <http://www.subcoast.eu/alfresco/d/d/workspace/SpacesStore/2be57ae8-a69c-48da-b06e-816a3f85e36d/D3.2.1%20Absolute%20Nation%20Wide%20Map.pdf> >, Accessed date: 17 June 2018.
- Hooper, A., Zebker, H., Segall, P., Kampes, B., 2004. A new method for measuring deformation on volcanoes and other natural terrains using InSAR persistent scatterers. *Geophys. Res. Lett.* 31 (23), L23611. <https://doi.org/10.1029/2004GL021737>.
- Hooper, A., 2008. A multi-temporal InSAR method incorporating both persistent scatterer and small baseline approaches. *Geophysical Research Letters* 35 (16). <https://doi.org/10.1029/2008GL034654>.
- Hopman, V., de Lange, G., Vonnhögen, L., Kruijver, P., van Leijen, F., Ianoschi, R., 2013. Report on Pilot Service Rhine-Meuse Delta, Subcoast Deliverable D3.2.3. Available at: http://www.subcoast.eu/alfresco/d/d/workspace/SpacesStore/d7ea539e-ae29-460b-be82-50ca2b2ab011/D3.2.3%20SubCoast%20Report%20Rhine%20Meuse%20Delta_final.pdf >, Accessed date: 24 July 2018.

- Humme, A.J.M., 2007. Point Density Optimization for SAR Interferometry: A Study Tested on Salt Mine Areas. Doctoral Dissertation, MS Thesis, Department of Earth Observation and Space Systems, Faculty of Aerospace Engineering, Delft University of Technology, Delft, the Netherlands.
- Ketelaar, V.B.H., 2009. Satellite Radar Interferometry: Subsidence Monitoring Techniques. *Remote Sens. and Digital Image Processing*, vol. 13 Springer (243 pp).
- Lu, Z., Kwoun, O.I., 2008. Radarsat-1 and ERS InSAR analysis over southeastern coastal Louisiana: Implications for mapping water-level changes beneath swamp forests. *IEEE Trans. Geosci. Remote Sens.* 46 (8), 2167–2184. <https://doi.org/10.1109/TGRS.2008.917271>.
- Marshall, C., Large, D.J., Athab, A., Evers, S.L., Sowter, A., Marsh, S., Sjögersten, S., 2018. Monitoring tropical peat related settlement using ISBAS InSAR, Kuala Lumpur International Airport (KLIA). *Eng. Geol.* 244, 57–65. <https://doi.org/10.1016/j.enggeo.2018.07.015>.
- NAM, 2015. Subsidence by Natural Gas Extraction. NAM Fields in Groningen, Friesland and the North of Drenthe: Status Report 2015 and Prognosis to the Year 2080. Nederlandse Aardolie Maatschappij, Assen, the Netherlands Available at. <http://www.commissiebodemdaling.nl/files/Status%20rapport%202015-final.pdf>.
- NAM, 2018. Land Subsidence GPS Measurements. [online] Available at. <https://nam-feitenencijfers.data-app.nl/embed/component/?id=Charts/bodemdaling/gps-metingen>, Accessed date: 27 July 2018.
- Ngan-Tillard, D., Venmans, A., Slob, E., 2010. Total engineering geology approach applied to motorway construction and widening in the Netherlands: part I: a pragmatic approach. *Eng. Geol.* 114 (3–4), 164–170. <https://doi.org/10.1016/j.enggeo.2010.04.013>.
- NGU, 2019. InSAR Norway. Geological Survey of Norway Available at. <https://insar.ngu.no/>, Accessed date: 4 February 2019.
- Oyen, A., 2017. Towards an InSAR Based Nationwide Monitoring Strategy in the Netherlands. Rijkswaterstaat (Ministry of Infrastructure and the Environment), the Netherlands Available at. <http://fringe.esa.int/files/presentation526.pdf>, Accessed date: 21 January 2018.
- Peduto, D., Huber, M., Speranza, G., van Ruijven, J., Cascini, L., 2016. DInSAR data assimilation for settlement prediction: case study of a railway embankment in the Netherlands. *Can. Geotech. J.* 54 (4), 502–517. <https://doi.org/10.1139/cgj-2016-0425>.
- Peduto, D., Nicodemo, G., Maccabiani, J., Ferlisi, S., 2017. Multi-scale analysis of settlement-induced building damage using damage surveys and DInSAR data: a case study in the Netherlands. *Eng. Geol.* 218, 117–133. <https://doi.org/10.1016/j.enggeo.2016.12.018>.
- Peduto, D., Elia, F., Montuori, R., 2018. Probabilistic analysis of settlement-induced damage to bridges in the city of Amsterdam (the Netherlands). *Transp. Geotech.* 14, 169–182. <https://doi.org/10.1016/j.trgeo.2018.01.002>.
- Pijpers, F., van der Laan, D.J., 2015. Phase 1 Update May 2015: Trend Changes in Ground Subsidence in Groningen. Statistics Netherlands Scientific Paper, CBS (14 pp).
- Rohmer, J., Loschetter, A., Raucoules, D., De Michele, M., Raffard, D., Le Gallo, Y., 2015. Revealing the surface deformation induced by deep CO₂ injection in vegetated/agricultural areas: the combination of corner-reflectors, reservoir simulations and spatio-temporal statistics. *Eng. Geol.* 197, 188–197. <https://doi.org/10.1016/j.enggeo.2015.08.005>.
- Sallandse Heuvelrug, 2018. About the Area. Nationaal Park De Sallandse Heuvelrug Available at. <http://www.sallandseheuvelrug.nl/over-het-park>, Accessed date: 24 July 2018.
- Sowter, A., Bateson, L., Strange, P., Ambrose, K., Syafiudin, M.F., 2013. DInSAR estimation of land motion using intermittent coherence with application to the South Derbyshire and Leicestershire coalfields. *Remote Sens. Lett.* 4 (10), 979–987. <https://doi.org/10.1080/2150704X.2013.823673>.
- Sowter, A., Amat, M.B.C., Cigna, F., Marsh, S., Athab, A., Alshammari, L., 2016. Mexico City land subsidence in 2014–2015 with Sentinel-1 IW TOPS: results using the Intermittent SBAS (ISBAS) technique. *Int. J. Appl. Earth Obs. Geoinf.* 52, 230–242. <https://doi.org/10.1016/j.jag.2016.06.015>.
- Sowter, A., Athab, A., Novellino, A., Grebby, S., Gee, D., 2018. Supporting energy regulation by monitoring land motion on a regional and national scale: a case study of Scotland. *Proc. Inst. Mech. Eng. A J. Power Energy* 232 (1), 85–99. <https://doi.org/10.1177/0957650917737225>.
- Themistocleous, K., Cuca, B., Agapiou, A., Lysandrou, V., Tzouvaras, M., Hadjimitsis, D.G., Kyriakides, P., Kouhartsiouk, D., Margottini, C., Spizzichino, D., Cigna, F., 2016. The protection of cultural heritage sites from geo-hazards: the PROTHEGO project. In: Euro-Mediterranean Conference. Springer International Publishing, pp. 91–98. https://doi.org/10.1007/978-3-319-48974-2_11. October.
- Torres, R., Snoeij, P., Geudtner, D., Bibby, D., Davidson, M., Attema, E., Potin, P., Rommen, B., Floury, N., Brown, M., Traver, I.N., 2012. GMES Sentinel-1 mission. *Remote Sens. Environ.* 120, 9–24. <https://doi.org/10.1016/j.rse.2011.05.028>.
- UKRI, 2018. InSAR as a Tool to Evaluate Peatland Sensitivity to Global Change (NE/P014100/1). United Kingdom Research and Innovation Available at. <http://gtr.ukri.org/projects?ref=NE%2FP014100%2F1>, Accessed date: 20 April 2018.
- Van der Meulen, M.J., Doornbal, J.C., Gunnink, J.L., Stafleu, J., Schokker, J., Vernes, R.W., Van Geer, F.C., Van Gessel, S.F., Van Heteren, S., Van Leeuwen, R.J.W., Bakker, M.A.J., 2013. 3D geology in a 2D country: perspectives for geological surveying in the Netherlands. *Neth. J. Geosci.* 92 (4), 217–241. <https://doi.org/10.1017/S0016774600000184>.
- Van Thienen-Visser, K., Breunese, J., 2015. Induced seismicity of the Groningen gas field: history and recent developments. In: *The Leading Edge, Special Issue Injection Induced Seismicity*, pp. 665–671. <https://doi.org/10.1190/tle34060664.1>.
- Van Thienen-Visser, K., Roholl, J.A., van Kempen, B.M.M., Muntendam-Bos, A.G., 2018. Categorizing seismic risk for the onshore gas fields in the Netherlands. *Eng. Geol.* 237, 198–207. <https://doi.org/10.1016/j.enggeo.2018.02.004>.
- Vervoort, A., Declercq, P.Y., 2017. Upward surface movement above deep coal mines after closure and flooding of underground workings. *Int. J. Min. Sci. Technol.* 28, 53–59. <https://doi.org/10.1016/j.ijmst.2017.11.008>.
- Vonhögen, L.M., Doornbal, P.J., De Lange, G., Fokker, P.A., Gunnink, J.L., 2012. Subsidence in the Holocene delta of the Netherlands. In: *Proceedings of EISOLS 2010: Land Subsidence, Associated Hazards and the Role of Natural Resources Development*.
- Van 't Hof, W., 2017. Gas Production From the Groningen Field. Netherlands Ministry of Economic Affairs Available at. https://www.unece.org/fileadmin/DAM/energy/se/pdfs/nat_gas/geg/geg4_March2017/Item_4_-_vant_Hof_Groningen_Web.pdf, Accessed date: 12 March 2018.
- de Waal, J.A., Roest, J.P.A., Fokker, P.A., Kroon, I.C., Breunese, J.N., Muntendam-Bos, A.G., Oost, A.P., van Wirdum, G., 2012. The effective subsidence capacity concept: how to assure that subsidence in the Wadden Sea remains within defined limits? *Neth. J. Geosci.* 91-3, 385–399. <https://doi.org/10.1017/S0016774600000512>.
- de Waal, J.A., Muntendam-Bos, A.G., Roest, J.P.A., 2015. Production induced subsidence in the Groningen gas field – can it be managed? *Proc. IAHS* 372, 129–139. <https://doi.org/10.5194/piahs-372-129-2015>.
- Wang, Y., Day, J.L., Davis, F.W., 1998. Sensitivity of modeled C- and L-band radar backscatter to ground surface parameters in loblolly pine forest. *Remote Sens. Environ.* 66, 331–342. [https://doi.org/10.1016/S0034-4257\(98\)00074-1](https://doi.org/10.1016/S0034-4257(98)00074-1).
- Zebker, H.A., Villasenor, J., 1992. Decorrelation in interferometric radar echoes. *IEEE Trans. Geosci. Remote Sens.* 30 (5), 950–959. <https://doi.org/10.1109/36.175330>.

6. Conclusions and Recommendations

This chapter provides a review of the thesis by revisiting the aim and objectives. Each objective is discussed and reviewed to determine to what extent it has been achieved and recommendations for further research are stated.

6.1. Review of Aims and Objectives

The overall aim of this thesis is to demonstrate the potential of the Intermittent SBAS processing method and Sentinel-1 SAR data for enhanced capability to monitor ground movements related to geological hazards, with a focus on coal mining. This was broken down into three objectives:

- 1) Examine the extent to which the deformation regime changes over the lifespan of the coalfield using results derived from archive and, newly available, Sentinel-1 data.
- 2) Assess the capability of ISBAS measurements to be utilized to infer information on changes in groundwater levels over abandoned coalfields.
- 3) Evaluate the potential and determine challenges of utilizing Sentinel-1 for wide-area operational geohazard monitoring.

6.1.1. Long Term Coalfield Deformation Monitoring

The initial study conducted over the Northumberland and Durham coalfield was designed to revisit previous research that had applied a PSI technique to ERS and ENVISAT data that covered the 1990s and 2000s. The ISBAS method was applied to the archive data to increase the spatial density of measurements to aid the geological interpretation. Additionally, data from the Sentinel-1 satellite was utilized to facilitate an investigation of deformation over a three-decade period. The ISBAS results show that unexpected and changing amounts of ground motion can be present in areas of former mining, occurring long after extraction has ceased. Such motions followed a pattern of localised areas of areal subsidence and broader regional areas of heave. A relationship was ascertained that in areas of former mining, rising groundwater can be important in influencing surface motion. The data shows how multifaceted post-closure ground deformation regimes can be with a complex interaction between the local stress field, regional groundwater recovery and accommodation and delimiting of motion by faults.

The study highlighted some areas for further development, both in the application of ISBAS to monitor abandoned coalfields and in the use of Sentinel-1 data. With respect to the former, potential relationships between the observed motion and the geological, mining and hydrogeological data were investigated. Most notably, the positive correlation established between rising groundwater and surface deformation suggested that surface deformation

could be modelled based upon the rates of groundwater rise and vice-versa. The near complete coverage of the ISBAS measurements afford an excellent source of data to validate any modelled deformation. This formed the theoretical basis for the work conducted in Chapter 4.

With regards to the Sentinel-1 data, due to the TOPSAR configuration of the Sentinel-1 sensor, whilst each burst always images the same ground target with every satellite pass, the divisions between image frames are not consistent over time, hence, the location of the image frame shifts in azimuth. As a result, the Northumberland and Durham study site was completely covered by some images within the stack but not by others. The images that did not fully cover the study site could not be included in the analysis, as this would have resulted in unsurveyed sections of the study area. The ISBAS processing chain was modified to enable the concatenation of multiple image frames from the same track, to create a seamless strip of imagery containing as many frames as was required. The seamless strips of imagery facilitate processing over wide areas, which was the origin for the work in Chapter 5.

6.1.2. Sentinel-1 and ISBAS to Infer Change in Groundwater Levels

A method to map changes in groundwater levels was proposed in Chapter 4. This is based upon the principle of effective stress and concept of mine water ponds. First, a forward analytical model was implemented to relate changes in groundwater, as measured in

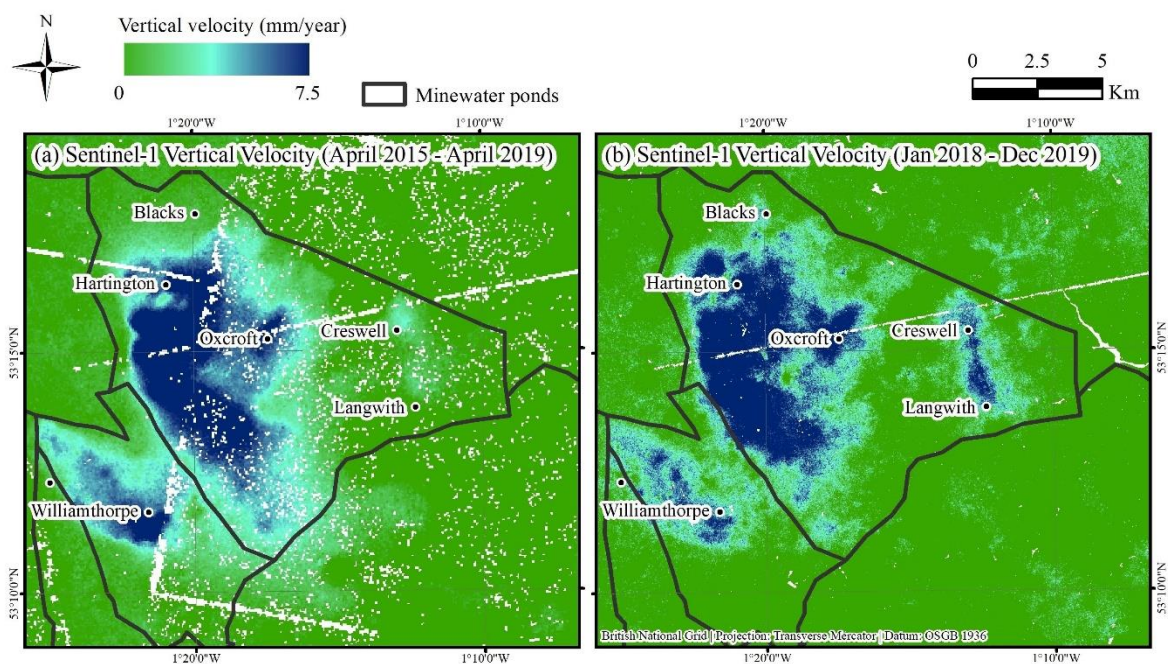


Figure 6.1. (a) Sentinel-1 vertical velocity (April 2015 – April 2019) and (b) Sentinel-1 vertical velocity (January 2018 – December 2019).

monitoring boreholes, to surface deformation. The 1D forward models at the borehole locations were calibrated using ISBAS deformation data. Subsequently, the calibrated forward model was implemented across the coalfield, before the ISBAS measurements were inverted to map the changes in groundwater with near complete spatial coverage. Finally, based upon the inverted measurements, the predicted time it will take for groundwater to discharge out of the Coal Measures rock was calculated.

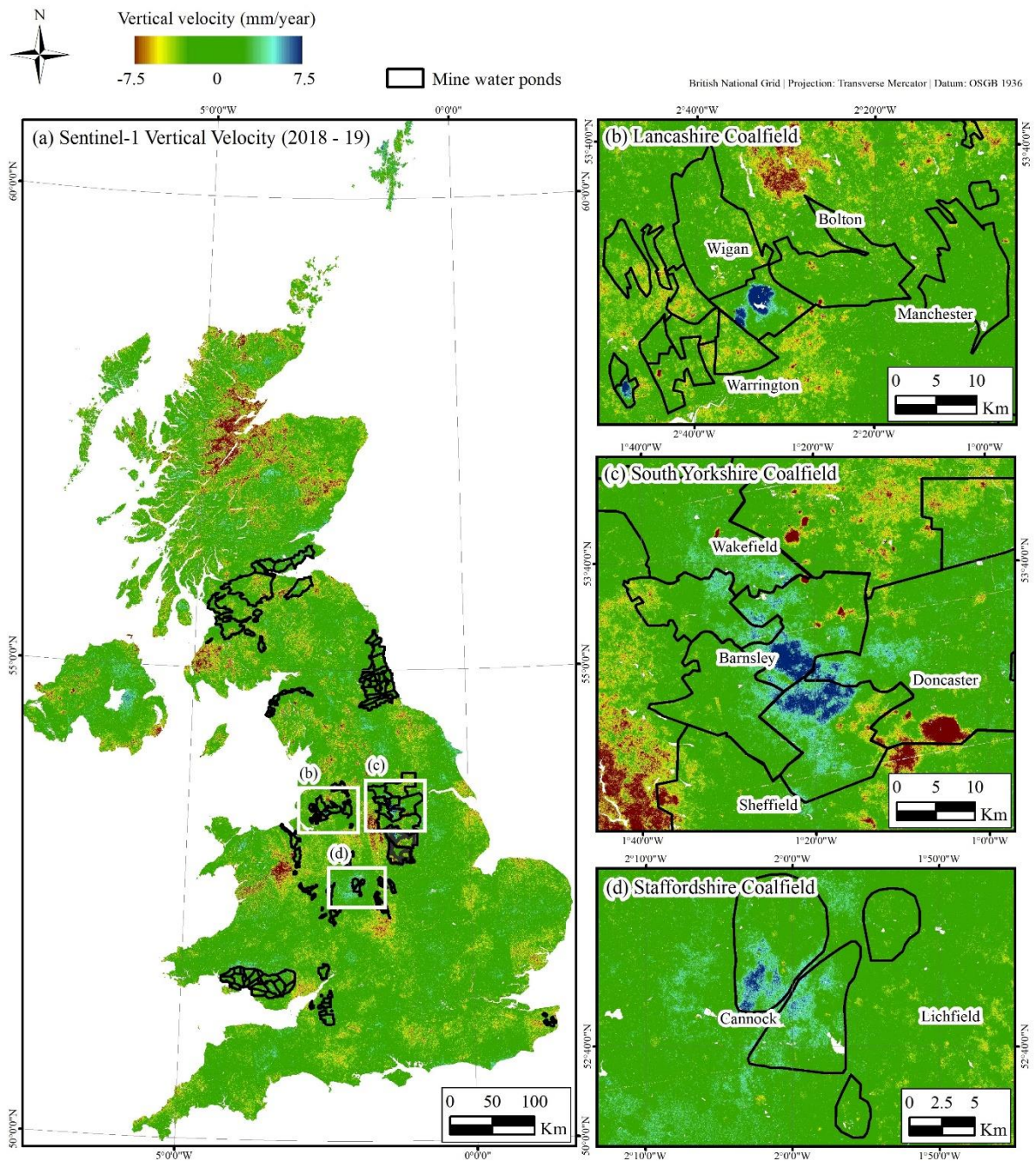


Figure 6.2. Average vertical velocity over the period January 2018 – December 2019: (a) United Kingdom; (b) Lancashire coalfield; (c) South Yorkshire coalfield; and (d) Staffordshire coalfield.

The investigation shows that ISBAS data can be utilized to help characterize flow and accumulation within recently abandoned coalfields. Such information can be utilized to aid the remediation strategy to enable decision makers to make more informed decisions regarding the need to pump at selected sites to avoid any undesired consequences of rising mine water. As previously noted, abandoned coalfields are highly dynamic and given the complexity and incomplete knowledge of the subsurface, groundwater can flow in unexpected directions.

The model was demonstrated over the recently abandoned Nottinghamshire coalfield. Rebound is expected in the North Deep pond, however, the Coal Authority note that this area is not behaving as expected and rebound is not occurring here. The ISBAS data support the Coal Authorities comment as no heave is measured in the Sentinel-1 analysis. This suggested that the connections to the Hartington pond are either not there or are located closer to the surface than expected. The ISBAS data utilized in Chapter 4 cover the period up to April 2019, more recent Sentinel-1 data processed up to December 2019 also do not measure any heave in the North Deep pond (Figure 6.1). However, an increase in the rate of heave is observed near the Creswell and Langwith boreholes which indicates a build-up of water on the barrier between the Hartington and North Deep pond. Continued monitoring of this area with ISBAS data will help to characterise any changes in groundwater regime and determine if/when a connection to the North Deep pond is established.

The groundwater mapping methodology proposed is relatively simple to apply and requires few parameters to be estimated, and therefore has the potential to be implemented over other recovering coalfields. An average velocity map of the United Kingdom, covering the years 2018 – 2019 (Figure 6.2), indicates that several other coalfields are currently undergoing rebound, including the Scottish, Lancashire, Yorkshire, Staffordshire and Leicestershire & South Derbyshire coalfields. Further research combining the wide-area mapping capability of Sentinel-1 and the modelling methodology proposed here, would provide the capability to estimate the change in groundwater levels in all UK coalfields. The Nottinghamshire coalfields are relatively well understood; however, fewer ground measurements are recorded in and less is known about other areas, such as the Lancashire coalfield. The use of InSAR would help to improve the understanding of the hydrogeology of such areas.

6.1.3. Wide-Area Operational Geohazard Monitoring

The study over the Netherlands demonstrated the wide-area potential of Sentinel-1 for operational monitoring. Six interferometric stacks were processed and mosaicked together containing over 19 million measurements. Measurements were generated over 94% of the land surface area, over agricultural fields, forests, semi-natural areas and wetlands. Such coverage was crucial due to the dominance of non-urban land cover and a statistical analysis demonstrated that ISBAS can provide reliable measurements in rural environments with a very high degree of confidence (5σ). Ground motion related to variety of potential geohazards was identified related to compressible soils, infrastructure settlement, peat

oxidation, gas production, salt mining and underground and opencast mining. Such motions were compared to, and saw good agreement with, ancillary data such as previous PSI-based deformation maps, models of subsidence and settlement susceptibility and GPS.

The calculation of the processing requirements for a Europe-wide map highlighted the substantial volume of imagery required, amount of data to be produced and number of measurements to be computed. The regular, near global, systematic acquisitions from the Sentinel-1 mission provides a valuable and unprecedented source of data for deformation monitoring. The Copernicus programme marks the transition into the era of big EO data. The shift from ad hoc production to scaled systematic processing presents new challenges as processing such a high volume and frequency of data outstrips conventional computing and storage capabilities. New solutions are required to help facilitate systematic and operational processing. The migration of the required software onto a Cloud computing environment provides a viable solution and have already demonstrated the potential to deliver efficient multi-user services for InSAR (e.g. Casu *et al.*, 2014; Zinno *et al.*, 2016; De Luca *et al.*, 2017). Such a configuration eliminates the need for physical servers and need to download Sentinel-1 scenes, which currently accounts for a sizeable proportion of the workflow, whereby access to all open data sets and full image archives are provided by web service access.

Central to efficient processing is automation; computation via the ISBAS method currently requires minimal operator interaction, such that only relatively minor modifications would be required to fulfil this objective. Procedures, such as the determination of temporal and perpendicular baselines, coherence and reference point could be selected during configuration. The minimum accepted threshold for coherent interferograms can be retrieved for an accepted spatial coverage or based upon a pre-determined acceptance of modelled standard error of velocities to guarantee a specified precision, as demonstrated on ERS data by Cigna & Sowter (2017). Terra Motion Limited are currently working to achieve this capability.

The modelled number of measurements over Europe was calculated as over 1700 million. Whilst the size of these data does not necessarily constitute a restriction, the ability to access and derive meaningful information in timely manner does. For example, the visualisation of this information in a point wise vector format far outstrips the capability of conventional GIS platforms and, therefore, restricts the ability of the end user to analyse it effectively. For ease of interpretation, outputs from the ISBAS method are in raster format which are more easily managed by end users. A more onerous challenge relates to the organisation and interpretation of time-series data, for which temporal information on the deformation is stored within each pixel. To gain real value from such measurements in a systematic and quantitative manner is beyond reasonable human competency and requires computation to detect patterns and change. Data mining tools are required to screen displacement time-series for the recognition of non-linear components, accelerations, decelerations and, more generally, any kind of deviation from a trend defined a priori. Automated and semi-automated classification methods for InSAR time-series, based upon statistical tests, have been previously proposed (e.g. Milone & Scepi, 2011, Cigna *et al.*, 2012, Berti *et al.*, 2013).

More recently, machine learning methods, which can be computationally less expensive and more scalable with large datasets, have been implemented for time-series change detection (e.g. Lattari *et al.*, 2019), as well as for short-term time-series forecasting (e.g. Ma *et al.*, 2020).

Finally, it is important that raw ground deformation data are managed with caution because they do not represent a quantitative assessment of risk, and without interpretation can be misleading to non-specialist users. Future services needed to be multi-disciplinary undertakings where InSAR measurements are combined with ancillary information such as lithological maps, land cover/use, DEMs, spatial development data and landslide inventories to produce individual application-based products where deformations are evaluated and validated geologists. For instance, a nation-scale change in mine water levels product could be generated over the UK, as discussed in Section 6.1.2.

6.2. Summary of Recommendations of Further Work

The following points have been drawn from the review of the aims and objectives as areas for further development and research:

- Investigate the application of the modelling methodology over other recently abandoned coalfields.
- Generate a value-add product from a wide-area mosaic, such as a quantitative estimate of the change in groundwater levels in UK coalfields.
- Increase the efficiency of the ISBAS analysis by full automation of the processing chain to facilitate operational wide-area processing. Investigate processing solutions on the Cloud.
- Implement statistical or machine learning methods to automatically analyse deformation time-series to detect trend deviations and change points.

6.3. Summary

Here, a review of the work conducted in this thesis has been presented. The aims and objectives of have been restated and reviewed to evaluate the extent to which these have been achieved. Subsequently, future areas of research have been discussed.

6.4. References

Berti, M., Corsini, A., Franceschini, S. and Iannacone, J.P., 2013. Automated classification of Persistent Scatterers Interferometry time series. *Natural Hazards and Earth System Sciences*, 13, pp.1945–1958. [http:// doi.org/10.5194/nhess-13-1945-2013](http://doi.org/10.5194/nhess-13-1945-2013)

Cigna, F. and Sowter, A., 2017. The relationship between intermittent coherence and precision of ISBAS InSAR ground motion velocities: ERS-1/2 case studies in the UK. *Remote Sensing of Environment*, 202, pp.177-198. <https://doi.org/10.1016/j.rse.2017.05.016>

Cigna, F., Tapete, D. and Casagli, N., 2012. Semi-automated extraction of Deviation Indexes (DI) from satellite Persistent Scatterers time series: tests on sedimentary volcanism and tectonically-induced motions. *Nonlinear processes in geophysics.*, 19(6), pp.643-655. <http://doi.org/10.5194/npg-19-643-2012>

Casu, F., Elefante, S., Imperatore, P., Zinno, I., Manunta, M., De Luca, C. and Lanari, R., 2014. SBAS-DInSAR parallel processing for deformation time-series computation. *IEEE Journal of Selected Topics in Applied Earth Observations and Remote Sensing*, 7(8), pp.3285-3296. <http://doi.org/10.1109/JSTARS.2014.2322671>.

De Luca, C., Zinno, I., Manunta, M., Lanari, R. and Casu, F., 2017. Large areas surface deformation analysis through a cloud computing P-SBAS approach for massive processing of DInSAR time series. *Remote Sensing of Environment*, 202, pp.3-17. <http://doi.org/10.1016/j.rse.2017.05.022>.

Lattari, F., Matteucci, M., Bonarini, A., Rucci, A., Bischoff, C., Basilico, M., Bianchi, M., Passera E., 2019. Recurrent Neural Networks for Trend Change Detection in InSAR Time Series. Available at:< <https://site.tre-altamira.com/wp-content/uploads/Recurrent-Neural-Networks-for-Trend-Change-Detection-in-InSAR-Time-Series.pdf>> [Accessed 12th August 2020]

Ma, P., Zhang, F. and Lin, H., 2020. Prediction of InSAR time-series deformation using deep convolutional neural networks. *Remote Sensing Letters*, 11(2), pp.137-145. <https://doi.org/10.1080/2150704X.2019.1692390>

Milone, G. and Scepi, G., 2011. A clustering approach for studying ground deformation trends in Campania region through PS-InSAR TM time series analysis. *J. Appl. Sci*, 11(4), pp.610-620. <http://doi.org/10.3923/jas.2011.610.620>

Zinno, I., Mossucca, L., Elefante, S., De Luca, C., Casola, V., Terzo, O., Casu, F. and Lanari, R., 2016. Cloud computing for earth surface deformation analysis via spaceborne radar imaging: A case study. *IEEE Transactions on Cloud Computing*, 4(1), pp.104-118. <http://doi.org/10.1109/TCC.2015.2440267>